eLIFE elifesciences.org

Appendix 1

RESEARCH ARTICLE

Dynamics of BMP signaling and distribution during zebrafish dorsal-ventral patterning

Autumn P Pomreinke†, Gary H Soh†, Katherine W Rogers†, Jennifer K Bergmann, Alexander J Bläßle, Patrick Müller*

Systems Biology of Development Group, Friedrich Miescher Laboratory of the Max Planck Society, Tübingen, Germany

Abstract During vertebrate embryogenesis, dorsal-ventral patterning is controlled by the BMP/Chordin activator/inhibitor system. BMP induces ventral fates, whereas Chordin inhibits BMP signaling on the dorsal side. Several theories can explain how the distributions of BMP and Chordin are regulated to achieve patterning, but the assumptions regarding activator/inhibitor diffusion and stability differ between models. Notably, 'shuttling' models in which the BMP distribution is modulated by a Chordin-mediated increase in BMP diffusivity have gained recent prominence. Here, we directly test five major models by measuring the biophysical properties of fluorescently tagged BMP2b and Chordin in zebrafish embryos. We found that BMP2b and Chordin diffuse and rapidly form extracellular protein gradients, Chordin does not modulate the diffusivity or distribution of BMP2b, and Chordin is not required to establish peak levels of BMP signaling. Our findings challenge current self-regulating reaction-diffusion and shuttling models and provide support for a graded source-sink mechanism underlying zebrafish dorsal-ventral patterning.
DOI: https://doi.org/10.7554/eLife.25861.001

***For correspondence:** pmueller@tuebingen.mpg.de

†These authors contributed equally to this work

Competing interests: The authors declare that no competing interests exist.

Funding: See page 27

Received: 08 February 2017
Accepted: 30 August 2017
Published: 31 August 2017

Reviewing editor: Deborah Yelon, University of California, San Diego, United States

Introduction

The dorsal-ventral axis is one of the earliest coordinate systems established during animal development and divides the embryo into dorsal (back) and ventral (belly) territories. This axis forms under the influence of the BMP/Chordin patterning system. The activator BMP induces the formation of ventral tissues, and BMP signaling is antagonized on the dorsal side by the inhibitor Chordin. There are currently several disparate models that can explain how BMP signaling is restricted to the ventral side (***Ben-Zvi et al., 2008***; ***Barkai and Ben-Zvi, 2009***; ***Francois et al., 2009***; ***Ben-Zvi et al., 2011b***; ***Inomata et al., 2013***; ***Ramel and Hill, 2013***; ***Ben-Zvi et al., 2014***), but the underlying biophysical assumptions have not been fully tested.

In the 'Graded source-sink + mobile BMP model' (Model 1), BMP is produced in a graded, ventrally biased source, and signaling from diffusing BMP is antagonized by binding to its inhibitor Chordin (***Figure 1—figure supplement 1***, ***Table 1***). Chordin (Chd) diffuses from a localized source on the opposing dorsal side and therefore provides a 'sink' that inactivates BMP molecules diffusing through the embryo, helping to shape the signaling distribution into a gradient that peaks ventrally. The distributions of *bmp* and *chd* mRNA in developing embryos are consistent with this idea – initially nearly uniform *bmp* expression refines to a ventrally biased gradient over time (***Ramel and Hill, 2013***; ***Zinski et al., 2017***), and *chd* expression is restricted to the dorsal region (***Miller-Bertoglio et al., 1997***).

Similar to Model 1, BMP signaling activity in the 'Graded source-sink + immobile BMP model' (Model 2, ***Figure 1—figure supplement 1***, ***Table 1***) is also restricted by the inhibitor Chordin diffusing from the dorsal side. However, Model 2 assumes that BMP does not diffuse (***Ramel and Hill,***

eLife digest Animals start life as clumps of cells that ultimately give rise to complex structures and organs. Over a century of research has revealed a small number of proteins that are crucial for complex structures to form from these clumps, including one protein called BMP. Different levels of BMP instruct cells to give rise to different tissues. In zebrafish, BMP is more abundant on one side of the embryo than the other. This gradient in BMP levels causes different tissues to form at distinct positions and helps coordinate embryo development.

Several theories have been proposed to explain how the BMP gradient is established. They all suggest that a second protein – Chordin – plays an important role in influencing how cells sense the BMP gradient by blocking BMP's activity. However, the exact role of Chordin in the formation of the BMP gradient is disputed. To address this, Pomreinke, Soh, Rogers et al. directly tested five theories of how BMP and Chordin molecules spread through embryos.

The experiments used microscopy to track the movements of fluorescent versions of both molecules in zebrafish embryos. The measurements contradict one theory stating that BMP does not move, and another in which Chordin increases the mobility of BMP. Pomreinke, Soh, Rogers et al. also found that embryos that lack Chordin have increased BMP signaling levels only on the side where Chordin is normally made but not on the opposite side where BMP is made, ruling out several of the theories. The findings are most consistent with the idea that the BMP gradient forms mainly as a result of higher production of BMP on one side of the embryo combined with movement of BMP away from where it is made. Chordin produced at the opposite end of the embryo helps to ensure that only the correct cells receive instructions from BMP.

In the future, two approaches could further clarify how the BMP gradient is formed. First, better techniques to directly observe the BMP gradient in normally developing embryos would be useful. Second, new theories that take into account additional players other than BMP and Chordin might help explain some features of development that current theories cannot address. Uncovering the mechanisms that control the formation of BMP gradients will improve our understanding of how clumps of cells can develop into animals.

DOI: https://doi.org/10.7554/eLife.25861.002

2013) and that it binds to Chordin with weaker affinity than in Model 1 (see Materials and methods). Proponents have argued that the similarities between the graded *bmp* mRNA distribution, signaling gradient, and target gene expression indicate negligible BMP diffusion during patterning (***Ramel and Hill, 2013***). Consistent with this, BMP4 was unable to induce long-range signaling in *Xenopus* experiments (***Jones et al., 1996***), although BMP target genes are induced outside of BMP-expressing clones in zebrafish (***Xu et al., 2014***). However, measuring the diffusivity of BMP *in vivo* is the most direct way to determine whether BMP is mobile (***Kicheva et al., 2007***; ***Zinski et al., 2017***).

Although these two relatively simple models are generally supported by biological observations, they do not take into account other regulators known to be crucial for dorsal-ventral patterning, such as the BMP-like ligand ADMP, and Sizzled, an inhibitor of the Chordin protease Tolloid/Xlr. Three models described below include these important dorsal-ventral regulators in addition to BMP and Chordin and have also been shown to explain scale-invariant patterning, a phenomenon in which embryos adjust their tissue proportions to differently sized patterning fields.

The recent 'Long-range accumulation and feedback model' (Model 3, ***Figure 1—figure supplement 1***, ***Table 1***) postulates that BMP and Chordin have equally high mobility, but that dorsal-ventral patterning is controlled by differences in BMP and Chordin protein stability (***Inomata et al., 2013***). In this model, BMP and ADMP induce the secreted, highly diffusible and stable Chordin protease inhibitor Sizzled. This protects Chordin from proteolysis and promotes its expansion towards the ventral side. Over time the resulting inhibition of BMP signaling leads to decreased Sizzled production, destabilizing Chordin and relieving inhibition of BMP. In this way, an appropriate balance between ventral BMP and dorsal Chordin levels can be established even in differently sized embryos.

In the 'Self-regulating reaction-diffusion model' (Model 4, ***Figure 1—figure supplement 1***, ***Table 1***), BMP and Chordin both have low diffusivities and equivalent protein stabilities. Interactions with highly mobile ADMP and Sizzled in two coupled reaction-diffusion networks eventually result in

Table 1. Summary of model assumptions, predictions, and experimental findings.
Model assumptions or predictions that are consistent with the experimental findings (gray) are highlighted in green. NA: no testable model assumptions or predictions.

	Model 1 Graded source-sink (mobile BMP)	Model 2 Graded source-sink (immobile BMP)	Model 3 Long-range accumulation and feedback	Model 4 Self-regulating reaction-diffusion system	Model 5 Shuttling	Experimental findings
Diffusivity of BMP and Chordin	D(BMP) > 0 D(BMP) < D(Chd)	D(BMP) ≈ 0 D(Chd) high	D(BMP) ≈ D(Chd) High	D(BMP) ≈ D(Chd) Low	D(BMP) << D(Chd)	D(BMP) ≤ D(Chd) (≈2 and 6 μm^2/s)
Effect of Chordin on BMP diffusivity	No effect	No effect	No effect	No effect	Chd enhances BMP diffusion	No effect
Half-life of BMP and Chordin	τ(BMP) ≈ τ(Chd)	Unconstrained	τ(BMP) >> τ(Chd)	τ(BMP) ≈ τ(Chd)	τ(BMP) > τ(Chd)*	τ(BMP) ≈ τ(Chd) (130 and 120 min)
pSmad gradient formation kinetics	Progressive rise ventrally, always low dorsally	Progressive rise ventrally, always low dorsally	Initially high dorsally and ventrally	Progressive rise ventrally, always low dorsally	Progressive rise ventrally, always low dorsally	Progressive rise ventrally, always low dorsally
Ventral pSmad peak decreased in the absence of Chordin?	No	No	No	No	Yes	No
Dorso-lateral pSmad expansion in the absence of Chordin?	Yes	Yes	Yes	No	Yes	Yes
Diffusivity of Sizzled relative to BMP/Chordin	NA	NA	D(ADMP) & D(Szl) ≈ D(BMP) & D (Chd)	D(ADMP) & D (Szl) >> D(BMP) & D (Chd)	NA	D(Szl) ≈ D(BMP) & D(Chd) (≈10, 2, and 6 μm^2/s)

*The simplified shuttling model without ADMP presented here is based on the experimentally measured clearance rate constants of BMP and Chordin; the full model for scale-invariant patterning including ADMP (***Ben-Zvi et al., 2008***) assumes a lower stability of Chordin due to Xlr-mediated degradation.
DOI: https://doi.org/10.7554/eLife.25861.003

the restriction of BMP signaling activity on the ventral side, assuming an initial dorsal Chordin or ventral BMP bias (***Francois et al., 2009***). Such a system self-regulates even with noisy initial conditions and could provide robustness during embryogenesis – e.g., the ability of developing organisms to withstand noise in gene expression or fluctuating environmental conditions – that can be difficult to explain with other models.

Finally, the prominent 'Shuttling model' (Model 5, ***Figure 1—figure supplement 1***, ***Table 1***) postulates that Chordin not only acts as an inhibitor of BMP, but also modulates the mobility and distribution of BMP protein (***Ben-Zvi et al., 2008***; ***Barkai and Ben-Zvi, 2009***; ***Ben-Zvi et al., 2011b***; ***Ben-Zvi et al., 2014***). In this model, BMP is poorly diffusive, Chordin is highly diffusive, and BMP mobility increases when bound to Chordin. Cleavage of the BMP/Chordin complex by the uniformly distributed protease Tolloid/Xlr combined with a flux of Chordin from the dorsal side is thought to 'shuttle' BMP towards the ventral side by facilitated diffusion over time. In this way, Chordin is responsible for the accumulation of BMP protein on the ventral side, and actively helps establish the subsequent ventral BMP signaling peak.

These five conflicting models postulate different diffusion (no diffusion, equal diffusion, differential diffusion, facilitated diffusion) and stability properties of BMP and Chordin proteins (***Table 1***, ***Figure 1—figure supplement 1***). However, these biophysical properties have not been fully measured experimentally, in part due to the lack of reagents and techniques to detect active BMP and Chordin in living vertebrate embryos. To test the biophysical tenets of these models, we developed active BMP and Chordin fluorescent fusion proteins, and used a combination of mathematical modeling and quantitative experiments to determine how BMP2b and Chordin gradients form. Additionally, we tested the distinct predictions that the five models make about how BMP signaling changes in the absence of Chordin. We found that (i) BMP2b and Chordin proteins have similar stabilities, (ii) both BMP2b and Chordin diffuse and form gradients in the extracellular space, and (iii) Chordin does not significantly facilitate BMP2b diffusion or play an active role in establishing peak ventral BMP signaling levels. Together, our results are most consistent with dorsal-ventral patterning mediated by Model 1, the 'Graded source-sink + mobile BMP' model.

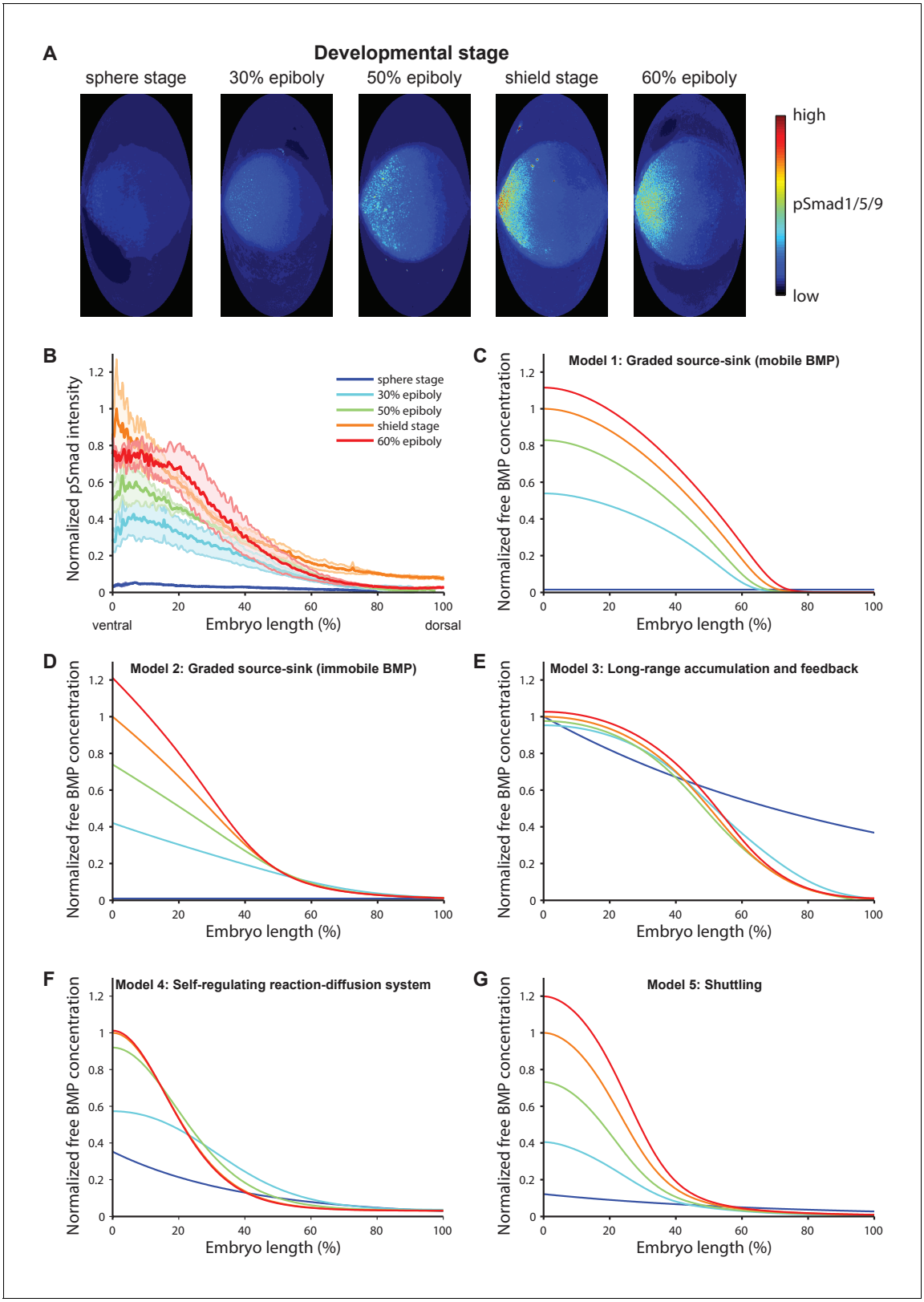

Figure 1. BMP signaling (pSmad1/5/9) gradient formation and simulations of five major dorsal-ventral patterning models over relevant zebrafish developmental stages (3 hr). (**A**) Two-dimensional Hammer-Aitoff projections (2D maps) of pSmad1/5/9-immunostained individual wild type zebrafish embryos at different developmental stages. Embryos were imaged using light sheet microscopy (see Materials and methods for details). (**B**) Quantification of ventral-to-dorsal average pSmad1/5/9 distributions in one-dimensional projections of 2D maps generated for embryos at different

Figure 1 continued on next page

Figure 1 continued

developmental stages (n = 3 for each stage) as in (**A**). Error bars denote standard error. (**C–G**) Gradient formation kinetics simulated for Models 1–5 at relevant zebrafish developmental stages.

DOI: https://doi.org/10.7554/eLife.25861.004

The following figure supplement is available for figure 1:

Figure supplement 1. Mathematical formulation of five major models of BMP/Chordin-mediated dorsal-ventral patterning.

DOI: https://doi.org/10.7554/eLife.25861.005

Results

Chordin does not actively establish peak ventral BMP signaling

BMP signaling induces phosphorylation and nuclear localization of the transcriptional effectors Smad1/5/9 (***Schier and Talbot, 2005***). To quantitatively measure BMP signaling activity during early dorsal-ventral patterning, we imaged pSmad1/5/9-immunostained zebrafish embryos fixed at different developmental stages using *in toto* light sheet microscopy, converted pSmad1/5/9 signaling activities into information-compressed two-dimensional maps (***Schmid et al., 2013***), and quantified pSmad1/5/9 intensities along the ventral-dorsal axis (***Figure 1A***, Materials and methods). Over the course of approximately 3 hr during early zebrafish development, BMP signaling rapidly shifts from a low-level near-uniform distribution to a gradient with peak levels on the ventral side (***Figure 1A+B***, ***Videos 1–5***) (***Tucker et al., 2008***), similar to changes in the distribution of *bmp2b* mRNA over time (***Ramel and Hill, 2013***; ***Zinski et al., 2017***). We simulated pSmad1/5/9 gradient formation kinetics predicted by each of the five models over a similar time period (***Figure 1C–G***). Our measurements are consistent with the gradient kinetics predicted by Models 1, 2, 4, and 5, whereas the dynamics predicted by Model 3 do not resemble the experimentally observed distributions.

All five major models of BMP/Chordin-mediated dorsal-ventral patterning qualitatively explain the formation of a ventral signaling peak, but they assign different roles to the inhibitor Chordin (***Figure 2A–E***, ***Table 1***, and ***Figure 1—figure supplement 1***). Models 1 and 2 assume that a flux of the inhibitor Chordin from the dorsal side restricts the range of BMP signaling activity throughout the embryo. They thus predict that in the absence of Chordin, BMP signaling should be expanded throughout the embryo with a small increase in the peak levels on the ventral side (***Figure 2A+B***). Model 3 adds an additional regulatory layer: Here, the abundance of Chordin is regulated by feedback interactions that modify its stability and affect ventral BMP signaling levels (***Figure 1—figure supplement 1***). Similar to Models 1 and 2, Model 3 also predicts that in the absence of Chordin, BMP signaling should be expanded throughout the embryo (***Figure 2C***).

In Model 4, two reaction-diffusion systems involving BMP/Sizzled and Chordin/ADMP are coupled. In a completely homogenous field of cells with no initial expression biases, this self-organizing system would give rise to both ventral and dorsal BMP peaks (***Francois et al., 2009***). To achieve a single ventral BMP peak, an initial dorsal Chordin or ventral BMP bias is required (see Materials and methods). Under these conditions, the initial advantage in BMP signaling on the ventral side is amplified by autoregulation of BMP production. Since Chordin inhibits the autoregulation of BMP production, the absence of Chordin leads to a more pronounced ventral BMP peak but has no effect in the rest of the embryo (***Figure 2D***). Model 4 thus predicts that in the absence of Chordin, pSmad1/5/9 levels would be increased on the ventral but not the dorsal side.

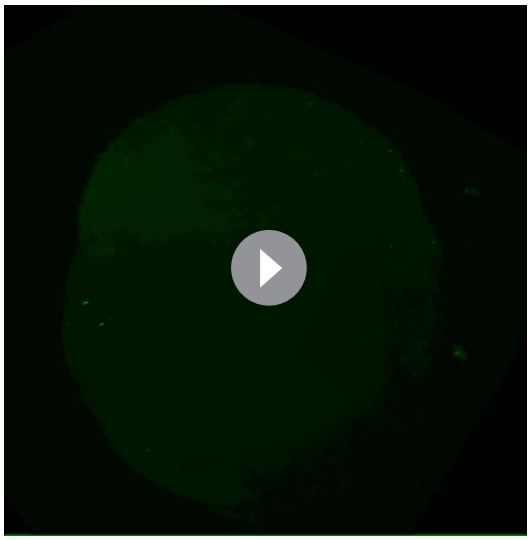

Video 1. 3D reconstruction of pSmad1/5/9 localization in a wild type sphere stage zebrafish embryo imaged by light sheet microscopy.

DOI: https://doi.org/10.7554/eLife.25861.006

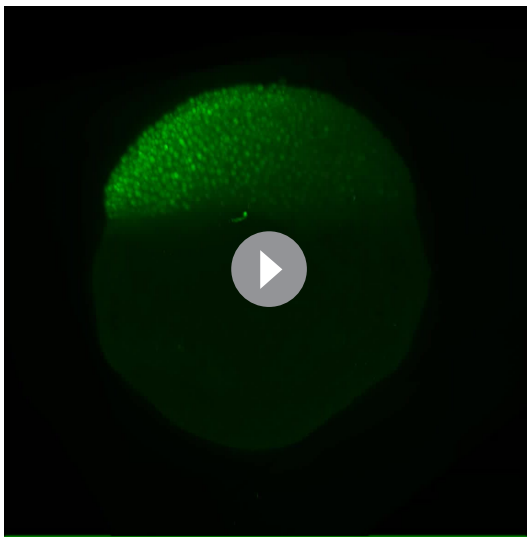

Video 2. 3D reconstruction of pSmad1/5/9 localization in a wild type 30% epiboly stage zebrafish embryo imaged by light sheet microscopy.
DOI: https://doi.org/10.7554/eLife.25861.007

Video 3. 3D reconstruction of pSmad1/5/9 localization in a wild type 50% epiboly stage zebrafish embryo imaged by light sheet microscopy.
DOI: https://doi.org/10.7554/eLife.25861.008

In contrast to Models 1–4, Model 5 assigns a more active role to Chordin in promoting the ventral BMP signaling peak. This model proposes that Chordin activity results in *increased* BMP signaling ventrally: Chordin increases ventral BMP levels by binding to and physically moving BMP protein towards the ventral side. This model therefore predicts that in embryos lacking Chordin, BMP signaling should be lower on the ventral side compared to wild type embryos (***Figure 2E***).

To experimentally test these predictions, we quantitatively measured BMP signaling activity in fixed *chordin*$^{-/-}$ zebrafish embryos (***Video 6***) and their wild type siblings using pSmad1/5/9 immunostaining and *in toto* light sheet microscopy. Strikingly, BMP signaling was increased in dorso-lateral domains in *chordin*$^{-/-}$ mutants compared to wild type embryos, but BMP signaling on the

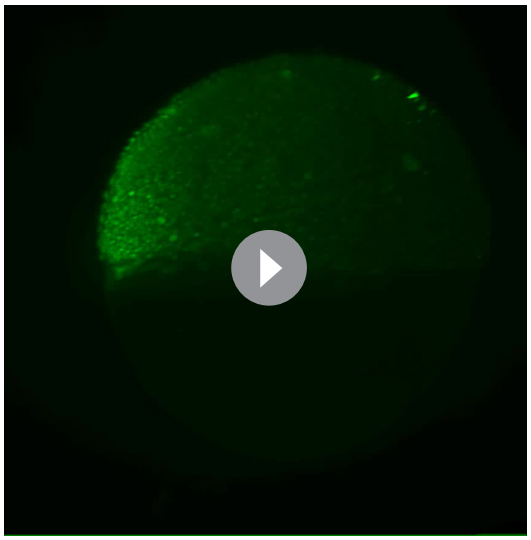

Video 4. 3D reconstruction of pSmad1/5/9 localization in a wild type shield stage zebrafish embryo imaged by light sheet microscopy.
DOI: https://doi.org/10.7554/eLife.25861.009

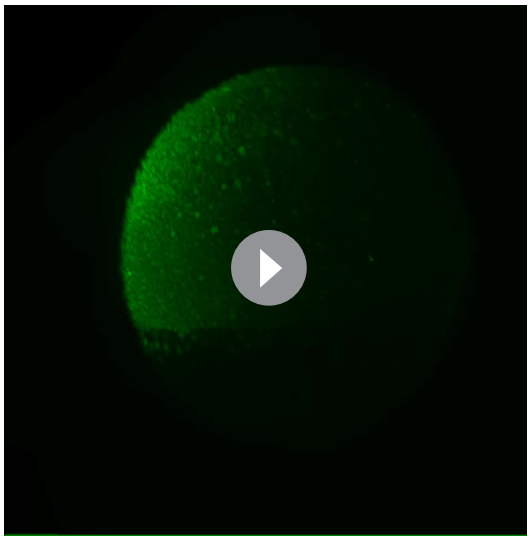

Video 5. 3D reconstruction of pSmad1/5/9 localization in a wild type 60% epiboly stage zebrafish embryo imaged by light sheet microscopy.
DOI: https://doi.org/10.7554/eLife.25861.010

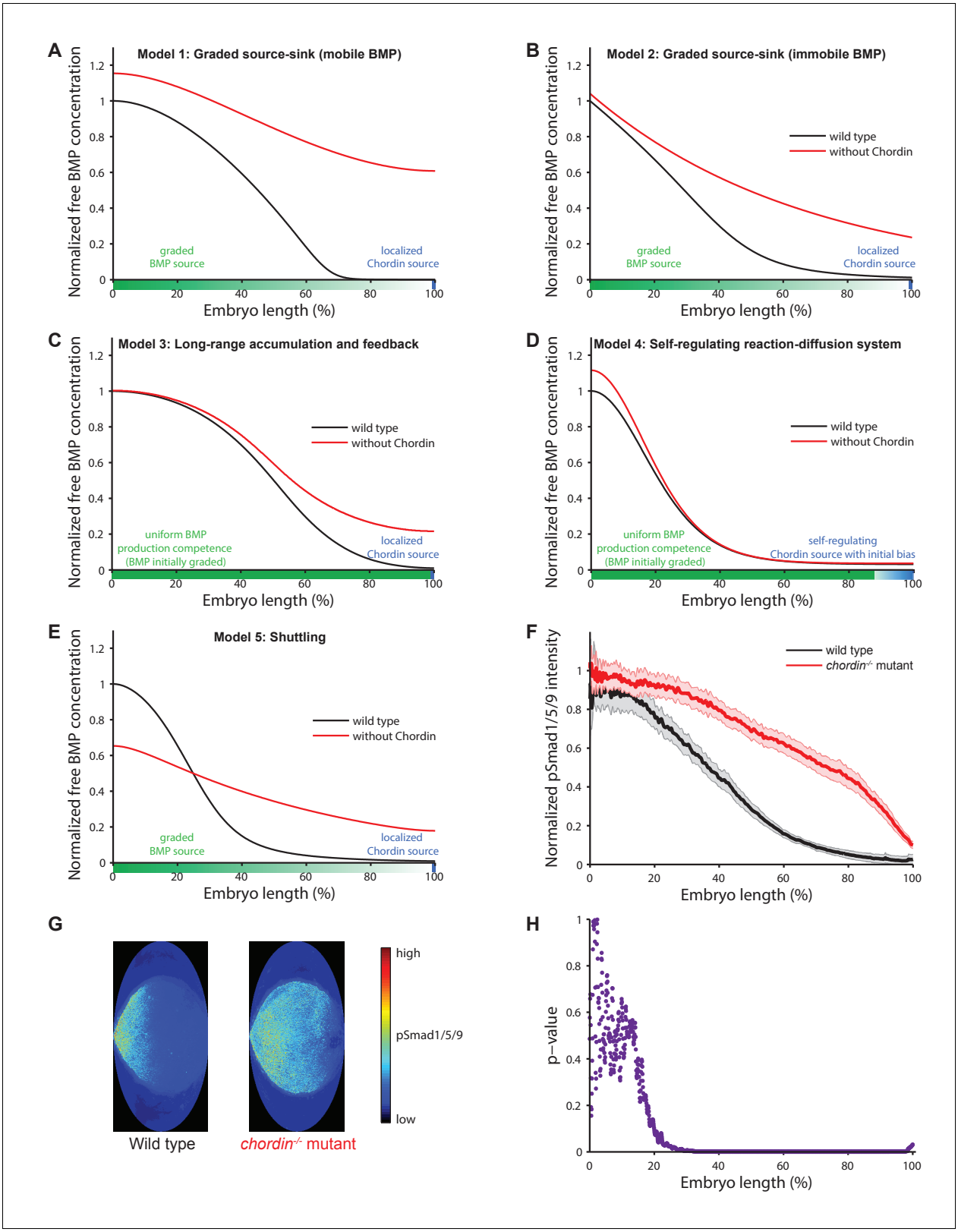

Figure 2. Theoretical predictions for the influence of the inhibitor Chordin on the BMP signaling gradient and experimental test. (**A–E**) Simulations of BMP distributions in five major models of dorsal-ventral patterning in the presence (black) or absence (red) of Chordin. The BMP and Chordin sources are indicated below each graph in green and blue, respectively. Note that the spatial production rates in Models 3 and 4 are modulated over time by feedback. (**F–G**) Quantification of average pSmad1/5/9 distributions in wild type (black) and *chordin*$^{-/-}$ (red) embryos using one-dimensional

Figure 2 continued on next page

Figure 2 continued

projections of 2D maps. Wild type n = 7, *chordin*$^{-/-}$ mutants n = 10. Error bars denote standard error. (**H**) p-values (unpaired two-tailed t-test assuming equal variance) calculated as a function of space between pSmad1/5/9 distributions in wild type and *chordin*$^{-/-}$ embryos shown in (**F**) indicate no significant difference of pSmad1/5/9 on the ventral side but a dramatic expansion into dorsal-lateral domains.

DOI: https://doi.org/10.7554/eLife.25861.011

ventral side was not significantly affected (***Figure 2F–H***), consistent with the predictions from Models 1–3 and observations in *Xenopus* and zebrafish embryos (***Plouhinec et al., 2013***; ***Zinski et al., 2017***), but not with the BMP signaling distributions predicted by Models 4 and 5 (***Table 1***).

BMP and Chordin fluorescent fusion proteins diffuse and rapidly form gradients *in vivo*

In order to understand the underlying basis of BMP/Chordin distribution and directly test the biophysical assumptions of the five dorsal-ventral patterning models, we developed fluorescent fusion proteins. We fused superfolder-GFP (sfGFP [***Pédelacq et al., 2006***]) and the photoconvertible protein Dendra2 (***Gurskaya et al., 2006***) to zebrafish Chordin and BMP2b, the major BMP ligand regulating zebrafish dorsal-ventral patterning (***Kishimoto et al., 1997***; ***Xu et al., 2014***). Basing our design on previously established fusions with small peptide tags (***Cui et al., 1998***; ***Degnin et al., 2004***; ***Sopory et al., 2006***), we inserted fluorescent proteins to label the mature signaling domains, and obtained fusion proteins that are processed similarly and have similar biological activity as untagged versions or constructs fused to small FLAG tags (***Figure 3A–E***, ***Figure 3—figure supplement 1***). Indeed, *BMP2b* mutants (*swr*$^{-/-}$, which are normally severely dorsalized [***Kishimoto et al., 1997***]) can be rescued by injection of mRNA encoding BMP2b-Dendra2 or BMP2b-sfGFP at levels equivalent to untagged BMP2b (***Figure 3C***). In these experiments, the injected mRNA should be uniformly distributed, highlighting the important role of Chordin or other antagonists in shaping the graded BMP signaling distribution.

To measure the kinetics of BMP and Chordin protein gradient formation, we expressed BMP2b-sfGFP and Chordin-sfGFP from local sources in wild type zebrafish embryos (***Müller et al., 2012***) and imaged the distribution profiles over time using light sheet microscopy (***Figure 3F–I***). Importantly, in previous experiments it has been demonstrated that BMP2b clones generated in a similar manner can recapitulate BMP signaling comparable to that observed along the dorsal-ventral axis (***Xu et al., 2014***). Strikingly, both BMP2b-sfGFP and Chordin-sfGFP are secreted and diffuse in the extracellular space (***Figure 3F+G***, ***Videos 7+8***), in contrast to the proposal of Model 2 that only Chordin – but not BMP – diffuses (***Ramel and Hill, 2013***) (***Table 1***) and the absence of long-range BMP4 signaling in *Xenopus* (***Jones et al., 1996***). Both BMP2b-sfGFP and Chordin-sfGFP rapidly establish concentration gradients over the course of one hour (***Figure 3H+I***), consistent with the rapid patterning of the dorsal-ventral axis during zebrafish development.

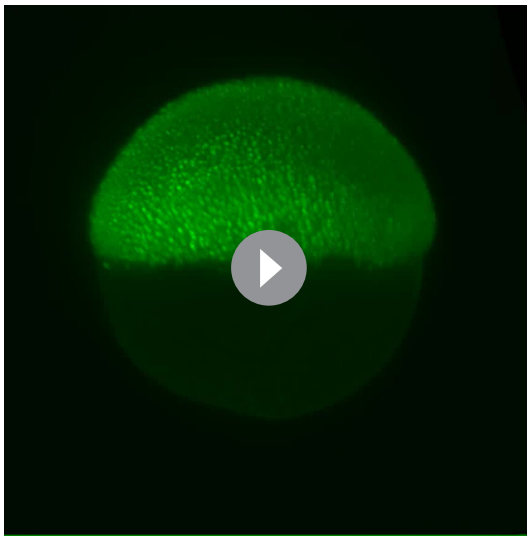

Video 6. 3D reconstruction of pSmad1/5/9 localization in a *chordin*$^{-/-}$ shield stage zebrafish embryo imaged by light sheet microscopy.

DOI: https://doi.org/10.7554/eLife.25861.012

BMP and Chordin fluorescent fusion proteins have similar stabilities *in vivo*

The gradient formed by Chordin-sfGFP has a moderately longer range than the one formed by BMP2b-sfGFP. For example, 60 min post-transplantation the BMP2b-sfGFP signal drops to 50% of the maximal concentration at a distance of 30–40 µm, whereas the gradient formed by Chordin-sfGFP reaches 50% of its maximal concentration at a distance of 50–60 µm from the source boundary at this time point (***Figure 3H+I***). This

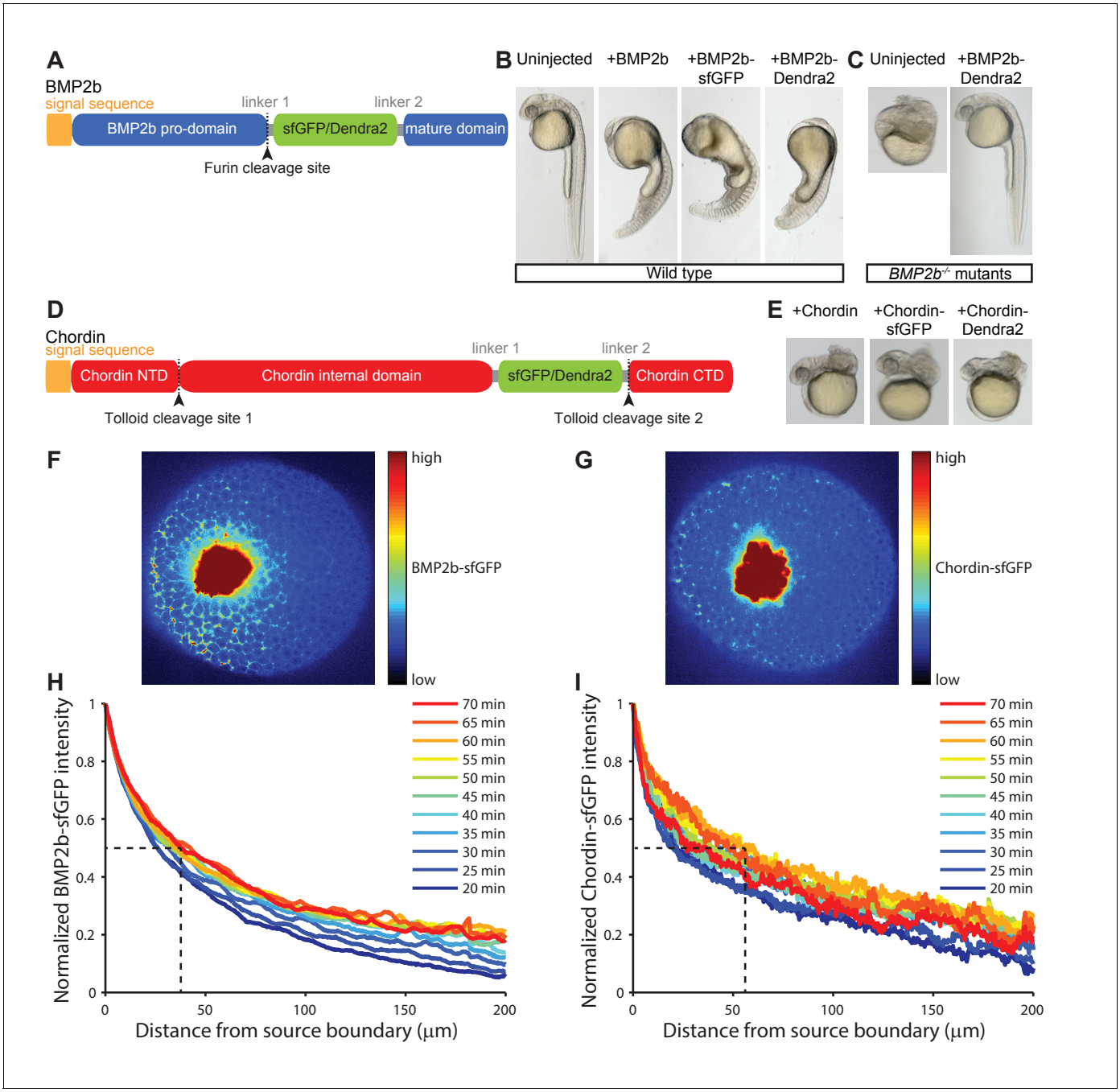

Figure 3. Gradient formation kinetics of fluorescently tagged BMP and Chordin. (**A**) Schematic of BMP2b-sfGFP and -Dendra2 fusion constructs. (**B**) Fluorescent BMP2b fusion constructs can induce ventralization, a BMP-overexpression phenotype (***Kishimoto et al., 1997***). mRNA amounts equimolar to 2 pg of *BMP2b* mRNA were injected at the one-cell stage, and images were taken 30 hr post-fertilization (hpf). (**C**) Rescue of a *BMP2b* mutant (*swr*$^{-/-}$) with BMP2b-Dendra2. 2.74 pg of BMP2b-Dendra2-encoding mRNA were injected at the one-cell stage, and images were taken at 30 hpf. In a separate experiment with 1 pg of BMP2b-sfGFP-encoding mRNA, 20% (9/44) of all injected *swr*$^{-/-}$ mutants were rescued, 16% (7/44) were ventralized, and 64% (28/44) were dorsalized. (**D**) Schematic of Chordin-sfGFP and -Dendra2 fusion constructs. (**E**) Fluorescent Chordin constructs can induce dorsalization, a *Chordin*-overexpression phenotype. mRNA amounts equimolar to 30 pg of *Chordin* mRNA were injected into wild type embryos at the one-cell stage, and images were taken at 30 hpf. F + G) Light sheet microscopy images of BMP- and Chordin-sfGFP gradients forming from a local source in live zebrafish embryos. Approximately 50–75 cells expressing *BMP2b-sfGFP* (**F**) or *Chordin-sfGFP* (**G**) were transplanted into host embryos at sphere stage (see Materials and methods for details). The images show gradient formation in single optical slices approximately 20 min after transplantation. H + I) Quantification of BMP2b-sfGFP (**H**) and Chordin-sfGFP (**I**) gradient formation kinetics from a local source (BMP2b-sfGFP: n = 8; Chordin-sfGFP: n = 5). Dashed lines indicate the distance at which the protein distributions drop to 50% of their maximal concentration 60 min post-transplantation.

Figure 3 continued on next page

Figure 3 continued

DOI: https://doi.org/10.7554/eLife.25861.013

The following figure supplements are available for figure 3:

Figure supplement 1. Detailed characterization of fluorescently tagged BMP2b and Chordin.

DOI: https://doi.org/10.7554/eLife.25861.014

Figure supplement 2. Modeling of BMP and Chordin gradient formation kinetics and comparison to measured gradients.

DOI: https://doi.org/10.7554/eLife.25861.015

suggests that stability or diffusivity might differ between these proteins (***Müller and Schier, 2011***; ***Müller et al., 2013***). Importantly, Models 3 and 5 assume that BMP is more stable than Chordin, whereas the other models assume either similar or unconstrained stabilities (***Table 1***).

To distinguish between these possibilities, we first determined protein stability in living zebrafish embryos using a Fluorescence Decrease After Photoconversion (FDAP) assay (***Müller et al., 2012***; ***Bläßle and Müller, 2015***; ***Rogers et al., 2015***). We expressed BMP2b and Chordin fused to the green-to-red photoconvertible protein Dendra2 uniformly in zebrafish embryos, used brief UV exposure to convert the signal from green to red to generate a pulsed protein pool, and monitored the decrease in extracellular red fluorescence over time (***Figure 4A+B***). For BMP2b-Dendra2, we found a clearance rate constant of $k_1 = (8.9 \pm 0.1) \times 10^{-5}$/s (half-life 130 min, ***Figure 4A***). For Chordin-Dendra2, we measured a similar clearance rate constant of $k_1 = (9.6 \pm 0.3) \times 10^{-5}$/s (half-life 120 min, ***Figure 4B***). The similar clearance rate constants suggest that differential protein stabilities cannot account for the different protein distributions of BMP2b and Chordin. Importantly, these results are inconsistent with the differential protein stabilities predicted by Models 3 and 5 (***Table 1***).

Diffusivity of BMP and Chordin fluorescent fusion proteins *in vivo*

Our finding that BMP2b- and Chordin-Dendra2 fusions have similar stabilities (***Figure 4A+B***) suggests that differences in diffusivity could account for the slight differences in gradient formation kinetics. Indeed, when we fitted a gradient formation model based on local production, uniform diffusion, and clearance constrained with our measured protein half-lives in a realistic three-dimensional zebrafish embryo-like geometry (***Müller et al., 2012***) to the measured protein distributions, we obtained the best agreement between model and data with lower diffusivity of BMP2b (4 μm^2/s) compared to Chordin (6 μm^2/s) (***Figure 3—figure supplement 2A+B***).

Importantly, the five models assume distinct BMP and Chordin diffusion properties (***Table 1***, ***Figure 1—figure supplement 1***), from no BMP diffusion (Model 2) to substantially higher Chordin

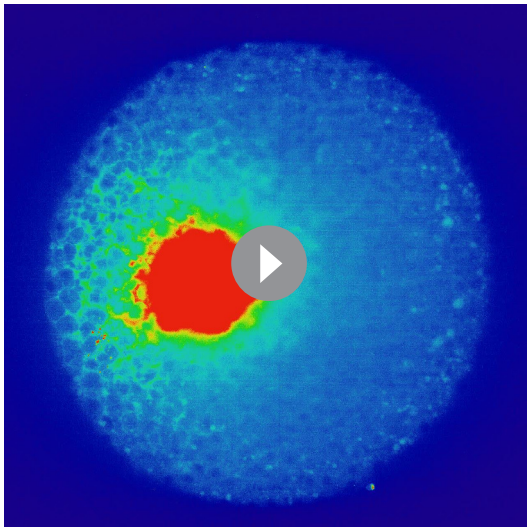

Video 7. Gradient formation in a dome stage wild type embryo with a BMP2b-sfGFP clone.

DOI: https://doi.org/10.7554/eLife.25861.016

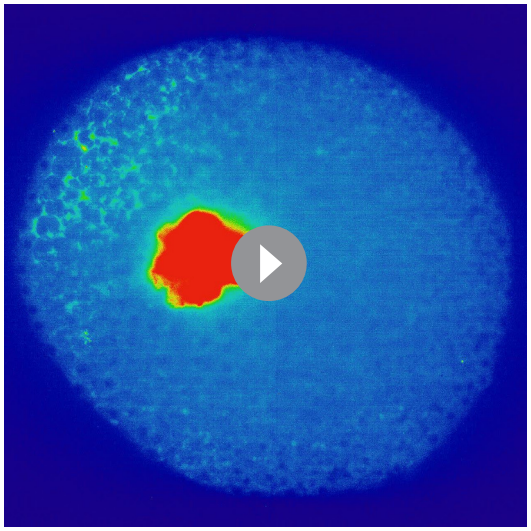

Video 8. Gradient formation in a dome stage wild type embryo with a Chordin-sfGFP clone.

DOI: https://doi.org/10.7554/eLife.25861.017

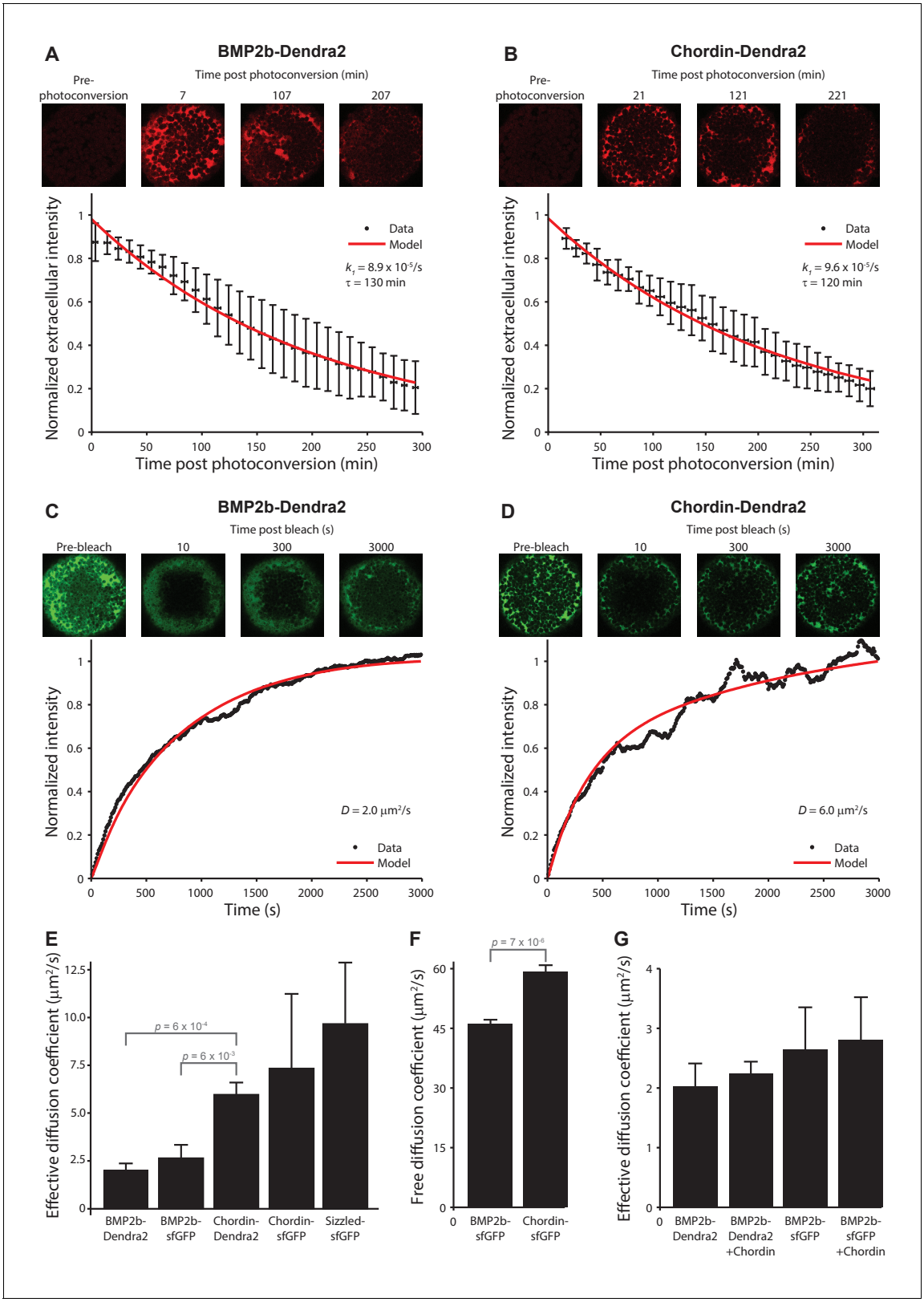

Figure 4. Biophysical measurements of BMP and Chordin protein stability and diffusivity. A + B) FDAP protein stability measurements for BMP2b-Dendra2 (**A**) and Chordin-Dendra2 (**B**). Error bars denote standard deviation. BMP2b-Dendra2: n = 22; Chordin-Dendra2: n = 6. C + D) FRAP effective protein diffusivity measurements for BMP2b-Dendra2 (**C**) and Chordin-Dendra2 (**D**). Data and fits from single experiments are shown. (**E**) Bar chart of the average effective diffusion coefficients from FRAP experiments. Error bars denote standard error. BMP2b-Dendra2: n = 6; BMP2b-sfGFP: n = 8;

Figure 4 continued on next page

Figure 4 continued

Chordin-Dendra2: n = 8; Chordin-sfGFP: n = 6; Sizzled-sfGFP: n = 12. (**F**) Free diffusion coefficients of BMP2b-sfGFP and Chordin-sfGFP measured by Fluorescence Correlation Spectroscopy (FCS) in a diffraction-limited spot within the zebrafish embryonic extracellular space far away from cell membranes (see Materials and methods for details). Error bars denote standard error. BMP2b-sfGFP: n = 17 measurements from 4 embryos; Chordin-sfGFP: n = 19 measurements from 5 embryos. (**G**) Negligible influence of Chordin on BMP2b effective diffusion. Untagged Chordin was co-expressed with BMP2b-Dendra2 (n = 8) or BMP2b-sfGFP (n = 9) in zebrafish embryos subjected to FRAP measurements at blastula stages. The data shown for BMP2b-Dendra2 and BMP2b-sfGFP FRAP experiments without co-expressed *Chordin* is identical to the data shown in (**E**). p-values (unpaired two-tailed t-test assuming equal variance) are shown for statistically significant ($p<0.05$) data sets.

DOI: https://doi.org/10.7554/eLife.25861.018

The following figure supplement is available for figure 4:

Figure supplement 1. Characterization of Sizzled diffusion and its role in gradient formation.

DOI: https://doi.org/10.7554/eLife.25861.019

mobility compared to BMP (Model 5). To directly test these predictions, we determined the effective diffusivities of fluorescently tagged BMP2b and Chordin moving through developing zebrafish embryos. We used a Fluorescence Recovery After Photobleaching (FRAP) assay (***Müller et al., 2012***) that measures the dynamics of re-appearance of fluorescence in a bleached region in embryos uniformly expressing fluorescent fusion proteins (***Figure 4C–E***). We found effective diffusion coefficients of 2–3 $\mu m^2/s$ for BMPs (BMP2b-Dendra2: 2.0 ± 0.4 $\mu m^2/s$; BMP2b-sfGFP: 2.6 ± 0.7 $\mu m^2/s$ (similar to [***Zinski et al., 2017***]) and of 6–7 $\mu m^2/s$ for Chordin (Chordin-Dendra2: 6.0 ± 0.7 $\mu m^2/s$; Chordin-sfGFP: 7.3 ± 3.9 $\mu m^2/s$), indicating that slight differences in diffusivities could underlie the differences in protein distributions. This idea is further supported by the agreement between gradients simulated with the measured diffusivities and clearance rate constants and our experimentally determined protein gradients (***Figure 3—figure supplement 2E–H***). The measured diffusion coefficients are most consistent with Models 1 and 4, which assume either similarly low diffusivities (Model 4) or that BMP has a moderately lower diffusion coefficient than Chordin (Model 1, ***Table 1***). As observed in the BMP2b-sfGFP gradient formation experiment (***Figure 3F–I***), our FRAP data demonstrate that BMP2b-sfGFP is mobile *in vivo*, inconsistent with Model 2.

Strikingly, local diffusion measurements in very small extracellular volumes far away from cell surfaces using Fluorescence Correlation Spectroscopy (FCS) assays showed that BMP2b-sfGFP (free diffusion coefficient: D_f = 46 ± 1 $\mu m^2/s$) and Chordin-sfGFP (free diffusion coefficient: D_f = 59 ± 2 $\mu m^2/$

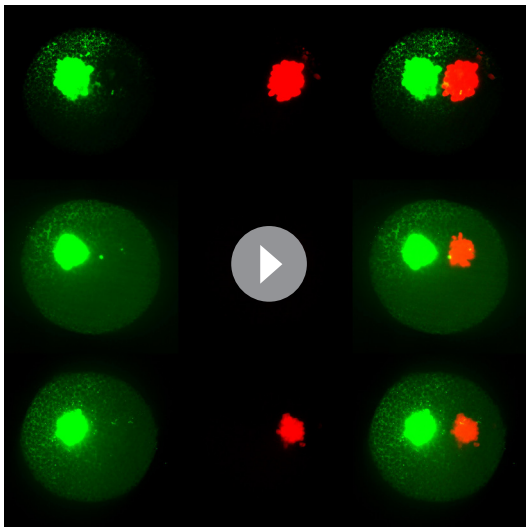

Video 9. Gradient formation in three representative dome stage wild type embryos with BMP2b-sfGFP clones (green) next to clones labeled with Alexa 546-coupled dextran (red).

DOI: https://doi.org/10.7554/eLife.25861.021

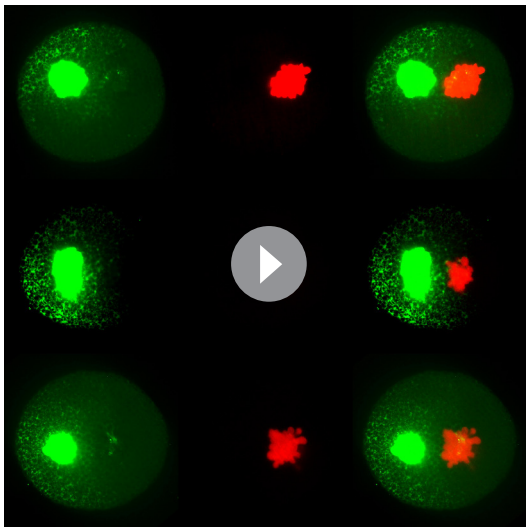

Video 10. Gradient formation in three representative dome stage wild type embryos with BMP2b-sfGFP clones (green) next to *chordin*-expressing clones labeled with Alexa 546-coupled dextran (red).

DOI: https://doi.org/10.7554/eLife.25861.022

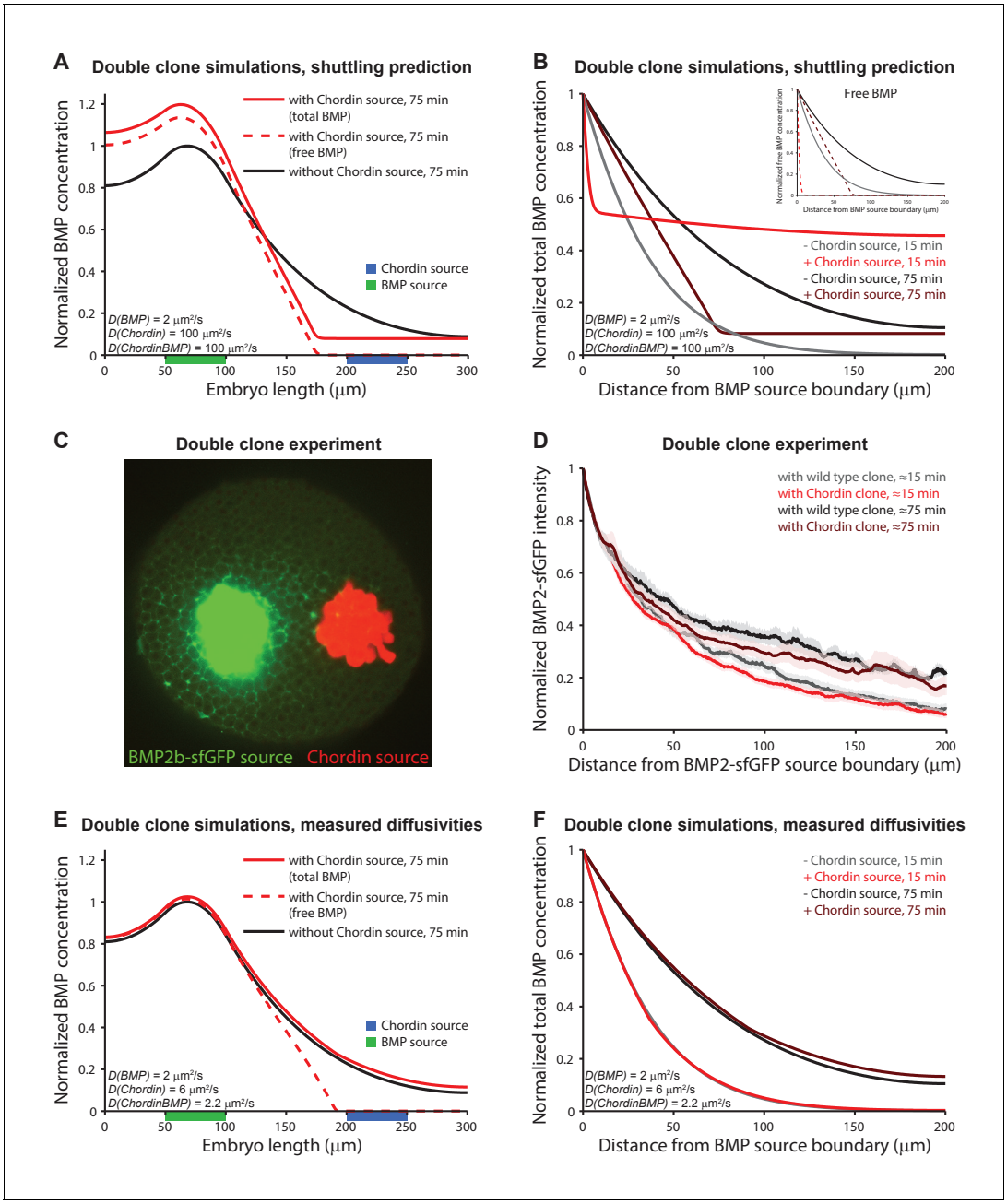

Figure 5. Testing shuttling of BMP2b predicted by Model 5. (**A**) One-dimensional model of two clones expressing BMP (green) or Chordin (blue) with D_{BMP} = 2 μm^2/s, D_{Chd} = 100 μm^2/s, and D_{ChdBMP} = 100 μm^2/s. BMP levels increase over time due to constant production. In the presence of Chordin, the BMP gradient is deflected away from the Chordin source indicative of shuttling (compare black and red lines). Solid lines show total BMP levels (i.e. BMP + ChdBMP in the presence of Chordin), and dashed line shows free BMP levels. (**B**) BMP gradients to the right of the BMP-expressing clone re-normalized to the BMP concentration at the source boundary to demonstrate that the range of BMP is decreased between the two clones in the presence of Chordin. The main panel shows total BMP levels (i.e., BMP + ChdBMP in the presence of Chordin), and the inset shows free BMP levels (dashed lines). (**C**) Experimental test of the predictions in (**A**) and (**B**). Clones of cells expressing BMP2b-sfGFP (green) were generated by transplanting approximately 50–75 cells from a donor embryo into wild type hosts at sphere stage (see Materials and methods for details). Another clone of cells (red) was transplanted next to the BMP2b-sfGFP-expressing clone shortly after. The red clone is marked by the presence of fluorescent Alexa 546-coupled dextran. Cells from red-labeled clones either contained only Alexa 546-coupled dextran (***Video 9***) or Alexa-546-coupled dextran and ectopic *chordin* mRNA (***Video 10***). 15–20 min after transplantation of the clones, embryos were imaged using light sheet microscopy. The image shows gradient formation in a single optical slice approximately 20 min after transplantation. (**D**) Quantification of average BMP2b-sfGFP gradients at ~15 min or ~75 min after transplantation in embryos generated as in (**C**) with (red/brown) or without (black/gray) ectopic Chordin sources. Error bars denote standard error. n = 8 for each condition. (**E**) One-dimensional simulation of two clones expressing BMP (green) or Chordin (blue) with the experimentally measured diffusion coefficients D_{BMP} = 2 μm^2/s, D_{Chd} = 6 μm^2/s, and D_{ChdBMP} = 2.2 μm^2/s. BMP levels increase over time due to constant production.

Figure 5 continued on next page

Figure 5 continued

Solid lines show total BMP levels (i.e. BMP + ChdBMP in the presence of Chordin), and the dashed line shows free BMP levels. Only the distribution of free BMP is affected as a consequence of Chordin binding, and the gradient of total BMP is not deflected away from the Chordin source (compare solid black and red lines). (**F**) Gradients of total BMP levels to the right of the BMP expressing clone simulated with the experimentally measured diffusion coefficients (D_{BMP} = 2 μm^2/s, D_{Chd} = 6 μm^2/s, and D_{ChdBMP} = 2.2 μm^2/s) and renormalized to the concentration at the boundary show that the range of BMP is not decreased between the two clones in the presence of Chordin.

DOI: https://doi.org/10.7554/eLife.25861.020

s) are highly mobile over short spatial and temporal scales (***Figure 4F***), whereas their diffusivities are reduced at the global scale when they move across a field of cells (***Figure 4E***). We hypothesize that the difference between effective diffusivities (measured by FRAP) and local diffusivities (measured by FCS) is due to binding to immobile extracellular molecules, which could serve as diffusion regulators that hinder the mobility of BMP2b and Chordin, similar to what has been proposed for other developmental signals such as Nodal and FGF (***Müller et al., 2012***; ***Müller et al., 2013***).

Sizzled, BMP, and Chordin diffusivities are within the same order of magnitude

Models 3 and 4 assign important roles to the secreted proteins ADMP and Sizzled in regulating BMP signaling and distribution. Model 3 postulates diffusivities of ADMP and Sizzled equivalent to BMP and Chordin, whereas Model 4 requires approximately 25-fold higher diffusivities of ADMP and Sizzled compared to BMP and Chordin (***Table 1***). To measure the diffusivities of ADMP and Sizzled and test these assumptions, we developed fluorescent ADMP and Sizzled fusion proteins (see Materials and methods). Whereas Sizzled fusion proteins had activity comparable to untagged Sizzled (***Figure 4—figure supplement 1A–C***), ADMP fusions with sfGFP or FLAG tags inserted 2, 5, or 11 amino acids after the Furin cleavage site were much less active than untagged ADMP (data not shown), and could therefore not be used for diffusion measurements. Using FRAP, we measured an effective diffusion coefficient of 9.7 ± 3.2 μm^2/s for Sizzled-sfGFP (***Figure 4E***, ***Figure 4—figure supplement 1D***). This measurement is consistent with Model 3, but not Model 4, the latter of which requires much higher Sizzled mobility (***Table 1***).

When parameterized with these measured diffusion coefficients and over a ~100-fold range of ADMP diffusion coefficients, Model 3 can form ventral-dorsal gradients over relevant time scales (***Figure 4—figure supplement 1F–J***), but the kinetics of gradient formation do not reflect the measurements of pSmad1/5/9 distribution profiles in ***Figure 1A+B***. Moreover, the relatively minor difference between BMP/Chordin and Sizzled diffusivity is not compatible with the 25-fold differential required for Model 4 (***Figure 4—figure supplement 1K–P***).

Chordin does not regulate BMP protein diffusivity or distribution

Model 5 (Shuttling) postulates that highly diffusive Chordin enhances the mobility of poorly diffusive BMPs (***Ben-Zvi et al., 2008***). In this model, Chordin is secreted dorsally, binds to relatively immobile BMP, and creates a highly mobile BMP/Chordin complex. This complex then diffuses until Chordin is cleaved by a protease (Xlr), rendering BMP immobile again (***Figure 1—figure supplement 1***). To investigate whether Chordin is not only an inhibitor of BMP, but also enhances BMP diffusivity, we increased Chordin levels and measured the effective diffusivity of fluorescent BMP2b. In embryos overexpressing Chordin, we did not observe a significant change in the effective diffusivity of fluorescently tagged BMP2b compared to embryos that did not overexpress Chordin (BMP2b-Dendra2 + Chordin: 2.2 ± 0.2 μm^2/s; BMP2b-sfGFP + Chordin: 2.8 ± 0.7 μm^2/s; ***Figure 4G***). The ability of Chordin to enhance the diffusivity of BMP, a major tenet of Model 5, is therefore not supported by FRAP data.

Model 5 also predicts that Chordin alters the distribution of BMP protein. Over time, the shuttling of BMP by Chordin causes BMP to accumulate away from the Chordin source, resulting in an opposing peak of BMP. Our observation that Chordin does not affect the diffusivity of BMP challenges this view (***Figure 4G***). However, to directly test whether a Chordin source can alter BMP distribution (***Figure 5A+B***), we juxtaposed clones of BMP2b-sfGFP-producing cells with clones of cells secreting untagged Chordin and imaged the formation of the BMP2b-sfGFP gradient over time using light sheet fluorescence microscopy (***Figure 5C+D***, ***Videos 9–10***). Model 5 predicts a steeper BMP2b-

sfGFP gradient in the presence of an adjacent Chordin-producing clone compared to a wild type clone (***Figure 5A+B***). Although BMP2b-sfGFP gradients tend to be slightly steeper in the presence of a neighboring Chordin-expressing clone compared to a non-Chordin-expressing clone (***Figure 5D***), this minor change is unlikely to account for the formation of a ventral peak in BMP signaling during the short time (hours) required to complete dorsal-ventral patterning (***Figure 1A+B***). We also failed to observe significant redistribution of BMP in simulations of adjacent BMP and Chordin clones using our measured diffusion coefficients and half-lives (***Figure 5E+F***). This suggests that shuttling of BMP2b by Chordin is not relevant for the early aspects of dorsal-ventral patterning in zebrafish embryos.

Discussion

The BMP signaling gradient patterns the dorsal-ventral axis during animal development. Five major models can explain how a ventral peak of BMP signaling forms, but the biophysical assumptions underlying these models differ widely (***Table 1***). After experimentally examining these assumptions, our findings lead to four main conclusions. First, Chordin does not play an active role in generating BMP signaling peaks, but only globally inhibits BMP (***Figure 2***). This is consistent with graded source-sink-type models (e.g. Models 1 and 2) and Model 3, but inconsistent with Models 4 and 5 (***Table 1***). Interestingly, BMP signaling in the absence of Chordin is not raised on the extreme dorsal side, indicating that other extracellular inhibitors such as Follistatin or Noggin (***Umulis et al., 2009***) or inhibitors of *bmp* expression (***Koos and Ho, 1999***; ***Leung et al., 2003***; ***Ramel and Hill, 2013***) that were not included in the tested models might further restrict BMP signaling in these regions. Second, BMP2b and Chordin both diffuse in the extracellular space (***Figure 3F–I***), challenging models involving immobile BMP (Model 2). Third, fluorescently tagged BMP2b and Chordin have similarly high local diffusivities (***Figure 4F***), but on a global scale they move much more slowly through the embryo (***Figure 4E***). These findings rule out Models 2, 3, and 5, but are consistent with Models 1 and 4. Fourth, Chordin does not significantly affect BMP2b diffusion or protein distribution in zebrafish embryos (***Figure 4G***, ***Figure 5***), undermining shuttling models in this developmental context. Instead, our data are most consistent with Model 1, the graded source-sink model of BMP/Chordin-mediated dorsal-ventral patterning during early zebrafish development. Our conclusions are also consistent with a recent complementary study (***Zinski et al., 2017***).

Notably, shuttling models (e.g. Model 5) have gained prominence in many developmental contexts including scale-invariant patterning (***Ben-Zvi et al., 2008***; ***Barkai and Ben-Zvi, 2009***; ***Francois et al., 2009***; ***Plouhinec and De Robertis, 2009***; ***Ben-Zvi and Barkai, 2010***; ***Ben-Zvi et al., 2011a***; ***Haskel-Ittah et al., 2012***), but the fundamental tenet, that is, whether putative shuttles such as Chordin change the diffusivity and distribution of signals such as BMP, has not been directly examined. Alternative models that do not invoke Chordin-dependent facilitated BMP diffusion (Model 4) (***Francois et al., 2009***) or that postulate differential protein stability (Model 3) (***Inomata et al., 2013***) can also explain scale-invariant patterning. Our data do not provide strong evidence for shuttling of BMP2b at time scales relevant for dorsal-ventral patterning during early zebrafish embryogenesis: We failed to observe a significant modulation of BMP2b-sfGFP or BMP2b-Dendra2 diffusivity or distribution by Chordin (***Figure 4G***, ***Figure 5***). It is, however, possible that other BMPs (e.g. BMP4, BMP7, ADMP) are shuttled by interactions with Chordin and its protease Tolloid/Xlr. Indeed, *tolloid* mutants display a mild patterning defect of the ventral tail fin (***Connors et al., 1999***) that might reflect a requirement for the ventral accumulation of a weakly active, dorsally expressed BMP ligand such as ADMP (***Dickmeis et al., 2001***; ***Lele et al., 2001***).

The graded source-sink model (Model 1) that is best supported by our data describes a system in which the graded, ventrally biased distribution of *bmp* mRNA and the dorsally localized *chd* mRNA distribution produce opposing sources of extracellular, diffusing BMP and Chordin protein, which together generate the BMP signaling gradient required for proper dorsal-ventral patterning. Notably, this model fails to take other known dorsal-ventral regulators into account (e.g., ADMP, Sizzled, Follistatin, Noggin). Furthermore, approximately one third of *bmp2b* and *chordin* mutant embryos can be rescued by apparently uniform *bmp* and *chordin* expression, respectively (***Kishimoto et al., 1997***; ***Fisher and Halpern, 1999***) (***Figure 3C***), arguing against a strong requirement for concurrent opposing BMP and Chordin sources as long as one component of the system is biased (i.e. ventrally biased *bmp2b* expression with uniform Chordin, or dorsally biased *chordin* expression with uniform

BMP). Thus, further adjustments to the basic Model 1 will be required to fully describe dorsal-ventral patterning.

Although our results support a role for BMP diffusion in dorsal-ventral patterning, the necessity of signal diffusion for developmental patterning has recently been challenged by several studies (**Brankatschk and Dickson, 2006**; **Roy and Kornberg, 2011**; **Alexandre et al., 2014**; **Dominici et al., 2017**; **Varadarajan et al., 2017**). It will be interesting to determine whether BMP diffusion is indeed required for proper patterning using emerging nanobody-mediated diffusion perturbations (**Harmansa et al., 2015**) or optogenetics-based cell-autonomous modulation of signaling range (**Sako et al., 2016**).

Materials and methods

Immunostainings

To visualize pSmad1/5/9, wild type TE embryos were dechorionated at the one-cell stage using 1 mg/ml of Pronase (Roche, Cat. No. 11 459 643 001). Dechorionated embryos were incubated at 28°C and fixed at different developmental stages in 4% formaldehyde (Roth) in PBS overnight at 4°C on a shaker. Embryos were then stored in 100% methanol at −20°C for at least 2 hr. All subsequent steps were carried out at room temperature. Embryos were re-hydrated with 70%, 50%, and 30% methanol in PBS for 10 min each. The embryos were then washed eight times with PBST (0.1% Tween) for 15 min and blocked twice with blocking solution (10% fetal bovine serum and 1% DMSO in PBST) for 1 hr, and incubated with 1:100 anti-pSmad1/5/9 antibody (Cell Signaling Technology, Cat. No. 9511) for 4 hr. Embryos were washed with blocking solution for 15 min, washed seven times with PBST, blocked with blocking solution for 1 hr, incubated with 1:500 Alexa 488-coupled goat anti-rabbit secondary antibody (Life Technologies, Cat. No. A11008) for 4 hr, and washed similarly to the procedure after primary antibody application. Embryos were then counterstained with DAPI solution (0.2 µg/ml in PBST) for 1 hr and washed with PBST. Immunostainings were performed using an In situ Pro hybridization robot (Abimed/Intavis).

To analyze pSmad1/5/9 distributions in the absence of Chordin, embryos from one pair of *chordin*^{tt250} (**Hammerschmidt et al., 1996**) heterozygous parents were collected, fixed, immunostained with anti-pSmad1/5/9 antibody (Cell Signaling Technology, Cat. No. 13820S) as above, and imaged simultaneously to minimize differences between samples. Embryos were treated as described above, except that progeny from *chordin*$^{+/-}$ incrosses were first permeabilized with ice-cold acetone at −20°C for 7 min before the re-hydration step. After imaging and DNA extraction (**Meeker et al., 2007**), progeny from the *chordin*^{tt250} heterozygote incross were identified as wild type, heterozygous, or homozygous mutant embryos by PCR amplification using the forward primer 5'-TTCG TTTGGAGGACAACTCG-3' and the reverse primer 5'-AACTCAGCAGCAGAAGTCAATTC-3' with an initial denaturation step of 94°C for 3 min; 39 cycles of 94°C for 30 s, 55°C for 40 s, and 72°C for 30 s; and a final extension at 72°C for 5 min with subsequent digestion with MspI (New England Biolabs, Cat. No. R0106) for 2 hr. The genotyping assay for the *chordin*^{tt250} line was designed by the Zebrafish International Resource Center (ZIRC) staff and downloaded from the ZIRC website at http://zebrafish.org.

Generation of fluorescent BMP2b fusions

All constructs were generated by PCR-based methods (**Horton et al., 1990**), contain the consensus Kozak sequence *gccacc* 5' of the start codon, and were inserted into the EcoRI and XhoI sites of the pCS2(+) vector. To generate BMP2b-sfGFP and BMP2b-Dendra2, sequences encoding sfGFP or Dendra2 flanked by LGDPPVAT linkers were inserted two amino acids downstream of the BMP2b Furin cleavage site. Sequences encoding the FLAG tag DYKDDDDK were inserted between the first linker and sfGFP or Dendra2 to generate BMP2b-sfGFP-FLAG and BMP2b-Dendra2-FLAG. To generate BMP2b-FLAG, the FLAG tag was inserted between two LGDPPVAT linkers two amino acids downstream of the BMP2b Furin cleavage site.

Generation of fluorescent Chordin fusions

All constructs were generated by PCR-based methods (**Horton et al., 1990**) and contain the consensus Kozak sequence *gccacc* 5' of the start codon. Chordin was inserted into the ClaI site of pCS2(+).

All other Chordin-containing constructs were inserted into the EcoRI and XbaI sites of the pCS2(+) vector. To generate Chordin-sfGFP and BMP2b-Dendra2, sequences encoding sfGFP or Dendra2 flanked by LGDPPVAT linkers were inserted immediately 5' of the Tolloid cleavage site 2. To generate Chordin-FLAG, sequences encoding the FLAG tag DYKDDDDK were inserted immediately 5' of the Tolloid cleavage site 2 without additional linkers. To generate Chordin-sfGFP-FLAG and Chordin-Dendra2-FLAG, sequences encoding the FLAG tag were inserted between the first linker and sfGFP or Dendra2 of Chordin-sfGFP and Chordin-Dendra2 constructs.

Generation of fluorescent Sizzled fusions

All Sizzled constructs were generated by PCR-based methods (**Horton et al., 1990**), contain the consensus Kozak sequence *gccacc* 5' of the start codon, and were inserted into the EcoRI and XbaI sites of the pCS2(+) vector. To generate Sizzled-sfGFP, sequences encoding sfGFP with an N-terminal LGLG linker were fused to the C-terminus of Sizzled. Sequences encoding the FLAG tag DYKDDDDK were inserted between the LGLG linker and sfGFP to generate Sizzled-sfGFP-FLAG. To generate Sizzled-FLAG, the FLAG tag was fused to the C-terminus of Sizzled separated by an LGLG linker.

mRNA *in vitro* synthesis

mRNA was generated using SP6 mMessage mMachine kits (Thermo Fisher) after vector linearization with NotI-HF (New England Biolabs, Cat. No. R3189). mRNA was purified using LiCl precipitation or Qiagen RNeasy kits following the manufacturers' instructions.

Phenotypic analysis

Scoring of ventralization and dorsalization was executed as previously described (**Mullins et al., 1996**; **Kishimoto et al., 1997**). Embryos were injected at the one- to two-cell stage with equimolar amounts of *BMP2b* (1 pg), *BMP2b-sfGFP* (1.49 pg), and *BMP2b-Dendra2* (1.47 pg) mRNA to assess ventralizing activity. At 1 day post-fertilization, BMP2b-injected embryos were classified as weakly ventralized (V1) to strongly ventralized (V4). V1 embryos have reduced eyes but a prominent head. V2 embryos have no eyes, reduction of the head, and expansion of posterior structures such as somites and tail. V3 embryos completely lack head structures and exhibit a further expanded tail and enlarged blood islands. Finally, V4 embryos lack most structures except for a short, protruding, and expanded tail.

To assess dorsalizing activity of the Chordin constructs, embryos were injected with equimolar amounts of *Chordin* (30 pg), *Chordin-sfGFP* (37 pg), *Chordin-Dendra2* (37 pg), and *Chordin-FLAG* mRNA (30 pg). Embryos were scored at 1 day post-fertilization and classified as weakly dorsalized (C1) to strongly dorsalized (C5) (**Kishimoto et al., 1997**). C1 embryos lack the ventral tail fin. C2 embryos have a further loss of ventral structures, such as the ventral tail vein, and a bent tail. C3 embryos exhibit a tail that is shortened and twisted. C4 embryos have observable head structures and develop eyes with twisting of the posterior structures above the yolk. C5 embryos are fully dorsalized and frequently lyse (**Mullins et al., 1996**; **Kishimoto et al., 1997**).

Rescue of *BMP2b* ($swr^{-/-}$) mutants

Injection of *BMP2b* mRNA can rescue *BMP2b* mutants (**Kishimoto et al., 1997**). To investigate whether tagged BMP2b constructs can rescue $swr^{tc300-/-}$ mutants (**Mullins et al., 1996**), the rescuing amount of *BMP2b* mRNA was first determined (1.8 pg), and equimolar amounts of mRNA encoding fluorescent fusion constructs were subsequently injected into the progeny of heterozygous $swr^{+/-}$ mutant incrosses. Embryos with wild type morphology at 24 hpf were anesthetized and mounted in 2% methylcellulose for imaging with an AxioZoom V16 (ZEISS) microscope at 30–33 hpf. To genotype embryos following DNA extraction (**Meeker et al., 2007**), PCR was performed to amplify a BMP2b fragment with the forward primer 5'-AAAAGCCGAGGAGAAAGCAC-3' and the reverse primer 5'-AGTCCTTCATTGGGGAGATTGTTC-3', and the following thermocycling parameters: An initial denaturation step of 94°C for 3 min; 39 cycles of 94°C for 30 s, 58°C for 40 s, and 72°C for 40 s; and a final extension at 72°C for 5 min. PCR amplicons were subsequently digested with HaeIII (New England Biolabs, Cat. No. R0108) at 37°C for 2 hr. The genotyping assay for the

swr^{tc300} line was designed by the Zebrafish International Resource Center (ZIRC) staff and downloaded from the ZIRC website at http://zebrafish.org.

Preparation of extracellularly enriched fractions for western blotting

Extracellularly enriched and cellular fractions from manually deyolked embryos between sphere and dome stage were obtained as described previously (**Müller et al., 2012**). mRNAs encoding FLAG-tagged constructs were injected at the one- or two-cell stage at equimolar amounts (*BMP2b-FLAG*: 444 pg, *BMP2b-sfGFP-FLAG*: 638 pg, *BMP2b-Dendra2-FLAG*: 630 pg; and *Chordin-FLAG*: 500 pg, *Chordin-sfGFP-FLAG*: 620 pg, *Chordin-Dendra2-FLAG*: 615 pg). For protein samples with BMP2b constructs, fractions from approximately 19 embryos were loaded and resolved by SDS-PAGE using 12% polyacrylamide gels. For protein samples with Chordin constructs, fractions from approximately 17–18 embryos were loaded and resolved in 8% polyacrylamide gels. Proteins were subsequently transferred onto PVDF membranes using a Trans-Blot Turbo Transfer System (Bio-Rad, Cat. No. 170–4272). Membranes were blocked with 5% non-fat milk (Roth, Cat. No. T145.2) in PBST (0.1% Tween) and incubated with anti-FLAG antibody (Sigma, Cat. No. F3165) at a concentration of 1:2000 in non-fat milk in PBST at 4°C overnight. HRP-coupled donkey anti-mouse secondary antibody (Jackson ImmunoResearch, Cat. No. 715-035-150) was used at concentration of 1:25,000 for 3 hr at room temperature. Chemiluminescence was detected using SuperSignal West Dura Extended Duration Substrate (Thermo Fisher, Cat. No. 34075) and imaged with a chemiluminescence imaging system (Fusion Solo, Vilber Lourmat).

Transplantations

To generate clonal sources secreting BMP2b-sfGFP, Chordin-sfGFP, and untagged Chordin (**Figures 3** and **5**), approximately 50–75 cells were transplanted from sphere stage wild type TE donor embryos expressing these constructs into uninjected, sphere stage sibling hosts (similar to [**Müller et al., 2012**]). Transplantations were carried out in 1 x Ringer's buffer. Cells were explanted from donors, extruded briefly into the buffer to wash away cellular debris and extracellular fluorescent protein, and then transplanted into host embryos.

Donor embryos were dechorionated with 1 mg/ml Pronase (Roche, Cat. No. 11 459 643 001) and injected with 1–2 nl injection mix at the one-cell stage. Sibling host embryos were dechorionated together with donors at the one-cell stage, and all embryos were incubated at 28°C until transplantation. Unfertilized or injured embryos were discarded.

For single (**Figure 3**) and double (**Figure 5**) transplantation experiments, BMP2b-sfGFP and Chordin-sfGFP donors were injected with 500 pg mRNA (**Figure 3—figure supplement 1F–H**).

For double transplantation experiments (**Figure 5**), embryos received one transplantation from a donor expressing BMP2b-sfGFP and a second transplantation from a donor injected at the one-cell stage with either 50 pg Alexa 546-coupled dextran (10 kDa, Molecular Probes, Cat. No. D22911) or 1000 pg Chordin mRNA + 50 pg Alexa 546-coupled dextran. Alexa 546-coupled dextran was used to mark the location of the second clone.

2–10 min post-transplantation, embryos were mounted in 1% low-melting NuSieve GTG agarose (Lonza, Cat. No. 50080) dissolved in embryo medium (250 mg/l Instant Ocean salt dissolved in reverse osmosis water). Embryos were immersed in 40°C molten low melting point agarose, pulled into 1.5 mm glass capillary tubes (ZEISS), and positioned with the animal pole perpendicular to the capillary using a metal probe. Agarose tubes were then suspended in embryo medium, and imaged at room temperature using a ZEISS Lightsheet Z.1 microscope (see *Light sheet microscopy* section for further imaging details).

Light sheet microscopy

Fluorescence images in **Figures 1**, **2**, **3** and **5**, and **Figure 3—figure supplement 1** were obtained using a Lightsheet Z.1 microscope (ZEISS). For fixed, immunostained embryos, samples were mounted into a glass capillary sample holder in 1% low-melting NuSieve GTG agarose (Lonza, Cat. No. 50080) in embryo medium with 0.2 µm dark red fluorescent FluoSpheres (Life Technologies, Cat. No. F8807) diluted 1:200,000 from a 2% solids stock. Embryos were imaged at 0°, 45°, 180° and 225° angles (**Schmid et al., 2013**) using identical imaging conditions. For 3D reconstruction, an interactive bead-based registration algorithm was used to determine the threshold that most accurately

selects the beads (**Preibisch et al., 2010**). Reconstructed images were converted to 8-bit format using ImageJ, and Imaris software (Bitplane) was used for 3D data visualization and video generation. The videos were cropped using Avidemux 2.6.

To visualize the entire embryo in a single image, reconstructed images were first converted to 16-bit files using ImageJ, and equirectangular 2D map projections were then generated (**Schmid et al., 2013**). The 2D maps were re-aligned into Hammer-Aitoff projections using Hugin panorama photo stitcher software (http://hugin.sourceforge.net) to orient the peak of pSmad1/5/9 intensity to the ventral pole (left in **Figure 1** panels) and the trough of pSmad1/5/9 intensity to the dorsal pole (right in **Figure 1** panels). For gradient quantifications in **Figure 1A+B** and **Figure 2F–H**, the embryo proper was masked using manual polygon selections in Fiji (**Schindelin et al., 2012**) in order to exclude signal from the yolk syncytial layer and yolk. The 'Plot Profile' function in Fiji was then applied to the entire masked image to determine ventral-to-dorsal gradients. The background signal of immunostained embryos was determined by finding the lowest value in the profiles of sphere stage embryos (**Figure 1A+B**) and the lowest value in the profiles of *chordin*$^{-/-}$ embryos (**Figure 2F+G**), respectively. These background values were subtracted from the data sets, and the profiles were normalized to the highest value in each data series. The mean and standard error of the normalized data sets was then calculated piece-wise for every point along the ventral-to-dorsal profile.

For transplantation experiments in **Figures 3** and **5**, imaging began 5 to 20 min post-transplantation and continued for approximately 1 hr (see *Transplantation* section for further details). The following imaging conditions were used:

- W Plan-Apochromat 20 x objective, 0.5 x zoom
- dual side light sheets
- 488 nm laser (100 mW) at 6% power (for sfGFP-containing constructs)
- 561 nm laser (20 mW) at 5% power (for double transplantations only; to detect Alexa 546 signal)
- separate exposure to 488/561 nm lasers (in double transplantation experiments only) to avoid cross-talk
- exposure time: 250 ms
- average light sheet thickness: 6.4 µm
- 3 µm intervals between z-slices; 60 slices per embryo (≈180 µm total)
- 5 min intervals between imaging

Gradients were quantified using maximum intensity projections of 15 z-slices similar to the approach in (**Müller et al., 2012**). A rectangular region of interest abutting the clone with a fixed height of 86.34 µm (corresponding to 189 pixels) and varying widths depending on embryo length was drawn in Fiji (**Schindelin et al., 2012**), and the average intensity in 0.457 µm strips was calculated from the maximum intensity projections. Background intensity resulting from autofluorescence was measured similarly in uninjected embryos (for single transplantation experiments, n = 4) or in uninjected embryos transplanted with a clone of cells containing Alexa 546-coupled dextran (for double transplantation experiments, n = 2). A single value for background subtraction was determined by calculating the average of the intensity profile values. After subtracting the background value from the experimental intensity profiles, the data was normalized to the value closest to the clonal source boundary. This approach allows for the comparison of the relative gradient range, which is independent of constant production rates. We assume constant production rates over the relatively short time scales of observation (≈80 min).

Embryos with low signal-to-noise ratios were excluded from analysis.

Fluorescence decrease after photoconversion (FDAP) experiments

FDAP experiments were carried out as described in (**Müller et al., 2012**; **Rogers et al., 2015**). Embryos were injected at the one-cell stage with either 60 pg *BMP2b-Dendra2* mRNA + 0.5 ng Alexa 488-dextran (3 kDa, Molecular Probes) or 150 pg *Chordin-Dendra2* mRNA + 0.5 ng Alexa 488-dextran. To assess background fluorescence, embryos were injected with 0.5 ng Alexa 488-dextran only. Embryos were mounted in 1% low melting point agarose in glass-bottom Petri dishes (MatTek Corporation) covered with embryo medium to hydrate the agarose during imaging.

FDAP experiments were performed using an LSM 780 (ZEISS) confocal microscope. Pre-conversion and post-conversion images were acquired using an LD C-Apochromat 40x/1.1 NA water

immersion objective. A single pre-photoconversion image was first acquired for each sample followed by photoconversion and multiposition time-lapse imaging with 10 min intervals for approximately 300 min. For photoconversion, embryos were illuminated with a Sola SE II LED lamp at 100% power for 30 s through a C-Apochromat 10x/0.45 NA objective and an AHF F36-500 UV filter cube. For both pre- and post-conversion images, Alexa 488 was excited using a 488 nm Argon laser, and a DPSS 561 nm laser was used to excite photoconverted Dendra2. The emission signal between 494–576 nm (Alexa 488) and 578–696 nm (photoconverted Dendra2) was collected using a 32 channel GaAsP QUASAR detector array. Embryos that produced only low levels of photoconverted Dendra2 signal or whose position shifted significantly over time as well as embryos with non-uniform signal distribution or embryos that died were excluded from analysis. Sample numbers: n = 22 for BMP2b-Dendra2 (with n = 17 background embryos); n = 6 for Chordin-Dendra2 (with n = 1 background embryo).

All experiments were analyzed using PyFDAP (**Bläßle and Müller, 2015**; **Rogers et al., 2015**), version 1.1.2. PyFDAP extracts the extracellular and intracellular photoconverted Dendra2 signal by masking the Alexa 488 signal, and fits the resulting average intensities with a linear decay model. The ordinary differential equation describing linear protein decay is given by

$$\frac{dc}{dt} = -k_1 c$$

where c is the concentration of the protein and k_1 is its clearance rate constant. We assume that Dendra2 signal is directly proportional to the protein concentration. The analytical solution of this equation is given by

$$c(t) = c_0 e^{-k_1 t} + y_0$$

where $c_0 + y_0$ is the protein's concentration at $t = 0$, and y_0 is the protein's concentration at $t = \infty$. The half-life τ of the protein can then be calculated as

$$\tau = \ln(2)/k$$

PyFDAP estimates a lower bound for y_0 by computing the maximum relative effect of photobleaching $F_{i,r}$. For each background data set, the strongest influence of photobleaching was computed by taking the minimum over all differences of background intensity $B_{j,r}$ and background noise N_i, and the difference between pre-conversion background intensity $B_{\mathrm{pre},i,r}$ and noise level. Here, r denotes the region under consideration, i.e. extracellular, intracellular, or the entire imaging slice; i indicates the ith data set, and j counts the background data sets. The average over all b background data sets was then taken to arrive at the mean effect of photobleaching. The factor

$$F_{i,r} = \frac{1}{b}\sum_{j=1}^{b} \min_t \left(\frac{B_{j,r}(t) - N_i}{B_{\mathrm{pre}_{j,r}} - N_i} \right)$$

was used to scale the pre-conversion intensity of the FDAP data set according to

$$y_{0_{i,r}} \geq F_{i,r}\left(I_{\mathrm{pre}_{i,r}} - N_i\right) + N_i$$

This lower bound was then used to constrain a Nelder-Mead simplex algorithm when minimizing

$$SSD = \sum_n (\bar{I}(t_n) - c(t_n))^2$$

Fluorescence recovery after photobleaching (FRAP) experiments

FRAP experiments and data analysis were carried out as previously described (**Müller et al., 2012**; **Müller et al., 2013**) using an LSM 780 NLO confocal microscope (ZEISS) and an LD LCI Plan-Apochromat 25x water immersion objective. Embryos were injected at the one-cell stage with 30 pg of mRNA encoding BMP2b-sfGFP, 60 pg of mRNA encoding BMP2b-Dendra2, 60 pg of mRNA encoding Chordin-sfGFP, 120 pg of mRNA encoding Chordin-Dendra2, or 30 pg of mRNA encoding Sizzled-sfGFP. To analyze the effect of Chordin on BMP2b diffusion, embryos were injected at the one-cell stage with 30 pg of mRNA encoding BMP2b-sfGFP plus 60 or 200 pg of mRNA encoding

Chordin, or 60 pg of mRNA encoding BMP2b-Dendra2 plus 200 pg of mRNA encoding Chordin. Embryos were mounted in 1% low-melting point agarose in glass-bottom Petri dishes (MatTek Corporation) covered with embryo medium to hydrate the agarose during imaging. Embryos with low or non-uniform fluorescence and embryos that died or whose position shifted significantly over time were excluded from analysis.

For FRAP data analysis, the fits of a model with uniform production, diffusion, and clearance were constrained with the clearance rate constants of BMP2b-Dendra2 and Chordin-Dendra2 fusions measured by FDAP in the present study (BMP2b-Dendra2: $k_1 = 8.9 \times 10^{-5}$/s; Chordin-Dendra2: $k_1 = 9.6 \times 10^{-5}$/s). Sizzled-sfGFP fits were constrained with the clearance constant measured for BMP2b-Dendra2 assuming similar protein stability. As shown previously, the estimation of diffusion coefficients does not sensitively depend on the values of clearance rate constants if the time scales of observation (here: 50 min) and protein stability (here: approximately 120 min) are similar (***Müller et al., 2012***).

Fluorescence correlation spectroscopy (FCS) experiments

The FCS experiments were done using an LD C-Apochromat 40x/1.1 NA water immersion objective on an LSM 780 NLO confocal microscope (ZEISS). Embryos were injected at the one-cell stage with 30 pg of mRNA encoding BMP2b-sfGFP or 60 pg of mRNA encoding Chordin-sfGFP. Embryos were mounted in 1% low-melting point agarose in glass-bottom Petri dishes (MatTek Corporation) and covered with embryo medium to hydrate the agarose during imaging. The fluorophores (sfGFP, Alexa 488) were excited using an Argon 488 nm laser, and the emission light between 494 and 542 nm was collected using a 32-channel GaAsP QUASAR detector array. Before each FCS experiment, the pinhole was aligned and set to 1 Airy unit, and the instrument was calibrated using a solution of 40 nM Alexa 488 dye (Thermo Fisher) in water. For each FCS sample, fluorescence fluctuations were measured for 10 s with 10 repeats, and any irregularities in the 100 s count trace resulting from cellular movements were excluded from analysis.

Auto-correlation curves for Alexa 488 were freely fitted to determine the structural parameter as well as the diffusion time, the triplet state fraction, and the triplet state relaxation time of Alexa 488 for every experiment. The auto-correlation curves for BMP2b-sfGFP and Chordin-sfGFP were fitted with a fixed structural parameter, fixed triplet state fraction, and fixed triplet relaxation time determined from the Alexa 488 calibration measurements. The curves were fitted using ZEISS ZEN Pro software with a one-component 'free diffusion with triplet state correction' model. The first 10^{-6} seconds lag time for the correlation curve was excluded in the fitting (***Yu et al., 2009***; ***Müller et al., 2013***). The diffusion coefficient was then calculated by comparing the diffusion time of BMP2b-sfGFP and Chordin-sfGFP with Alexa 488 (reference diffusion coefficient: 435 μm^2/s [***Petrásek and Schwille, 2008***]).

Since the values of the triplet state fraction and the triplet state relaxation time of sfGFP are unknown and not necessarily identical to those of Alexa 488, we also freely fitted the autocorrelation curves for BMP2b-sfGFP and Chordin-sfGFP with the experimentally measured structural parameter as the only constraint, and determined free diffusion coefficients of $D = 35 \pm 2$ μm^2/s for BMP2b-sfGFP (n = 17 measurements from 4 embryos) and $D = 50 \pm 3$ μm^2/s for Chordin-sfGFP (n = 19 measurements from 5 embryos), within a deviation of approximately 20–30% compared to the diffusion coefficients determined by constraining the fits with a fixed structural parameter, fixed triplet state fraction, and fixed triplet relaxation time ($D = 46 \pm 1$ μm^2/s for BMP2b-sfGFP, and $D = 59 \pm 2$ μm^2/s for Chordin-sfGFP; values reported in ***Figure 4***). The similar diffusion coefficients determined by differently constrained fits indicate that the diffusion time measured in our experiments does not sensitively depend on the values of the triplet state fraction and triplet state relaxation time.

Mathematical modeling of BMP2b-sfGFP and Chordin-sfGFP gradient formation

The geometry of the zebrafish blastoderm was approximated by the complement of two spheres with a columnar subdomain placed off-center to represent the signal source region with the same parameters as described in ***Müller et al. (2012)***. Gradient formation was simulated with the source-diffusion-sink model

$$\frac{\partial c}{\partial t} = D\nabla^2 c - k_1 c + \delta_s k_2$$

with

$$\delta_s = \begin{cases} 1 & \text{in the source} \\ 0 & \text{otherwise} \end{cases}$$

For ***Figure 3—figure supplement 2***, the experimental data were fitted with solutions from a 50 × 50 parameter grid spanning all possible combinations of 50 diffusion coefficients (logarithmically spaced from 0.1 $\mu m^2/s$ to 50 $\mu m^2/s$) and 50 clearance rate constants (logarithmically spaced from 1 × 10^{-5}/s to 5 × 10^{-4}).

Simulations of previous models

The finite element method was used for all numerical simulations. All geometries are one-dimensional representations of embryos. The solution at each time step in the discretized geometries was determined using a sparse LU factorization algorithm (UMFPACK), and the time stepping was computed using a backward Euler step method (Comsol Multiphysics). Simulations in ***Figure 1C–E,G*** (Models 1, 2, 3, and 5) were executed for a total of 10080 s (i.e., for approximately 3 hr from sphere to shield stage during zebrafish embryogenesis [***Kimmel et al., 1995***]) and read out every 2520 s (i.e., approximately every 42 min at relevant zebrafish stages). The simulation in ***Figure 1F*** (Model 4) was executed for a total of 20 time steps near steady state and read out at every fifth time step.

The following model descriptions comprise the complete wild type systems. For simulations of *chordin* mutants, the Chordin flux was set to 0 (Models 1, 2, 3, and 5), or the Chordin-dependent terms were removed from the equations and the initial concentration of Chordin was set to 0 (Model 4). To focus on the role of Chordin in regulating BMP signaling and distribution, we did not include other negative regulators of BMP such as Noggin and Follistatin (***Umulis et al., 2009***). For the interpretation of the simulations, we assume that the distribution of free BMPs is correlated with BMP signaling and the distribution of pSmad1/5/9.

To facilitate comparison of the models, the distribution profiles of free BMP are shown as a function of relative embryo length, and the solutions were normalized to the ventral-most free BMP concentration at shield stage (i.e., at t = 7560 s for Models 1, 2, 3, and 5, and at t = 15 for Model 4) in wild type simulations.

Model 1: Graded source-sink (mobile BMP)

In the graded source-sink model, the BMP source $\rho_{BMP}(x)$ was modeled after the known distribution of *bmp2b* mRNA between sphere stage and 30% epiboly (***Ramel and Hill, 2013***). The model does not include autoregulation of BMP production since positive feedback only appears to be important for later stages of development (***Ramel and Hill, 2013***; ***Zinski et al., 2017***). Chordin binds BMP irreversibly and acts as a sink. The model was simulated using the following equations:

$$\frac{\partial[\mathrm{BMP}]}{\partial t} = D_{\mathrm{BMP}}\nabla^2[\mathrm{BMP}] - \kappa[\mathrm{Chd}][\mathrm{BMP}] - \lambda_{\mathrm{BMP}}[\mathrm{BMP}] + \rho_{\mathrm{BMP}}(x)$$

$$\frac{\partial[\mathrm{Chd}]}{\partial t} = D_{\mathrm{Chd}}\nabla^2[\mathrm{Chd}] - \kappa[\mathrm{Chd}][\mathrm{BMP}] - \lambda_{\mathrm{Chd}}[\mathrm{Chd}]$$

$$\frac{\partial[\mathrm{ChdBMP}]}{\partial t} = D_{\mathrm{ChdBMP}}\nabla^2[\mathrm{ChdBMP}] + \kappa[\mathrm{Chd}][\mathrm{BMP}] - \lambda_{\mathrm{Chd}}[\mathrm{ChdBMP}]$$

Embryo geometry and boundary conditions

Embryo length: 300 × 10^{-6} m (300 µm, the typical length of the zebrafish blastoderm)
Constant Chordin flux from the dorsal boundary: 5 × 10^{-14} mol/(m^2•s)
No-flux boundary condition for all other species on both ventral and dorsal boundaries

Parameter values

D_{BMP} = 2 $\mu m^2/s$ (measured in the present study)
D_{Chd} = 7 $\mu m^2/s$ (measured in the present study)
D_{ChdBMP} = 7 $\mu m^2/s$

λ_{BMP} = 8.9 × 10^{-5}/s (measured in the present study)
λ_{Chd} = 9.6 × 10^{-5}/s (measured in the present study)
κ = 400 × 10^{3} m^3/(mol•s)
$\rho_{BMP}(x)$ = 0.57 × 10^{-9} × e^{-5000x} mol/m^3 (accounting for the inhomogeneous ventrally peaking distribution of *bmp2b* mRNA in zebrafish embryos)

Initial conditions

BMP initial concentration: 2.85 × 10^{-8} mol/m^3 everywhere (one-twentieth of the concentration used for *Xenopus* frogs in [***Inomata et al., 2013***])
Chordin initial concentration: 0 mol/m^3 everywhere
Chordin-BMP complex initial concentration: 0 mol/m^3 everywhere

Model 2: Graded source-sink (immobile BMP)

As for Model 1, the graded source-sink model (immobile BMP) was modeled without autoregulation of BMP production since positive feedback only appears to be important for later stages of development (***Ramel and Hill, 2013***; ***Zinski et al., 2017***). Here κ, which reflects the binding between Chordin and BMP, is smaller than in Model 1 to obtain a realistic-free BMP distribution; using the same value for κ as in Model 1 creates an unrealistically steep free BMP gradient. The model was simulated using the following equations:

$$\frac{\partial[\mathrm{BMP}]}{\partial t} = -\kappa[\mathrm{Chd}][\mathrm{BMP}] - \lambda_{\mathrm{BMP}}[\mathrm{BMP}] + \rho_{\mathrm{BMP}}(x)$$

$$\frac{\partial[\mathrm{Chd}]}{\partial t} = D_{\mathrm{Chd}}\nabla^2[\mathrm{Chd}] - \kappa[\mathrm{Chd}][\mathrm{BMP}] - \lambda_{\mathrm{Chd}}[\mathrm{Chd}]$$

$$\frac{\partial[\mathrm{ChdBMP}]}{\partial t} = D_{\mathrm{ChdBMP}}\nabla^2[\mathrm{ChdBMP}] + \kappa[\mathrm{Chd}][\mathrm{BMP}] - \lambda_{\mathrm{Chd}}[\mathrm{ChdBMP}]$$

Embryo geometry and boundary conditions

Embryo length: 300 × 10^{-6} m (300 µm, the typical length of a zebrafish blastoderm)
Constant Chordin flux from the dorsal boundary: 5 × 10^{-14} mol/(m^2•s)
No-flux boundary condition for all other species on both ventral and dorsal boundaries

Parameter values

D_{Chd} = 7 μm^2/s (measured in the present study)
D_{ChdBMP} = 7 μm^2/s
λ_{BMP} = 8.9 × 10^{-5}/s (measured in the present study)
λ_{Chd} = 9.6 × 10^{-5}/s (measured in the present study)
κ = 4 × 10^{3} m^3/(mol•s)
$\rho_{BMP}(x)$ = 0.57 × 10^{-9} × e^{-5000x} mol/m^3 (accounting for the inhomogenous ventrally peaking distribution of *bmp2b* mRNA in zebrafish embryos)

Initial conditions

BMP initial concentration: 2.85 × 10^{-8} mol/m^3 everywhere (one-twentieth of the concentration used for *Xenopus* frogs in [***Inomata et al., 2013***]).
Chordin initial concentration: 0 mol/m^3 everywhere
Chordin-BMP complex initial concentration: 0 mol/m^3 everywhere

Model 3: Long-range accumulation and feedback

The model was developed for frog embryogenesis. For the simulations in the present study the equations, geometry, initial conditions, and parameters used were exactly as described in (***Inomata et al., 2013***):

$$\frac{\partial[\mathrm{BMP}]}{\partial t} = D\nabla^2[\mathrm{BMP}] + \frac{v_{\mathrm{BMP}}([\mathrm{ADMP}]+[\mathrm{BMP}])^{10}}{k_{\mathrm{BMP}}^{10}+([\mathrm{ADMP}]+[\mathrm{BMP}])^{10}} - \lambda_{\mathrm{BMP}}[\mathrm{BMP}]$$

$$+\frac{\lambda_{\mathrm{Chd}}[\mathrm{ChdBMP}]}{1+\frac{[\mathrm{Szl}]}{ki}+\frac{[\mathrm{Chd}]+[\mathrm{ChdBMP}]+[\mathrm{ChdADMP}]}{km}} - k[\mathrm{Chd}][\mathrm{BMP}]$$

$$\frac{\partial[\mathrm{Chd}]}{\partial t} = D\nabla^2[\mathrm{Chd}] + \frac{v_{\mathrm{Chd}}k_{\mathrm{Chd}}^{10}}{k_{\mathrm{Chd}}^{10}+([\mathrm{ADMP}]+[\mathrm{BMP}])^{10}} - \frac{\lambda_{\mathrm{Chd}}[\mathrm{Chd}]}{1+\frac{[\mathrm{Szl}]}{ki}+\frac{[\mathrm{Chd}]+[\mathrm{ChdBMP}]+[\mathrm{ChdADMP}]}{km}}$$

$$-k[\mathrm{Chd}][\mathrm{BMP}] - k[\mathrm{Chd}][\mathrm{ADMP}]$$

$$\frac{\partial[\mathrm{ADMP}]}{\partial t} = D\nabla^2[\mathrm{ADMP}] + \frac{v_{\mathrm{ADMP}}k_{\mathrm{ADMP}}^{10}}{k_{\mathrm{ADMP}}^{10}+([\mathrm{ADMP}]+[\mathrm{BMP}])^{10}} - \lambda_{\mathrm{BMP}}[\mathrm{ADMP}]$$

$$+\frac{\lambda_{\mathrm{Chd}}[\mathrm{ChdADMP}]}{1+\frac{[\mathrm{Szl}]}{ki}+\frac{[\mathrm{Chd}]+[\mathrm{ChdBMP}]+[\mathrm{ChdADMP}]}{km}} - k[\mathrm{Chd}][\mathrm{ADMP}]$$

$$\frac{\partial[\mathrm{Szl}]}{\partial t} = D\nabla^2[\mathrm{Szl}] + \frac{v_{\mathrm{Szl}}([\mathrm{ADMP}]+[\mathrm{BMP}])^{20}}{k_{\mathrm{Szl}}^{20}+([\mathrm{ADMP}]+[\mathrm{BMP}])^{20}} - \lambda_{\mathrm{Szl}}[\mathrm{Szl}]$$

$$\frac{\partial[\mathrm{ChdBMP}]}{\partial t} = D\nabla^2[\mathrm{ChdBMP}] - \frac{\lambda_{\mathrm{Chd}}[\mathrm{ChdBMP}]}{1+\frac{[\mathrm{Szl}]}{ki}+\frac{[\mathrm{Chd}]+[\mathrm{ChdBMP}]+[\mathrm{ChdADMP}]}{km}} + k[\mathrm{Chd}][\mathrm{BMP}]$$

$$\frac{\partial[\mathrm{ChdADMP}]}{\partial t} = D\nabla^2[\mathrm{ChdADMP}] - \frac{\lambda_{\mathrm{Chd}}[\mathrm{ChdADMP}]}{1+\frac{[\mathrm{Szl}]}{ki}+\frac{[\mathrm{Chd}]+[\mathrm{ChdBMP}]+[\mathrm{ChdADMP}]}{km}} + k[\mathrm{Chd}][\mathrm{ADMP}]$$

Embryo geometry and boundary conditions

Embryo length: 1000 × 10^{-6} m (1000 µm, the typical length of a frog embryo)
Constant Chordin flux from the dorsal boundary: 4.8 × 10^{-12} mol/(m^2•s)
No-flux boundary condition for all other species on both ventral and dorsal boundaries

Parameter values

km = 25 × 10^{-6} mol/m^3
ki = 25 × 10^{-6} mol/m^3
v_{Chd} = 5 × 10^{-10} mol/(m^3•s)
k_{Chd} = 7 × 10^{-8} mol/m^3
v_{BMP} = 1.4 × 10^{-10} mol/(m^3•s)
k_{BMP} = 3.5 × 10^{-7} mol/m^3
v_{Szl} = 100 × 10^{-6} mol/(m^3•s)
k_{Szl} = 1 × 10^{-6} mol/m^3
v_{ADMP} = 3.2 × 10^{-9} mol/(m^3•s)
k_{ADMP} = 3 × 10^{-8} mol/m^3
λ_{Chd} = 1 × 10^{-3}/s
λ_{BMP} = 2 × 10^{-4}/s
λ_{Szl} = 3.8 × 10^{-5}/s
D = 15 µm^2/s
k = 280 m^3/(mol•s)

Initial conditions

BMP initial concentration: 0.57 × 10^{-6} × e^{-1000x} mol/m^3 throughout the embryo (the amplitude of this distribution is the same as in [***Inomata et al., 2013***], but the initial BMP profile was modeled as a gradient instead of uniform)
Chordin initial concentration: 0 mol/m^3 everywhere

ADMP initial concentration: 0 mol/m^3 everywhere
Sizzled initial concentration: 0 mol/m^3 everywhere
Chordin-BMP complex initial concentration: 0 mol/m^3 everywhere
Chordin-AMP complex initial concentration: 0 mol/m^3 everywhere

For the simulations in ***Figure 4—figure supplement 1E–J***, all parameters were identical to the parameter values listed above except for *D*(BMP) = 3 µm^2/s, *D*(Chd) = 6 µm^2/s, *D*(ChdADMP) = 10 µm^2/s, and *D*(ChdBMP) = 10 µm^2/s. *D*(Sizzled) was set to 150 µm^2/s in ***Figure 4—figure supplement 1E***, and to 10 µm^2/s in ***Figure 4—figure supplement 1F–J***. *D*(ADMP) was varied from 0.1 µm^2/s to 150 µm^2/s as indicated in ***Figure 4—figure supplement 1E–J***.

Model 4: Self-regulating reaction-diffusion system

The non-dimensional model, geometry, initial conditions, and parameters used for the simulations were similar to the ones described in [***Francois et al., 2009***]:

$$\frac{\partial[\mathrm{BMP}]}{\partial t} = D_{\mathrm{BMP}}\nabla^2[\mathrm{BMP}] + \frac{[\mathrm{BMP}]^2}{(1+[\mathrm{Chd}])[\mathrm{Szl}]} - \mu_{\mathrm{BMP}}[\mathrm{BMP}] + \rho_{\mathrm{BMP}}$$

$$\frac{\partial[\mathrm{Chd}]}{\partial t} = D_{\mathrm{Chd}}\nabla^2[\mathrm{Chd}] + \frac{[\mathrm{Chd}]^2}{[\mathrm{ADMP}]} - \mu_{\mathrm{Chd}}[\mathrm{Chd}] + \rho_{\mathrm{Chd}}$$

$$\frac{\partial[\mathrm{ADMP}]}{\partial t} = D_{\mathrm{ADMP}}\nabla^2[\mathrm{ADMP}] + [\mathrm{Chd}]^2 - \mu_{\mathrm{ADMP}}[\mathrm{ADMP}]$$

$$\frac{\partial[\mathrm{Szl}]}{\partial t} = D_{\mathrm{Szl}}\nabla^2[\mathrm{Szl}] + [\mathrm{BMP}]^2 - \mu_{\mathrm{Szl}}[\mathrm{Szl}]$$

Embryo geometry and boundary conditions

Embryo length: 25
No-flux boundary conditions on the ventral and dorsal boundaries

Parameter values

$D_{Chd} = D_{BMP} = 6$
$\mu_{Chd} = \mu_{BMP} = 1.2$
$\rho_{Chd} = \rho_{BMP} = 0.1$
$\mu_{ADMP} = \mu_{Szl} = 1.5$
$D_{ADMP} = D_{Szl} = 150$

Initial conditions

BMP initial concentration: $\rho_{BMP} = e^{-0.1x}$
Chordin initial concentration of 1 from position 0 to 24 and Chordin initial concentration of 10 from 24 to 25 (i.e., the dorsal organizer) in the simulated embryo
ADMP initial concentration: 1 everywhere
Sizzled initial concentration: 1 everywhere

For the simulations in ***Figure 4—figure supplement 1K–P***, all parameters were identical to the parameter values listed above except for *D*(BMP) = 3 and *D*(Chd) = 6. *D*(Sizzled) was set to 150 in ***Figure 4—figure supplement 1K***, and to 10 in ***Figure 4—figure supplement 1L–P***. *D*(ADMP) was varied from 0.1 to 150 as indicated in ***Figure 4—figure supplement 1K–P***.

Model 5: Shuttling

For Model 5, a minimal transport model that excludes the effects of downstream patterning circuits was used to illustrate the biophysical aspects of shuttling (***Ben-Zvi et al., 2008***):

$$\frac{\partial[\mathrm{BMP}]}{\partial t} = D_{\mathrm{BMP}}\nabla^2[\mathrm{BMP}] - \kappa[\mathrm{Chd}][\mathrm{BMP}] + \lambda[\mathrm{Xlr}][\mathrm{ChdBMP}] - \lambda_{\mathrm{BMP}}[\mathrm{BMP}] + \rho_{\mathrm{BMP}}(x)$$

$$\frac{\partial[\mathrm{Chd}]}{\partial t} = D_{\mathrm{Chd}}\nabla^2[\mathrm{Chd}] - \kappa[\mathrm{Chd}][\mathrm{BMP}] - \lambda_{\mathrm{Chd}}[\mathrm{Chd}]$$

$$\frac{\partial[\mathrm{ChdBMP}]}{\partial t} = D_{\mathrm{ChdBMP}}\nabla^2[\mathrm{ChdBMP}] + \kappa[\mathrm{Chd}][\mathrm{BMP}] - \lambda[\mathrm{Xlr}][\mathrm{ChdBMP}] - \lambda_{\mathrm{Chd}}[\mathrm{ChdBMP}]$$

Embryo geometry and boundary conditions

Embryo length: 300×10^{-6} m (300 µm)
Constant Chordin flux from the dorsal boundary: 3×10^{-14} mol/(m^2•s)
No-flux boundary condition for all other species on both ventral and dorsal boundaries

Parameter values

D_{BMP} = 0.1 µm^2/s
D_{Chd} = 10 µm^2/s
D_{ChdBMP} = 10 µm^2/s
$\lambda_{BMP} = 8.9 \times 10^{-5}$/s (measured in the present study)
$\lambda_{Chd} = 9.6 \times 10^{-5}$/s (measured in the present study)
$\kappa = 100 \times 10^3$ m^3/(mol•s)
$\lambda = \kappa$
[Xlr] = 2×10^{-8} mol/m^3
$\rho_{BMP}(x) = 0.57 \times 10^{-10} \times e^{-5000x}$ mol/m^3 (accounting for the inhomogeneous ventrally peaking distribution of *bmp2b* mRNA in zebrafish embryos)

Initial conditions

BMP initial concentration: $0.57 \times 10^{-7} \times e^{-5000x}$ mol/m^3 throughout the embryo
Chordin initial concentration: 0 mol/m^3 everywhere
Chordin-BMP complex initial concentration: 0 mol/m^3 everywhere

Shuttling simulations of adjacent BMP and Chordin clones shown in *Figure 5*

The one-dimensional simulations in ***Figure 5*** were executed similarly to the ones described above and solved at 15 and 75 min for comparison to the zebrafish embryo double transplantation experiments. The solutions in ***Figure 5A*** and ***Figure 5E*** were normalized to the highest free BMP concentration in the simulation without the Chordin source, and the solutions in ***Figure 5B*** and ***Figure 5F*** were normalized to the free BMP concentration at the BMP source boundary (at 100 µm) for each condition to facilitate comparison between the gradient ranges.

The double transplantation experiments were modeled using the following equations:

$$\frac{\partial[\mathrm{BMP}]}{\partial t} = D_{\mathrm{BMP}}\nabla^2[\mathrm{BMP}] - \lambda_{\mathrm{BMP}}[\mathrm{BMP}] - \kappa[\mathrm{Chd}][\mathrm{BMP}] + \lambda[\mathrm{Xlr}][\mathrm{ChdBMP}] + \delta_{\mathrm{BMP}}\eta_{\mathrm{BMP}}$$

$$\frac{\partial[\mathrm{Chd}]}{\partial t} = D_{\mathrm{Chd}}\nabla^2[\mathrm{Chd}] - \kappa[\mathrm{Chd}][\mathrm{BMP}] + \delta_{\mathrm{Chd}}\eta_{\mathrm{Chd}}$$

$$\frac{\partial[\mathrm{ChdBMP}]}{\partial t} = D_{\mathrm{ChdBMP}}\nabla^2[\mathrm{ChdBMP}] + \kappa[\mathrm{Chd}][\mathrm{BMP}] - \lambda[\mathrm{Xlr}][\mathrm{ChdBMP}]$$

with

$$\delta_{\mathrm{BMP}} = \begin{cases} 1 \text{ in the BMP source} \\ 0 \text{ otherwise} \end{cases}$$

and

$$\delta_{\mathrm{Chd}} = \begin{cases} 1 \text{ in the Chordin source} \\ 0 \text{ otherwise} \end{cases}$$

Embryo geometry and boundary conditions

Embryo length: 300×10^{-6} m (300 µm)
BMP source: between 50 and 100 µm from the left boundary
Chordin source: between 200 and 250 µm from the left boundary
No-flux boundary conditions on the left and right boundaries

Parameter values for simulations of shuttling predictions (***Figure 5A+B***)

D_{BMP} = 2 µm^2/s (measured in the present study)
λ_{BMP} = 0.0001/s (similar to measurements in the present study)
η_{BMP} = 5×10^{-5} mol/(m^3•s)
η_{Chd} = 5×10^{-5} mol/(m^3•s)
D_{Chd} = 100 µm^2/s
$D_{ChdBMP} = D_{Chd}$
$\kappa = 10 \times 10^3$ m^3/(mol•s)
$\lambda = \kappa$
[Xlr] = 2×10^{-7} mol/m^3

Parameter values for simulations with experimentally measured diffusivities (***Figure 5E+F***)

D_{BMP} = 2 µm^2/s (measured in the present study)
λ_{BMP} = 0.0001/s (similar to measurements in the present study)
η_{BMP} = 5×10^{-5} mol/(m^3•s)
η_{Chd} = 5×10^{-5} mol/(m^3•s)
D_{Chd} = 6 µm^2/s (measured in the present study)
D_{ChdBMP} = 2.2 µm^2/s (measured in the present study)
$\kappa = 10 \times 10^3$ m^3/(mol s)
$\lambda = \kappa$
[Xlr] = 2×10^{-7} mol/m^3

Initial conditions

BMP initial concentration: 0 mol/m^3 everywhere
Chordin initial concentration: 0 mol/m^3 everywhere
Chordin-BMP complex initial concentration: 0 mol/m^3 everywhere

Acknowledgements

We are grateful to Hans Meinhardt for valuable discussions of BMP/Chordin-mediated dorsal-ventral patterning mechanisms. We thank Edgar Herrera and Luciano Marcon for support with immunostainings, light sheet microscopy, data reconstruction, and helpful discussions. We acknowledge Matteo Pilz and Sarah Keim for technical assistance. This work was supported by the Max Planck Society and a Human Frontier Science Program (HFSP) Career Development Award to PM.

Additional information

Funding

Funder	Grant reference number	Author
Max-Planck-Gesellschaft		Patrick Müller
Human Frontier Science Program	Career Development Award (CDA00031/2013-C)	Patrick Müller

The funders had no role in study design, data collection and interpretation, or the decision to submit the work for publication.

Author contributions

Autumn P Pomreinke, Gary H Soh, Data curation, Formal analysis, Investigation, Visualization, Methodology, Writing—review and editing; Katherine W Rogers, Conceptualization, Resources, Data curation, Formal analysis, Investigation, Visualization, Methodology, Writing—review and editing; Jennifer K Bergmann, Resources, Data curation, Formal analysis, Investigation, Visualization; Alexander J Bläßle, Data curation, Software, Formal analysis, Investigation, Visualization, Methodology, Writing—review and editing; Patrick Müller, Conceptualization, Resources, Data curation, Software, Formal analysis, Supervision, Funding acquisition, Validation, Investigation, Visualization, Methodology, Writing—original draft, Project administration, Writing—review and editing

Author ORCIDs

Katherine W Rogers, http://orcid.org/0000-0001-5700-2662
Patrick Müller, http://orcid.org/0000-0002-0702-6209

Decision letter and Author response

Decision letter https://doi.org/10.7554/eLife.25861.024
Author response https://doi.org/10.7554/eLife.25861.025

Additional files

Supplementary files

- Transparent reporting form

DOI: https://doi.org/10.7554/eLife.25861.023

References

Alexandre C, Baena-Lopez A, Vincent JP. 2014. Patterning and growth control by membrane-tethered Wingless. *Nature* **505**:180–185. DOI: https://doi.org/10.1038/nature12879, PMID: 24390349

Barkai N, Ben-Zvi D. 2009. 'Big frog, small frog'–maintaining proportions in embryonic development: delivered on 2 July 2008 at the 33rd FEBS Congress in Athens, Greece. *The FEBS Journal* **276**:1196–1207. DOI: https://doi.org/10.1111/j.1742-4658.2008.06854.x, PMID: 19175672

Ben-Zvi D, Shilo BZ, Fainsod A, Barkai N. 2008. Scaling of the BMP activation gradient in Xenopus embryos. *Nature* **453**:1205–1211. DOI: https://doi.org/10.1038/nature07059, PMID: 18580943

Ben-Zvi D, Barkai N. 2010. Scaling of morphogen gradients by an expansion-repression integral feedback control. *PNAS* **107**:6924–6929. DOI: https://doi.org/10.1073/pnas.0912734107, PMID: 20356830

Ben-Zvi D, Pyrowolakis G, Barkai N, Shilo BZ. 2011a. Expansion-repression mechanism for scaling the Dpp activation gradient in Drosophila wing imaginal discs. *Current Biology* **21**:1391–1396. DOI: https://doi.org/10.1016/j.cub.2011.07.015, PMID: 21835621

Ben-Zvi D, Shilo BZ, Barkai N. 2011b. Scaling of morphogen gradients. *Current Opinion in Genetics & Development* **21**:704–710. DOI: https://doi.org/10.1016/j.gde.2011.07.011, PMID: 21873045

Ben-Zvi D, Fainsod A, Shilo BZ, Barkai N. 2014. Scaling of dorsal-ventral patterning in the Xenopus laevis embryo. *BioEssays* **36**:151–156. DOI: https://doi.org/10.1002/bies.201300136, PMID: 24323952

Bläßle A, Müller P. 2015. PyFDAP: automated analysis of fluorescence decay after photoconversion (FDAP) experiments. *Bioinformatics* **31**:972–974. DOI: https://doi.org/10.1093/bioinformatics/btu735, PMID: 25380959

Brankatschk M, Dickson BJ. 2006. Netrins guide Drosophila commissural axons at short range. *Nature Neuroscience* **9**:188–194. DOI: https://doi.org/10.1038/nn1625, PMID: 16429137

Connors SA, Trout J, Ekker M, Mullins MC. 1999. The role of tolloid/mini fin in dorsoventral pattern formation of the zebrafish embryo. *Development* **126**:3119–3130. PMID: 10375503

Cui Y, Jean F, Thomas G, Christian JL. 1998. BMP-4 is proteolytically activated by furin and/or PC6 during vertebrate embryonic development. *The EMBO Journal* **17**:4735–4743. DOI: https://doi.org/10.1093/emboj/17.16.4735, PMID: 9707432

Degnin C, Jean F, Thomas G, Christian JL. 2004. Cleavages within the prodomain direct intracellular trafficking and degradation of mature bone morphogenetic protein-4. *Molecular Biology of the Cell* **15**:5012–5020. DOI: https://doi.org/10.1091/mbc.E04-08-0673, PMID: 15356272

Dickmeis T, Rastegar S, Aanstad P, Clark M, Fischer N, Korzh V, Strähle U. 2001. Expression of the anti-dorsalizing morphogenetic protein gene in the zebrafish embryo. *Development Genes and Evolution* **211**:568–572. DOI: https://doi.org/10.1007/s00427-001-0190-3, PMID: 11862464

Dominici C, Moreno-Bravo JA, Puiggros SR, Rappeneau Q, Rama N, Vieugue P, Bernet A, Mehlen P, Chédotal A. 2017. Floor-plate-derived netrin-1 is dispensable for commissural axon guidance. *Nature* **545**:350–354. DOI: https://doi.org/10.1038/nature22331, PMID: 28445456

Fisher S, Halpern ME. 1999. Patterning the zebrafish axial skeleton requires early chordin function. *Nature Genetics* **23**:442–446. DOI: https://doi.org/10.1038/70557, PMID: 10581032

Francois P, Vonica A, Brivanlou AH, Siggia ED. 2009. Scaling of BMP gradients in Xenopus embryos. *Nature* **461**: E1. DOI: https://doi.org/10.1038/nature08305, PMID: 19736667

Gurskaya NG, Verkhusha VV, Shcheglov AS, Staroverov DB, Chepurnykh TV, Fradkov AF, Lukyanov S, Lukyanov KA. 2006. Engineering of a monomeric green-to-red photoactivatable fluorescent protein induced by blue light. *Nature Biotechnology* **24**:461–465. DOI: https://doi.org/10.1038/nbt1191, PMID: 16550175

Hammerschmidt M, Pelegri F, Mullins MC, Kane DA, van Eeden FJ, Granato M, Brand M, Furutani-Seiki M, Haffter P, Heisenberg CP, Jiang YJ, Kelsh RN, Odenthal J, Warga RM, Nüsslein-Volhard C. 1996. dino and mercedes, two genes regulating dorsal development in the zebrafish embryo. *Development* **123**:95–102. PMID: 9007232

Harmansa S, Hamaratoglu F, Affolter M, Caussinus E. 2015. Dpp spreading is required for medial but not for lateral wing disc growth. *Nature* **527**:317–322. DOI: https://doi.org/10.1038/nature15712, PMID: 26550827

Haskel-Ittah M, Ben-Zvi D, Branski-Arieli M, Schejter ED, Shilo BZ, Barkai N. 2012. Self-organized shuttling: generating sharp dorsoventral polarity in the early Drosophila embryo. *Cell* **150**:1016–1028. DOI: https://doi.org/10.1016/j.cell.2012.06.044, PMID: 22939625

Horton RM, Cai ZL, Ho SN, Pease LR. 1990. Gene splicing by overlap extension: tailor-made genes using the polymerase chain reaction. *BioTechniques* **8**:528–535. DOI: https://doi.org/10.2144/000114017, PMID: 2357375

Inomata H, Shibata T, Haraguchi T, Sasai Y. 2013. Scaling of dorsal-ventral patterning by embryo size-dependent degradation of Spemann's organizer signals. *Cell* **153**:1296–1311. DOI: https://doi.org/10.1016/j.cell.2013.05.004, PMID: 23746842

Jones CM, Armes N, Smith JC. 1996. Signalling by TGF-beta family members: short-range effects of Xnr-2 and BMP-4 contrast with the long-range effects of activin. *Current Biology* **6**:1468–1475. DOI: https://doi.org/10.1016/S0960-9822(96)00751-8, PMID: 8939607

Kicheva A, Pantazis P, Bollenbach T, Kalaidzidis Y, Bittig T, Jülicher F, González-Gaitán M. 2007. Kinetics of morphogen gradient formation. *Science* **315**:521–525. DOI: https://doi.org/10.1126/science.1135774, PMID: 17255514

Kimmel CB, Ballard WW, Kimmel SR, Ullmann B, Schilling TF. 1995. Stages of embryonic development of the zebrafish. *Developmental Dynamics* **203**:253–310. DOI: https://doi.org/10.1002/aja.1002030302, PMID: 8589427

Kishimoto Y, Lee KH, Zon L, Hammerschmidt M, Schulte-Merker S. 1997. The molecular nature of zebrafish swirl: BMP2 function is essential during early dorsoventral patterning. *Development* **124**:4457–4466. PMID: 9409664

Koos DS, Ho RK. 1999. The nieuwkoid/dharma homeobox gene is essential for bmp2b repression in the zebrafish pregastrula. *Developmental Biology* **215**:190–207. DOI: https://doi.org/10.1006/dbio.1999.9479, PMID: 10545230

Lele Z, Nowak M, Hammerschmidt M. 2001. Zebrafish admp is required to restrict the size of the organizer and to promote posterior and ventral development. *Developmental Dynamics* **222**:681–687. DOI: https://doi.org/10.1002/dvdy.1222, PMID: 11748836

Leung T, Bischof J, Söll I, Niessing D, Zhang D, Ma J, Jäckle H, Driever W. 2003. bozozok directly represses bmp2b transcription and mediates the earliest dorsoventral asymmetry of bmp2b expression in zebrafish. *Development* **130**:3639–3649. DOI: https://doi.org/10.1242/dev.00558, PMID: 12835381

Meeker ND, Hutchinson SA, Ho L, Trede NS. 2007. Method for isolation of PCR-ready genomic DNA from zebrafish tissues. *BioTechniques* **43**:610–614. DOI: https://doi.org/10.2144/000112619, PMID: 18072590

Miller-Bertoglio VE, Fisher S, Sánchez A, Mullins MC, Halpern ME. 1997. Differential regulation of chordin expression domains in mutant zebrafish. *Developmental Biology* **192**:537–550. DOI: https://doi.org/10.1006/dbio.1997.8788, PMID: 9441687

Mullins MC, Hammerschmidt M, Kane DA, Odenthal J, Brand M, van Eeden FJ, Furutani-Seiki M, Granato M, Haffter P, Heisenberg CP, Jiang YJ, Kelsh RN, Nüsslein-Volhard C. 1996. Genes establishing dorsoventral pattern formation in the zebrafish embryo: the ventral specifying genes. *Development* **123**:81–93. PMID: 9007231

Müller P, Schier AF. 2011. Extracellular movement of signaling molecules. *Developmental Cell* **21**:145–158. DOI: https://doi.org/10.1016/j.devcel.2011.06.001, PMID: 21763615

Müller P, Rogers KW, Jordan BM, Lee JS, Robson D, Ramanathan S, Schier AF. 2012. Differential diffusivity of Nodal and Lefty underlies a reaction-diffusion patterning system. *Science* **336**:721–724. DOI: https://doi.org/10.1126/science.1221920, PMID: 22499809

Müller P, Rogers KW, Yu SR, Brand M, Schier AF. 2013. Morphogen transport. *Development* **140**:1621–1638. DOI: https://doi.org/10.1242/dev.083519, PMID: 23533171

Petrásek Z, Schwille P. 2008. Precise measurement of diffusion coefficients using scanning fluorescence correlation spectroscopy. *Biophysical Journal* **94**:1437–1448. DOI: https://doi.org/10.1529/biophysj.107.108811, PMID: 17933881

Plouhinec JL, De Robertis EM. 2009. Systems biology of the self-regulating morphogenetic gradient of the Xenopus gastrula. *Cold Spring Harbor Perspectives in Biology* **1**:a001701. DOI: https://doi.org/10.1101/cshperspect.a001701, PMID: 20066084

Plouhinec JL, Zakin L, Moriyama Y, De Robertis EM. 2013. Chordin forms a self-organizing morphogen gradient in the extracellular space between ectoderm and mesoderm in the Xenopus embryo. *PNAS* **110**:20372–20379. DOI: https://doi.org/10.1073/pnas.1319745110, PMID: 24284174

Preibisch S, Saalfeld S, Schindelin J, Tomancak P. 2010. Software for bead-based registration of selective plane illumination microscopy data. *Nature Methods* **7**:418–419. DOI: https://doi.org/10.1038/nmeth0610-418, PMID: 20508634

Pédelacq JD, Cabantous S, Tran T, Terwilliger TC, Waldo GS. 2006. Engineering and characterization of a superfolder green fluorescent protein. *Nature Biotechnology* **24**:79–88. DOI: https://doi.org/10.1038/nbt1172, PMID: 16369541

Ramel MC, Hill CS. 2013. The ventral to dorsal BMP activity gradient in the early zebrafish embryo is determined by graded expression of BMP ligands. *Developmental Biology* **378**:170–182. DOI: https://doi.org/10.1016/j.ydbio.2013.03.003, PMID: 23499658

Rogers KW, Blässle A, Schier AF, Müller P. 2015. Measuring protein stability in living zebrafish embryos using fluorescence decay after photoconversion (FDAP). *Journal of Visualized Experiments*:52266. DOI: https://doi.org/10.3791/52266, PMID: 25650549

Roy S, Kornberg TB. 2011. Direct delivery mechanisms of morphogen dispersion. *Science Signaling* **4**:pt8. DOI: https://doi.org/10.1126/scisignal.2002434, PMID: 22114143

Sako K, Pradhan SJ, Barone V, Inglés-Prieto Á, Müller P, Ruprecht V, Čapek D, Galande S, Janovjak H, Heisenberg CP. 2016. Optogenetic control of nodal signaling reveals a temporal pattern of nodal signaling regulating cell fate specification during gastrulation. *Cell Reports* **16**:866–877. DOI: https://doi.org/10.1016/j.celrep.2016.06.036, PMID: 27396324

Schier AF, Talbot WS. 2005. Molecular genetics of axis formation in zebrafish. *Annual Review of Genetics* **39**:561–613. DOI: https://doi.org/10.1146/annurev.genet.37.110801.143752, PMID: 16285872

Schindelin J, Arganda-Carreras I, Frise E, Kaynig V, Longair M, Pietzsch T, Preibisch S, Rueden C, Saalfeld S, Schmid B, Tinevez JY, White DJ, Hartenstein V, Eliceiri K, Tomancak P, Cardona A. 2012. Fiji: an open-source platform for biological-image analysis. *Nature Methods* **9**:676–682. DOI: https://doi.org/10.1038/nmeth.2019, PMID: 22743772

Schmid B, Shah G, Scherf N, Weber M, Thierbach K, Campos CP, Roeder I, Aanstad P, Huisken J. 2013. High-speed panoramic light-sheet microscopy reveals global endodermal cell dynamics. *Nature Communications* **4**:2207. DOI: https://doi.org/10.1038/ncomms3207, PMID: 23884240

Sopory S, Nelsen SM, Degnin C, Wong C, Christian JL. 2006. Regulation of bone morphogenetic protein-4 activity by sequence elements within the prodomain. *Journal of Biological Chemistry* **281**:34021–34031. DOI: https://doi.org/10.1074/jbc.M605330200, PMID: 16966322

Tucker JA, Mintzer KA, Mullins MC. 2008. The BMP signaling gradient patterns dorsoventral tissues in a temporally progressive manner along the anteroposterior axis. *Developmental Cell* **14**:108–119. DOI: https://doi.org/10.1016/j.devcel.2007.11.004, PMID: 18194657

Umulis D, O'Connor MB, Blair SS. 2009. The extracellular regulation of bone morphogenetic protein signaling. *Development* **136**:3715–3728. DOI: https://doi.org/10.1242/dev.031534, PMID: 19855014

Varadarajan SG, Kong JH, Phan KD, Kao TJ, Panaitof SC, Cardin J, Eltzschig H, Kania A, Novitch BG, Butler SJ. 2017. Netrin1 Produced by Neural Progenitors, Not Floor Plate Cells, Is Required for Axon Guidance in the Spinal Cord. *Neuron* **94**:790–799. DOI: https://doi.org/10.1016/j.neuron.2017.03.007, PMID: 28434801

Xu PF, Houssin N, Ferri-Lagneau KF, Thisse B, Thisse C. 2014. Construction of a vertebrate embryo from two opposing morphogen gradients. *Science* **344**:87–89. DOI: https://doi.org/10.1126/science.1248252, PMID: 24700857

Yu SR, Burkhardt M, Nowak M, Ries J, Petrásek Z, Scholpp S, Schwille P, Brand M. 2009. Fgf8 morphogen gradient forms by a source-sink mechanism with freely diffusing molecules. *Nature* **461**:533–536. DOI: https://doi.org/10.1038/nature08391, PMID: 19741606

Zinski J, Bu Y, Wang X, Dou W, Umulis D, Mullins M. 2017. Systems biology derived source-sink mechanism of BMP gradient formation. *eLife* **6**:e22199. DOI: https://doi.org/10.7554/eLife.22199, PMID: 28826472

eLIFE elifesciences.org

RESEARCH ARTICLE

Figures and figure supplements

Dynamics of BMP signaling and distribution during zebrafish dorsal-ventral patterning

Autumn P Pomreinke *et al*

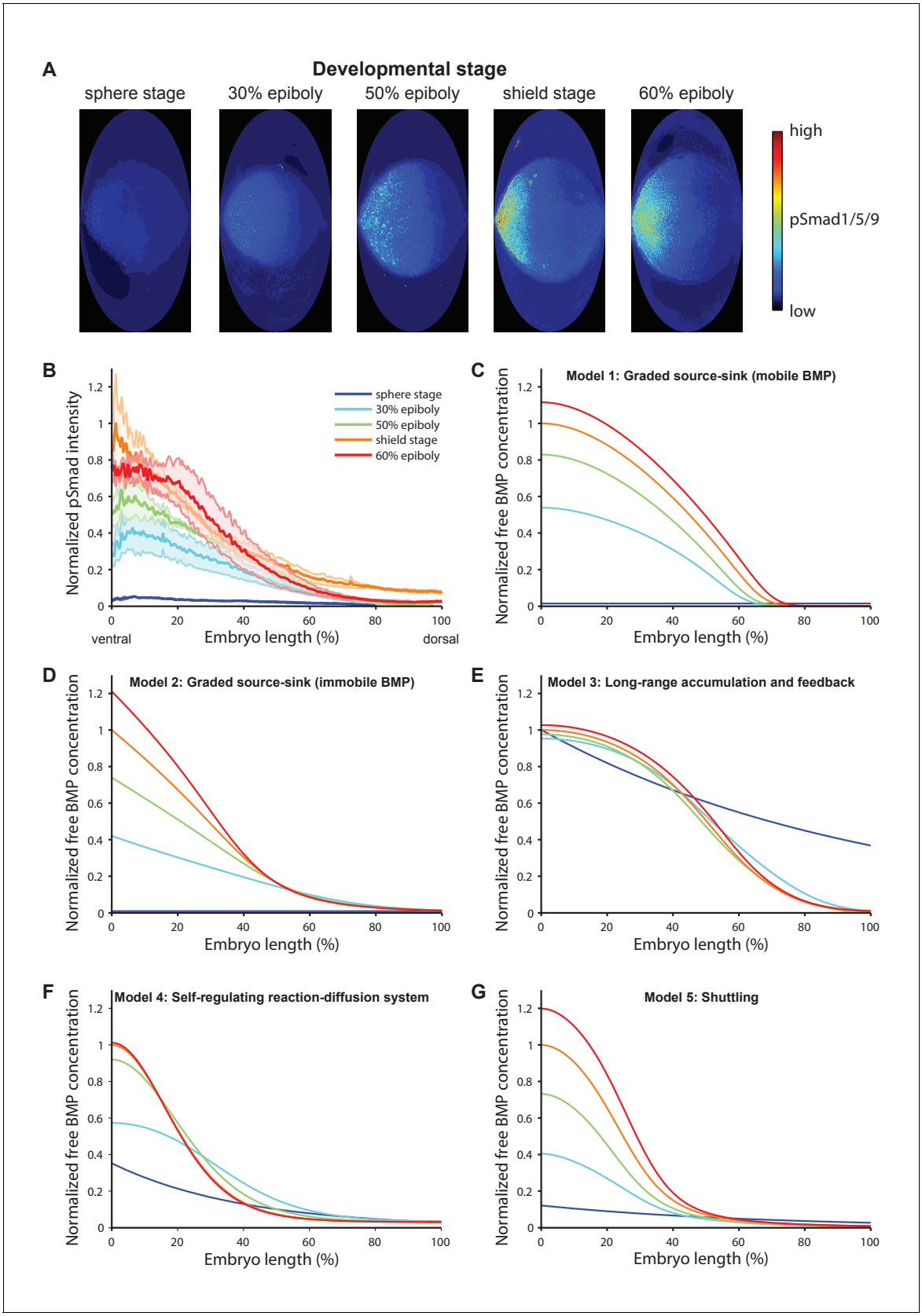

Figure 1. BMP signaling (pSmad1/5/9) gradient formation and simulations of five major dorsal-ventral patterning models over relevant zebrafish developmental stages (3 hr). (**A**) Two-dimensional Hammer-Aitoff projections (2D maps) of pSmad1/5/9-immunostained individual wild type zebrafish

Figure 1 continued on next page

Figure 1 continued

embryos at different developmental stages. Embryos were imaged using light sheet microscopy (see Materials and methods for details). (**B**) Quantification of ventral-to-dorsal average pSmad1/5/9 distributions in one-dimensional projections of 2D maps generated for embryos at different developmental stages (n = 3 for each stage) as in (**A**). Error bars denote standard error. (**C–G**) Gradient formation kinetics simulated for Models 1–5 at relevant zebrafish developmental stages.

DOI: https://doi.org/10.7554/eLife.25861.004

little to no diffusion
moderate diffusion
high diffusion

A Model 1: Graded source-sink (mobile BMP)

$$\frac{\partial[\mathrm{BMP}]}{\partial t} = D_{\mathrm{BMP}}\nabla^2[\mathrm{BMP}] - \kappa[\mathrm{Chd}][\mathrm{BMP}] - \lambda_{\mathrm{BMP}}[\mathrm{BMP}] + \rho_{\mathrm{BMP}}(x)$$

$$\frac{\partial[\mathrm{Chd}]}{\partial t} = D_{\mathrm{Chd}}\nabla^2[\mathrm{Chd}] - \kappa[\mathrm{Chd}][\mathrm{BMP}] - \lambda_{\mathrm{Chd}}[\mathrm{Chd}]$$

$$\frac{\partial[\mathrm{ChdBMP}]}{\partial t} = D_{\mathrm{ChdBMP}}\nabla^2[\mathrm{ChdBMP}] + \kappa[\mathrm{Chd}][\mathrm{BMP}] - \lambda_{\mathrm{Chd}}[\mathrm{ChdBMP}]$$

B Model 2: Graded source-sink (immobile BMP)

$$\frac{\partial[\mathrm{BMP}]}{\partial t} = -\kappa[\mathrm{Chd}][\mathrm{BMP}] - \lambda_{\mathrm{BMP}}[\mathrm{BMP}] + \rho_{\mathrm{BMP}}(x)$$

$$\frac{\partial[\mathrm{Chd}]}{\partial t} = D_{\mathrm{Chd}}\nabla^2[\mathrm{Chd}] - \kappa[\mathrm{Chd}][\mathrm{BMP}] - \lambda_{\mathrm{Chd}}[\mathrm{Chd}]$$

$$\frac{\partial[\mathrm{ChdBMP}]}{\partial t} = D_{\mathrm{ChdBMP}}\nabla^2[\mathrm{ChdBMP}] + \kappa[\mathrm{Chd}][\mathrm{BMP}] - \lambda_{\mathrm{Chd}}[\mathrm{ChdBMP}]$$

C Model 3: Long-range accumulation and feedback

$$\frac{\partial[\mathrm{BMP}]}{\partial t} = D\nabla^2[\mathrm{BMP}] + \frac{v_{\mathrm{BMP}}([\mathrm{ADMP}]+[\mathrm{BMP}])^{10}}{k_{\mathrm{BMP}}{}^{10} + ([\mathrm{ADMP}]+[\mathrm{BMP}])^{10}} - \lambda_{\mathrm{BMP}}[\mathrm{BMP}] + \frac{\lambda_{\mathrm{Chd}}[\mathrm{ChdBMP}]}{1 + \frac{[\mathrm{Szl}]}{ki} + \frac{[\mathrm{Chd}]+[\mathrm{ChdBMP}]+[\mathrm{ChdADMP}]}{km}} - k[\mathrm{Chd}][\mathrm{BMP}]$$

$$\frac{\partial[\mathrm{Chd}]}{\partial t} = D\nabla^2[\mathrm{Chd}] + \frac{v_{\mathrm{Chd}}k_{\mathrm{Chd}}{}^{10}}{k_{\mathrm{Chd}}{}^{10} + ([\mathrm{ADMP}]+[\mathrm{BMP}])^{10}} - \frac{\lambda_{\mathrm{Chd}}[\mathrm{Chd}]}{1 + \frac{[\mathrm{Szl}]}{ki} + \frac{[\mathrm{Chd}]+[\mathrm{ChdBMP}]+[\mathrm{ChdADMP}]}{km}} - k[\mathrm{Chd}][\mathrm{BMP}] - k[\mathrm{Chd}][\mathrm{ADMP}]$$

$$\frac{\partial[\mathrm{ADMP}]}{\partial t} = D\nabla^2[\mathrm{ADMP}] + \frac{v_{\mathrm{ADMP}}k_{\mathrm{ADMP}}{}^{10}}{k_{\mathrm{ADMP}}{}^{10} + ([\mathrm{ADMP}]+[\mathrm{BMP}])^{10}} - \lambda_{\mathrm{BMP}}[\mathrm{ADMP}] + \frac{\lambda_{\mathrm{Chd}}[\mathrm{ChdADMP}]}{1 + \frac{[\mathrm{Szl}]}{ki} + \frac{[\mathrm{Chd}]+[\mathrm{ChdBMP}]+[\mathrm{ChdADMP}]}{km}} - k[\mathrm{Chd}][\mathrm{ADMP}]$$

$$\frac{\partial[\mathrm{Szl}]}{\partial t} = D\nabla^2[\mathrm{Szl}] + \frac{v_{\mathrm{Szl}}([\mathrm{ADMP}]+[\mathrm{BMP}])^{20}}{k_{\mathrm{Szl}}{}^{20} + ([\mathrm{ADMP}]+[\mathrm{BMP}])^{20}} - \lambda_{\mathrm{Szl}}[\mathrm{Szl}]$$

$$\frac{\partial[\mathrm{ChdBMP}]}{\partial t} = D\nabla^2[\mathrm{ChdBMP}] - \frac{\lambda_{\mathrm{Chd}}[\mathrm{ChdBMP}]}{1 + \frac{[\mathrm{Szl}]}{ki} + \frac{[\mathrm{Chd}]+[\mathrm{ChdBMP}]+[\mathrm{ChdADMP}]}{km}} + k[\mathrm{Chd}][\mathrm{BMP}]$$

$$\frac{\partial[\mathrm{ChdADMP}]}{\partial t} = D\nabla^2[\mathrm{ChdADMP}] - \frac{\lambda_{\mathrm{Chd}}[\mathrm{ChdADMP}]}{1 + \frac{[\mathrm{Szl}]}{ki} + \frac{[\mathrm{Chd}]+[\mathrm{ChdBMP}]+[\mathrm{ChdADMP}]}{km}} + k[\mathrm{Chd}][\mathrm{ADMP}]$$

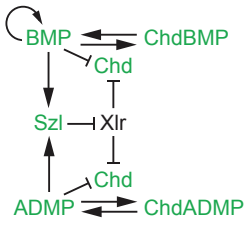

D Model 4: Self-regulating reaction-diffusion system

$$\frac{\partial[\mathrm{BMP}]}{\partial t} = D_{\mathrm{BMP}}\nabla^2[\mathrm{BMP}] + \frac{[\mathrm{BMP}]^2}{(1+[\mathrm{Chd}])[\mathrm{Szl}]} - \mu_{\mathrm{BMP}}[\mathrm{BMP}] + \rho_{\mathrm{BMP}}$$

$$\frac{\partial[\mathrm{Chd}]}{\partial t} = D_{\mathrm{Chd}}\nabla^2[\mathrm{Chd}] + \frac{[\mathrm{Chd}]^2}{[\mathrm{ADMP}]} - \mu_{\mathrm{Chd}}[\mathrm{Chd}] + \rho_{\mathrm{Chd}}$$

$$\frac{\partial[\mathrm{ADMP}]}{\partial t} = D_{\mathrm{ADMP}}\nabla^2[\mathrm{ADMP}] + [\mathrm{Chd}]^2 - \mu_{\mathrm{ADMP}}[\mathrm{ADMP}]$$

$$\frac{\partial[\mathrm{Szl}]}{\partial t} = D_{\mathrm{Szl}}\nabla^2[\mathrm{Szl}] + [\mathrm{BMP}]^2 - \mu_{\mathrm{Szl}}[\mathrm{Szl}]$$

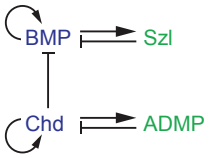

E Model 5: Shuttling

$$\frac{\partial[\mathrm{BMP}]}{\partial t} = D_{\mathrm{BMP}}\nabla^2[\mathrm{BMP}] - \kappa[\mathrm{Chd}][\mathrm{BMP}] + \lambda[\mathrm{Xlr}][\mathrm{ChdBMP}] - \lambda_{\mathrm{BMP}}[\mathrm{BMP}] + \rho_{\mathrm{BMP}}(x)$$

$$\frac{\partial[\mathrm{Chd}]}{\partial t} = D_{\mathrm{Chd}}\nabla^2[\mathrm{Chd}] - \kappa[\mathrm{Chd}][\mathrm{BMP}] - \lambda_{\mathrm{Chd}}[\mathrm{Chd}]$$

$$\frac{\partial[\mathrm{ChdBMP}]}{\partial t} = D_{\mathrm{ChdBMP}}\nabla^2[\mathrm{ChdBMP}] + \kappa[\mathrm{Chd}][\mathrm{BMP}] - \lambda[\mathrm{Xlr}][\mathrm{ChdBMP}] - \lambda_{\mathrm{Chd}}[\mathrm{ChdBMP}]$$

Figure 1—figure supplement 1. Mathematical formulation of five major models of BMP/Chordin-mediated dorsal-ventral patterning. See Materials and methods for details. Selected essential features of the models are illustrated on the right. (**A**) Model 1: Graded source-sink (mobile BMP). In this model, BMP diffuses from a ventrally biased graded source, and Chordin produced from the dorsal side inhibits BMP by irreversible binding. (**B**) Model 2: Graded source-sink (immobile BMP). In this model, BMP diffusion is negligible (D = 0 $\mu m^2/s$). The mechanism of restricting BMP signaling by Chordin irreversibly binding to BMP is the same as in Model 1, but with weaker binding kinetics. (**C**) Model 3: Long-range accumulation and feedback. Model and parameters were adapted from (***Inomata et al., 2013***). (**D**) Model 4: Self-regulating reaction-diffusion system. Model and parameters were adapted

Figure 1—figure supplement 1 continued on next page

Figure 1—figure supplement 1 continued

from (***Francois et al., 2009***). (**E**) Model 5: Shuttling. A simplified model without feedback to purely illustrate the biophysical aspects of shuttling was adapted from (***Ben-Zvi et al., 2008***).

DOI: https://doi.org/10.7554/eLife.25861.005

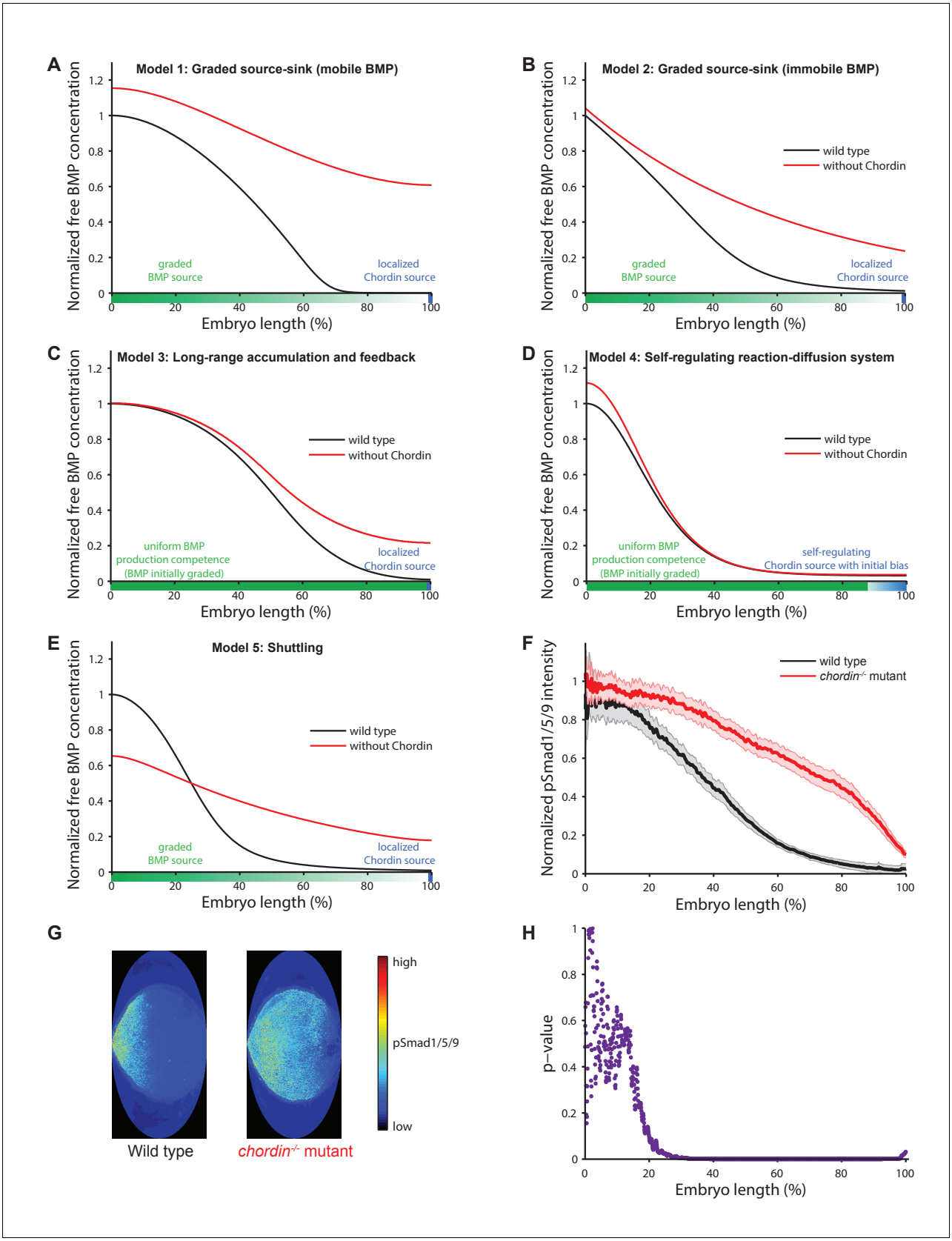

Figure 2. Theoretical predictions for the influence of the inhibitor Chordin on the BMP signaling gradient and experimental test. (**A–E**) Simulations of BMP distributions in five major models of dorsal-ventral patterning in the presence (black) or absence (red) of Chordin. The BMP and Chordin sources

Figure 2 continued on next page

Figure 2 continued

are indicated below each graph in green and blue, respectively. Note that the spatial production rates in Models 3 and 4 are modulated over time by feedback. (**F–G**) Quantification of average pSmad1/5/9 distributions in wild type (black) and *chordin*$^{-/-}$ (red) embryos using one-dimensional projections of 2D maps. Wild type n = 7, *chordin*$^{-/-}$ mutants n = 10. Error bars denote standard error. (**H**) p-values (unpaired two-tailed t-test assuming equal variance) calculated as a function of space between pSmad1/5/9 distributions in wild type and *chordin*$^{-/-}$ embryos shown in (**F**) indicate no significant difference of pSmad1/5/9 on the ventral side but a dramatic expansion into dorsal-lateral domains.

DOI: https://doi.org/10.7554/eLife.25861.011

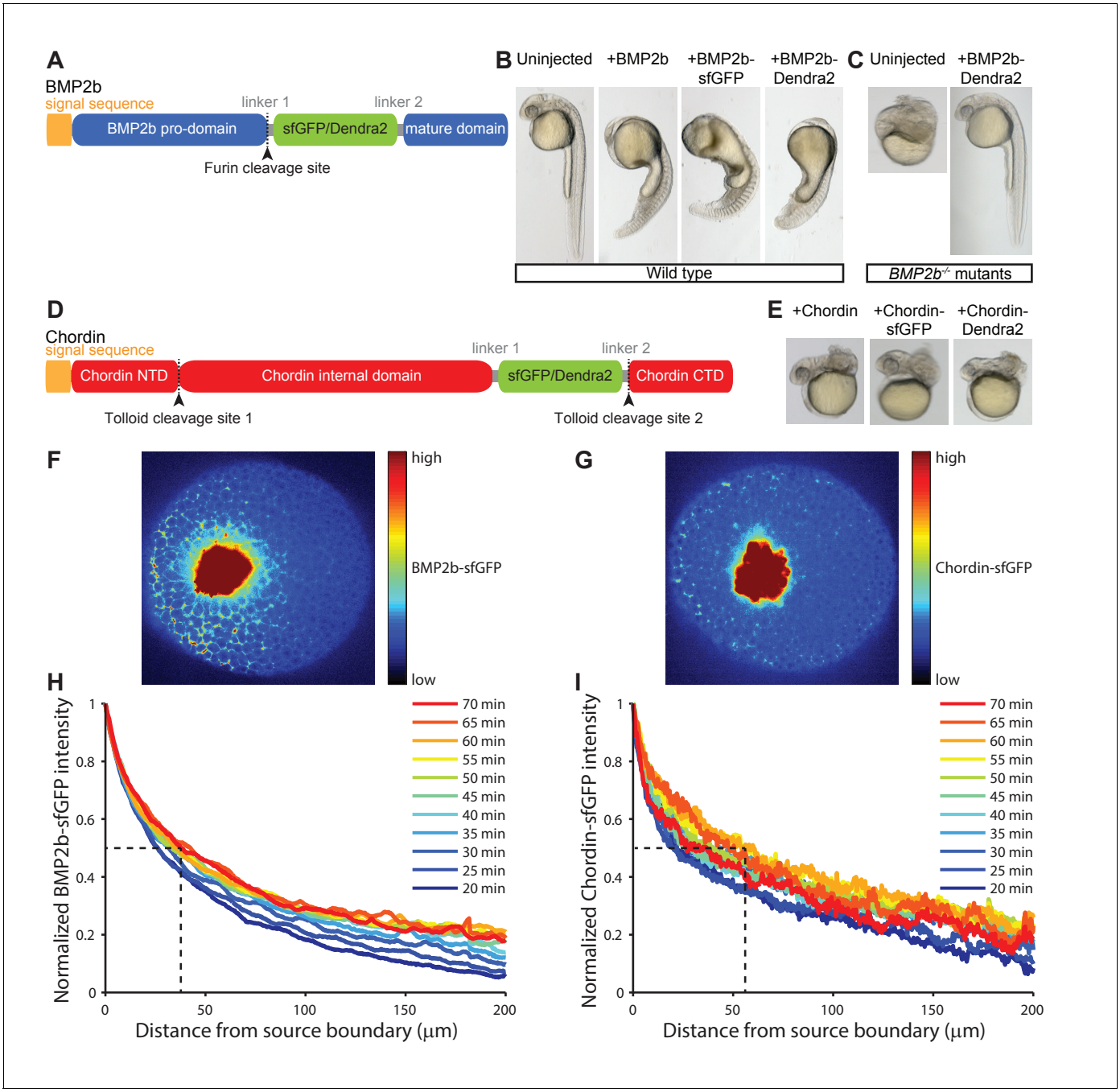

Figure 3. Gradient formation kinetics of fluorescently tagged BMP and Chordin. (**A**) Schematic of BMP2b-sfGFP and -Dendra2 fusion constructs. (**B**) Fluorescent BMP2b fusion constructs can induce ventralization, a BMP-overexpression phenotype (***Kishimoto et al., 1997***). mRNA amounts equimolar to 2 pg of *BMP2b* mRNA were injected at the one-cell stage, and images were taken 30 hr post-fertilization (hpf). (**C**) Rescue of a *BMP2b* mutant ($swr^{-/-}$) with BMP2b-Dendra2. 2.74 pg of BMP2b-Dendra2-encoding mRNA were injected at the one-cell stage, and images were taken at 30 hpf. In a separate experiment with 1 pg of BMP2b-sfGFP-encoding mRNA, 20% (9/44) of all injected $swr^{-/-}$ mutants were rescued, 16% (7/44) were ventralized, and 64% (28/44) were dorsalized. (**D**) Schematic of Chordin-sfGFP and -Dendra2 fusion constructs. (**E**) Fluorescent Chordin constructs can induce dorsalization, a *Chordin*-overexpression phenotype. mRNA amounts equimolar to 30 pg of *Chordin* mRNA were injected into wild type embryos at the one-cell stage, and images were taken at 30 hpf. F + G) Light sheet microscopy images of BMP- and Chordin-sfGFP gradients forming from a local source in live zebrafish embryos. Approximately 50–75 cells expressing *BMP2b-sfGFP* (**F**) or *Chordin-sfGFP* (**G**) were transplanted into host embryos at sphere stage (see Materials and methods for details). The images show gradient formation in single optical slices approximately 20 min after transplantation. H + I) Quantification of BMP2b-sfGFP (**H**) and Chordin-sfGFP (**I**) gradient formation kinetics from a local source (BMP2b-sfGFP: n = 8;

Figure 3 continued on next page

Figure 3 continued

Chordin-sfGFP: n = 5). Dashed lines indicate the distance at which the protein distributions drop to 50% of their maximal concentration 60 min post-transplantation.

DOI: https://doi.org/10.7554/eLife.25861.013

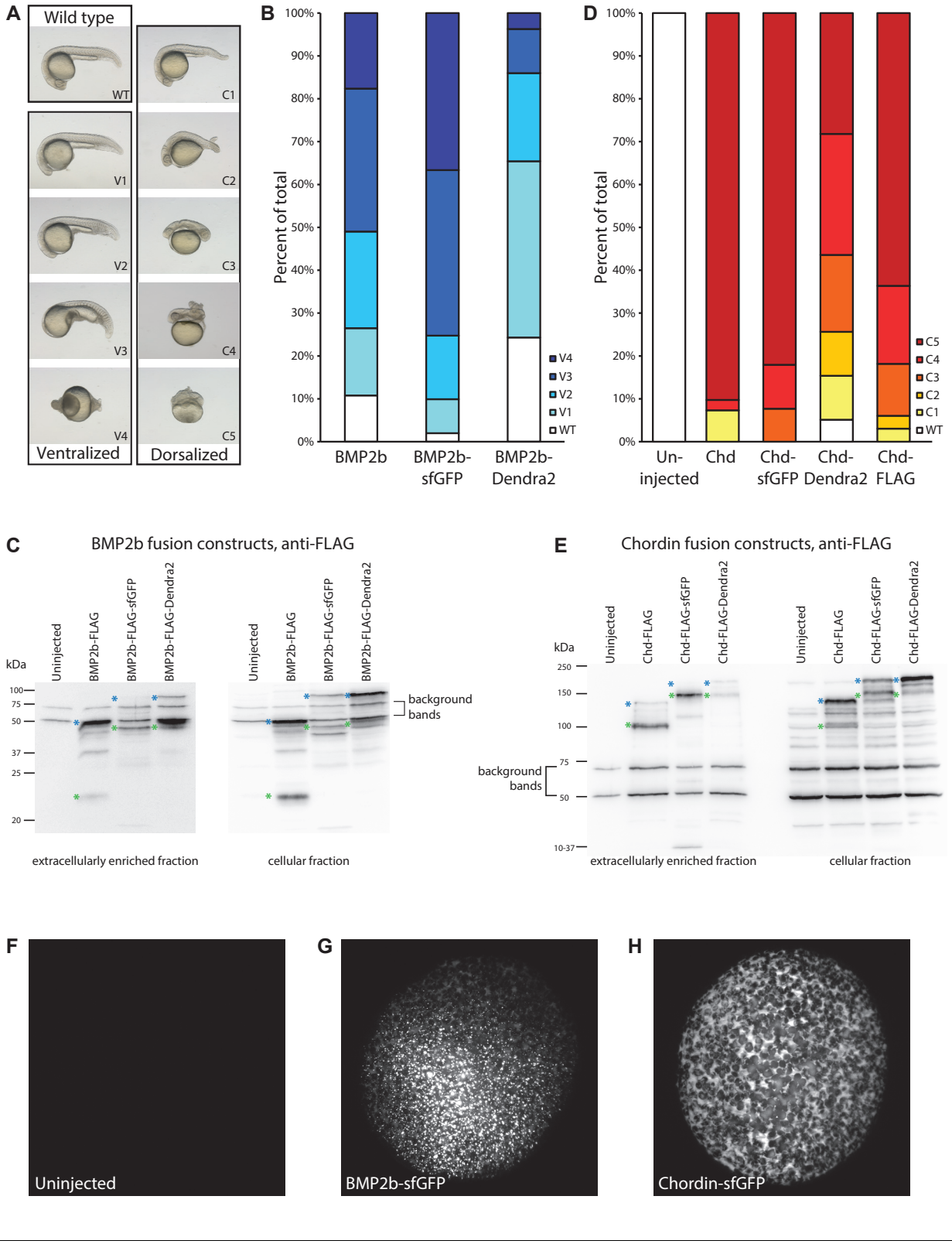

Figure 3—figure supplement 1. Detailed characterization of fluorescently tagged BMP2b and Chordin. (**A**) Ventralized and dorsalized phenotypes at 24 hr post-fertilization (hpf) were categorized using established classification schemes (***Mullins et al., 1996***; ***Kishimoto et al., 1997***). (**B**) Embryos were

Figure 3—figure supplement 1 continued on next page

Figure 3—figure supplement 1 continued

injected with equimolar amounts of mRNA encoding BMP2b (1 pg, n = 102), BMP2b-sfGFP (1.49 pg, n = 101), and BMP2b-Dendra2 (1.47 pg, n = 107) at the one-cell stage. BMP2b-sfGFP induced stronger ventralization, and BMP2b-Dendra2 induced weaker ventralization compared to untagged BMP2b. (**C**) To determine whether the differences in the degree of ventralization (**B**) are due to changes in protein activity or protein levels, extracellularly enriched extracts were obtained from zebrafish embryos injected with mRNA amounts equimolar to 444 pg BMP2b-FLAG-encoding mRNA. Levels and processing of FLAG-tagged BMP ligands were assessed using anti-FLAG western blots. Green asterisks to the left of a band indicate properly processed mature BMP2b ligand; blue asterisks indicate unprocessed full-length pro-protein. Similar to FLAG-tagged BMP2b, FLAG-tagged BMP2b-sfGFP and -Dendra2 are properly processed and mostly secreted as mature ligands into the extracellular space. BMP2b-sfGFP-FLAG protein levels are higher compared to FLAG-tagged BMP2b, possibly owing to the rapid folding kinetics of sfGFP (***Pédelacq et al., 2006***); in contrast, BMP2b-Dendra2-FLAG levels are lower. The correlation between protein levels and activity (**B**) suggests that the fluorescent BMP2b constructs are equivalent to untagged BMP2b in inducing downstream signaling responses. (**D**) Phenotype distributions at 24 hpf. Zebrafish embryos were injected at the one-cell stage with equimolar amounts of mRNA encoding Chordin (30 pg, n = 41), Chordin-sfGFP (37 pg, n = 39), Chordin-Dendra2 (37 pg, n = 39), and Chordin-FLAG (30 pg, n = 33) (uninjected: n = 49). (**E**) Extracellularly enriched fractions were obtained from zebrafish embryos injected with mRNA equimolar to 500 pg of Chordin-FLAG-encoding mRNA. Levels and processing of FLAG-tagged Chordin constructs were assessed using anti-FLAG western blots. Green asterisks indicate properly processed mature Chordin; blue asterisks indicate unprocessed full-length protein. Similar to the correlation between BMP2b construct levels and ventralization activity, the dorsalization activity of Chordin constructs (**D**) is correlated with protein levels. (**F–H**) Distribution of BMP2b/Chordin-sfGFP in transplantation donors similar to those used in experiments shown in ***Figures 3*** and ***5*** . Embryos were injected at the one-cell stage with 500 pg BMP2b-sfGFP- (**G**) or 1000 pg Chordin-sfGFP- (**H**) encoding mRNA (compare to uninjected embryo (**F**)). Embryos were imaged using light sheet microscopy at sphere stage (5–5.5 hpf), when transplantations were carried out in the experiments shown in ***Figures 3*** and ***5***. Maximum intensity projections are shown.

DOI: https://doi.org/10.7554/eLife.25861.014

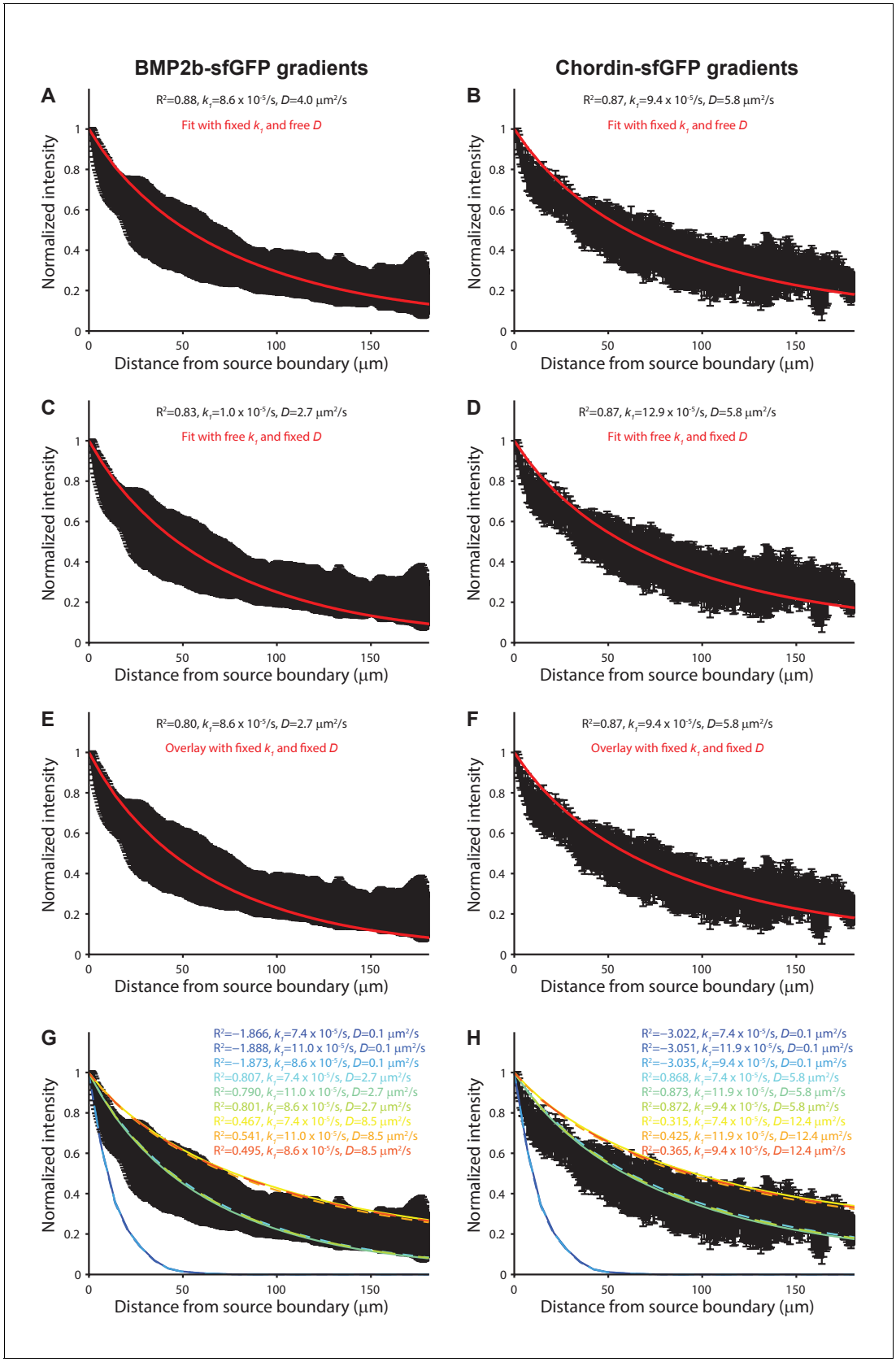

Figure 3—figure supplement 2. Modeling of BMP and Chordin gradient formation kinetics and comparison to measured gradients. Gradient simulations were executed in a three-dimensional embryo-like geometry with a local production source and uniform diffusion and clearance as in

Figure 3—figure supplement 2 continued on next page

Figure 3—figure supplement 2 continued

(***Müller et al., 2012***). Gradient formation was simulated for 70 min and compared to gradients measured in vivo ≈70–75 min post-transplantation. A 50 by 50 logarithmically spaced parameter grid was simulated for diffusion coefficients (*D*) ranging from 0.1 to 50 $\mu m^2/s$ and clearance rate constants (k_1) ranging from to $1 \times 10^{-5}/s$ to $5 \times 10^{-4}/s$. The fits in (**A**) and (**B**) were constrained with the measured clearance rate constants of BMP2b-Dendra2 and Chordin-Dendra2 and fitted with *D* as the free parameter. The fits in (**C**) and (**D**) were constrained with the measured diffusion coefficients of fluorescent BMP2b and Chordin constructs and fitted with k_1 as the free parameter. The data in (**E**) and (**F**) was overlaid with simulations using the measured *D* and k_1 values. (**G–H**) Sensitivity analysis of gradient simulations with all combinations of measured *D* and k_1 values as well as *D* and k_1 values three standard deviations above and below the measured averages (rainbow colors) overlaid with the experimental data (black). R^2 values indicate the goodness of the fit. Error bars denote standard deviation.

DOI: https://doi.org/10.7554/eLife.25861.015

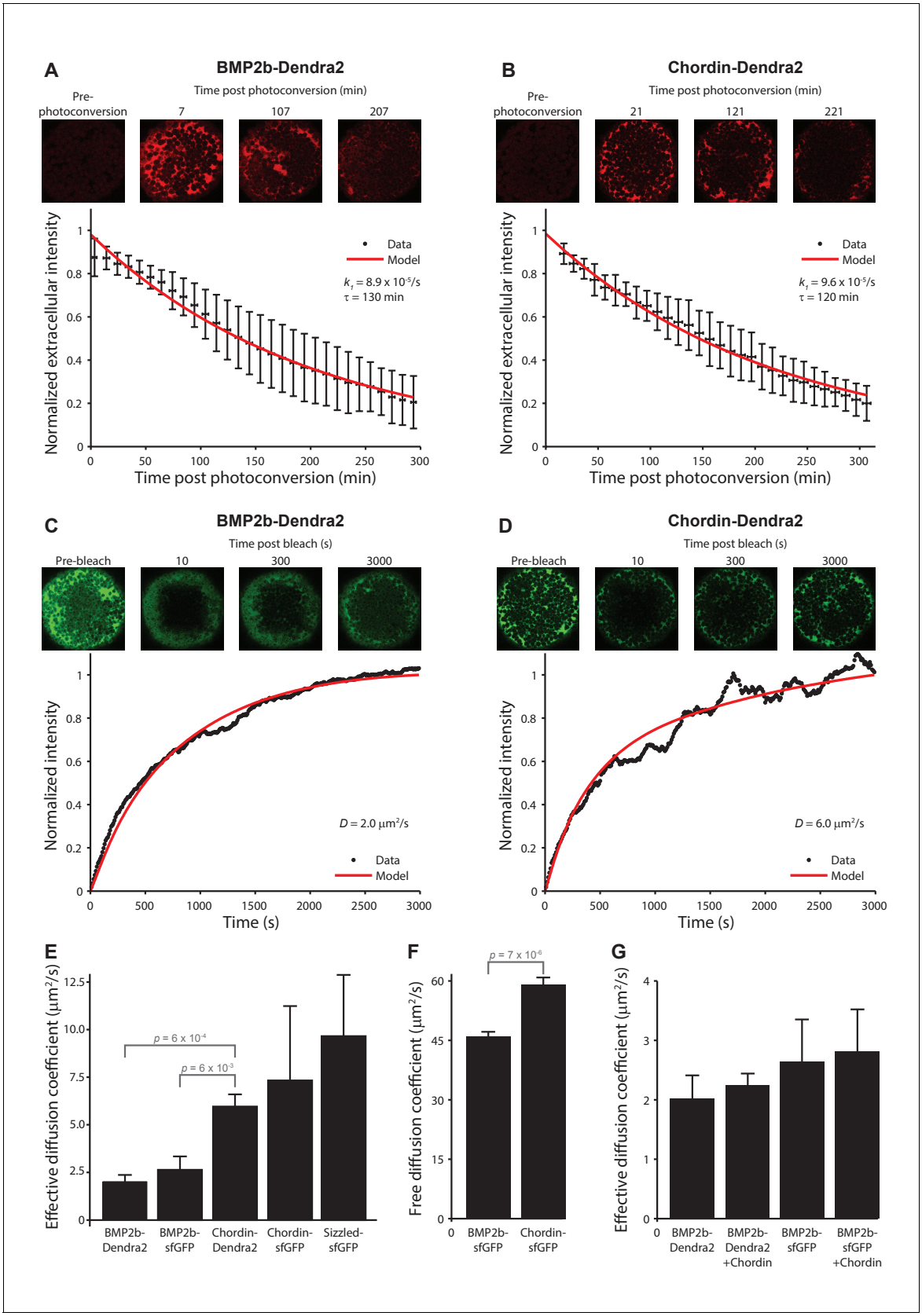

Figure 4. Biophysical measurements of BMP and Chordin protein stability and diffusivity. A + B) FDAP protein stability measurements for BMP2b-Dendra2 (**A**) and Chordin-Dendra2 (**B**). Error bars denote standard deviation. BMP2b-Dendra2: n = 22; Chordin-Dendra2: n = 6. C + D) FRAP effective

Figure 4 continued on next page

Figure 4 continued

protein diffusivity measurements for BMP2b-Dendra2 (**C**) and Chordin-Dendra2 (**D**). Data and fits from single experiments are shown. (**E**) Bar chart of the average effective diffusion coefficients from FRAP experiments. Error bars denote standard error. BMP2b-Dendra2: n = 6; BMP2b-sfGFP: n = 8; Chordin-Dendra2: n = 8; Chordin-sfGFP: n = 6; Sizzled-sfGFP: n = 12. (**F**) Free diffusion coefficients of BMP2b-sfGFP and Chordin-sfGFP measured by Fluorescence Correlation Spectroscopy (FCS) in a diffraction-limited spot within the zebrafish embryonic extracellular space far away from cell membranes (see Materials and methods for details). Error bars denote standard error. BMP2b-sfGFP: n = 17 measurements from 4 embryos; Chordin-sfGFP: n = 19 measurements from 5 embryos. (**G**) Negligible influence of Chordin on BMP2b effective diffusion. Untagged Chordin was co-expressed with BMP2b-Dendra2 (n = 8) or BMP2b-sfGFP (n = 9) in zebrafish embryos subjected to FRAP measurements at blastula stages. The data shown for BMP2b-Dendra2 and BMP2b-sfGFP FRAP experiments without co-expressed *Chordin* is identical to the data shown in (**E**). p-values (unpaired two-tailed t-test assuming equal variance) are shown for statistically significant ($p<0.05$) data sets.

DOI: https://doi.org/10.7554/eLife.25861.018

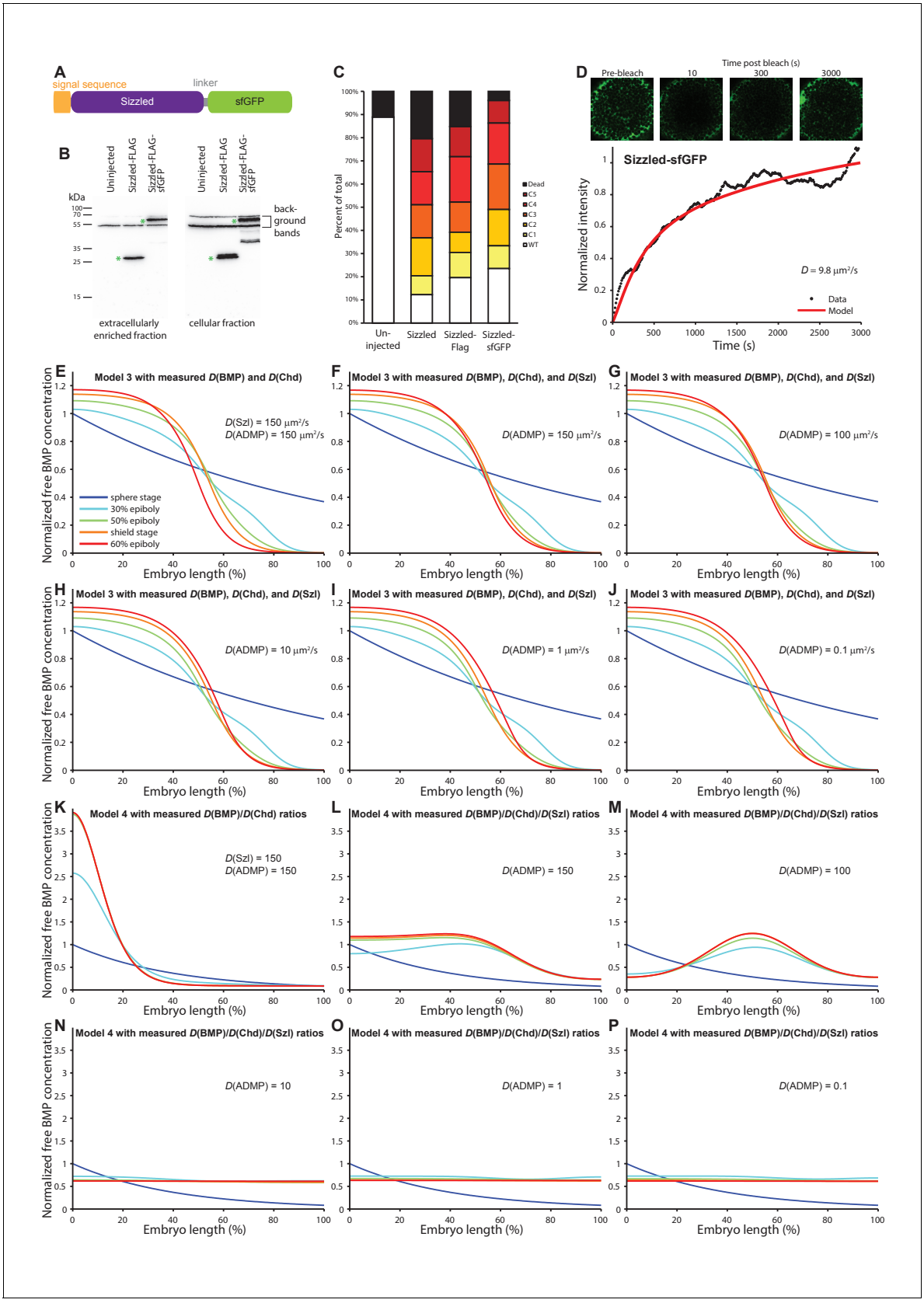

Figure 4—figure supplement 1. Characterization of Sizzled diffusion and its role in gradient formation. (**A**) Schematic of the Sizzled-sfGFP fusion protein. (**B**) Anti-FLAG western blot analysis of Sizzled-sfGFP. Green asterisks indicate full-length Sizzled fusions. (**C**) Characterization of phenotypes

Figure 4—figure supplement 1 continued on next page

Figure 4—figure supplement 1 continued

after overexpression of Sizzled fusion proteins (mRNA injections at the one-cell stage equivalent to 1 pg *sizzled* mRNA; uninjected n = 45, Sizzled n = 49, Sizzled-FLAG n = 46, Sizzled-sfGFP n = 51). (**D**) FRAP analysis of Sizzled-sfGFP effective diffusion (D = 9.7 ± 3.2 $\mu m^2/s$, n = 12). Data and fit from a single experiment is shown. (**E–J**) Simulations of Model 3 using the effective diffusion coefficients of BMP2b and Chordin measured here instead of the previously assumed value D = 15 $\mu m^2/s$ (***Inomata et al., 2013***). The diffusion coefficient of Sizzled was set to 150 $\mu m^2/s$ in (**E**) and to the measured value of 10 $\mu m^2/s$ in (**F–J**). ADMP diffusivity was varied from 0.1 $\mu m^2/s$ to 150 $\mu m^2/s$ as indicated in (**E–J**). Gradients form over time, but the gradient evolution profiles are not consistent with the pSmad1/5/9 distribution measurements in ***Figure 1B***. (**K–P**) Simulations of Model 4 using the ratio of effective BMP/Chordin diffusion coefficients (i.e. Chordin is approximately two to three times more diffusive than BMP; D(BMP) = 3, D(Chordin) = 6) measured here. The diffusion coefficient of Sizzled was set to 150 in (**K**) as in (***Francois et al., 2009***) and to 10 in (**L–P**), reflecting the ~3 fold higher measured diffusivity of Sizzled compared to BMP2b. ADMP diffusivity was varied from 0.1 to 150 (***Francois et al., 2009***) as indicated in (**K–P**). With 50-fold higher diffusion coefficients for ADMP and Sizzled compared to BMP (**K**) gradients peaking on the ventral side form over time, but with realistic diffusion ratios relevant gradients do not form (**L–P**).

DOI: https://doi.org/10.7554/eLife.25861.019

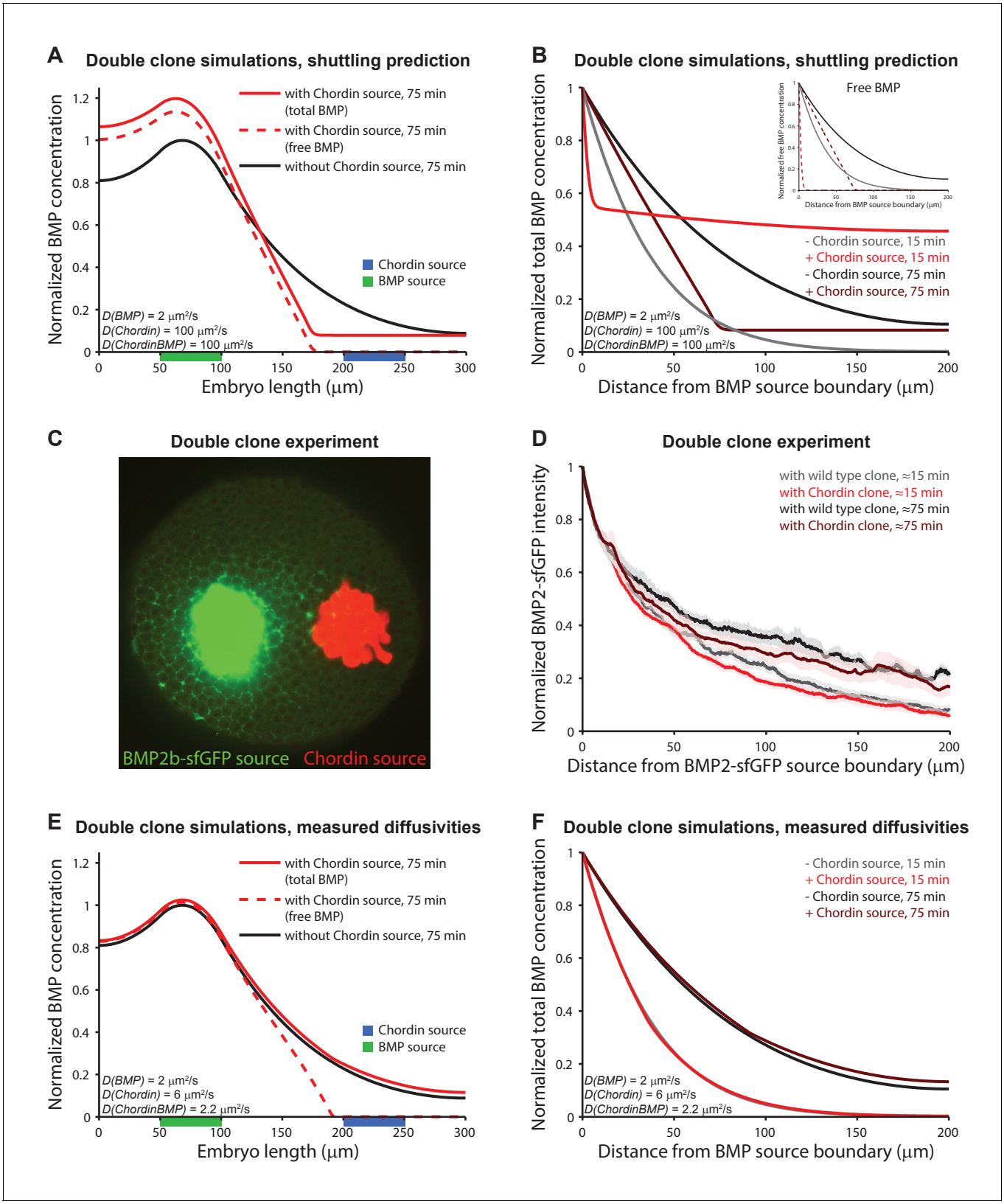

Figure 5. Testing shuttling of BMP2b predicted by Model 5. (**A**) One-dimensional model of two clones expressing BMP (green) or Chordin (blue) with D_{BMP} = 2 μm^2/s, D_{Chd} = 100 μm^2/s, and D_{ChdBMP} = 100 μm^2/s. BMP levels increase over time due to constant production. In the presence of Chordin, the BMP gradient is deflected away from the Chordin source indicative of shuttling (compare black and red lines). Solid lines show total BMP levels (i.e.

Figure 5 continued on next page

Figure 5 continued

BMP + ChdBMP in the presence of Chordin), and dashed line shows free BMP levels. (**B**) BMP gradients to the right of the BMP-expressing clone re-normalized to the BMP concentration at the source boundary to demonstrate that the range of BMP is decreased between the two clones in the presence of Chordin. The main panel shows total BMP levels (i.e., BMP + ChdBMP in the presence of Chordin), and the inset shows free BMP levels (dashed lines). (**C**) Experimental test of the predictions in (**A**) and (**B**). Clones of cells expressing BMP2b-sfGFP (green) were generated by transplanting approximately 50–75 cells from a donor embryo into wild type hosts at sphere stage (see Materials and methods for details). Another clone of cells (red) was transplanted next to the BMP2b-sfGFP-expressing clone shortly after. The red clone is marked by the presence of fluorescent Alexa 546-coupled dextran. Cells from red-labeled clones either contained only Alexa 546-coupled dextran (***Video 9***) or Alexa-546-coupled dextran and ectopic *chordin* mRNA (***Video 10***). 15–20 min after transplantation of the clones, embryos were imaged using light sheet microscopy. The image shows gradient formation in a single optical slice approximately 20 min after transplantation. (**D**) Quantification of average BMP2b-sfGFP gradients at ~15 min or ~75 min after transplantation in embryos generated as in (**C**) with (red/brown) or without (black/gray) ectopic Chordin sources. Error bars denote standard error. n = 8 for each condition. (**E**) One-dimensional simulation of two clones expressing BMP (green) or Chordin (blue) with the experimentally measured diffusion coefficients D_{BMP} = 2 $\mu m^2/s$, D_{Chd} = 6 $\mu m^2/s$, and D_{ChdBMP} = 2.2 $\mu m^2/s$. BMP levels increase over time due to constant production. Solid lines show total BMP levels (i.e. BMP + ChdBMP in the presence of Chordin), and the dashed line shows free BMP levels. Only the distribution of free BMP is affected as a consequence of Chordin binding, and the gradient of total BMP is not deflected away from the Chordin source (compare solid black and red lines). (**F**) Gradients of total BMP levels to the right of the BMP expressing clone simulated with the experimentally measured diffusion coefficients (D_{BMP} = 2 $\mu m^2/s$, D_{Chd} = 6 $\mu m^2/s$, and D_{ChdBMP} = 2.2 $\mu m^2/s$) and renormalized to the concentration at the boundary show that the range of BMP is not decreased between the two clones in the presence of Chordin.

DOI: https://doi.org/10.7554/eLife.25861.020

nature COMMUNICATIONS

Appendix 2

ARTICLE

DOI: 10.1038/s41467-018-03975-6 OPEN

Quantitative diffusion measurements using the open-source software PyFRAP

Alexander Bläßle[1], Gary Soh[1], Theresa Braun[1,3], David Mörsdorf[1], Hannes Preiß[1], Ben M. Jordan[2] & Patrick Müller[1]

Fluorescence Recovery After Photobleaching (FRAP) and inverse FRAP (iFRAP) assays can be used to assess the mobility of fluorescent molecules. These assays measure diffusion by monitoring the return of fluorescence in bleached regions (FRAP), or the dissipation of fluorescence from photoconverted regions (iFRAP). However, current FRAP/iFRAP analysis methods suffer from simplified assumptions about sample geometry, bleaching/photoconversion inhomogeneities, and the underlying reaction-diffusion kinetics. To address these shortcomings, we developed the software PyFRAP, which fits numerical simulations of three-dimensional models to FRAP/iFRAP data and accounts for bleaching/photoconversion inhomogeneities. Using PyFRAP we determined the diffusivities of fluorescent molecules spanning two orders of magnitude in molecular weight. We measured the tortuous effects that cell-like obstacles exert on effective diffusivity and show that reaction kinetics can be accounted for by model selection. These applications demonstrate the utility of PyFRAP, which can be widely adapted as a new extensible standard for FRAP analysis.

[1] Friedrich Miescher Laboratory of the Max Planck Society, Max-Planck-Ring 9, 72076 Tübingen, Germany. [2] Department of Organismic and Evolutionary Biology, Harvard University, 26 Oxford Street, Cambridge, MA 02138, USA. [3] Present address: University of Konstanz, Universitätsstraße 10, 78457 Konstanz, Germany. Correspondence and requests for materials should be addressed to P.Mül. (email: patrick.mueller@tuebingen.mpg.de)

The diffusion of molecules is important for almost any process across all scales of biological organisation, from transcription factors finding their targets on DNA to signalling molecules spreading through tissues during development and homoeostasis[1–3]. The biological function of a molecule is affected by its action range and therefore its mobility; however, effective diffusion of molecules moving through complex tissues is difficult to measure quantitatively. More than 40 years ago, Poo & Cone[4] and Liebman & Entine[5] developed a method to assess the diffusivities of fluorescent molecules. In these fluorescence recovery after photobleaching (FRAP) experiments, the fluorescence of molecules in a small region of the sample is bleached by exposure to a strong laser pulse[6]. The dynamics of fluorescence recovery in the bleached region can then be used to infer the mobility of the fluorescent molecules (Fig. 1a). Inverted FRAP (iFRAP) assays have recently been developed as an extension of FRAP experiments[7–10], which eliminate the often harsh bleaching conditions used in FRAP experiments. iFRAP assays utilise photoconvertible molecules that can be induced to alter their fluorescence excitation/emission properties after exposure to 'photoconverting' light. In iFRAP experiments, the spread of signal from a small photoconverted domain into the neighbouring regions of the sample is monitored over time and thus represents an experimental mirror image of FRAP (Fig. 1b).

Diffusion coefficients are commonly extracted from FRAP experiments by fitting analytical solutions computed from theoretical models to the measured recovery curves[11–18], and a few simulation-based analysis methods have been developed[19–21]. Although this allows for a rapid assessment of qualitative mobility differences in identical experimental settings, current approaches rely on several assumptions that can affect the accuracy of the analysis. First, most current methods reduce the FRAP analysis to one-dimensional or two-dimensional simplifications[11–21], often assuming that the fluorescent pool is infinitely large[11–14,16,17], or ignoring more complex geometries of biological samples that could play important roles in molecule movement (Fig. 1c). Recent studies have argued that geometry is crucial for dynamic biological processes[22,23], and must be taken into account for accurate analysis of FRAP data. Indeed, false assumptions about the FRAP sample geometry can drastically affect diffusion coefficient estimates (Fig. 1d).

Second, the bleaching process in FRAP experiments is often inaccurately modelled. Bleaching is posited to be homogeneous or to follow a Gaussian distribution throughout bleached circular or rectangular regions, while the molecules outside of the bleached region are assumed to remain unbleached[11–13, 15–18]. However, molecules diffusing during the bleaching process can create inhomogeneities both inside and outside of the bleached region; moreover, a delay between bleaching and the start of the recovery measurement can lead to further inhomogeneities (Fig. 1c). Incorrect assumptions about the bleaching process can thus lead to a severe misestimation of diffusion coefficients[14, 24–27] (Fig. 1e).

Third, in vivo FRAP experiments can be strongly influenced by reaction kinetics such as production or degradation of fluorescent molecules, which can contribute to the observed recovery curve (Fig. 1c). However, this is mostly neglected in classical FRAP analysis models and can lead to erroneous diffusion estimates (Fig. 1f)[11–17].

To address these shortcomings, we developed the versatile Python-based FRAP analysis software PyFRAP (available at https://mueller-lab.github.io/PyFRAP). To facilitate data analysis, PyFRAP is equipped with an intuitive graphical user interface (GUI, Fig. 2a), which gives users without a computational background access to a sophisticated FRAP data analysis workflow from image analysis to statistical model comparison methods (Fig. 2b). PyFRAP applies the first post-bleach image as initial condition (Fig. 2c), and numerically simulates the FRAP experiment in realistic two-dimensional or three-dimensional experiment geometries (Fig. 2d, e); the solution from this simulation is then fitted to the experimental data. Furthermore, PyFRAP can accurately account for both uniform production and degradation during FRAP experiments. PyFRAP saves all analysed data and settings in a logical data structure that can be shared with collaborators or re-used for later analyses (Fig. 2f). The software is freely available, and the open-source environment allows for rapid expansion through collaborative work[28] to adjust analysis methods to the users' needs.

To demonstrate the utility of PyFRAP, we conducted several typical in vitro and in vivo FRAP experiments (Supplementary Fig. 1). PyFRAP accurately determines the diffusion coefficients of fluorescent molecules ranging from 3 to 500 kDa in both artificial and biological contexts. In contrast to currently available software, PyFRAP's flexible initial conditions also allow analysis of iFRAP experiments, producing results comparable to FRAP. We used PyFRAP to measure the influence that obstacles such as cells exert on the movement of diffusing molecules, and found that such geometric hindrance decreases diffusivity by about one-third. Moreover, PyFRAP provides accurate modelling of reaction kinetics, including production and degradation. Finally, to test the impact of extracellular binding on protein diffusivity, we measured the diffusion of signalling molecules in living zebrafish embryos. We found that the effective diffusivity of a signalling molecule in developing zebrafish was reduced to about one-tenth of its predicted value, in agreement with hindered diffusion models postulating interactions of embryonic signals with diffusion regulators[22,29]. Altogether, our analyses highlight how detailed examination of FRAP data can be used to determine the contribution of individual factors to the movement of molecules in controlled artificial and biological contexts[30].

Results

PyFRAP is a versatile FRAP/iFRAP analysis package. Current FRAP analysis methods often make simplified assumptions about FRAP experimental conditions to aid in the derivation of analytical solutions[11–16,18], and to facilitate numerical simulations[20,21]. Such assumptions include reducing complex sample geometries to lower dimensions, idealising the initial bleaching profile, or ignoring additional reaction kinetics potentially underlying fluorescence recovery (Fig. 1c). Unless the experiment is well approximated by these assumptions (e.g., simple geometry, small bleach spot compared to a large sample volume, sharp bleach profile, no reactions), this can lead to erroneous diffusion estimates (Fig. 1d–f). To address these shortcomings, we developed PyFRAP. PyFRAP numerically simulates FRAP experiments in realistic three-dimensional geometries using an interpolation of the first post-bleach image as initial condition. This simulation is then fitted to the experimental data, incorporating reaction kinetics such as uniform production and degradation.

PyFRAP is an open-source Python-based FRAP analysis software that runs on the major operating systems Microsoft Windows, Mac OSX and Linux. Over the past 20 years, Python has become the standard programming language for scientific research because of the availability of versatile add-on packages and its intuitive and simple syntax[31]. Building on the resourcefulness of Python, PyFRAP is based on commonly used packages such as PyQT, SciPy and FiPy[32–36]. PyFRAP comes with an intuitive graphical user interface (GUI, Fig. 2a) and a fully documented application programming interface (API) allowing

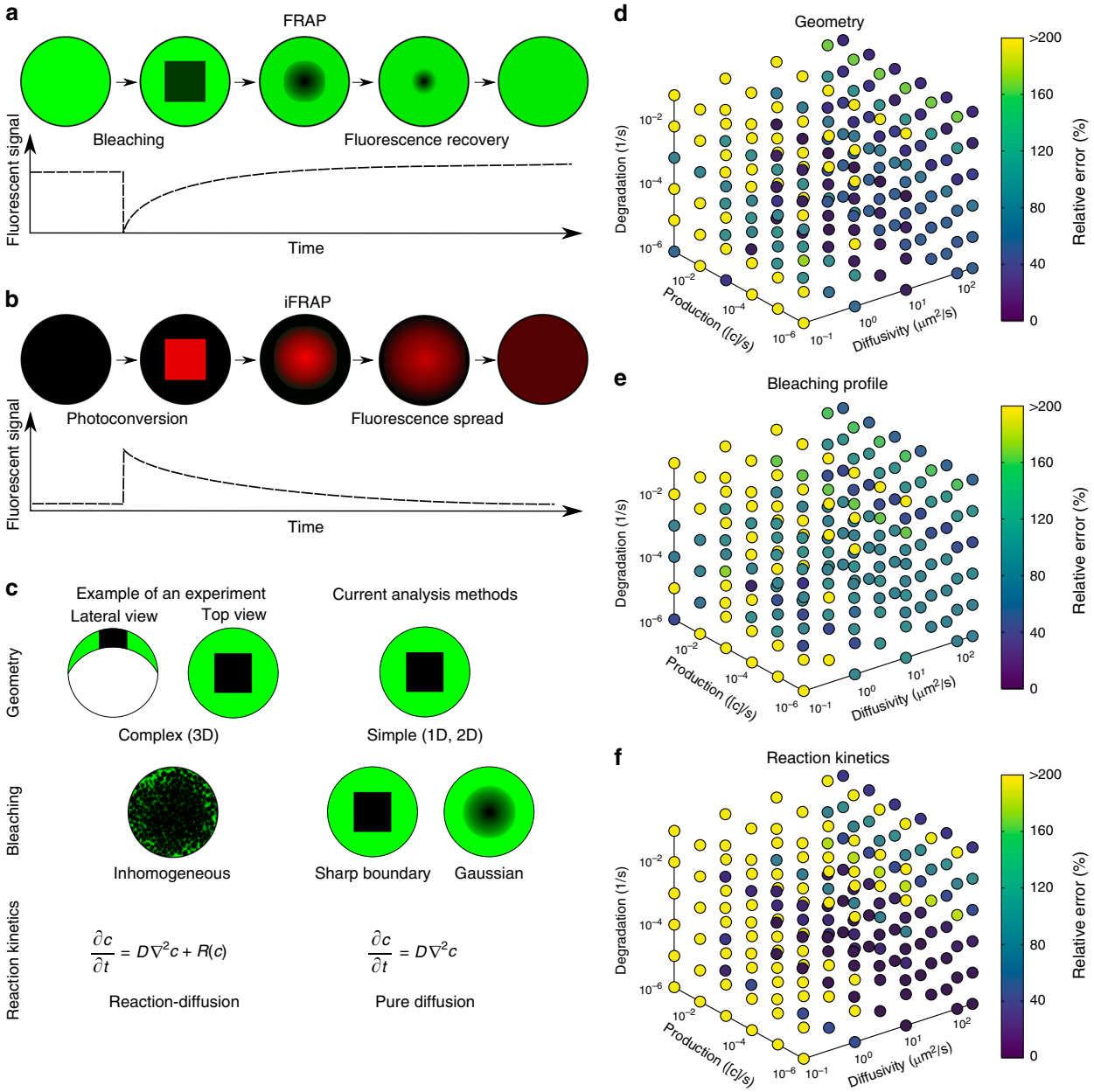

Fig. 1 Fluorescence perturbation techniques used for effective diffusion measurements, and drawbacks of current analysis methods. **a** In fluorecence recovery after photobleaching (FRAP) experiments, a small region in the sample is bleached. After bleaching, the diffusion-driven recovery in the bleached region is monitored. **b** Inverse FRAP (iFRAP) is an experimental mirror image of FRAP: Molecules in a given region are photoconverted and then spread throughout the sample, resulting in the loss of fluorescent signal in the region of photoconversion. **c** Drawbacks of current analysis methods exemplified with zebrafish development at late blastula stages. Current analysis methods simplify sample geometry, idealise bleaching profiles, or ignore underlying reaction kinetics. **d**–**f** Possible relative error in diffusion coefficient estimates that can occur if false assumptions are made about sample geometry (**d**), bleaching conditions (**e**), or reaction kinetics (**f**), respectively. The maximum displayed error was capped to a value of 200%, but can be up to 1000%

quick development of scripts or modifications of the PyFRAP code. PyFRAP's functionalities include sophisticated image processing functions useful for FRAP analysis, customisable geometry and analysis region definitions, a finite element partial differential equation (PDE) solver that simulates FRAP/iFRAP experiments with adjustable options, statistical tools for averaging and model comparison, and multiple plotting and input/output functions (see Methods section and Supplementary Note 1 for details). To make the software easily accessible, dialogue boxes (software wizards) guide the user step-by-step through data import, image analysis, simulation and fitting.

We programmed PyFRAP to import image data from most common microscope formats, such as .tif, .lsm and .czi. Users can define arbitrary regions of interests (ROIs) that are then used for image analysis, simulation and fitting (Supplementary Fig. 2a). For some experimental setups, the imaged sample might be larger than the field of view. In these cases, the concentration of molecules in regions outside of the image can be estimated from selected areas in the first image of the recovery image series (Supplementary Fig. 2b). Uneven illumination is a common artefact in FRAP experiments. PyFRAP can correct this artefact by normalisation using pre-bleach images or using a correction matrix computed from a secondary data set generated with a

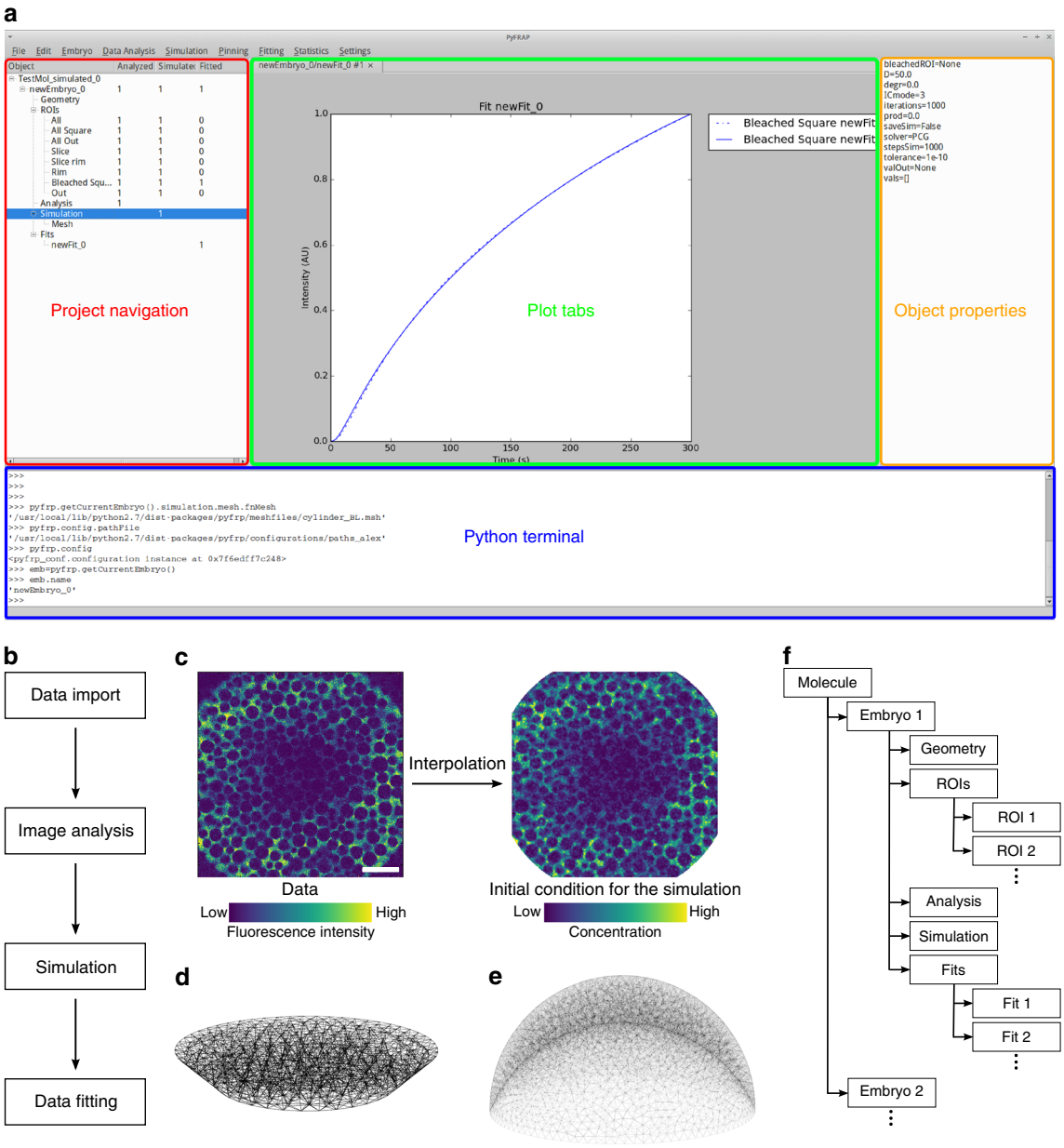

Fig. 2 The PyFRAP software package. **a** Annotated snapshot of the PyFRAP main GUI with project navigation tree (red), plot tabs (green), object property display (orange), and integrated Python terminal (blue). **b** PyFRAP work flow. **c** PyFRAP's interpolation of the first post-bleach image as initial condition for FRAP simulations. The length of the white scale bar represents 100 µm. **d**, **e** Spatial discretisation of geometries resembling **d** a frustum and **e** a zebrafish embryo at late blastula stages (dome stage). **f** PyFRAP's data structure

homogeneously distributed fluorophore[37–39] (see Methods section and Supplementary Fig. 2c for details). To avoid numerical instabilities, PyFRAP allows the user to smooth or denoise the image data using a Gaussian or median filter (see Methods section, Supplementary Note 1, Supplementary Fig. 3, and Supplementary Table 1 for details).

FRAP and iFRAP experiments have been performed in a variety of contexts, from the cigar-shaped *Drosophila* embryo and the relatively flat *Drosophila* wing disc to the dome-shaped pre-gastrula stage zebrafish embryo[10,22,29, 40–42]. These structures have distinct geometries that could impact fluorescence recovery. In fact, we found that simplifying the three-dimensional zebrafish embryo to a two-dimensional disc can frequently lead up to a >200% error in estimated diffusion coefficients (Fig. 1d). In PyFRAP, users can define arbitrary two-dimensional and three-dimensional geometries using Gmsh[43] or CAD STereoLithography (.stl) files that are then spatially discretised into tetrahedral meshes by Gmsh in combination with TetGen[44]. PyFRAP provides various meshing options, such as local mesh refinements, boundary layer meshes and attractor meshes, allowing users to adapt the mesh to experimental details (see Fig. 2d, e and Supplementary Fig. 4c for example geometries and meshes).

In current FRAP analysis methods, the initial condition of the FRAP experiment is often simplified to a simple rectangular function or a Gaussian profile to approximate sharp or blurred bleach boundaries, respectively[11,12, 14–18, 45–47]. However, light scattering, imperfect bleaching and diffusion during the bleaching process can lead to more complex bleaching profiles and thus need to be considered during FRAP analysis to avoid misestimation of diffusion coefficients[24,25,30,48]. To overcome this issue, PyFRAP uses a bilinear interpolation between pixels of the first

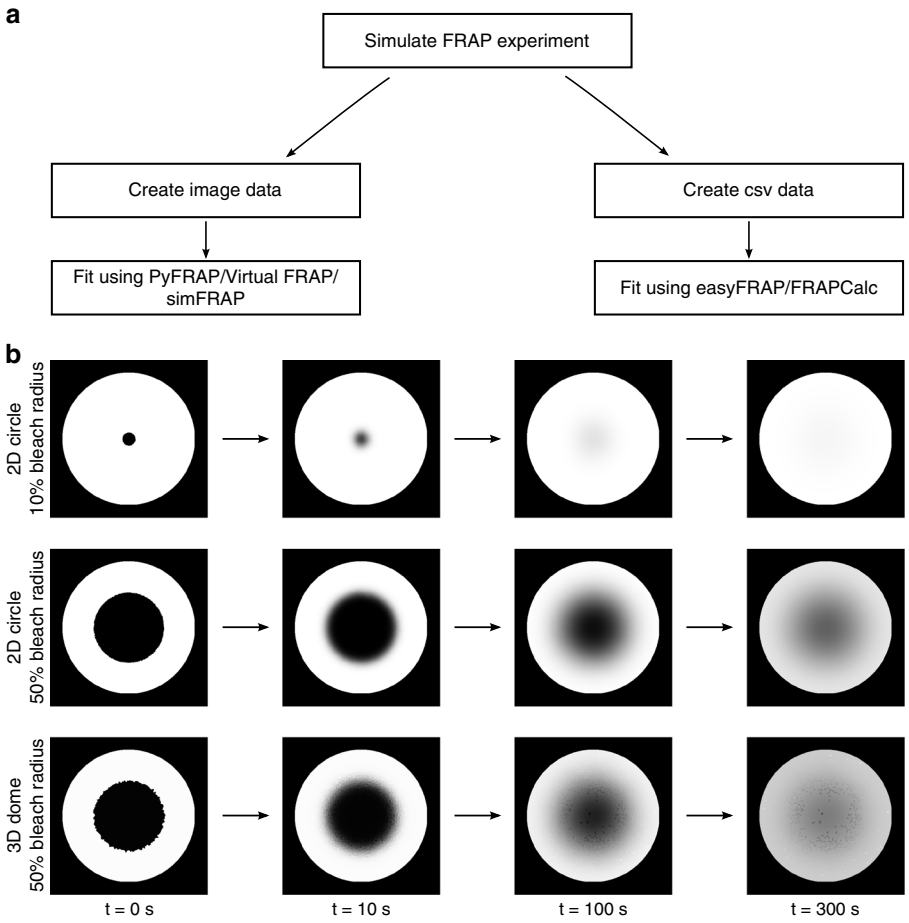

c

Geometry	Bleach domain radius (%)	Simulated D (μm²/s)	PyFRAP D (μm²/s)	FrapCalc D (μm²/s)	easyFRAP* D (μm²/s)	simFRAP D (μm²/s)	virtualFRAP D (μm²/s)
2D circle	5	10	9.8	9.0	14.0	9.3	9.1
2D circle	10	10	9.7	9.7	21.5	9.5	9.1
2D circle	50	10	9.8	10.4	89.1	13.1	10.3
2D circle	5	50	47.5	37.2	38.2	39.8	44.2
2D circle	10	50	49.5	45.2	70.7	47.9	44.3
2D circle	50	50	48.4	63.6	260.5	19.0	42.0
2D circle	5	200	245.0	112.7	67.3	n.a.	39.3
2D circle	10	200	179.0	157.6	161.0	8.7	177.8
2D circle	50	200	197.1	503.1	910.0	n.a.	191.7
3D dome	5	10	11.9	n.a.	17.2	9.7	11.3
3D dome	10	10	9.0	n.a.	23.8	10.1	9.0
3D dome	50	10	10.3	24.0	83.3	12.7	13.3
3D dome	5	50	56.9	n.a.	61.5	47.7	41.8
3D dome	10	50	44.2	n.a.	90.7	49.5	43.4
3D dome	50	50	47.4	n.a.	310.4	48.7	34.1
3D dome	5	200	211.6	n.a.	139.2	185.6	40.5
3D dome	10	200	172.4	n.a.	264.5	192.5	188.0
3D dome	50	200	191.1	n.a.	1021.9	177.3	113.5

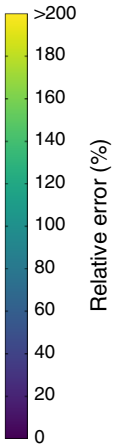

Fig. 3 PyFRAP benchmarking simulation experiment. **a** Workflow of PyFRAP benchmarking. **b** Examples of simulated data sets for different bleach spot sizes and geometries. **c** Benchmarking results of PyFRAP against currently available software packages using simulated FRAP experiments. Simulation experiments varied in bleached region size, diffusion coefficient and experiment geometry. All diffusion coefficients and estimates are given in units of μm²/s. n.a. indicates that the software was not able to fit the simulated data. Colours indicate relative estimation error in %. Diffusion coefficients determined by easyFRAP (asterisk) were computed in combination with an equation providing a relationship between recovery rate, bleached domain size and diffusivity[45]

post-bleach image to estimate the initial condition for mesh cells. This initial condition closely resembles initial experimental bleaching profiles and concentration distributions (Fig. 2c). Moreover, in contrast to most current FRAP analysis methods[11–18,46,47], PyFRAP does not fit a mathematical expression based on simplified assumptions to the data; instead, PyFRAP uses FiPy[32] to simulate the experiment numerically, resulting in a solution that incorporates the realistic three-dimensional geometry and initial conditions. The numerical simulation is then fitted to the FRAP data by minimising the sum of squared differences using classical optimisation algorithms[49–51] (see Methods section for details).

In typical FRAP and iFRAP experiments, a protein of interest is tagged with a fluorescent protein and expressed within a tissue. In such an experiment, the fusion protein is often actively produced at the same time that FRAP is carried out; additionally, fusion proteins undergo degradation over time. Depending on how the fusion protein is expressed (promoter-driven expression, mRNA injection, etc.), its degradation kinetics, and the timescale of the FRAP/iFRAP experiment, production and degradation can dramatically influence recovery curves. Ignoring reaction kinetics in FRAP experiments could therefore lead to erroneous diffusion coefficient estimates. Indeed, recovery curves with pure diffusion fitted to a simulated reaction-dominant data set often resulted in a >200% error in the estimated diffusion coefficients (Fig. 1f). To ensure that the appropriate reaction kinetics are considered when analysing FRAP data, PyFRAP is equipped with four models: (1) Pure diffusion, (2) diffusion with production, (3) diffusion with degradation and (4) diffusion with production and degradation (see Methods section for details). The model can be constrained with previous reaction rate measurements from assays such as fluorescence decay after photoconversion (FDAP) [52,53]; alternatively, production and degradation rates can be directly obtained from fitting the FRAP data. Below, we discuss methods to determine which approaches are most appropriate for a given data set.

An advantage of PyFRAP is its ability to assess FRAP data using multiple models of varying complexity, from pure diffusion to combined reaction-diffusion kinetics. However, determining which model is appropriate for a given data set can be challenging. Choosing the incorrect model can lead to overfitting and potentially false diffusion coefficients[54]. The Akaike information criterion (AIC) is a statistical tool that can aid in model selection[55]. PyFRAP's implementation of the AIC allows users to compare the models mentioned above and determines the most likely model based on a relative weighted measure that includes both the model's log-likelihood and its degrees of freedom, i.e., the number of model parameters. Moreover, PyFRAP provides several statistical tests (Supplementary Table 2) to assess differences between measurements and obtained fits, such as Student's *t*-test[56] for normally distributed data or the Mann–Whitney-U-test[57], which does not require normally distributed data. The Shapiro–Wilk-test can be used to assess whether the measured diffusivities follow a normal distribution[58] and whether application of Student's *t*-test or the Mann–Whitney-U-test is justified.

PyFRAP's object-oriented data structure (Fig. 2f) can be saved into serialised objects and easily loaded for further analysis or shared with collaborators. In addition, PyFRAP lets users visualise every aspect of PyFRAP's analysis work flow and save plots and images into publication-ready figures.

Benchmarking PyFRAP. To validate PyFRAP, we first determined whether it can recover true diffusion coefficients and reaction kinetics from simulated data. We used our previous in-house solution[22,29,42] based on the commercial programs MATLAB and COMSOL multiphysics to simulate 24 FRAP experiments with different reaction kinetics and diffusion coefficients. Using PyFRAP, the simulated data sets were fitted with all four possible reaction-diffusion models (see above). We determined a maximal error of 10% (average error: 2%, Supplementary Table 3) between simulated and estimated diffusion coefficients, demonstrating that PyFRAP recovers correct diffusion coefficients within the error tolerance of the numerical simulations.

Next, we tested whether PyFRAP's implementation of the AIC allows identification of the models used to create the simulated data. When the data were simulated with models describing either pure diffusion, diffusion and degradation, or diffusion and production, the AIC predicted the correct underlying model (Supplementary Table 3). However, the model selection based on the AIC did not favour the correct model for data sets that included diffusion combined with both production and degradation, since models with fewer degrees of freedom provided smaller Akaike weight values. Simulations involving diffusion, production and degradation can generate data effectively indistinguishable from data simulated with only diffusion and production or diffusion and degradation, explaining why the AIC cannot predict the correct model in this case.

To assess PyFRAP's performance in comparison with other available software packages based on analytical[17,46,47,59] or numerical[20,21,60] approaches (Supplementary Table 4), we used easyFRAP[47], Virtual FRAP[20], FrapCalc[46], simFRAP[21] and PyFRAP itself to analyse simulated FRAP experiments (Supplementary Note 2, Fig. 3). We simulated 18 experiments in which geometry, relative bleach window size, and diffusion coefficients differed. Simulations were conducted either in a simple circular two-dimensional domain or a complex three-dimensional zebrafish embryo-like geometry (Fig. 2e). FrapCalc and easyFRAP assume circular bleach windows[12,46,47]; to facilitate comparison, we therefore simulated FRAP experiments with circular bleach windows. Bleach window sizes comprised 5, 10 or 50% of the slice diameter, representing different proportions between fluorescent and bleached pools (Fig. 3b). Simulations were performed with three biologically relevant diffusion coefficients: 10, 50 and 200 $\mu m^2/s$.

Simulation-based programs (PyFRAP, virtualFRAP and simFRAP) generally provided better results than analytical solutions (easyFRAP and FrapCalc): FrapCalc and easyFRAP were either unable to determine diffusion coefficients, or provided diffusivities that were off by at least 20% for most experiments (Fig. 3c). Fast recovery dynamics were challenging for all tested software. One reason for this is that fewer data points were recorded during the actual recovery process of highly diffusive molecules due to a fixed frame rate of 1 frame/s in the simulated test data sets, leading to larger errors; moreover, for fast recovery dynamics errors from interpolating simulations onto images are more severe. The analytical software packages provided better results for the two-dimensional compared to three-dimensional geometries, while simulation-based approaches showed no clear trend regarding geometry. In terms of bleach window radius, the analytical solutions performed worst if the window diameter was 50% of the slice diameter. This effect might be due to the assumption of an infinite pool of fluorescent molecules outside of the bleached region[12]—when the bleach window is very large, the pool of unbleached fluorescent molecules is small, which conflicts with the assumption of an infinite pool. In contrast, PyFRAP outperformed all current software packages and exhibited the smallest error between predicted and simulated diffusion coefficients (Fig. 3c).

Applications of PyFRAP to measure diffusion hindrance. In vivo, it is thought that the overall movement of molecules is affected by binding interactions and by the presence of obstacles such as cells, resulting in a reduced effective diffusion coefficient of secreted proteins that move through tissues[22]. However, the effects of these interactions have not been rigorously tested experimentally. We therefore employed PyFRAP to examine the effects of obstacles and binding partners on the effective diffusivity of dextrans and proteins in experimentally controlled in vitro geometries and in living zebrafish embryos.

First, we measured diffusion coefficients of a wide range of differently sized molecules (Supplementary Table 5) in a simple in vitro context in the absence of binding partners or obstacles. We performed FRAP experiments with different bleach

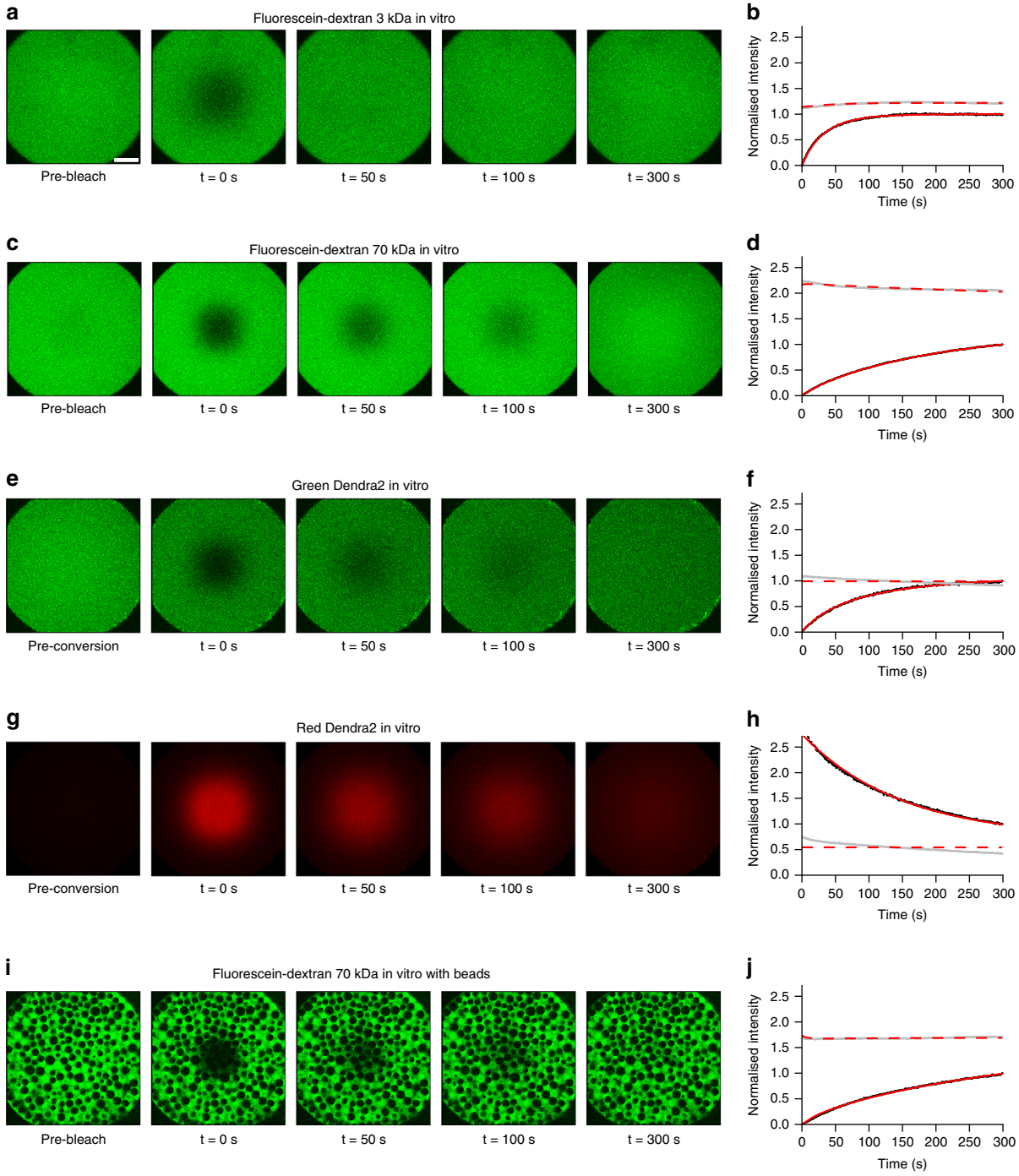

Fig. 4 Examples of in vitro FRAP and iFRAP experiments and the resulting fits to measure free diffusion. **a**, **c**, **e**, **g**, **i** In vitro FRAP and iFRAP experiment images and **b**, **d**, **f**, **h**, **j** fits with PyFRAP. Black and grey dots represent data points of bleached and slice ROI, respectively. Red solid and dashed lines show the respective fits. **a**–**d** FRAP experiments with 3 and 70 kDa fluorescent dextrans (see Supplementary Fig. 5 for the full data set with fluorescent dextrans between 3 and 500 kDa). **e**–**h** iFRAP experiment with photoconverted Dendra2 protein showing data for the green (**e**, **f**) and the red (**g**, **h**) channel. **i**, **j** FRAP experiment with 70 kDa fluorescent dextran in the presence of polyacrylamide beads. Recovery curves were normalised between 0 (intensity in the bleached ROI at the first post-bleach time point) and 1 (intensity in the bleached ROI at the last post-bleach time point) to allow comparison across data sets. The length of the white scale bar in **a** represents 100 μm, and all images were acquired with the same magnification

geometries using fluorophore-coupled dextrans ranging from 3 to 500 kDa in molecular weight (Fig. 4a–d, Supplementary Figs. 5 and 6), and compared the results with theoretical predictions and literature values. Fluorescence recovery in these in vitro experiments should be purely defined by diffusion, and the theoretical diffusivities D of spherical molecules can be calculated from their radii r based on the relationship $D \sim 1/r$ as postulated by the Einstein–Stokes equation (Supplementary Note 3). The diffusion coefficients determined by PyFRAP were in good agreement with literature values and theoretical predictions (Fig. 5a, Supplementary Tables 6 and 7).

A variant of FRAP that allows exclusion of reaction kinetics, such as production, and thus decrease the number of unknown experimental parameters is iFRAP (Fig. 1b). To perform in vitro iFRAP experiments, we used the green-to-red photoconvertible protein Dendra2[61]. Since photoconverting Dendra2 from green to red can also be interpreted as bleaching the original green fluorescence, measuring unconverted and converted protein distributions produces both FRAP and iFRAP experiments at the same time. To test whether PyFRAP correctly analyses iFRAP data, we used the experimental FRAP and iFRAP sets independently and assessed whether the obtained diffusion values are equal (Fig. 4e–h). Using FRAP we measured a Dendra2 diffusivity of 52.9 ± 5.2 (standard deviation) $\mu m^2/s$, and using iFRAP we obtained a similar value of $53.3 \pm 3.1\ \mu m^2/s$ (Fig. 5b, average difference between the two diffusivities per data set: $2.6 \pm 1.5\ \mu m^2/s$).

Next, we examined the effect of tortuosity on diffusion. In biological samples, the path length that molecules take increases as they move around obstacles such as cells. The effect of this

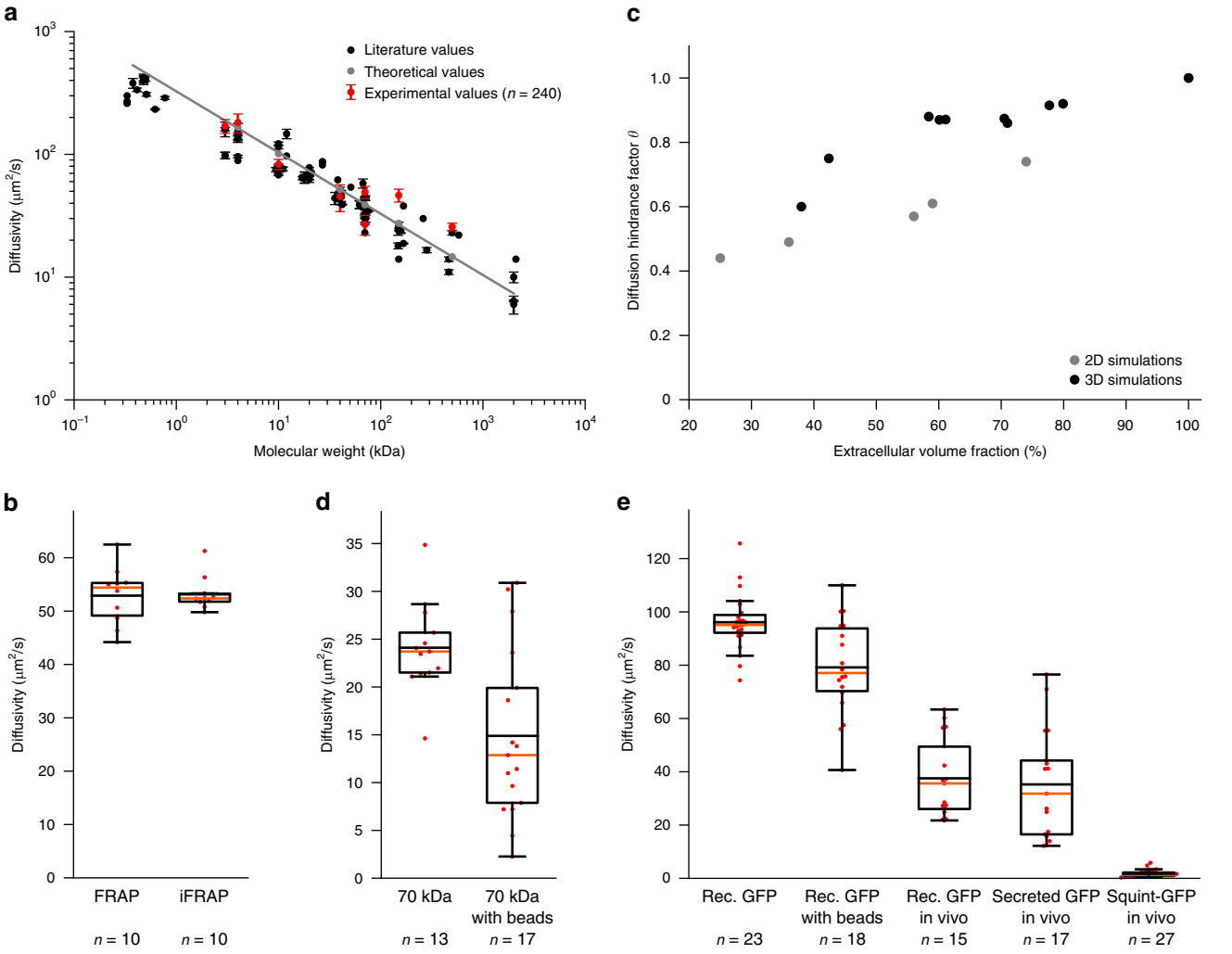

Fig. 5 Effective diffusion coefficients determined by PyFRAP. **a** Results of in vitro experiments and PyFRAP analysis for freely diffusing fluorescent dextrans of different molecular weights. Black markers indicate literature values for fluorescent dextrans, red markers the mean effective diffusion estimates obtained by in vitro experiments and PyFRAP analysis, and grey markers the theoretical estimates derived from the Einstein-Stokes equation (see Supplementary Note 3). Red error bars show the standard deviation of PyFRAP's effective diffusion estimates, and black error bars show the standard deviation of the literature values listed in Supplementary Table 7. The grey line represents a linear regression fit to the theoretical values. **b** Results of FRAP/iFRAP experiments for the photoconvertible protein Dendra2. **c** Results of simulations investigating the influence of tortuosity on effective diffusion for differently packed bead experiments. Grey and black markers indicate 2D and 3D simulation results, respectively. **d** Results of fluorescent dextran experiments demonstrating the impact of tortuosity on effective diffusivities. **e** Results of GFP experiments to analyse the impact of tortuosity, embryonic extracelluar environment, protein production, and extracellular binding on effective diffusion estimates. Box plots in **b**, **d**, **e** show median (orange line), mean (black horizontal line inside box), 25% quantiles (box), and all included data points (red markers). Whiskers extend to the smallest data point within the 1.5 interquartile range of the lower quartile, and to the largest data point within the 1.5 interquartile range of the upper quartile

tortuous movement can be described by the diffusion hindrance factor (also known as diffusion permeability[62]) $\theta = 1/\lambda^2 = D^*/D$, where λ is the tortuosity, D^* is the effective diffusion coefficient (with obstacles), and D is the free diffusion coefficient (without obstacles). To assess the expected magnitude of tortuosity on altering effective diffusivity, we first performed numerical simulations of FRAP experiments with and without radial obstacles in two- and three-dimensional geometries. Radial obstacles were either placed regularly, randomly, or following a nearly-ideal packing scheme, resulting in an extracellular volume fraction (EVF, i.e., the space available for molecules to diffuse) ranging from 78% down to 25% (Supplementary Fig. 7). These simulations demonstrated that recovery rates are slowed down as the EVF decreases (Fig. 5c, Supplementary Table 8). If the geometry is two-dimensional, an EVF of 25% results in an expected reduction in effective diffusivity of approximately 66%. In three-dimensional simulation experiments, we obtained a reduction of effective diffusion coefficients by 40% when the EVF was decreased to 38% (Supplementary Note 3).

To determine whether the presence of obstacles decreases effective diffusivity as predicted by our simulations, we performed FRAP assays in vitro with a fluorescein-coupled 70 kDa dextran (Fig. 4i, j) or recombinant GFP (Supplementary Fig. 8) in the presence of polyacrylamide beads. Consistent with our predictions, recovery was slower in the presence of beads, and the effective diffusivity of fluorescein-coupled 70 kDa dextran dropped from 24.1 ± 0.4 (standard error) μm^2/s to 14.9 ± 0.5 μm^2/s, suggesting an EVF of 39% ($\theta = 0.61$) (Fig. 5c, d, Supplementary Tables 8 and 9). Similarly, for recombinant GFP effective diffusivity dropped by 18% (Fig. 5e, Supplementary Table 10, Supplementary Fig. 8a–d).

To assess diffusion hindrance in vivo, we injected recombinant GFP protein into the extracellular space of living zebrafish embryos. We found that the effective diffusivity in vivo was 60% lower than for freely diffusing GFP, and 53% lower than in in vitro experiments with beads (Fig. 5e, Supplementary Table 10, Supplementary Fig. 8e, f). This suggests that tortuosity in zebrafish embryos is higher than in the in vitro bead assay. Importantly, we found similar diffusion coefficients of 36 μm^2/s in vivo for extracellularly injected recombinant GFP and secreted GFP constantly produced from injected mRNA, showing that PyFRAP can properly account for both diffusion and production (Fig. 5e, Supplementary Table 10, Supplementary Fig. 8g, h).

Finally, we examined the effects of binding interactions on effective diffusivity. GFP presumably does not experience significant binding interactions with extracellular molecules in zebrafish embryos, although its movement is affected by obstructions like cells and cellular extensions. In contrast, secreted signalling molecules are expected to interact with extracellular molecules such as receptors and extracellular matrix components[22]. To assess the effect that interactions with extracellular molecules might have on secreted signalling molecules, we injected mRNA encoding the TGFβ-superfamily member Squint fused to GFP into zebrafish embryos[29]. Squint-GFP is approximately 1.5 times larger than GFP and according to the Einstein-Stokes equation (Supplementary Note 3) would be predicted to have an approximately 1.14 times smaller diffusion coefficient than GFP (effective diffusivity D(GFP) = 36 μm^2/s, expected effective diffusivity D(Squint-GFP) = 31 μm^2/s). However, we measured an effective diffusion coefficient of approximately 2 μm^2/s for Squint-GFP in living zebrafish embryos, ~90% lower than the predicted diffusion coefficient (Fig. 5e, Supplementary Table 10, Supplementary Figs. 8i, j and 9). These findings are consistent with previous measurements[29] and with the idea that interactions with so far unidentified binding partners slow down the effective diffusion of embryonic signalling molecules like Squint-GFP[22,29].

Discussion

Although FRAP analyses have long been used to measure relative differences in mobilities between macromolecules, analysis tools to accurately and quantitatively determine effective diffusion coefficients from FRAP data are lacking. Current analysis tools impose several simplifications including one-dimensional or two-dimensional reductions of complex three-dimensional geometries, idealised bleaching conditions, and the absence of important reaction kinetics. When the experimental conditions closely resemble the simplified assumptions, e.g., small bleach domains and negligible reaction kinetics, these tools can rapidly provide reasonable diffusion estimates (Fig. 3c). However, experimental conditions are often more complex, and the use of simplified assumptions may yield drastically divergent diffusion coefficients (Fig. 1d–f). PyFRAP addresses these shortcomings by providing a simulation-based analysis that incorporates realistic geometries, bleaching conditions and reaction kinetics.

We found that PyFRAP's data analysis pipeline is numerically reliable, recovered the correct diffusion coefficients and reaction kinetics, and additionally predicted the correct underlying reaction-diffusion models for simulated test data sets with known diffusion, production, and degradation parameters. PyFRAP consistently outperformed all other tested software packages, demonstrating its strength as a novel FRAP analysis method. Furthermore, PyFRAP was able to determine diffusion coefficients comparable to both theoretical and previously experimentally measured estimates for macromolecules with molecular weights ranging over two orders of magnitude. Since PyFRAP can analyse data independently of any assumptions about the initial conditions, it is suitable to analyse both FRAP and iFRAP experiments. iFRAP has recently been developed as an alternative to FRAP due the increasing availability of photoconvertible proteins and allows ignoring reaction kinetics such as production. We performed tandem FRAP/iFRAP experiments to analyse the diffusion of the photoconvertible protein Dendra2 and found equal diffusion coefficients in vitro with both methods.

FRAP experiments are typically performed in tissues in which macromolecules need to move around cellular obstacles, resulting in slower fluorescence recovery. To determine how this tortuosity might affect diffusion coefficients estimated from FRAP experiments, we first simulated FRAP experiments in two- and three-dimensional geometries introducing radial beads at different densities to vary the extracellular volume fraction (EVF). Our simulations showed a strong correlation between tortuosity and effective diffusivity and agree with previous theoretical work including Monte-Carlo simulations and homogenisation theory[62–65]. We then tested the predictions from these simulations with in vitro experiments using polyacrylamide beads to mimic cells. Compared to experiments without beads, the effective diffusion coefficient decreased by 39% (diffusion hindrance factor $\theta = 0.61$) for 70 kDa fluorescein-dextran and 18% ($\theta = 0.82$) for recombinant GFP. In living zebrafish embryos, effective diffusivity is much further reduced (Fig. 5e). It is unlikely that this is due to different viscosity of the extracellular medium in vivo, since free GFP diffusion is only marginally reduced in zebrafish embryos[22]. Instead, it is plausible that the complex geometries of real extracelluar environments—which include filopodia, extracellular matrix, and cavities that might act as dead end pores—could further increase tortuosity[62]. Finally, most in vivo FRAP experiments are affected by biochemical reactions such as

production and degradation of proteins, which must be taken into account for accurate diffusion coefficient estimates (Fig. 1c, f). PyFRAP offers various models for different reaction kinetics and can accurately estimate diffusion coefficients from data sets that include constant production and degradation.

PyFRAP measures effective diffusion, but due to its built-in PDE solver it could be extended in the future to consider spatially inhomogeneous kinetics and advective fluxes and to perhaps even determine the diffusivities of individual species in polydisperse mixtures of fluorescent molecules[66,67]. While PyFRAP can simulate three-dimensional FRAP experiments, FRAP data is currently almost exclusively obtained from two-dimensional confocal microscopy. In recent years, the development of light-sheet microscopy made fast three-dimensional imaging with low phototoxicity feasible[68]. In the future, PyFRAP's image analysis tools could be extended to fit light-sheet microscopy data, which might provide deeper insights into the three-dimensional dynamics of molecule movement including convective flows or spatially inhomogeneous diffusion.

Methods

FRAP/iFRAP experiments in vitro. FRAP experiments to measure pure diffusion and tortuosity effects were conducted in a frustum-like plexiglass hole. Holes around 700 µm in diameter and about 100 µm in depth were drilled into a plexiglass block using a dental drill. Due to the small depth, the resulting shape was frustum-like with an upper base of 510 µm diameter.

Holes were filled with aqueous solutions of FITC-/fluorescein-labelled dextrans of different sizes, recombinant GFP, or Dendra2 protein (Supplementary Table 5) using a micro-pipette. Dendra2 protein was centrifuged at 16,000 × *g* for 30 min at 4 °C to remove protein aggregates. Excess liquid was removed from the hole by pipetting under observation with a stereo microscope.

To model the effect of tortuosity in the in vitro FRAP experiments, polyacrylamide beads were added to the sample solution. The microbeads (Bio-Gel P-2 Gel, <45 µm wet bead size) were first soaked in distilled water overnight for hydration. The beads were then centrifuged at 300 × *g*, the supernatant removed, and the required quantity of beads transferred to another tube for resuspension in fluorescein-dextran or GFP+BSA solution. This was repeated and followed by removal of the supernatant, leaving a concentrated slurry of beads and fluorescent solution for the experiments. The beads were transferred into the plexiglass template and settled within 1–2 min.

To prevent evaporation, mineral oil (Sigma) was placed around the solution before sealing the hole with a cover slip (No 1.5). Supplementary Fig. 1a outlines the sample preparation process for in vitro experiments. The sample was upended carefully and mounted on an inverted confocal microscope. Images were taken using an LSM 780 NLO microscope (ZEISS) with an LD LCI Plan-Apochromat 25×/0.8 Imm Korr DIC objective (ZEISS) and immersion oil (Immersol TM W, $n = 1.334$ at 23 °C, ZEISS). First, a plane approximately in the middle of the hole was chosen and the *z*-position set to zero. Then, the position of the highest and lowest point was determined. Cuboid volumes (141.42 µm × 141.42 µm × 100 µm) were bleached by imaging a *z*-stack at highest laser power (488 nm) or photoconverted at moderate laser power. Time series of 300 images (512 pixels × 512 pixels) were taken with a speed of 1 frame/s (pixel dwell time: 3.15 µs) over a duration of 5 min. The zoom was set to 0.7, and the resulting images had a size of 566.79 µm × 566.79 µm.

After the FRAP experiment, the template was cleaned using distilled water, soap, and an interdental toothbrush.

FRAP experiments in vivo. Zebrafish embryos (*Danio rerio*) were collected 10 min after mating and proteolytically dechorionated[22,29,42]. For the experiments with recombinant GFP, 100 pg of recombinant GFP were injected into the extracelluar space when zebrafish embryos reached high stage[22,29,69] (Supplementary Table 10). For experiments with secreted GFP[29], 100 pg of the mRNA encoding the fluorescent protein were injected at the one-cell stage. For experiments with Squint-GFP[29], either 30 or 200 pg of mRNA were injected at the one-cell stage. At dome stage, embryos were mounted in drops of 1% low-melting-point agarose animal pole down onto a glass-bottom dish (MatTek Corp. P35G-1.5-20-C), and as soon as the drops solidified covered with Danieau's medium[29,42] to prevent the embryos from drying out. Supplementary Fig. 1b outlines the in vivo sample preparation process.

Confocal images were taken roughly at a depth of 40 µm from the animal pole into the embryo. For data sets injected with 200 pg of Squint-GFP-encoding mRNA, images were acquired with the same settings as described for the in vitro experiments either with 1 frame/s for 300 s, or 1 frame/10 s for 3000 s. Images of embryos injected with 30 pg of Squint-GFP-encoding mRNA were taken with a spatial resolution of 340.08 µm × 340.08 µm and 1 frame/10 s for 3000 s. Data sets for recombinant GFP in vivo were acquired with the same microscope settings as the experiments conducted in vitro.

ROI selection. PyFRAP's image analysis depends on defining specific ROIs for the experimental data and simulations. Users can define multiple different geometrical shapes of ROIs in three-dimensional space such as cylinders, prisms, and any kind of addition or subtraction between ROIs. The specified ROIs are then used for image analysis, estimating concentrations outside the field of view, evaluating the simulation, and fitting to the analysed data. PyFRAP is equipped with an ROI manager and wizards for several standard sets of ROIs.

Image analysis. Let Ω_i (with $i \in \{1, 2, \ldots, n_\Omega\}$ and n_Ω the number of ROIs) be the list of ROIs specified for PyFRAP's analysis. The mean intensity over the ROI Ω_i at time t_j (with $j \in \{1, 2, \ldots, n_t\}$ and n_t the number of images) is then calculated by

$$\bar{I}_{\Omega_i}(t_j) = \frac{1}{A_i} \sum_{(x_k, y_l) \in \Omega_i} I(x_k, y_l, t_j) \quad (1)$$

where A_i is the area of Ω_i, and $I(x_k, y_l, t_j)$ is the intensity at pixel (x_k, y_l) (with $k \in \{1, 2, \ldots, n_x\}$ and n_x the number of rows in the images, and with $l \in \{1, 2, \ldots, n_y\}$ and n_y the number of columns in the images).

FRAP image data were analysed within the ROIs Ω_{bleached} and Ω_{slice}. Ω_{slice} was defined as a circular domain with centre C_{slice} and radius r_{slice}. Since the imaging depth varied between experiments, both C_{slice} and r_{slice} were cropped for each data set. The bleached ROI Ω_{bleached} was defined as a square with sidelength s_{bleached} and left-lower corner at $O_{\text{bleached}} = C_{\text{slice}} - \frac{1}{2}(s_{\text{bleached}}, s_{\text{bleached}})$. The definition of both ROIs is shown in Supplementary Fig. 2a.

Accounting for uneven illumination. Uneven imaging due to inhomogeneous sample illumination is a common problem in microscopy[37–39]. We implemented two solutions in PyFRAP to address this problem: (1) Normalisation by an image acquired before bleaching, and (2) applying a flattening mask derived from imaging a homogeneous fluorescent sample. The pixel-wise mean image over n_t images can be defined as

$$M(x_k, y_l, t_j) = \frac{1}{n_t} \sum_{j=1}^{n_t} I(x_k, y_l, t_j) \quad (2)$$

To avoid noise-induced singularities when normalising, PyFRAP computes a mean normalisation mask M_{pre} over multiple pre-bleach images, and then divides each image of the recovery time series pixel-wise by the computed mask

$$\tilde{I}(x_k, y_l, t_j) = \frac{I(x_k, y_l, t_j) + O_{\text{norm}}}{M_{\text{pre}}(x_k, y_l) + O_{\text{norm}}} \quad (3)$$

where O_{norm} is the optimal data offset computed via

$$O_{\text{norm}} = \max\left\{ \min_{k,j}\left(I(x_k, y_l, t_j)\right), \min_{k,j}\left(M_{\text{pre}}(x_k, y_l, t_j)\right) \right\} + 1 \quad (4)$$

Similarly, the flattening mask F is computed using the mean over multiple images of a fluorophore spread homogeneously across a cover slip, M_{flat}:

$$F(x_k, y_l) = \frac{\max_k(M_{\text{flat}}(x_k, y_l)) + O_{\text{flat}}}{M_{\text{flat}}(x_k, y_l) + O_{\text{flat}}} \quad (5)$$

Similar to the normalisation in Eq. (4), the optimal data offset O_{flat} is obtained by taking the maximum over all minimum intensities of images in both recovery and flattening data sets. The recovery data set is obtained by pixel-wise multiplication of the recovery image with the flattening mask obtained in Eq. (5):

$$\tilde{I}(x_k, y_l, t_j) = F(x_k, y_l) \cdot I(x_k, y_l, t_j) \quad (6)$$

An outline of both correction methods is shown in Supplementary Fig. 2c.

In the present study, two pre-bleach images were acquired per sample for the normalisation mask, and two images of fluorescein conjugated to a 40 kDa dextran or recombinant GFP homogeneously spread on a cover slip were acquired for the flattening approach. The effects of flattening and normalisation on data analysis are described in Supplementary Note 1.

Accounting for background fluorescence. Background subtraction is a standard procedure to extract the true signal of microscope images[38,39]. Similar to the flattening and normalisation masks, PyFRAP takes the average over multiple pixels to obtain a background mask and then subtracts it pixel-wise[38,39]:

$$\tilde{I}(x_k, y_l, t_j) = I(x_k, y_l, t_j) - M_{\text{bkgd}}(x_k, y_l) \quad (7)$$

The mean of two images without a sample was determined to compute a background mask. The effect of background subtraction is discussed in Supplementary Note 1.

Application of filters for noise reduction. Microscope data sets are often noisy, causing problems for normalisation and simulation. PyFRAP smooths noisy pixels by either applying a Gaussian blur with standard deviation σ_{gauss}, or a median filter with filter window radius r_{median}. We found that $\sigma_{gauss} = 2$ and $r_{median} = 5$ provided good results for the data in the present study (see Supplementary Note 1).

Accounting for fluorescence outside of the imaging view. In some cases it is not possible to capture the whole sample in one field of view under the microscope, and the concentration in the non-imaged regions needs to be estimated. PyFRAP solves this by letting users define an ROI Ω_{rim} to select an approximation of the average unbleached intensity from the first image of the recovery image series:

$$c_{rim} = \frac{1}{A_{rim}} \sum_{(x_k, y_l) \in \Omega_{rim}} I(x_k, y_l, t_0) \tag{8}$$

Ω_{rim} is defined by $\Omega_{rim} = \Omega_{slice} - \Omega_{centre}$, where

$$\Omega_{center} = \left\{ (x_k, y_l) | \sqrt{(x_k - x_c)^2 + (y_l - yc)^2} < \rho_{rim} r_{slice} \right\} \tag{9}$$

with (x_c, y_c) the centre pixel coordinates of the image. Ω_{rim} thus defines a small annulus comprising all pixels (x_k, y_l) inside Ω_{slice} that have a distance of at least $\rho_{rim} r_{slice}$ from the centre of the image (Supplementary Fig. 2b). $\rho_{rim} = 0.66$ and $\rho_{rim} = 0.4585$ were found to provide good values for the in vitro and in vivo experiments, respectively.

Simulations. PyFRAP simulates FRAP experiments numerically. Ignoring reaction kinetics, a FRAP experiment can be described by the diffusion equation

$$\frac{\partial c(\mathbf{x}, t)}{\partial t} = D \nabla^2 c(\mathbf{x}, t), \mathbf{x} \in \Omega \tag{10}$$

where $c(\mathbf{x}, t)$ is the concentration of the measured molecule at position $\mathbf{x} = \langle x, y, z \rangle$ and time t inside the domain Ω, and D is its scalar diffusion coefficient. The diffusion coefficient is assumed to be constant and homogeneous.

Since the sample is assumed to be a closed system, no-flux Neumann boundary conditions were defined as

$$\frac{\partial c(\mathbf{x}, t)}{\partial \mathbf{n}} = 0, \mathbf{x} \in \partial\Omega \tag{11}$$

where $\mathbf{n}$ is the normal vector of the boundary $\partial\Omega$ at position $\mathbf{x}$.

Initial conditions for simulations. The initial conditions are given by the bilinear interpolation P between pixels of the initial post-bleaching image:

$$P(x, y) = \frac{(x_2 - x, x - x_1)}{(x_1 - x_2)(y_2 - y_1)} \cdot \begin{pmatrix} I(x_1, y_1) & I(x_1, y_2) \\ I(x_2, y_1) & I(x_2, y_2) \end{pmatrix} \cdot \begin{pmatrix} y_2 - y \\ y - y_1 \end{pmatrix} \tag{12}$$

$I(x_{k'}, y_{l'})$ with $k', l' \in \{1, 2\}$ represents the intensities in the initial image of the four pixels surrounding (x, y). If (x, y) is outside of the visible ROI in the initial image (Ω_1), the rim concentration c_{rim} given in Eq. (8) is combined piece-wise with Eq. (12) to give the initial condition

$$c(\mathbf{x}, 0) = \begin{cases} P(x, y) & \text{if} (x, y) \in \Omega_1 \forall z \\ c_{rim} & \text{otherwise} \end{cases} \tag{13}$$

Simulation geometry. PyFRAP comes with its own geometry definition tool. Geometry definitions can then be converted into the Gmsh format[43] for meshing. PyFRAP can read Gmsh's geometry definition files, use Gmsh's mesh files, or import STereoLithography (.stl) files, allowing users to define arbitrary two- and three-dimensional geometries. This gives users the ability to describe a realistic FRAP experiment geometry with the necessary precision.

The simulation geometry Ω for the in vitro experiments was a conical frustum with upper radius $r_{upper} = 317.65$ pixels, lower radius $r_{lower} = 224.25$ pixels, and height $h \approx 90.33$ pixels (Supplementary Fig. 4b). For the in vivo experiments, the simulation geometry resembled a zebrafish embryo at dome stage, i.e., the intersection of two hemispheres intersecting each other at the equator of the outer hemisphere. Since the geometry depends on the radius of the embryo in the initial image, $r_{imaging}$ was calculated separately for each experiment[29,70]. Assuming that the radius of the inner hemisphere r_{inner} is 10% larger than the one of the outer hemisphere, r_{outer}, the geometry can be computed by

$$\begin{aligned} r_{outer} &= \frac{r_{imaging}^2 + h_{imaging}^2}{-2h_{imaging}} \\ r_{inner} &= 1.1 \cdot r_{outer} \\ d_{center} &= \sqrt{r_{inner}^2 - r_{outer}^2} \end{aligned} \tag{14}$$

where d_{centre} is the distance between the two centres of the hemispheres. Supplementary Fig. 4a shows a schematic of the zebrafish dome stage geometry.

Meshing for simulations. PyFRAP discretises simulation geometries using Gmsh[43] in combination with TetGen[44] into tetrahedral meshes. PyFRAP utilises almost all functionalities of Gmsh—such as boundary layer meshes, attractor meshes, mesh merging and mesh refinement—allowing users to apply fine meshes where they are needed.

The overall default element size in the present study was $\nu = 25$ pixels^3. To overcome numerical instabilities, such as Gibbs phenomena at the boundary of $\Omega_{bleached}$, the mesh around the bleached area boundary was refined using a boundary layer mesh of thickness $w_{BL} = 30$ pixels and element size $\nu_{BL} = 15$ pixels^3. Since only the simulation inside Ω_{slice} and $\Omega_{bleached}$ is used to fit the FRAP experiments, the mesh inside Ω_{slice} was also refined to an element size of $\nu_{slice} = 15$ pixels^3. Supplementary Fig. 4c, e shows an example of a tetrahedral mesh with both slice refinement and boundary layer meshes for the zebrafish dome geometry described in the previous section.

PDE solver. All partial differential equations (PDEs) were simulated using the FiPy toolbox[32]. The LU factorisation algorithm or the Preconditioned-Conjugated-Gradient algorithm implemented in PySparse were used to solve the linear system at each time step.

Simulation parameters. All simulations were performed with a reference diffusion coefficient of $D = 50$ pixels^2/s. To ensure that the simulations run long enough to capture the full recovery of the FRAP experiment, the end time point of the simulation was set to $t_{sim,end} = 1680$ s for experiments conducted with an acquisition interval of $\Delta t = 1$ s. Since the recovery is steepest at the beginning of the simulations, a logarithmic time-stepping scheme was used, making early time steps shorter to achieve greater accuracy. A summary of all simulation parameters used to analyse the FRAP data in the present study is given in Supplementary Table 11.

Fitting. To avoid the need to re-simulate the FRAP experiment for each choice of diffusion coefficient D, PyFRAP uses the self-similarity property of the solution to Eq. (10). For example, a simulated FRAP experiment with the diffusion coefficient $D = 50$ pixels^2/s results in the same recovery behaviour as an experiment with the diffusion coefficient $D = 200$ pixels^2/s, just four times slower. This can be described as

$$c(\mathbf{x}, t, D) = c\left(\mathbf{x}, \frac{D_{ref}}{D} t, D_{ref}\right) \tag{15}$$

where D_{ref} is the reference diffusion coefficient, i.e., the diffusion coefficient used for the simulation of Eq. (10). Supplementary Fig. 4d shows simulated recovery curves for various diffusion coefficients illustrating this self-similarity property.

PyFRAP allows users to fit four different models to FRAP data: (1) Pure diffusion, (2) diffusion and production, (3) diffusion and degradation, (4) diffusion with degradation and production, and each of these models with an additional set of equalisation parameters (see below). In case of pure diffusion, the solution for the diffusion coefficient D over a given ROI Ω_i is simply given by the volume integral of the solution in Eq. (15):

$$\bar{c}(\Omega_i, t, D) \equiv \int_{\mathbf{x} \in \Omega_i} c(\mathbf{x}, t, D) \mathrm{d}V \tag{16}$$

A summary of all parameters used to fit the FRAP data in the present study is given in Supplementary Table 12.

Extending the diffusion model with reaction kinetics. Spatially uniform production was added to the scaled FRAP model defined in Eq. (15) or in Eq. (20) by

$$\bar{c}(\Omega_i, t, D) = c(\Omega_i, t, D) + k_2 t \tag{17}$$

where k_2 is the production rate. To add spatially uniform degradation, the resulting solution is given by

$$\bar{c}(\Omega_i, t, D) = c(\Omega_i, t, D) e^{-k_1 t} \tag{18}$$

The parameter k_1 represents the degradation rate constant. Adding both degradation and production to the system results in the following superposition of solutions:

$$\bar{c}(\Omega_i, t, D) = c(\Omega_i, t, D) e^{-k_1 t} + \left(1 + e^{-k_1 t}\right) \frac{k_2}{k_1} \tag{19}$$

Accounting for varying fluorophore fractions by equalisation. FRAP experiments can vary in intensity during the experiment due to, for example, an increase or decrease in extracellular volume fraction, due to molecules moving in and out of the imaging plane, or due to an immobile fraction of fluorescent molecules. These effects are accounted for by equalisation, which normalises both simulation and data recovery curves to an equivalent scale between 0 and 1. During

the fitting process, the simulated recovery curves are slightly lifted or lowered to better resemble overall fluorescence levels. This can be written as

$$\tilde{c}(\Omega_i, t, D) = \frac{1}{\bar{c}_{\max} E_i}\left(\int_{\mathbf{x}\in\Omega_i} \bar{c}(\mathbf{x}, t, D)\mathrm{d}V - \bar{c}_{\min}\right) \quad (20)$$

where E_i is the equalisation factor for ROI Ω_i. The background $\bar{c}_{\min}$ was chosen to be the smallest concentration of the bleached ROI inside the imaging region (Ω_{bleached}), over the whole time series

$$\bar{c}_{\min} = \min_t \int_{\mathbf{x}\in\Omega_{\text{bleached}}} \bar{c}(\mathbf{x}, t)\mathrm{d}V \quad (21)$$

and the normalisation value $\bar{c}_{\max}$ to be the maximum concentration inside the whole imaging ROI (Ω_{slice}), over the whole time series

$$\bar{c}_{\max} = \max_t \int_{\mathbf{x}\in\Omega_{\text{slice}}} \bar{c}(\mathbf{x}, t)\mathrm{d}V \quad (22)$$

Minimisation and parameter estimation. Choosing one of the models defined in Eqs. (15), (16), (17), (18) and (19), the sum of squared differences, SSD, was calculated by

$$\mathrm{SSD} = \sum_{\mathrm{i}}\sum_{\mathrm{t_j}}\left(\mathrm{e}\left(\Omega_{\mathrm{i}}, \mathrm{t_j}, \mathrm{D}\right) - \mathrm{I}_{\Omega_{\mathrm{i}}}\left(\mathrm{t_j}\right)\right)^2 \quad (23)$$

where $t_j \in 0, .., T$ are all time points of the FRAP data set, and $\Omega_i \in \Omega_{\text{bleached}}, \Omega_{\text{slice}}$ are the two ROIs of interest yielding a mean optimal fit between all fitted ROIs. The minimisation of Eq. (23) was carried out using a constrained Nelder–Mead algorithm[49]. Since especially for a larger number of degrees of freedom the minimisation algorithm tended to stop in local minima, initial guesses for the diffusion coefficient D were tested over two orders of magnitude, and the fit yielding the minimum SSD was considered optimal.

Analysis speed. Details of the method to determine PyFRAP's performance in terms of analysis speed are described in Supplementary Note 4 and Supplementary Tables 13 and 14.

Statistics. PyFRAP offers four statistical tools (Supplementary Table 2) allowing users to test whether the estimated diffusion coefficient for one experimental group is significantly different from another one. The statistical tools include the two most prominent parametric significance tests, the Student's t-test[56] and a modification of this test, Welch's t-test[71], which both assume normally distributed test groups. PyFRAP also provides the Shapiro–Wilk test, allowing PyFRAP users to quickly assess whether the estimated diffusion coefficients follow a normal distribution. The Shapiro–Wilk test was recently found to have the best sensitivity compared to other common normality tests[72]. If normality cannot be guaranteed, PyFRAP offers two non-parametric ranked hypothesis tests: The Wilcoxon signed-rank test[73] and the Mann–Whitney U test[57].

Often, the underlying reaction kinetics of FRAP experiments or the relevance of their contribution might be unknown[54]. However, models with more parameters generally provide better fits than simpler models. The AIC[55] allows users to evaluate which model fits the data the best while keeping model complexity low. For this, let

$$\Theta := (k_1, k_2, D, E_1, E_2, \dots) \quad (24)$$

be the vector of unknown diffusion coefficient D, reaction rates k_1 and k_2, and E_1, E_2, … a list of equalisation factors. Moreover, let $m = m(\Theta)$ be the model prediction using Θ. Assuming that the data is distributed normally around the model

$$d_i - m_i \sim \mathcal{N}(\mu, \sigma) \quad (25)$$

the log-likelihood function at data point i, L_i becomes

$$L_i(\Theta|d_i - m_i) = (d_i - m_i)^2 \quad (26)$$

and is thus identical with the sum of squared differences used for optimisation in Eq. (23):

$$L(\Theta) = \sum_i L_i(\Theta) = \mathrm{SSD} \quad (27)$$

The AIC is then given by

$$\mathrm{AIC} = 2\mathrm{k} - 2\mathrm{L}\left(\hat{\Theta}\right) \quad (28)$$

where k is the number of parameters of model m and

$$\hat{\Theta} = \mathrm{argmin}(L(\Theta|d_i - m_i, i = 1...n)) \quad (29)$$

is the parameter configuration Θ minimising the log-likelihood function (Eq. (27)), i.e., the parameter configuration returned from fitting the model to data. The best model according to the AIC is then $m(\mathrm{argmin}(\mathrm{AIC}_i - \mathrm{AIC}_{\min}))$. If the number of sample points is small, the corrected AIC (AICc) provides a more accurate model selection technique:

$$\mathrm{AICc} = \mathrm{AIC} + \frac{2\mathrm{k}(\mathrm{k}+1)}{\mathrm{n}-\mathrm{k}-1} \quad (30)$$

where n is the number of data points. A rule of thumb for when the AIC (Eq. (28)) or its corrected version (Eq. (30)) should be used is

$$\frac{n}{k} > 40 \quad (31)$$

PyFRAP automatically selects which statistical model is more appropriate if not specified differently.

PyFRAP also provides R^2-values for each fit: An R^2-value for each fitted ROI and the product and mean of these values. In general, PyFRAP computes an R^2-value of an ROI by

$$R^2 = 1 - \frac{\sum_i m_i - d_i}{\sum_i d_i - \bar{d}} \quad (32)$$

where m_i and d_i are model and data at time i, and $\bar{d}$ is the mean over all data points.

Data exclusion. We performed a rigorous screen of all data sets, and we excluded data sets that showed strong radial inhomogeneities in the first post-bleach image due to inhomogeneous distribution of fluorescent molecules. Moreover, we excluded in vitro data sets that showed unstable distributions in the overall fluorescence intensity levels, indicating incomplete bleaching through the depth of the sample.

Code availability. PyFRAP is freely available from https://mueller-lab.github.io/PyFRAP.

Data availability. All data is available from the corresponding author upon request.

Received: 24 September 2017 Accepted: 26 March 2018
Published online: 20 April 2018

References

1. Crick, F. Diffusion in embryogenesis. *Nature* **255**, 420–422 (1970).
2. Lander, A. D., Nie, Q. & Wan, F. Y. M. Do morphogen gradients arise by diffusion? *Dev. Cell.* **2**, 785–796 (2002).
3. Müller, P. & Schier, A. F. Extracellular movement of signaling molecules. *Dev. Cell.* **21,**145-158 (2011).
4. Poo, M. M. & Cone, R. A. Lateral diffusion of rhodopsin in Necturus rods. *Exp. Eye Res.* **17**, 503–507 (1973).
5. Liebman, P. A. & Entine, G. Lateral diffusion of visual pigment in photoreceptor disk membranes. *Science* **185**, 457–459 (1974).
6. Loren, N. et al. Fluorescence recovery after photobleaching in material and life sciences: putting theory into practice. *Q. Rev. Biophys.* **48**, 323–387 (2015).
7. Lippincott-Schwartz, J., Altan-Bonnet, N. & Patterson, G. H. Photobleaching and photoactivation: following protein dynamics in living cells. *Nat. Cell Biol.* **5**, S7–S14 (2003).
8. Bancaud, A., Huet, S., Rabut, G. & Ellenberg, J. Fluorescence perturbation techniques to study mobility and molecular dynamics of proteins in live cells: FRAP, photoactivation, photoconversion, and FLIP. *Cold Spring Harb. Protoc.* **12**, 1303–1325 (2010).
9. Griffin, E. E., Odde, D. J. & Seydoux, G. Regulation of the MEX-5 gradient by a spatially segregated kinase/phosphatase cycle. *Cell* **146**, 955–958 (2011).
10. Zhou, S. et al. Free extracellular diffusion creates the Dpp morphogen gradient of the *Drosophila* wing disc. *Curr. Biol.* **22**, 668–675 (2012).
11. Axelrod, D., Koppel, D. E., Schlessinger, J., Elson, E. & Webb, W. W. Mobility measurement by analysis of fluorescence photobleaching recovery kinetics. *Biophys. J.* **16**, 1055–1069 (1976).

12. Soumpasis, D. Theoretical analysis of fluorescence photobleaching recovery experiments. *Biophys. J.* **41**, 95–97 (1983).
13. Sprague, B. L. & McNally, J. G. FRAP analysis of binding: proper and fitting. *Trends Cell Biol.* **15**, 84–91 (2005).
14. Kang, M., Day, C. A., Drake, K., Kenworthy, A. K. & DiBenedetto, E. A generalization of theory for two-dimensional Fluorescence Recovery After Photobleaching applicable to confocal laser scanning microscopes. *Biophys. J.* **97**, 1501–1511 (2009).
15. Deschout, H. et al. Straightforward FRAP for quantitative diffusion measurements with a laser scanning microscope. *Opt. Express* **18**, 22886–22905 (2010).
16. Kang, M., Day, C. A., Kenworthy, A. K. & DiBenedetto, E. Simplified equation to extract diffusion coefficients from confocal FRAP data. *Traffic* **13**, 1589–1600 (2012).
17. Kraft, L. J., Dowler, J. & Kenworthy, A. K. *Frap-toolbox: Software for the Analysis of Fluorescence Recovery after Photobleaching*. http://www.fraptoolbox.com Accessed 12 Dec 2016 (2014).
18. Lin, L. & Othmer, H. G. Improving parameter inference from FRAP data: an analysis motivated by pattern formation in the *Drosophila*wing disc. *Bull. Math. Biol.* **79**, 448–497 (2017).
19. Beaudouin, J., Mora-Bermúdez, F., Klee, T., Daigle, N. & Ellenberg, J. Dissecting the contribution of diffusion and interactions to the mobility of nuclear proteins. *Biophys. J.* **90**, 1878–1894 (2006).
20. Schaff, J. C., Cowan, A. E., Loew, L. M. & Moraru, I. I. Virtual FRAP-an experiment-oriented simulation tool. *Biophys. J.* **96**, 30a (2009).
21. Blumenthal, D., Goldstien, L., Edidin, M. & Gheber, L. A. Universal approach to FRAP analysis of arbitrary bleaching patterns. *Sci. Rep.* **5**, 11655 (2015).
22. Müller, P., Rogers, K. W., Yu, S. R., Brand, M. & Schier, A. F. Morphogen transport. *Development* **140**, 1621–1638 (2013).
23. Umulis, D. M. & Othmer, H. G. The importance of geometry in mathematical models of developing systems. *Curr. Opin. Genet. Dev.* **22**, 547–552 (2012).
24. Weiss, M. Challenges and artifacts in quantitative photobleaching experiments. *Traffic* **5**, 662–671 (2004).
25. Mazza, D., Cella, F., Vicidomini, G., Krol, S. & Diaspro, A. Role of three-dimensional bleach distribution in confocal and two-photon fluorescence recovery after photobleaching experiments. *Appl. Opt.* **46**, 7401–7411 (2007).
26. Machán, R., Foo, Y. H. & Wohland, T. On the equivalence of FCS and FRAP: simultaneous lipid membrane measurements. *Biophys. J.* **111**, 152–161 (2016).
27. Braga, J., Desterro, J. M. & Carmo-Fonseca, M. Intracellular macromolecular mobility measured by Fluorescence Recovery After Photobleaching with confocal laser scanning microscopes. *Mol. Biol. Cell.* **10**, 4749–4760 (2004).
28. Blischak, J. D., Davenport, E. R. & Wilson, G. A quick introduction to version control with Git and GitHub. *PLoS. Comput. Biol.* **12**, e1004668 (2016).
29. Müller, P. et al. Differential diffusivity of Nodal and Lefty underlies a reaction-diffusion patterning system. *Science* **336**, 721–724 (2012).
30. Sigaut, L., Ponce, M. L., Colman-Lerner, A. & Dawson, S. P. Optical techniques provide information on various effective diffusion coefficients in the presence of traps. *Phys. Rev. E* **82**, 051912 (2010).
31. Millman, K. J. & Aivazis, M. Python for scientists and engineers. *Comput. Sci. Eng.* **13**, 9–12 (2011).
32. Guyer, J. E., Wheeler, D. & Warren, J. A. FiPy: partial differential equations with Python. *Comput. Sci. Eng.* **11**, 6–15 (2009).
33. van der Walt, S. et al. scikit-image: Image processing in Python. *PeerJ* **2**, e453 (2014).
34. Jones, E. et al. *SciPy: Open source scientific tools for Python* (2001). http://www.scipy.org/
35. van der Walt, S., Colbert, C. & Varoquaux, G. The numpy array: a structure for efficient numerical computation. *Comput. Sci. Eng.* **13**, 22–30 (2011).
36. Hunter, J. D. Matplotlib: a 2D graphics environment. *Comput. Sci. Eng.* **9**, 90–95 (2007).
37. Lindblad, J. & Bengtsson, E. in *Proceedings of the 12th Scandinavian Conference on Image Analysis (SCIA)*, 264–271 (2001).
38. Waters, J. C. Accuracy and precision in quantitative fluorescence microscopy. *J. Cell. Biol.* **185**, 1135–1148 (2009).
39. Schwarzfischer, M. et al. in *Proceedings of Microscopic Image Analysis with Applications in Biology* (2011).
40. Gregor, T., Bialek, W., de Ruyter van Steveninck, R. R., Tank, D. W. & Wieschaus, E. F. Diffusion and scaling during early embryonic pattern formation. *Proc. Natl Acad. Sci. USA* **102**, 18403–18407 (2005).
41. Kicheva, A. et al. Kinetics of morphogen gradient formation. *Science* **5811**, 521–525 (2007).
42. Pomreinke, A. P. et al. Dynamics of BMP signaling and distribution during zebrafish dorsal-ventral patterning. *eLife* **6**, e25861 (2017).
43. Geuzaine, C. & Remacle, J.-F. Gmsh: a 3-D finite element mesh generator with built-in pre- and post-processing facilities. *Int. J. Numer. Methods Eng.* **79**, 1309–1331 (2009).
44. Si, H. Tetgen, a delaunay-based quality tetrahedral mesh generator. *ACM Trans. Math. Softw.* **41**, 11:1–11:36 (2015).
45. Sprague, B. L., Pego, R. L., Stavreva, D. A. & McNally, J. G. Analysis of binding reactions by fluorescence recovery after photobleaching. *Biophys. J.* **86**, 3473–3495 (2004).
46. Miura, K. *Frapcalc*. http://wiki.cmci.info/downloads/frap_analysis Accessed 12 Dec 2016 (2016).
47. Rapsomaniki, M. A. et al. EasyFRAP: an interactive, easy-to-use tool for qualitative and quantitative analysis of FRAP data. *Bioinformatics* **28**, 1800–1801 (2012).
48. Castle, B. T., Howard, S. A. & Odde, D. J. Assessment of transport mechanisms underlying the Bicoid morphogen gradient. *Cell. Mol. Bioeng.* **4**, 116–121 (2011).
49. Nelder, J. A. & Mead, R. A simplex method for function minimization. *Comput. J.* **7**, 308–313 (1965).
50. Nash, S. G. Newton-type minimization via the Lanczos method. *SIAM J. Numer. Anal.* **21**, 770–788 (1984).
51. Nocedal, J. & Wright, S. J. *Numerical optimization*. 2nd edn, (Springer, NY, 2006).
52. Bläßle, A. & Müller, P. PyFDAP: automated analysis of fluorescence decay after photoconversion (FDAP) experiments. *Bioinformatics* **6**, 972–974 (2015).
53. Rogers, K. W., Bläßle, A., Schier, A. F. & Müller, P. Measuring protein stability in living zebrafish embryos using fluorescence decay after photoconversion (FDAP). *J. Vis. Exp.* **95**, e52266 (2015).
54. Mai, J. et al. Are assumptions about the model type necessary in reaction-diffusion modeling? A FRAP application. *Biophys. J.* **100**, 1178–1188 (2011).
55. Akaike, H. A new look at the statistical model identification. *IEEE Trans. Autom. Control* **19**, 716–723 (1974).
56. Student. The probable error of a mean. *Biometrika* **6**, 1–25 (1908).
57. Mann, H. B. & Whitney, D. R. On a test of whether one of two random variables is stochastically larger than the other. *Ann. Math. Stat.* **18**, 50–60 (1947).
58. Shapiro, S. S. & Wilk, M. B. An analysis of variance test for normality (complete samples). *Biometrika* **52**, 591–611 (1965).
59. Aaron, J. *FRAP* https://de.mathworks.com/matlabcentral/fileexchange/47327-frap-zip Accessed 12 Dec 2016 (2016).
60. Ulrich, M. et al. Tropical-parameter estimation and simulation of reaction-diffusion models based on spatio-temporal microscopy images. *Bioinformatics* **22**, 2709–2710 (2006).
61. Gurskaya, N. G. et al. Engineering of a monomeric green-to-red photoactivatable fluorescent protein induced by blue light. *Nat. Biotechnol.* **24**, 461–465 (2006).
62. Hrabe, J., Hrabetová, S. & Segeth, K. A model of effective diffusion and tortuosity in the extracellular space of the brain. *Biophys. J.* **87**, 1606–1617 (2004).
63. Tao, L. & Nicholson, C. Maximum geometrical hindrance to diffusion in brain extracellular space surrounding uniformly spaced convex cells. *J. Theor. Biol.* **229**, 59–68 (2004).
64. Novak, I. L., Kraikivski, P. & Slepchenko, B. M. Diffusion in cytoplasm: effects of excluded volume due to internal membranes and cytoskeletal structures. *Biophys. J.* **97**, 758–767 (2009).
65. Donovan, P., Chehreghanianzabi, Y., Rathinam, M. & Zustiak, S. P. Homogenization theory for the prediction of obstructed solute diffusivity in macromolecular solutions. *PLoS ONE* **11**, e0146093 (2016).
66. Periasamy, N. & Verkman, A. S. Analysis of fluorophore diffusion by continuous distributions of diffusion coefficients: application to photobleaching measurements of multicomponent and anomalous diffusion. *Biophys. J.* **75**, 557–567 (1998).
67. Xiong, R. et al. Sizing nanomaterials in bio-fluids by cFRAP enables protein aggregation measurements and diagnosis of bio-barrier permeability. *Nat. Commun.* **7**, 12982 (2016).
68. Höckendorf, B., Thumberger, T. & Wittbrodt, J. Quantitative analysis of embryogenesis: a perspective for light sheet microscopy. *Dev. Cell.* **23**, 1111–1120 (2012).
69. Yu, S. R. et al. Fgf8 morphogen gradient forms by a source-sink mechanism with freely diffusing molecules. *Nature* **461**, 533–536 (2009).
70. Kimmel, C. B., Ballard, W. W., Kimmel, S. R., Ullmann, B. & Schilling, T. F. Stages of embryonic development of the zebrafish. *Dev. Dyn.* **203**, 253–310 (1995).
71. Welch, B. L. The generalisation of Student's problems when several different population variances are involved. *Biometrika* **34**, 28–35 (1947).
72. Razali, N. M. & Wah, Y. B. Power comparisons of Shapiro-Wilk, Kolmogorov-Smirnov, Lilliefors and Anderson-Darling tests. *J. Stat. Model. Anal.* **2**, 21–33 (2011).
73. Wilcoxon, F. Individual comparisons by ranking methods. *Biom. Bull.* **1**, 80–83 (1945).

Acknowledgements

We thank Ekkehard Kröwerath (University Hospital Tübingen, Centre for Dentistry, Oral Medicine, and Maxillofacial Surgery) for the preparation of plexiglass holes, Katherine Rogers and Fabian Fröhlich for discussions and suggestions, and Sarah Keim and Katherine Rogers for testing PyFRAP. This work was supported by the Emmy Noether Programme of the Deutsche Forschungsgemeinschaft, the Max Planck Society, and an ERC Starting Grant to P.M.

Author contributions

A.B., B.M.J. and P.M. conceived the study. A.B. and P.M. designed the software and performed data analysis and simulations. A.B. implemented the software. G.S., T.B., D.M. and H.P. conducted experiments. A.B. and P.M. wrote the manuscript.

Additional information

Supplementary Information accompanies this paper at https://doi.org/10.1038/s41467-018-03975-6.

Competing interests: The authors declare no competing interests.

Reprints and permission information is available online at http://npg.nature.com/reprintsandpermissions/

Publisher's note: Springer Nature remains neutral with regard to jurisdictional claims in published maps and institutional affiliations.

Supplementary Information for

Quantitative diffusion measurements using the open-source software PyFRAP

Alexander Bläßle[1], Gary Soh[1], Theresa Braun[1,2], David Mörsdorf[1], Hannes Preiß[1], Ben M. Jordan[3], and Patrick Müller[1,*]

[1]Friedrich Miescher Laboratory of the Max Planck Society, Tübingen, Germany
[2]Present address: University of Konstanz, Konstanz, Germany
[3]Department of Organismic and Evolutionary Biology, Harvard University, Cambridge, USA

[*]Correspondence to: patrick.mueller@tuebingen.mpg.de (P.M.)

This PDF includes:
Supplementary Notes 1-4
Supplementary Tables 1-14
Supplementary Figures 1-9
Supplementary References 1-43

Supplementary Note 1: Analysis method selection

To assess how image correction by flattening, normalisation, background subtraction, Gaussian blur, and median filter application affects effective diffusion estimates from FRAP experiments, we tested the 24 analysis combinations listed in Supplementary Table 1. We assessed whether 1) the resulting diffusion estimate D is affected, 2) the standard deviation σ of the estimated diffusion coefficients is affected (i.e. whether correcting and smoothing the images makes the diffusion estimates more exact), and 3) the goodness of the fits (i.e. R^2-values) is affected. We quantified the effect of an analysis option by

$$H(v, \alpha) = \frac{v(\alpha)}{v(\alpha_0)} \tag{1}$$

where $\alpha = \{n, f, b, g, m\}$ represents an analysis option defined by five binary entries indicating whether normalisation n, flattening f, background subtraction b, Gaussian blur g, or a median filter m was used. If we did not correct images, we denote this by α_0. The variable v describes the quantified result, such as the mean diffusion coefficient. Supplementary Fig. 3 shows a subset of this analysis for three different variables v: The mean diffusion coefficient D, the variance of diffusion coefficients σ, and the fit quality R^2. FRAP experiments performed in the present study were grouped by condition (*in vitro* experiments with free diffusion, *in vitro* experiments with beads, and *in vivo* experiments) to isolate condition-specific effects. We did not correct for potential illumination inhomogeneities in *in vivo* experiments, since these only covered a small centered area of the total image, and illumination is homogeneous in this region. Moreover, normalisation cannot be used for the analysis of *in vitro* experiments containing beads, since normalisation would introduce artificially high intensity areas at the locations of the beads.

If only normalisation and flattening were applied, we observed an increase of the apparent diffusion coefficients and an improvement in fit quality for free diffusion (Supplementary Fig. 3a,c). Both techniques only mildly affected the variance of diffusion coefficients (Supplementary Fig. 3b). Background subtraction had no effect on any measure (Supplementary Fig. 3a-c). Moreover, noise reduction or smoothing via median filter or Gaussian blur application tended to decrease the variance in all conditions (Supplementary Fig. 3b) and improve the fits for free diffusion (Supplementary Fig. 3b).

We also tested whether a combination of an illumination correction technique (n or f) with the remaining three manipulation techniques (b, g and m) can further improve the analysis. Supplementary Fig. 3d shows that this can lead to an increase in mean apparent diffusion estimates similar to those observed in Supplementary Fig. 3a. Moreover, applying a median filter or Gaussian blur in combination with flattening improves fit quality and decreases diffusion estimate variance (Supplementary Fig. 3e,f).

To keep the extent of image manipulation as minimal as possible while obtaining comparable low-variance estimates from high-quality fits, we only applied flattening to correct the images from *in vitro* experiments. Since both Gaussian blur and median filter treatments appeared to stabilise diffusion coefficient estimates (i.e. reducing their variance) to a similar extent, we restricted image smoothing to the application of a median filter for all other analyses.

Supplementary Note 2: Comparison of PyFRAP to other FRAP analysis software

We selected four current FRAP analysis software packages for comparison with PyFRAP: The two analytical programs easyFRAP[1] and FrapCalc[2], and the two numerical packages virtualFRAP[3] and simFRAP[4] (Supplementary Table 4).

To assess the performance of PyFRAP in comparison with other FRAP analysis software solutions, we created simulated FRAP data sets using PyFRAP's simulation toolbox. We found that PyFRAP and our in-house software based on MATLAB and COMSOL Multiphysics[5–7] produced identical simulated data, and we subsequently chose to use PyFRAP to simulate the experiments due to the ease of PyFRAP's scripting abilities. We simulated two-dimensional or three-dimensional FRAP experiments with circular bleaching spots of various sizes for a 300 s time-course. Two-dimensional simulated experiments were conducted in a circle with radius 215 μm, and three-dimensional experiments resembled a zebrafish at dome stage with $r_{\text{imaging}} = 215$ μm and $h_{\text{imaging}} = 80$ μm (see Methods section for details). Molecules were allowed to move with diffusion coefficients of 10 μm^2/s, 50 μm^2/s, or 200 μm^2/s, covering a range of typical diffusivities in biological samples. Bleached spots were placed in the center of the simulation geometry and comprised 5%, 10%, or 50% of the slice radius. We chose the boundary layer mesh described in the Methods section to envelope the bleached spot, guaranteeing numerical accuracy of the simulation experiments. PDEs were simulated over 4000 logarithmically-spaced time steps. The simulations were saved in a csv sheet specifically formatted for the use of easyFRAP or FrapCalc, or in 301 images by interpolation of the numerical solution onto a 512 μm $\times$ 512 μm grid. We then either imported and analysed the csv sheet using FrapCalc (`https://github.com/miura/FrapCalc` for IgorPro7) or easyFRAP, or read in and analysed the simulated images using simFRAP or virtualFRAP. The benchmarking analysis was performed using Microsoft Windows 8.1.

In contrast to other programs that determine absolute diffusion coefficients, easyFRAP only provides recovery half times ($1/\tau_{\frac{1}{2}}$). Thus, to compute diffusion coefficients from easyFRAP, we used the well-established[8] equation

$$D = \frac{-\omega^2 \ln\left(\frac{1}{2}\right)}{\tau_{\frac{1}{2}}}$$

with various dimensions of the bleached spot ω.

We used PyFRAP's standard pipeline to analyse the saved simulated FRAP images files in an unbiased manner, only constraining imaging depth and radius.

As mentioned in the main text, PyFRAP outperformed all tested software packages and exhibited the smallest error between predicted and simulated diffusion coefficients (Fig. 3c).

Supplementary Note 3: Data analysis and control experiments

Computation of theoretical diffusion coefficients

We compared our *in vitro* FRAP results for differently sized fluorescein-labeled dextrans to predictions derived from the Einstein-Stokes equation

$$D = \frac{k_{\mathrm{B}}T}{6\pi\eta r} \tag{2}$$

where $k_{\mathrm{B}} = 1.380\,648\,52 \times 10^{-23}\ \mathrm{m^2\,kg\,s^{-2}\,K^{-1}}$ is the Boltzmann constant. The FRAP experiments were conducted in an aqueous solution with viscosity $\eta = 0.9321 \times 10^{-3}\ \mathrm{kg\,s^{-1}\,m^{-1}}$ at $T = 296\ \mathrm{K}$. Stokes radii r of the fluorescent molecules were obtained from the manufacturers' websites and are listed along with the calculated theoretical diffusion coefficients in Supplementary Table 5.

FRAP experiments with different bleach window sizes

To test whether different bleach window size might lead to different diffusion coefficient estimates, we performed FRAP experiments with three different bleach window sizes: 34.01 $\mu\mathrm{m}$, 141.7 $\mu\mathrm{m}$, and 242.91 $\mu\mathrm{m}$. Using fluorescein-labeled dextrans of 40 kDa and 70 kDa molecular weight, we found that different bleach window sizes do not affect diffusion coefficient estimates determined by PyFRAP (Supplementary Fig. 6).

FRAP experiments can be executed over different spatial scales, from subcellular to tissue-level measurements. Our experiments were performed on spatial scales that are three orders of magnitude larger than the microscope's resolution limit. However, it is possible that FRAP experiments in very small samples with subcellular bleach areas may be affected by the imaging resolution, and future deconvolution-based approaches could be helpful to improve the measurement accuracy of PyFRAP in these cases.

Simulating tortuosity

The movement of molecules during FRAP experiments in biological samples is affected by obstacles such as cells, nuclei, or filopodia, and such tortuous molecule movements have been suggested to alter recovery rates and diffusion estimates[6].

To obtain a better understanding of how obstacles alter effective diffusion coefficients, we performed a simulation study in two- and three-dimensional geometries. We placed objects with a radius of $r_{\mathrm{Bead}} \approx 20\ \mu\mathrm{m}$ (similar to the dimensions of cells and beads used in the present study) in each geometry in three different ways: 1) Equally sized beads aligned as a regular grid (Supplementary Fig. 7a), 2) randomly placed within the domain with radii drawn from a cut-off normal distribution (Supplementary Fig. 7b,d), and 3) equally sized beads placed according to a hexagonal close-packing (Supplementary Fig. 7c). Beads were placed with different minimal gaps between them, ranging from 0.05 $\mu\mathrm{m}$ to 10 $\mu\mathrm{m}$. For 2D simulations, the overall geometry was a circle with radius 300 $\mu\mathrm{m}$. We chose a cylinder with equal radius and height of 100 $\mu\mathrm{m}$ or a cuboid with dimensions 600 $\mu\mathrm{m} \times 600\ \mu\mathrm{m} \times 100\ \mu\mathrm{m}$ for all 3D simulations experiments. The combination between various placement methods and gap sizes allowed us to vary the extracellular volume fraction (EVF) – i.e. the space available for the diffusing molecules – from 25% to 78%.

Confirming previous analyses[9–12], we found that the introduction of beads delayed molecule recovery in the bleached ROI, and the effect of tortuosity increased as the EVF decreased (Fig. 5b, Supplementary Fig. 7e,f, Supplementary Table 8). Moreover, the effect in two-dimensional experiments was more severe. For example, FRAP simulations with EVF $= 36\%$ reduced diffusion by 51% compared to only 40% for EVF $= 38\%$ in a three-dimensional simulation. Both observations are in line with theoretical predictions and previous results[9–12].

BSA does not affect fluorophore diffusivity

We found a stronger effect of bead-mediated tortuosity on 70 kDa fluorescein-labeled dextran molecules than on GFP *in vitro* (Fig. 5d,e). BSA was added to the aqueous solution with GFP to prevent the fluorescent protein from interacting with the plexiglass surface of the drilled hole in the *in vitro* experiments. To test whether BSA might also interact with the polyacrylamide beads and thus distort FRAP results, we repeated the experiments with 70 kDa fluorescein-labeled dextran both for pure diffusion with beads in addition to experiments with 70 kDa fluorescein-labeled dextran + BSA + beads. We found that BSA had no influence on the recovery rates, yielding equal results within standard error, i.e. 14.9 ± 2.1 μm^2/s for bead experiments and 15.1 ± 2.4 μm^2/s for experiments with additional BSA (Supplementary Fig. 9a).

Varying the experimental settings for Squint-GFP FRAP experiments does not consistently affect measured diffusion coefficients

For the FRAP experiments with Squint-GFP produced from injected mRNA, we acquired data sets varying the amount of injected mRNA, the frame rate and length of image acquisition, and the zoom factor of the microscope. Results were partitioned into three experimental groups, i.e. images recorded with 1) a frame rate of 1 frames/10 s for 3000 s with 30 pg of injected mRNA and a spatial resolution of 340.08 $\mu m \times 340.08$ μm, 2) a frame rate of 1 frame/10 s for 3000 s with 200 pg of injected mRNA and a spatial resolution of 566.79 $\mu m \times 566.79$ μm, and 3) a frame rate of 1 frame/s for 300 s with 200 pg of injected mRNA and a spatial resolution of 566.79 $\mu m \times 566.79$ μm.

There were no clear trends between different acquisition methods (Supplementary Fig. 9b). However, acquiring images at a higher frame rate for a shorter period of time appeared to make experiments and thus apparent diffusion coefficients more noisy, possibly resulting from the slow transport process underlying Squint-GFP diffusion.

Supplementary Note 4: PyFRAP analysis speed

To evaluate PyFRAP's analysis speed, we tested several analysis settings on different operating systems and computers. We designed three test cases: 1) A two-dimensional circular geometry similar to those used for the benchmarking simulations described in Supplementary Note 2, 2) a three-dimensional frustum geometry identical to the ones used to analyse the *in vitro* FRAP experiments described in the present work, and 3) a three-dimensional geometry resembling a zebrafish embryo at dome stage similar to our analysis of the *in vivo* experiments. The test data sets had identical properties as the data described for the respective experiments. A summary of all relevant test parameters can be found in Supplementary Table 13. All cases were tested on the three common operating systems Mac OSX, Microsoft Windows, and Ubuntu Linux, and the time from analysing the image data to mesh generation, simulation, and model fitting was measured for each test case. The results of these tests are summarised in Supplementary Table 14.

Note that PyFRAP does not allow parallel processing and only uses a single core of a CPU.

Supplementary Table 1. Combinations of image correction and smoothing methods used to analyse FRAP experiments. See Supplementary Fig. 3 for the results of this analysis. Note that flattening and normalisation were never applied at the same time since this would have distorted the image data.

Combination	Normalisation	Flattening	Background subtraction	Gaussian filter	Median filter
1	Off	Off	Off	Off	Off
2	Off	Off	Off	Off	On
3	Off	Off	Off	On	Off
4	Off	Off	Off	On	On
5	Off	Off	On	Off	Off
6	Off	Off	On	Off	On
7	Off	Off	On	On	Off
8	Off	Off	On	On	On
9	Off	On	Off	Off	Off
10	Off	On	Off	Off	On
11	Off	On	Off	On	Off
12	Off	On	Off	On	On
13	Off	On	On	Off	Off
14	Off	On	On	Off	On
15	Off	On	On	On	Off
16	Off	On	On	On	On
17	On	Off	Off	Off	Off
18	On	Off	Off	Off	On
19	On	Off	Off	On	Off
20	On	Off	Off	On	On
21	On	Off	On	Off	Off
22	On	Off	On	Off	On
23	On	Off	On	On	Off
24	On	Off	On	On	On

Supplementary Table 2. Statistical tools available in PyFRAP.

Method	Purpose	Type	Publication
Student's t-test	Significance testing	Parametric	[13]
Welch's t-test	Significance testing	Parametric	[14]
Wilcoxon signed-rank test	Significance testing	Non-parametric	[15]
Mann-Whitney U test	Significance testing	Non-parametric	[16]
Shapiro-Wilk test	Normality testing	Parametric	[17]
Akaike Information Criterion (AIC)	Model comparison	Parametric	[18]

Supplementary Table 3. Benchmarking PyFRAP against an in-house software combination of MATLAB and COMSOL Multiphysics. Data was simulated with MATLAB and COMSOL Multiphysics[5–7], and then fitted with PyFRAP for each of the four available reaction-diffusion models.

MATLAB + COMSOL Multiphysics			***PyFRAP***			***R^2-value***		***AIC***
D (μm^2/s)	**Degradation (10^{-4}/s)**	**Production (10^{-4} [c]/s)**	**D (μm^2/s)**	**Degradation (10^{-4}/s)**	**Production (10^{-4} [c]/s)**	**Bleached window**	**Slice**	**Correct model prediction**
Pure diffusion								
1	0	0	1.0	0	0	0.998	0.972	yes
5	0	0	4.8	0	0	1.000	0.910	yes
10	0	0	9.5	0	0	1.000	0.932	yes
40	0	0	39.1	0	0	0.999	0.870	yes
110	0	0	109.4	0	0	0.999	0.984	yes
200	0	0	199.1	0	0	0.999	0.990	yes
Diffusion + degradation								
1	5.0	0	1.0	5.8	0	0.998	0.921	yes
5	5.0	0	4.9	5.5	0	1.000	0.959	yes
10	5.0	0	9.7	5.4	0	1.000	0.972	yes
40	5.0	0	39.0	5.0	0	0.999	0.950	yes
110	5.0	0	108.1	4.9	0	0.999	0.943	yes
200	5.0	0	198.0	5.0	0	0.999	0.982	yes
Diffusion + production								
1	0	5.0	1.0	0	4.4	0.999	0.950	yes
5	0	5.0	5.0	0	4.6	1.000	0.972	yes
10	0	5.0	9.8	0	4.7	1.000	0.978	yes
40	0	5.0	38.9	0	5.0	1.000	0.991	yes
110	0	5.0	108.3	0	5.1	1.000	0.998	yes
200	0	5.0	198.4	0	5.0	1.000	0.999	yes
Diffusion + production + degradation								
1	5.0	7.0	1.1	4.8	6.2	0.992	0.845	no
5	5.0	7.0	5.0	4.8	6.4	1.000	0.894	no
10	5.0	7.0	9.5	5.9	7.5	1.000	0.910	no
40	5.0	7.0	39.2	4.1	6.3	1.000	0.979	no
110	5.0	7.0	105.2	9.7	12.0	0.999	0.995	no
200	5.0	7.0	192.6	11.6	13.3	1.000	0.996	no

Supplementary Table 4. Selection of current FRAP analysis software packages.

Software	Fit type	Result type	Input data	Publication	Platform	Tested	Comments
easyFRAP	Analytical	Qualitive	CSV	[1]	Windows, Mac OSX	Yes	Requires MATLAB Runtime, only produces $\tau_{1/2}$
FrapCalc	Analytical	Qualitive	CSV	[2]	Windows, Mac OSX	Yes	Requires IgorPro
FRAP	Analytical	Qualitive	Image files	[19]	Cross-platform	No	Requires specialised MATLAB toolboxes
simFRAP	Simulation	Quantitive	Image files	[4]	Cross-platform	Yes	Fiji Plugin
virtualFRAP	Simulation	Quantitive	Image files	[3]	Windows	Yes	
FRAPToolbox	Simulation	Quantitive	Image files	[20]	Cross-platform	No	Unable to read non-OME formats
Tropical	Simulation	Quantitive	Image files	[21]	Windows, Linux	No	Software unavailable

Supplementary Table 5. Fluorescent samples used for *in vitro* experiments, and their calculated theoretical diffusion coefficients. Theoretical values were only computed if an estimate of the molecule's Stokes radius could be found (see Supplementary Note 3 for details).

Fluorophore	**Molecular weight (kDa)**	**Concentration (µM)**	**Manufacturer**	**Stokes radius (nm)**	**Theoretical D ($\mu m^2/s$)**
Fluorescein-dextran	3	1	Thermo Fisher	1.36	171
Fluorescein-dextran	4	1, 15, 100	Sigma-Aldrich	1.4	166
Fluorescein-dextran	10	1	Thermo Fisher	2.3	101
Fluorescein-dextran	40	1	Thermo Fisher	4.5	52
Fluorescein-dextran	70	1	Sigma-Aldrich	6.0	39
Fluorescein-dextran	70	1	Thermo Fisher	6.0	39
Fluorescein-dextran	150	1	Sigma-Aldrich	8.5	27
Fluorescein-dextran	500	1	Thermo Fisher	15.8	15
GFP	32.7	4	Biovision	n.a.	n.a.
Dendra2	27.5	0.5	Hoelzel Diagnostics	n.a	n.a.

Supplementary Table 6. Diffusion coefficients determined by *in vitro* experiments and PyFRAP analysis. Theoretical values were only computed if an estimate of the molecule's Stokes radius could be found. Mean D values determined by PyFRAP as well as literature values are given with standard deviation.

			PyFRAP		***Literature***		
Dextran size (kDa)	**Manufacturer**	**D ($\mu m^2/s$) theoretical**	**D ($\mu m^2/s$) experimental**	**n**	**D ($\mu m^2/s$) experimental**	**Technique**	**Reference**
3	Thermo Fisher	171	170.3 ± 21.9	19	161 ± 22	FCS	[22]
4	Sigma-Aldrich	166	181.1 ± 31.6	44	135 ± 10	FRAP	[23]
10	Thermo Fisher	101	83.1 ± 8.0	12	122 ± 4	FCS	[22]
40	Thermo Fisher	52	45.3 ± 11.1	57	47 ± 2	FCS	[22]
70	Thermo Fisher	39	26.9 ± 4.9	35	37 ± 7	FCS	[22]
70	Sigma-Aldrich	39	49.2 ± 5.6	31	30 ± 2	FRAP	[24]
150	Sigma-Aldrich	27	46.4 ± 5.6	31	26 ± 2	FRAP	[24]
500	Thermo Fisher	15	25.7 ± 1.8	11	23.2 ± 1.1	FRAP	[25]

Supplementary Table 7. Literature values used for Fig. 5.

Molecule	MW (kDa)	Temperature during measurement (°C)	Manufacturer	D ($\mu m^2/s$)	Stdev ($\mu m^2/s$)	Technique	Reference
Fluorescein	0.33	22	Sigma-Aldrich	300	n.a.	FCS	[24]
Fluorescein	0.33	23	n.a.	270	n.a.	FRAP	[26]
Fluorescein	0.33	23	n.a.	260	n.a.	FRAP	[26]
Na2-Fluorescein	0.376	25	Fluka	380	35	FRAP	[27]
Oregon Green 488 carboxylic acid	0.41230	23	Thermo Fisher	336	11	FCS	[22]
Rhodamine B	0.47901	23	Fluka	420	20	FCS	[22]
Rhodamine B	0.47901	22.5	Sigma-Aldrich	420	30	FCS	[28]
Rhodamine 6 G	0.47901	22.5	Molecular Probes	400	30	FCS	[28]
Rhodamine 6 G	0.47901	23	Thermo Fisher	400	20	FCS	[22]
Tetramethyl-Rhodamine methyl ester	0.50093	23	Thermo Fisher	412	18	FCS	[22]
Oregon Green 488 carboxylic acid succinimidyl ester	0.50938	23	Thermo Fisher	308	10	FCS	[22]
Rhodamine green succinimidyl ester	0.621	20	Molecular Probes	233	3	FCS	[29]
Alexa488 alkyne	0.774	32	Life Technologies	288	8	FCS	[30]
Fluorescent dextran	3	23	Thermo Fisher	161	22	FCS	[22]
Alexa488-dextran	3	32	Life Technologies	160	5	FCS	[30]
FITC-dextran	3	22	Pharmacia	98	6	FRAP	[31]
FITC-dextran	3	n.a.	Pharmacia	98	6	FRAP	[32]
FITC-dextran	4	25	Sigma-Aldrich	149	n.a.	FRAP	[33]
FITC-dextran	4	25	Sigma-Aldrich	135	10	FRAP	[23]
FITC-dextran	4	32	Sigma-Aldrich	135	6	FCS	[30]
FITC-dextran	4	20	Sigma-Aldrich	96	2.4	FCS	[34]
FITC-dextran	4	22	Sigma-Aldrich	89	n.a.	FRAP	[35]
FITC-dextran	4	19	Sigma-Aldrich	155	23	FRAP	[36]
FITC-dextran	9.4	20	Sigma-Aldrich	75	3	FRAP	[37]
Fluorescent dextran	10	23	Thermo Fisher	122	4	FCS	[22]
Rhodamine green dextran	10	20	Molecular Probes	115	4	FCS	[29]
Alexa488-dextran	10	32	Life Technologies	82	1.4	FCS	[30]
FITC-dextran	10	22	Sigma-Aldrich	76	n.a.	FRAP	[31]
FITC-dextran	10	20	Sigma-Aldrich	68	1	FCS	[34]
FITC-dextran	11	n.a.	Sigma-Aldrich	76	2.5	FRAP	[32]
FITC-dextran	11	22	Sigma-Aldrich	76	3	FRAP	[31]
FITC-dextran	12	25	Sigma-Aldrich	97	n.a.	FRAP	[33]
FITC-Insulin	12	25	Sigma-Aldrich	147	13	FRAP	[33]
FITC-dextran	17	22	Sigma-Aldrich	65	n.a.	FRAP	[31]
FITC-dextran	17.2	20	Sigma-Aldrich	64	2	FRAP	[37]
FITC-dextran	18	22	Sigma-Aldrich	65	7	FRAP	[31]
FITC-dextran	18	n.a.	Sigma-Aldrich	65	6.5	FRAP	[32]
FITC-dextran	20	22	Sigma-Aldrich	78	n.a.	FCS	[24]
FITC-dextran	20	22	Sigma-Aldrich	64	2	FRAP	[24]
FITC-dextran	20	29	Sigma-Aldrich	70	8	FRAP	[36]
FITC-dextran	20	22	Sigma-Aldrich	63	4	FRAP	[25]
FITC-dextran	21	25	Sigma-Aldrich	71	n.a.	FRAP	[33]
GFP	26.9	25	custom-made	87	n.a.	FCS	[38]
GFP	26.9	n.a.	custom-made	87	n.a.	FRAP	[39]
GFP	26.9	22	Clontech	82	n.a.	FCS	[24]

FITC-dextran	35.6	20	Sigma-Aldrich	44	5	FRAP	[37]
FITC-dextran	38	25	Sigma-Aldrich	62	n.a.	FRAP	[33]
Fluorescent dextran	40	23	Thermo Fisher	47	2	FCS	[22]
FITC-dextran	40	22	Sigma-Aldrich	45	n.a.	FCS	[40]
FITC-dextran	40	22	Sigma-Aldrich	45	n.a.	FCS	[24]
FITC-dextran	40	32	Sigma-Aldrich	45	1.1	FCS	[30]
FITC-dextran	40	22	Sigma-Aldrich	44	5	FRAP	[24]
FITC-dextran	40	22	Sigma-Aldrich	52	2	FRAP	[25]
FITC-dextran	41	22	Sigma-Aldrich	46	5	FRAP	[31]
FITC-dextran	41	n.a.	Sigma-Aldrich	46	4.6	FRAP	[32]
FITC-dextran	42	20	Sigma-Aldrich	39	0.4	FCS	[34]
FITC-dextran	51	25	Sigma-Aldrich	54	n.a.	FRAP	[33]
FITC-dextran	62	n.a.	Sigma-Aldrich	39	2.6	FRAP	[32]
FITC-dextran	62	22	Sigma-Aldrich	39	3	FRAP	[31]
FITC-BSA	67	25	n.a.	58	5	FRAP	[33]
FITC-dextran	70	22	Sigma-Aldrich	38	n.a.	FCS	[24]
FITC-dextran	70	22	Sigma-Aldrich	38	n.a.	FCS	[40]
Fluorescent dextran	70	23	Thermo Fisher	37	7	FCS	[22]
FITC-dextran	70	n.a.	Fluka	33	2.1	FCS	[41]
FITC-dextran	70	22	Sigma-Aldrich	30	2	FRAP	[24]
FITC-dextran	70	25	Thermo Fisher	30	3.1	FRAP	[27]
FITC-dextran	70	23	n.a.	23	n.a.	FRAP	[26]
FITC-dextran	70	22	Sigma-Aldrich	44	1	FRAP	[25]
FITC-dextran	71	25	Sigma-Aldrich	44	2	FRAP	[23]
FITC-dextran	71.2	20	Sigma-Aldrich	30	2	FRAP	[37]
FITC-dextran	77	20	Sigma-Aldrich	35	0.6	FCS	[34]
FITC-dextran	148	20	Sigma-Aldrich	25	3.1	FCS	[34]
FITC-dextran	148	20	Sigma-Aldrich	18	1	FRAP	[37]
FITC-dextran	150	22	Sigma-Aldrich	26	2	FRAP	[24]
FITC-dextran	150	22	Sigma-Aldrich	24	n.a.	FCS	[40]
FITC-dextran	150	22	Sigma-Aldrich	24	n.a.	FCS	[24]
FITC-dextran	150	20	Sigma-Aldrich	14	n.a.	FRAP	[42]
FITC-dextran	157	n.a.	Sigma-Aldrich	24	1.3	FRAP	[32]
FITC-dextran	157	22	Sigma-Aldrich	24	1	FRAP	[31]
FITC-dextran	167	25	Sigma-Aldrich	38	n.a.	FRAP	[33]
FITC-dextran	167	n.a.	Sigma-Aldrich	18.8	0.2	FRAP	[43]
FITC-dextran	260	25	Sigma-Aldrich	30	n.a.	FRAP	[33]
FITC-dextran	282	20	Sigma-Aldrich	16.6	0.8	FCS	[34]
FITC-dextran	464	20	Sigma-Aldrich	14	0.6	FCS	[34]
FITC-dextran	464	n.a.	Sigma-Aldrich	11	0.5	FRAP	[43]
FITC-dextran	500	22	Sigma-Aldrich	23	1	FRAP	[25]
FITC-dextran	580	25	Sigma-Aldrich	22	n.a.	FRAP	[33]
FITC-dextran	2000	25	Sigma-Aldrich	10	1	FRAP	[23]
Fluorescent dextran	2000	23	Thermo Fisher	6	1	FCS	[22]
FITC-dextran	2000	n.a.	Sigma-Aldrich	6.4	0.09	FRAP	[43]
FITC-dextran	2101	25	Sigma-Aldrich	14	n.a.	FRAP	[33]

Supplementary Table 8. Summary of tortuosity simulations.

Dimension	Geometry	Packing	Extracelluar volume fraction (EVF) (%)	Diffusion hindrance factor θ
2D	Circle	Regular	74	0.74
2D	Circle	Regular	59	0.61
2D	Circle	Random	56	0.57
2D	Circle	Random	36	0.49
2D	Circle	Ideal	25	0.44
3D	Cylinder	Regular	71	0.86
3D	Cylinder	Random	78	0.92
3D	Cylinder	Random	58	0.88
3D	Cylinder	Ideal	78	0.92
3D	Cylinder	Ideal	71	0.874
3D	Cylinder	Ideal	61	0.871
3D	Cylinder	Ideal	60	0.870
3D	Cylinder	Ideal	42	0.75
3D	Cuboid	Ideal	38	0.60

Supplementary Table 9. Diffusion coefficients determined by *in vitro* experiments and PyFRAP analysis in the presence of polyacrylamide beads. Mean diffusion values are given with standard error.

Dextran size (kDa)	Manufacturer	Condition	D ($\mu m^2/s$)	n
70	Thermo Fisher	Free	24.1 ± 0.4	13
70	Thermo Fisher	Beads	14.9 ± 0.5	17

Supplementary Table 10. Diffusion coefficients determined by *in vitro* and *in vivo* experiments and PyFRAP analysis with GFP and GFP fusion proteins. Mean diffusion values are given with standard error.

Molecule	**Manufacturer**	**Source**	**Condition**	**Context**	**D (µm^2/s) PyFRAP**	**n**
Recombinant GFP	Biovision	Protein	Free	*In vitro*	96.1 ± 2.2	23
Recombinant GFP	Biovision	Protein	Beads	*In vitro*	79.2 ± 4.1	18
Recombinant GFP	Biovision	Injected protein	Extracelluar matrix	*In vivo*	37.6 ± 3.7	15
Secreted GFP	In-house	Injected mRNA	Extracelluar matrix + production	*In vivo*	35.3 ± 4.8	17
Squint-GFP	In-house	Injected mRNA	Extracelluar matrix + production + binding	*In vivo*	1.7 ± 0.25	27

Supplementary Table 11. Parameters used for the simulation of FRAP experiments.

Variable	Definition	Default value
	Simulation	
D	Diffusion coefficient	$D = 50$ pixels^2/s
	Time stepping	
$t_{\mathrm{sim,start}}$	Simulation start time	0 s
$t_{\mathrm{sim,end}}$	Simulation end time	1680 s
n_{sim}	Number of time steps	4000
t_{scale}	Time-stepping scheme	Logarithmic
	Geometry	
r_{upper}	Upper radius of frustum	317.65 pixels
r_{lower}	Lower radius of frustum	224.25 pixels
h	Height of frustum	90.33 pixels
	Meshing	
v	Mesh element size	25 pixels^3
v_{BL}	Boundary layer element size	15 pixels^3
v_{slice}	Slice refinement element size	15 pixels^3
w_{BL}	Boundary layer thickness	30 pixels
	Solver	
ϵ	Solver tolerance	10^{-10}
N_{iter}	Solver iterations	1000

Supplementary Table 12. Fitting and model parameters, initial guesses, and bounded ranges. Note that we tried different initial guesses for the diffusion coefficient D, which prevented the minimisation algorithm from stopping at a local minimum. We then then took the fit that yielded the global minimum SSD.

Initial guesses		
Parameter	**Initial guess**	**Allowed range**
D (pixels^2/s)	1 - 200	0.01 - 400
k_1 (1/s)	0	0 - 100
k_2 ($[c]$/s)	0	0 - 100
E_{bleached}	1	0.1 - 3
E_{slice}	1	0.1 - 3
Fitting convergence		
Parameter	**Definition**	**Default value**
$N_{\max}$	Maximum number of function calls	1000
δ	Tolerance of termination	10^{-10}

Supplementary Table 13. Test data and settings to measure PyFRAP analysis speed.

	2D	**Frustum**	**Dome**
Geometry	2D circle	3D frustum	3D zebrafish dome
Number of images	301	301	301
Number of mesh cells	7000	20000	35000
Number of time steps	1000	3000	3000
Illumination correction	No	Yes	Yes
Median filter application	No	Yes	Yes

Supplementary Table 14. PyFRAP analysis speed.

Operating system	Version	Processor	Memory	2D test (s)	Frustum test (s)	Dome test (s)
Ubuntu	14.04 LTS	Intel Core i7-3520M 2.90 GHz	8 GB	97	378	489
Ubuntu	16.04 LTS	Intel Core i5-4210 2.60 GHz	8 GB	125	521	743
Ubuntu	16.04 LTS	Intel Xeon E3-1275 3.60 GHz	64 GB	73	347	437
Mac OS X	10.13.3	Intel Core i7-4790K 4.00 GHz	32 GB	79	282	386
Windows	8.1	Intel Core i7-5600U 2.60 Ghz	8 GB	91	373	567

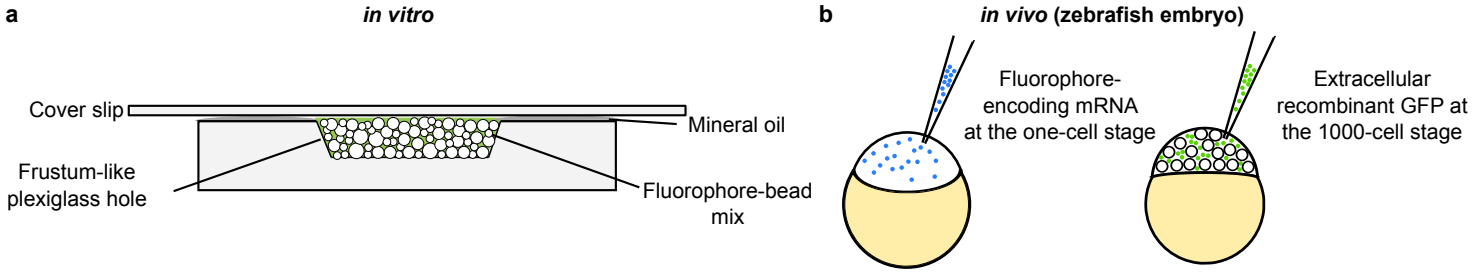

Supplementary Figure 1 | Sample preparation for *in vitro* and *in vivo* FRAP experiments. (a) *In vitro* experiments. Fluorophore solution was pipetted into a frustum-like plexiglass hole. The hole was then sealed with mineral oil and covered with a cover slip. The sample was flipped and placed under an inverted confocal microscope. **(b)** *In vivo* experiments in zebrafish embryos. mRNA encoding a fluorophore was injected into embryos at the one-cell stage, or recombinant GFP was injected into the extracellular space of embryos at the 1000-cell stage.

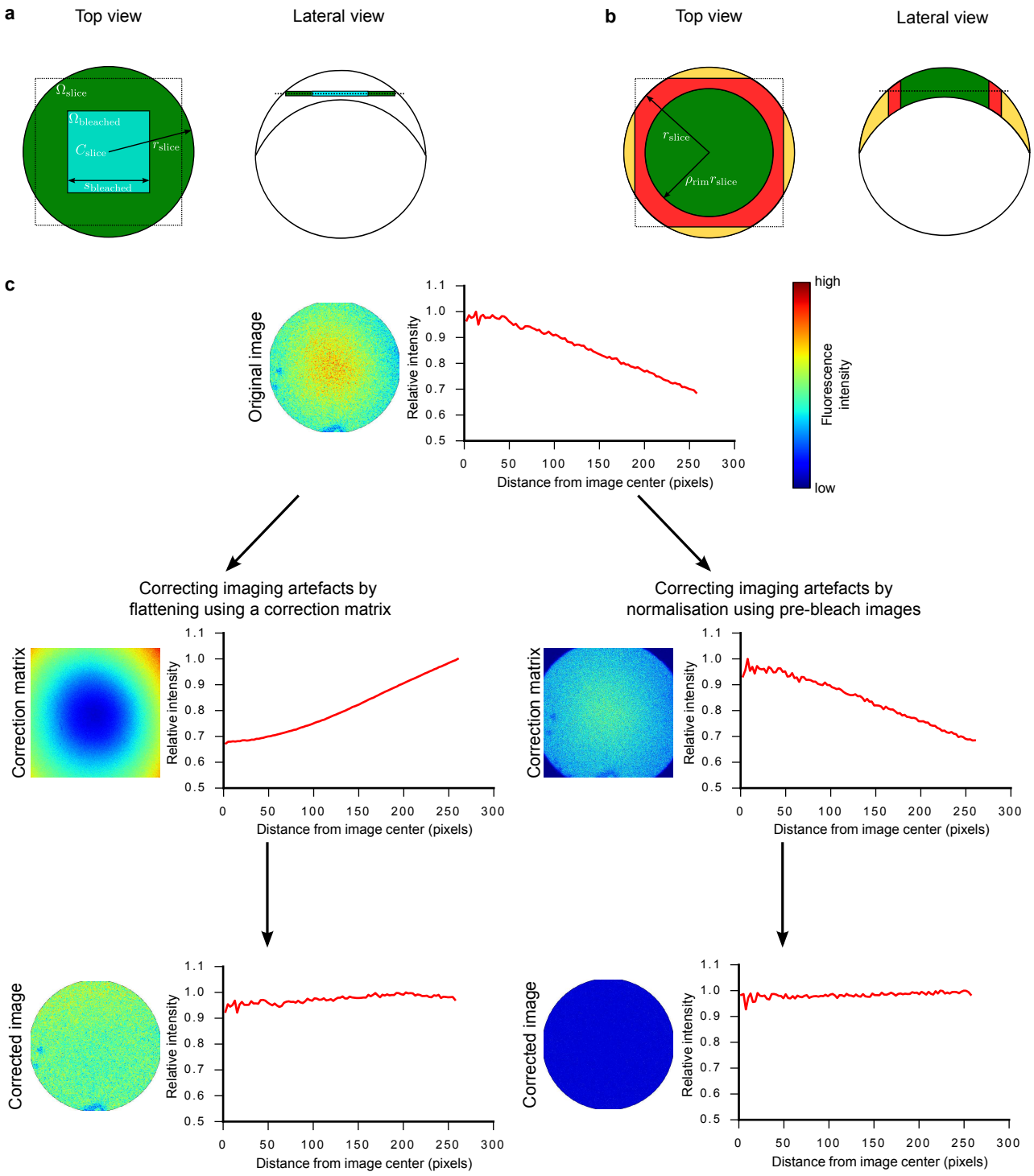

Supplementary Figure 2 | Image analysis in PyFRAP. (a) Basic regions of interest (ROIs) of FRAP analysis: The cyan square indicates the bleached region of the FRAP experiment inside the complete circular geometry within the imaging slice. The dashed lines indicate the location of the acquired image data. **(b)** Rim concentration calculation: Hypothetical data (orange) outside the acquired image (dashed line) is extrapolated through the average concentration in a slim rim of the visible fraction in the imaging slice (red). **(c)** Image manipulation techniques used to correct uneven illumination: Correction was either performed by multiplying the data with a correction matrix (flattening), or by dividing the data through an average pre-bleach image (normalisation). The original image shows a pre-bleach measurement of a uniformly distributed fluorophore. Deviations from the theoretical flat intensity profile are due to imaging artefacts.

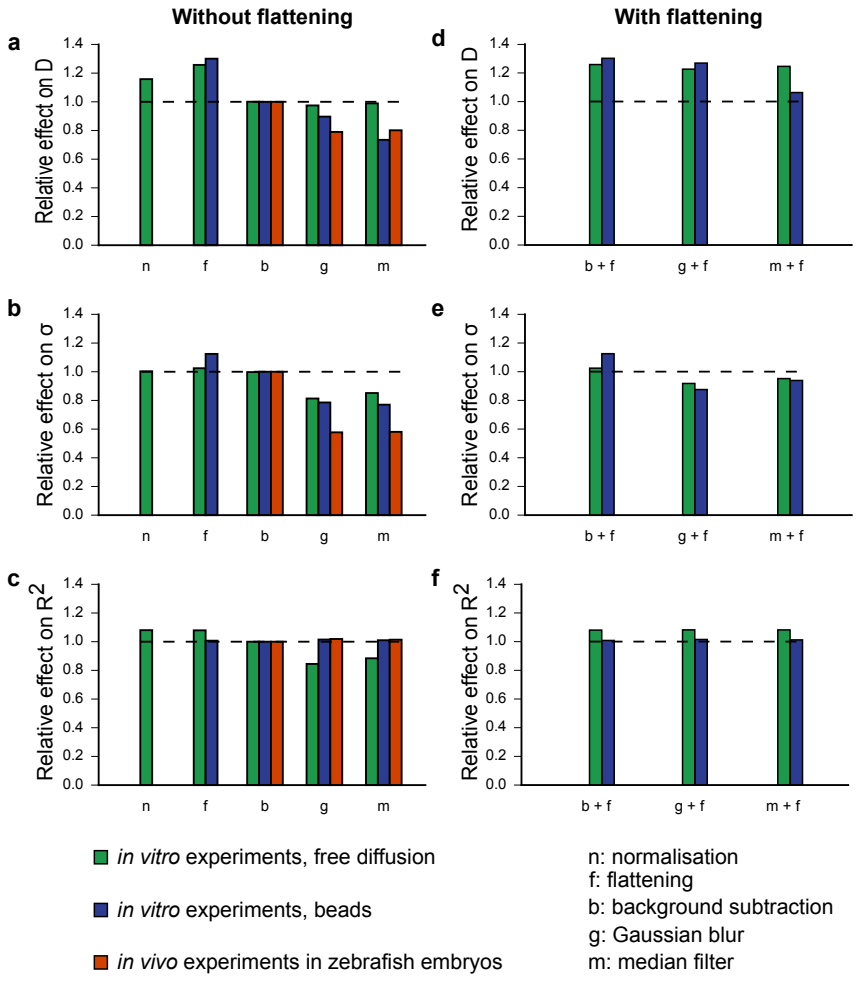

Supplementary Figure 3 | Analysis subset of image correction and smoothing techniques. Data sets were grouped by condition (*in vitro* experiments with free diffusion (green), *in vitro* experiments with beads (blue), and *in vivo* experiments in zebrafish embryos (orange)). Bar plots show the effect of each manipulation (n: normalisation, f: flattening, b: background subtraction, g: Gaussian blur, m: median filter) compared to analyses in which no manipulation was applied. Values above or below the dashed line indicate that the manipulation had an effect. **(a,b,c)** Effect on mean diffusion coefficient D, standard deviation σ, and R^2-value if only one of the five image manipulation techniques was applied, respectively. **(e,d,f)** Effect if flattening and one of the three remaining manipulation techniques was applied. *In vivo* experiments with zebrafish embryos were excluded for this analysis (see Supplementary Note 1 for details).

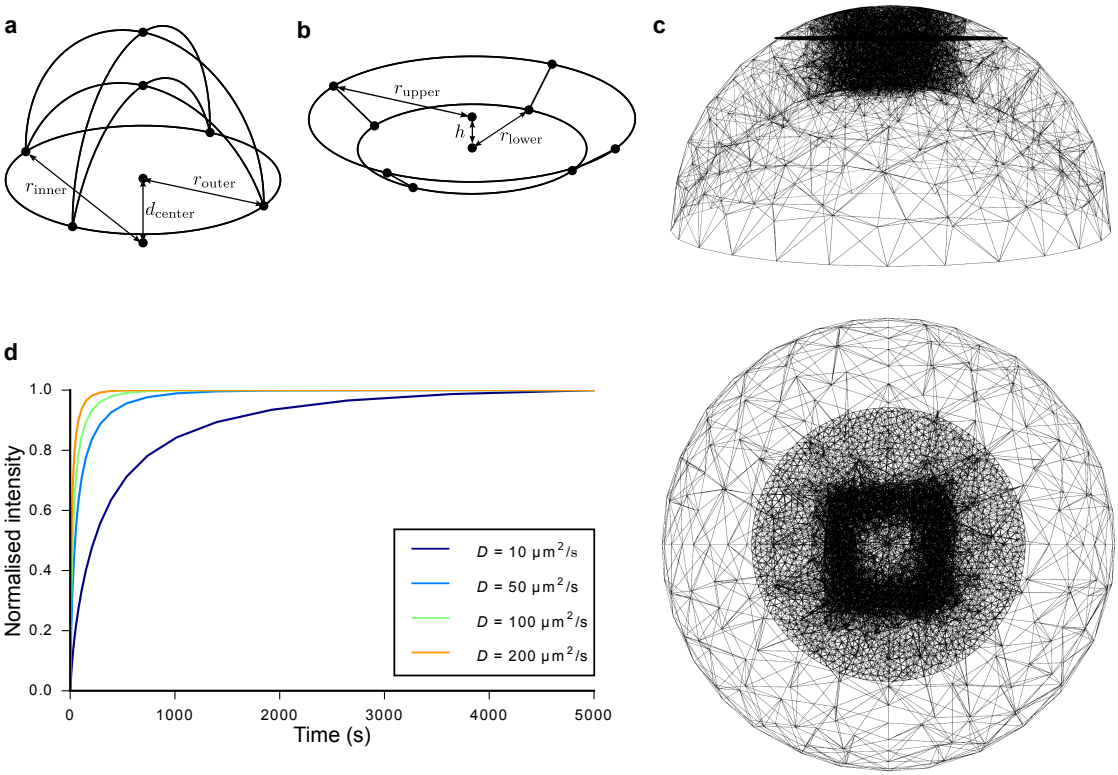

Supplementary Figure 4 | Simulation details for PyFRAP analysis. (a) The zebrafish dome geometry used to analyse *in vivo* experiments is described by the distance between the centers (d_{center}) and the radii (r_{inner}, r_{outer}) of two hemispheres. **(b)** The frustum geometry used to analyse *in vitro* experiments is described by the upper (r_{upper}) and lower (r_{lower}) radius and its height h. **(c)** Lateral and top views of tetrahedral meshes in the zebrafish dome geometry with a boundary layer mesh around the bleached area and a refined mesh in the imaging slice. **(d)** Scaling solution of a simulated FRAP recovery curve for different diffusion coefficients.

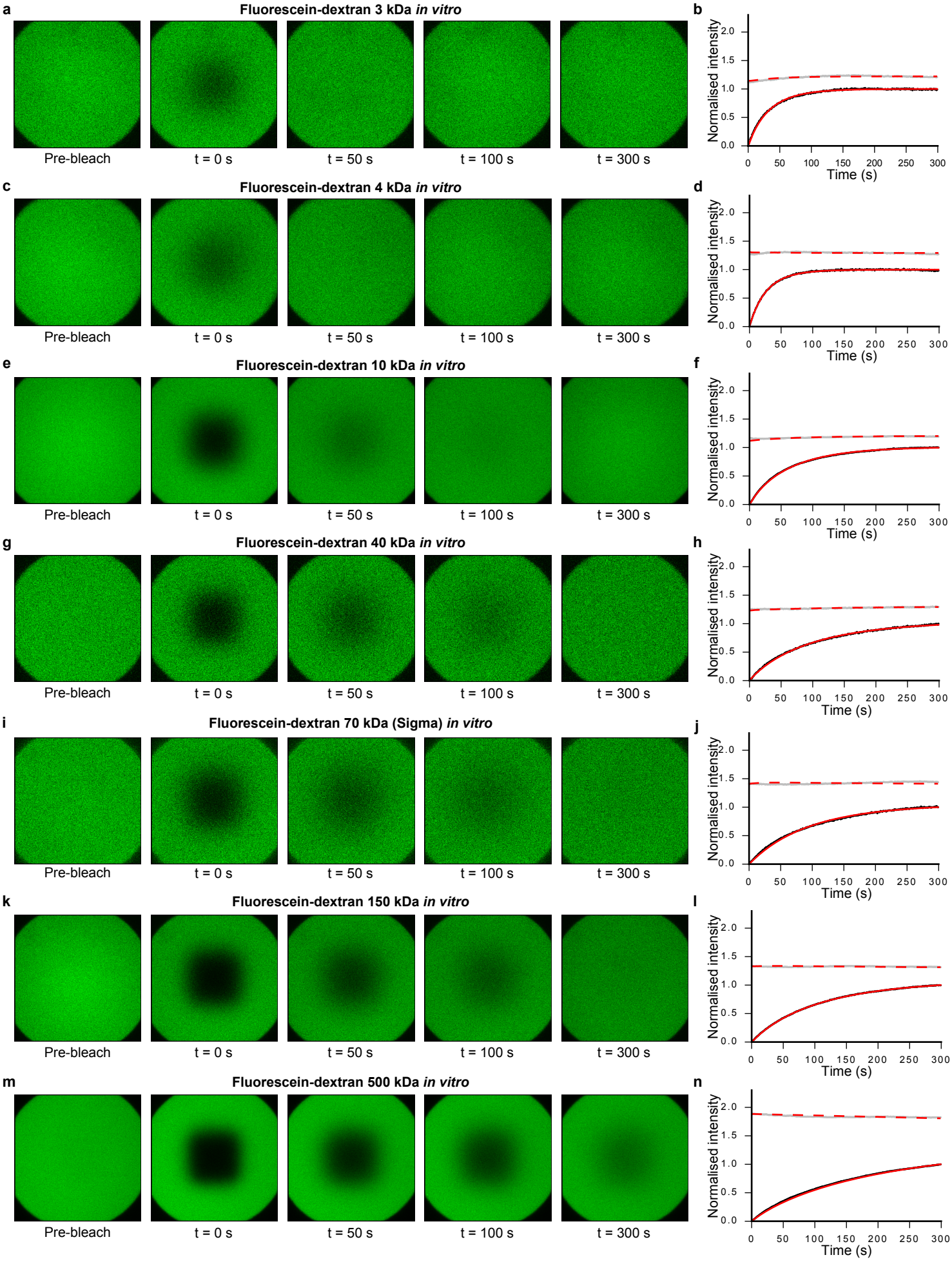

Supplementary Figure 5 | Examples of *in vitro* experiments and the resulting fits to measure free diffusion. (a,c,e,g,i,k,m) *In vitro* FRAP experiments with FITC-dextrans ranging from 3 kDa to 500 kDa. Maximum image intensities are the average pre-conversion intensities to facilitate comparison across data sets. **(b,d,f,h,j,l,n)** Black and grey dots represent data points of bleached and slice ROI, respectively. Red solid and dashed lines show the respective fits. Recovery curves were normalised between 0 (intensity in the bleached ROI at the first post-bleach time point) and 1 (intensity in the bleached ROI at the last post-bleach time point) to facilitate comparison across data sets.

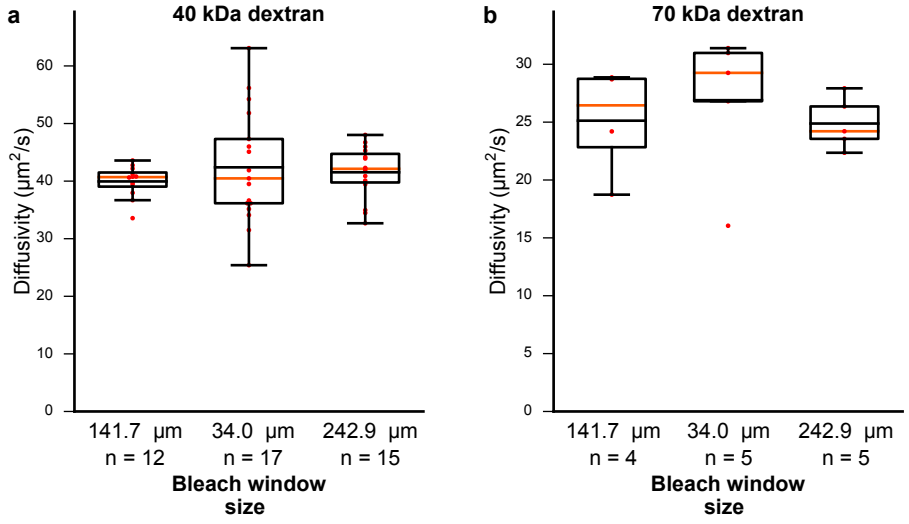

Supplementary Figure 6 | Different bleach window sizes do not affect diffusion coefficient estimates. (a) Results of control experiments with fluorescent dextran (40 kDa) for differently sized bleach windows. **(b)** Results of control experiments with fluorescent dextran (70 kDa) for differently sized bleach windows. Box plots in (a) and (b) show median (orange line), mean (black line), 25% quantiles (box), and all included data points (red markers). Whiskers extend to the smallest data point within the 1.5 interquartile range of the lower quartile, and to the largest data point within the 1.5 interquartile range of the upper quartile.

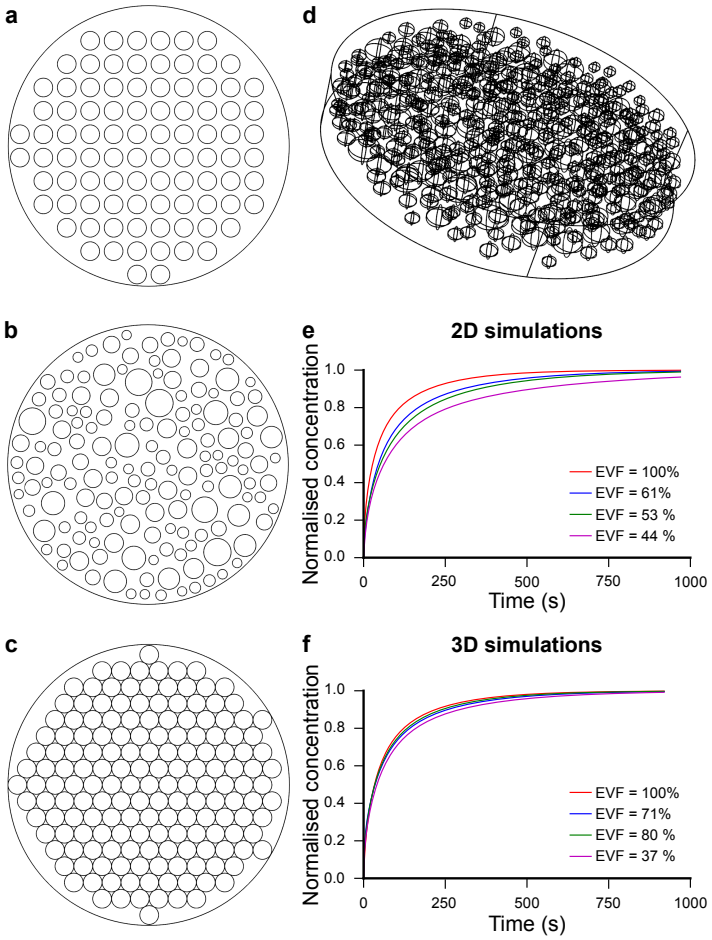

Supplementary Figure 7 | Simulations of tortuous environments in bead experiments. (a,b,c) Regularly (EVF = 59%), randomly (EVF = 56%), and ideally (EVF = 25%) placed beads in a two-dimensional circular domain. **(d)** Randomly (EVF = 78%) placed beads in a three-dimensional cylindrical domain. **(e,f)** Comparison between recovery curves in 2D and 3D bead simulations. Red lines indicate simulations without beads, blue lines indicate simulations with regularly placed beads, green lines indicate simulations with randomly placed beads, and magenta lines indicate simulations with ideally placed beads.

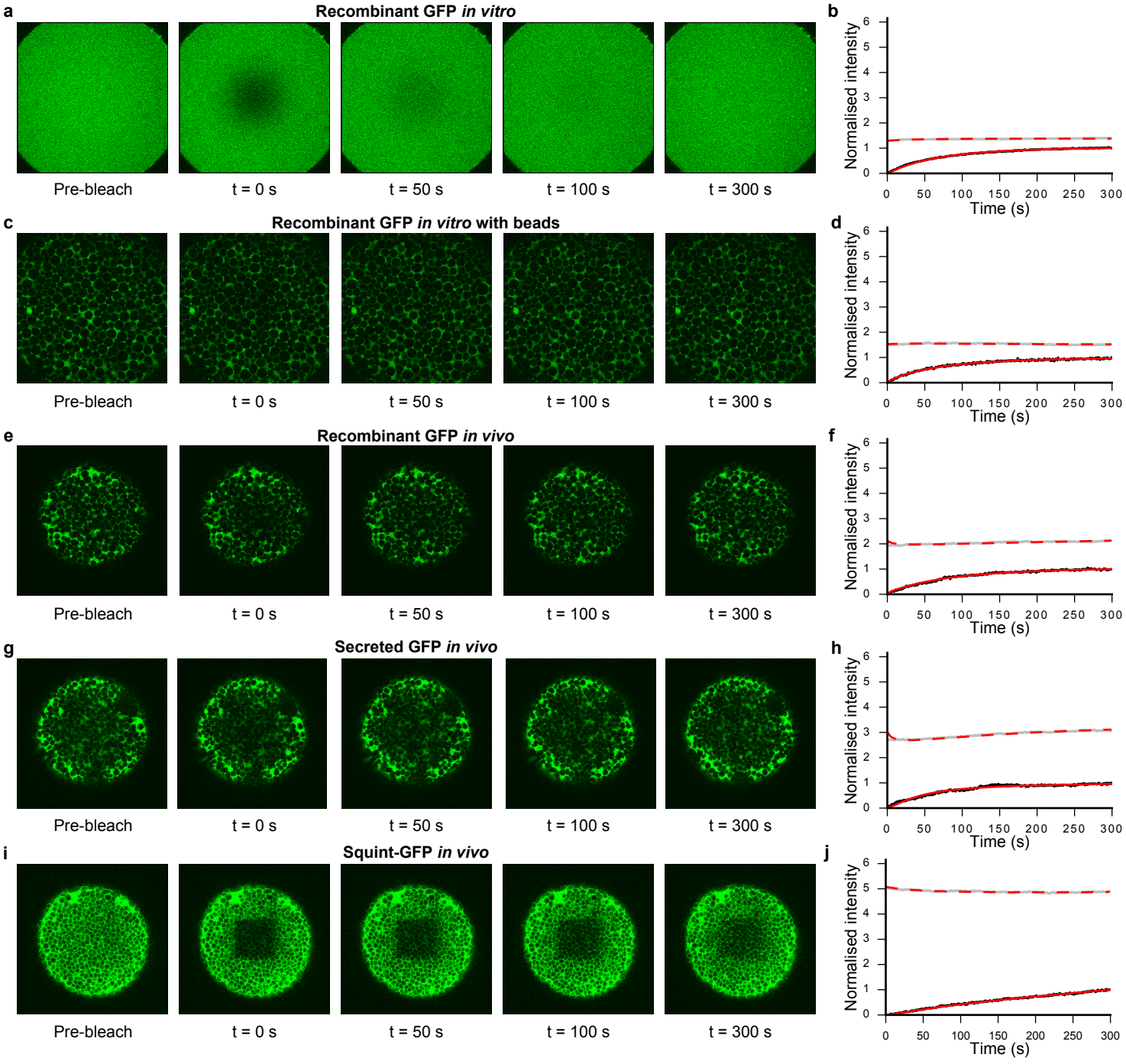

Supplementary Figure 8 | Examples of *in vitro* and *in vivo* experiments and the resulting fits. (a,b) *In vitro* FRAP experiment with recombinant GFP. **(c,d)** *In vitro* FRAP experiment with recombinant GFP mixed with polyacrylamide beads. **(e,f,g,h,i,j)** *In vivo* FRAP experiment in zebrafish embryos with recombinant GFP, secreted GFP, and Squint-GFP, respectively. **(b,d,f,h,j)** Black and grey dots represent data points of bleached and slice ROI, respectively. Red solid and dashed lines show the respective fits. Recovery curves were normalised between 0 (intensity in the bleached ROI at the first post-bleach time point) and 1 (intensity in the bleached ROI at the last post-bleach time point) to facilitate comparison across data sets.

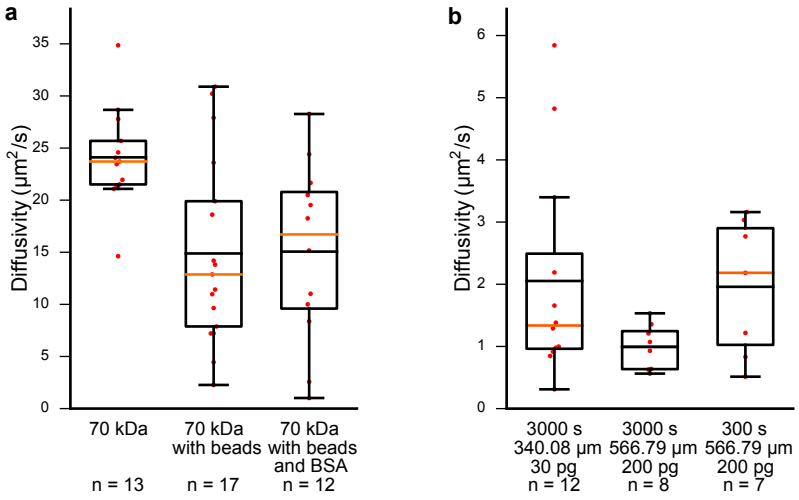

Supplementary Figure 9 | Results of control experiments for *in vitro* and *in vivo* FRAP experiments. (a) Results of control experiments with fluorescent dextran (70 kDa), and beads with or without BSA. BSA does not influence the diffusion of the fluorescent dextran. **(b)** Results of control experiments for different amounts (30 - 200 pg) of injected *Squint-GFP* mRNA, varying length of experiments (300 - 3000 s) and magnification (image size: 340.08 - 566.79 µm). Different imaging settings do not affect the measured diffusion coefficient of Squint-GFP. Box plots in (a) and (b) show median (orange line), mean (black line), 25% quantiles (box), and all included data points (red markers). Whiskers extend to the smallest data point within the 1.5 interquartile range of the lower quartile, and to the largest data point within the 1.5 interquartile range of the upper quartile.

Supplementary References

1. Rapsomaniki, M. A. *et al.* EasyFRAP: An interactive, easy-to-use tool for qualitative and quantitative analysis of FRAP data. *Bioinformatics* **28,** 1800–1801 (2012).
2. Miura, K. *FrapCalc* (accessed: 2016-12-12). `http://wiki.cmci.info/downloads/frap_analysis` (2016).
3. Schaff, J. C., Cowan, A. E., Loew, L. M. & Moraru, I. I. Virtual FRAP - an experiment-oriented simulation tool. *Biophysical Journal* **96,** 30a (2009).
4. Blumenthal, D., Goldstien, L., Edidin, M. & Gheber, L. A. Universal approach to FRAP analysis of arbitrary bleaching patterns. *Scientific Reports* **5,** 11655 (2015).
5. Müller, P. *et al.* Differential diffusivity of Nodal and Lefty underlies a reaction-diffusion patterning system. *Science* **336,** 721–724 (2012).
6. Müller, P., Rogers, K. W., Yu, S. R., Brand, M. & Schier, A. F. Morphogen transport. *Development* **140,** 1621–1638 (2013).
7. Pomreinke, A. P. *et al.* Dynamics of BMP signaling and distribution during zebrafish dorsal-ventral patterning. *Elife* **6,** e25861 (2017).
8. Sprague, B. L., Pego, R. L., Stavreva, D. A. & McNally, J. G. Analysis of binding reactions by Fluorescence Recovery After Photobleaching. *Biophysical Journal* **86,** 3473–3495 (2004).
9. Hrabe, J., Hrabetová, S. & Segeth, K. A model of effective diffusion and tortuosity in the extracellular space of the brain. *Biophysical Journal* **87,** 1606–1617 (2004).
10. Tao, L. & Nicholson, C. Maximum geometrical hindrance to diffusion in brain extracellular space surrounding uniformly spaced convex cells. *Journal of Theoretical Biology* **229,** 59–68 (2004).
11. Novak, I. L., Kraikivski, P. & Slepchenko, B. M. Diffusion in cytoplasm: Effects of excluded volume due to internal membranes and cytoskeletal structures. *Biophysical Journal* **97,** 758–767 (2009).
12. Donovan, P., Chehreghanianzabi, Y., Rathinam, M. & Zustiak, S. P. Homogenization theory for the prediction of obstructed solute diffusivity in macromolecular solutions. *PLoS ONE* **11,** e0146093 (2016).
13. Student. The probable error of a mean. *Biometrika* **6,** 1–25 (1908).
14. Welch, B. L. The generalisation of Student's problems when several different population variances are involved. *Biometrika* **34,** 28–35 (1947).
15. Wilcoxon, F. Individual comparisons by ranking methods. *Biometrics Bulletin* **1,** 80–83 (1945).
16. Mann, H. B. & Whitney, D. R. On a test of whether one of two random variables is stochastically larger than the other. *The Annals of Mathematical Statistics* **18,** 50–60 (1947).
17. Shapiro, S. S. & Wilk, M. B. An analysis of variance test for normality (complete samples). *Biometrika* **52,** 591–611 (1965).
18. Akaike, H. A new look at the statistical model identification. *IEEE Transactions on Automatic Control* **19,** 716–723 (1974).
19. Aaron, J. *FRAP* (accessed: 2016-12-12). `https://de.mathworks.com/matlabcentral/fileexchange/47327-frap-zip` (2016).
20. Kraft, L. J., Dowler, J. & Kenworthy, A. K. *Frap-Toolbox: Software for the analysis of Fluorescence Recovery After Photobleaching* (accessed: 2016-12-12). `http://www.fraptoolbox.com` (2014).

21. Ulrich, M. *et al.* Tropical-parameter estimation and simulation of reaction-diffusion models based on spatio-temporal microscopy images. *Bioinformatics* **22,** 2709–2710 (2006).

22. Zhang, Z., Nadezhina, E. & Wilkinson, K. J. Quantifying diffusion in a biofilm of Streptococcus mutans. *Antimicrobial Agents and Chemotherapy* **3,** 1075–1081 (2011).

23. Pluen, A., Netti, P. A., Jain, R. K. & Berk, D. A. Diffusion of macromolecules in agarose gels: Comparison of linear and globular configurations. *Biophysical Journal* **1,** 542–552 (1999).

24. Guiot, E. *et al.* Molecular dynamics of biological probes by Fluorescence Correlation Microscopy with two-photon excitation. *Journal of Fluorescence* **4,** 413–419 (2000).

25. Braga, J., Desterro, J. M. & Carmo-Fonseca, M. Intracellular macromolecular mobility measured by Fluorescence Recovery After Photobleaching with confocal laser scanning microscopes. *Molecular Biology of the Cell* **15,** 4749–4760 (2004).

26. Periasamy, N. & Verkman, A. Analysis of fluorophore diffusion by continuous distributions of diffusion doefficients: application to photobleaching measurements of multicomponent and anomalous diffusion. *Biophysical Journal* **1,** 557–567 (1998).

27. Schuster, E., Hermansson, A. M., Öhgren, C., Rudemo, M. & Lorén, N. Interactions and diffusion in fine-stranded β-lactoglobulin gels determined via FRAP and binding. *Biophysical Journal* **1,** 253–262 (2014).

28. Gendron, P. O., Avaltroni, F. & Wilkinson, K. J. Diffusion coefficients of several rhodamine derivatives as determined by pulsed field gradient-nuclear magnetic resonance and Fluorescence Correlation Spectroscopy. *Journal of Fluorescence* **6,** 1093–1101 (2008).

29. Visser, N. V., Hink, M. A., Hoek, A. V. & Visser, A. J. Comparison between Fluorescence Correlation Spectroscopy and time-resolved fluorescence anisotropy as illustrated with a fluorescent dextran conjugate. *Journal of Fluorescence* **3,** 251–255 (1999).

30. Kihara, T., Ito, J. & Miyake, J. Measurement of biomolecular diffusion in extracellular matrix condensed by fibroblasts using Fluorescence Correlation Spectroscopy. *PLoS ONE* **11** (2013).

31. Peters, R. Nucleo-cytoplasmic flux and intracellular mobility in single hepatocytes measured by fluorescence microphotolysis. *The EMBO Journal* **8,** 1831–6 (1984).

32. Lang, I., Scholz, M. & Peters, R. Molecular mobility and nucleocytoplasmic flux in hepatoma cells. *Journal of Cell Biology* **4,** 1183–1190 (1986).

33. Gribbon, P. & Hardingham, T. E. Macromolecular diffusion of biological polymers measured by confocal Fluorescence Recovery After Photobleaching. *Biophysical Journal* **2,** 1032–1039 (1998).

34. Gorisch, S. M. Histone acetylation increases chromatin accessibility. *Journal of Cell Science* **24,** 5825–5834 (2005).

35. Keminer, O. & Peters, R. Permeability of single nuclear pores. *Biophysical Journal* **1,** 217–228 (1999).

36. Floury, J., Madec, M. N., Waharte, F., Jeanson, S. & Lortal, S. First assessment of diffusion coefficients in model cheese by Fluorescence Recovery After Photobleaching (FRAP). *Food Chemistry* **2,** 551–556 (2012).

37. Arrio-Dupont, M., Cribier, S., Foucault, G., Devaux, P. & D'Albis, A. Diffusion of fluorescently labeled macromolecules in cultured muscle cells. *Biophysical Journal* **5,** 2327–2332 (1996).

38. Terry, B., Matthews, E. & Haseloff, J. Molecular characterization of recombinant green fluorescent protein by Fluorescence Correlation Microscopy. *Biochemical and Biophysical Research Communications* **1,** 21–27 (1995).

39. Swaminathan, R., Hoang, C. & Verkman, A. Photobleaching recovery and anisotropy decay of green fluorescent protein GFP-S65T in solution and cells: cytoplasmic viscosity probed by green fluorescent protein translational and rotational diffusion. *Biophysical Journal* **4,** 1900–1907 (1997).

40. Gulot, E. *et al.* Heterogeneity of diffusion inside microbial biofilms determined by Fluorescence Correlation Spectroscopy under two-photon excitation. *Photochemistry and Photobiology* **6,** 570–8 (2002).

41. Müller, K. P. *et al.* Multiscale analysis of dynamics and interactions of heterochromatin protein 1 by fluorescence fluctuation microscopy. *Biophysical Journal* **11,** 2876–2885 (2009).

42. Waharte, F., Steenkeste, K., Briandet, R. & Fontaine-Aupart, M. P. Diffusion measurements inside biofilms by image-based Fluorescence Recovery After Photobleaching (FRAP) analysis with a commercial confocal laser scanning microscope. *Applied and Environmental Microbiology* **17,** 5860–5869 (2010).

43. Braeckmans, K., Peeters, L., Sanders, N. N., De Smedt, S. C. & Demeester, J. Three-dimensional Fluorescence Recovery After Photobleaching with the confocal scanning laser microscope. *Biophysical Journal* **4,** 2240–2252 (2003).

Appendix 3

Chapter 6

FRAP Analysis of Extracellular Diffusion in Zebrafish Embryos

Gary H. Soh and Patrick Müller

Abstract

Morphogens are signaling molecules that provide positional information to cells during development. They must move through embryonic tissues in order to coordinate patterning. The rate of a morphogen's movement through a tissue—its effective diffusivity—affects the morphogen's distribution and therefore influences patterning. Fluorescence recovery after photobleaching (FRAP) is a powerful method to measure the effective diffusion of molecules through cells and tissues, and has been successfully employed to examine morphogen mobility and gain important insights into embryogenesis. Here, we provide detailed protocols for FRAP assays in vitro and in living zebrafish embryos, and we explain how to analyze FRAP data using the open-source software PyFRAP to determine effective diffusion coefficients.

Key words Fluorescence Recovery After Photobleaching, FRAP, Zebrafish, Morphogens, Extracellular signaling molecules, Developmental biology

1 Introduction

Gradients of signaling molecules known as morphogens have long been proposed to direct the formation of tissues during embryogenesis by providing positional information [1, 2]. In the classical model of morphogen-mediated patterning, morphogens diffuse from localized morphogen-producing source cells into the surrounding tissue to form concentration gradients [3, 4]. Morphogen mobility has been demonstrated to be crucial in several patterning contexts. For example, hindering the mobility of the secreted morphogen Dpp abolishes its ability to pattern developing *Drosophila* wings [5]. Differences in the mobility of extracellular signaling molecules are also thought to be important in patterning processes. During zebrafish germ layer patterning, poorly diffusive Nodal signals form short-range gradients that induce and pattern endoderm and mesoderm, whereas Nodal signaling is antagonized by highly diffusive Leftys to allow ectoderm formation [6, 7]. Similarly, the diffusion of BMP and its antagonist Chordin is critical to

Julien Dubrulle (ed.), *Morphogen Gradients: Methods and Protocols*, Methods in Molecular Biology, vol. 1863,
https://doi.org/10.1007/978-1-4939-8772-6_6,

pattern the dorsal–ventral axis during zebrafish development, and recent measurements of BMP and Chordin diffusion coefficients clarified the mechanism by which gradients of these proteins are established [7–9]. Therefore, measuring the mobility of signaling molecules is crucial to understand the dynamics of the biological processes they control.

Fluorescence Recovery After Photobleaching (FRAP) assays were developed more than 40 years ago [10, 11] and have been used extensively to assess the diffusion of molecules in living cells and tissues [12]. FRAP experiments measure effective diffusion, which takes into account diffusion hindrance by geometrical obstacles in the tissue as well as interactions with binding partners. Such interactions can significantly slow down the movement of diffusing molecules, and effective diffusion coefficients are typically smaller than the molecules' free unhindered diffusivities [2]. In FRAP assays, fluorescent molecules are bleached in a selected region by exposure to a strong laser pulse, and the movement of unbleached molecules from surrounding areas into the bleached region is recorded by quantitative time lapse microscopy (Fig. 1). The faster the fluorescent molecules diffuse, the faster the bleached region regains fluorescence (Fig. 1a, b). The average intensity within the bleached region over time is calculated from the images, and mathematical models of diffusive processes are fitted to the data to determine the diffusivity of the fluorescent molecules. Since the bleached region can be tailored to different samples, FRAP can be used to measure effective diffusion in complex tissues of many shapes and sizes, including those undergoing morphogen-mediated patterning [2, 6, 13–15].

Here, we provide detailed protocols and data analysis methods for FRAP experiments to measure the effective diffusivity of extracellular molecules in living zebrafish embryos at blastula stages. To ensure accurate measurements, two controls are crucial. First, a linear relationship between fluorophore concentration and intensity must be established because analysis methods assume that a change in fluorescence intensity is due to a proportional change in fluorophore concentration. Second, the ability of the experimental system to accurately determine diffusivities should be validated using an in vitro system with a defined geometry and fluorescent molecules of known diffusion coefficients.

Once the accuracy of the experimental setup has been confirmed, in vivo measurements of extracellular diffusion can be executed. In addition to explaining how to carry out FRAP experiments, we describe how to use the versatile, open-source software PyFRAP [16] to process raw images and compute diffusion coefficients. PyFRAP interpolates the first postbleach image onto a three-dimensional mesh approximating the shape of the sample for numerical simulations of fluorescence recovery. This allows the software to properly account for sample geometry and potential

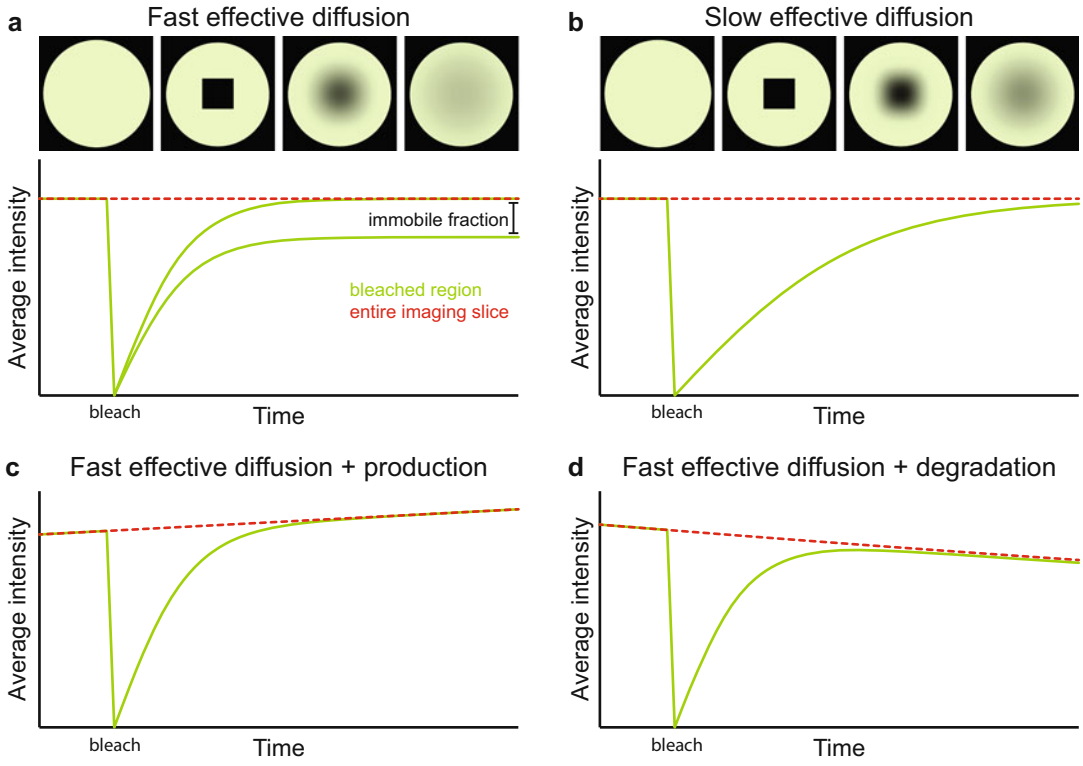

Fig. 1 Overview of Fluorescence Recovery After Photobleaching (FRAP) experiments to measure extracellular diffusion in zebrafish embryos. (**a**) Schematic of a FRAP experiment with a highly diffusive secreted molecule. A cross-section ("imaging slice") through the zebrafish blastoderm is shown. Fluorescence in embryos uniformly expressing a secreted signaling molecule (light green) is bleached (black square), and average fluorescence intensities in the bleached region (green line) and in the entire imaging slice (red dashed line) are monitored. Failure of the curves describing intensity changes in the bleached region and in the entire imaging slice to converge at long time scales is indicative of an immobile fraction that cannot recover by diffusion [6]. (**b**) Schematic of a FRAP experiment with a poorly diffusive molecule. The recovery is slower than in panel (**a**). (**c** and **d**) Schematic of FRAP experiments with a highly diffusive molecule that continues to be produced (**c**) or that is significantly degraded (**d**) throughout the experiment

experimental artifacts discussed in detail below. The solution from the numerical simulation is then fitted to the experimental data. Additional reaction kinetics such as production or degradation (Fig. 1c, d) can also be taken into account to compute accurate effective diffusion coefficients.

2 Materials

2.1 Molecules for Fluorescent Samples

1. Recombinant green fluorescent protein (GFP, diffusion coefficient $D = 96 \pm 2\ \mu m^2/s$ [16]).
2. Solid bovine serum albumin (BSA).

3. Fluorescein-coupled dextrans with known diffusivities and with excitation–emission spectra similar to the fluorescent protein to be analyzed (*see* **Note 1**).
4. mRNA encoding a fluorescently tagged secreted protein (*see* **Note 2**).

2.2 Embryo Manipulation

1. Glass pipettes with flame-polished tips (*see* **Note 3**).
2. Pipette pump (*see* **Note 3**).
3. Dissection needle or eyelash glued to a glass pipette (*see* **Note 4**).
4. E3 medium: 5.03 mM NaCl, 0.17 mM KCl, 0.33 mM $CaCl_2$, 0.33 mM $MgSO_4$, 0.1% (w/v) methylene blue [17].
5. 6-well tissue culture plates coated with 2% agarose in E3 medium.
6. Microinjection apparatus with a micrometer calibration slide (*see* **Note 5**).
7. 5 mg/mL pronase dissolved in E3 medium.
8. Microinjection dish to hold embryos during microinjection (described in The Zebrafish Book [18], https://zfin.org/zf_info/zfbook/chapt5/5.1.html).
9. Binocular dissection stereomicroscope for manipulating and orienting embryos.
10. Small glass petri dish for pronase-mediated embryo dechorionation. The glass petri dish has to be small enough to fit into a 200 mL glass beaker.
11. 200 mL glass beaker for washing dechorionated embryos.
12. Incubator set to a temperature of 28 °C to incubate zebrafish embryos.

2.3 Imaging

1. 35 mm uncoated glass bottom microscopy dishes, No. 1.5 Coverslip, 10 mm glass diameter.
2. Rectangular coverslips, 60 mm × 24 mm, No. 1.5, 0.17 mm thickness.
3. Square coverslips, 24 mm × 24 mm.
4. Transparent plastic block (*see* **Note 6**), approximately 2.7 cm × 1.5 cm × 3 mm (Fig. 2). Create a small well in the center ~700 μm in diameter and ~100 μm in depth with a dental drill such as the Gates Glidden drill #2.
5. Heavy mineral oil.
6. E3 medium without methylene blue: 5.03 mM NaCl, 0.17 mM KCl, 0.33 mM $CaCl_2$, 0.33 mM $MgSO_4$ [17].
7. Molten 1% low melting point agarose in E3 medium in a 1.5 mL microcentrifuge tube.

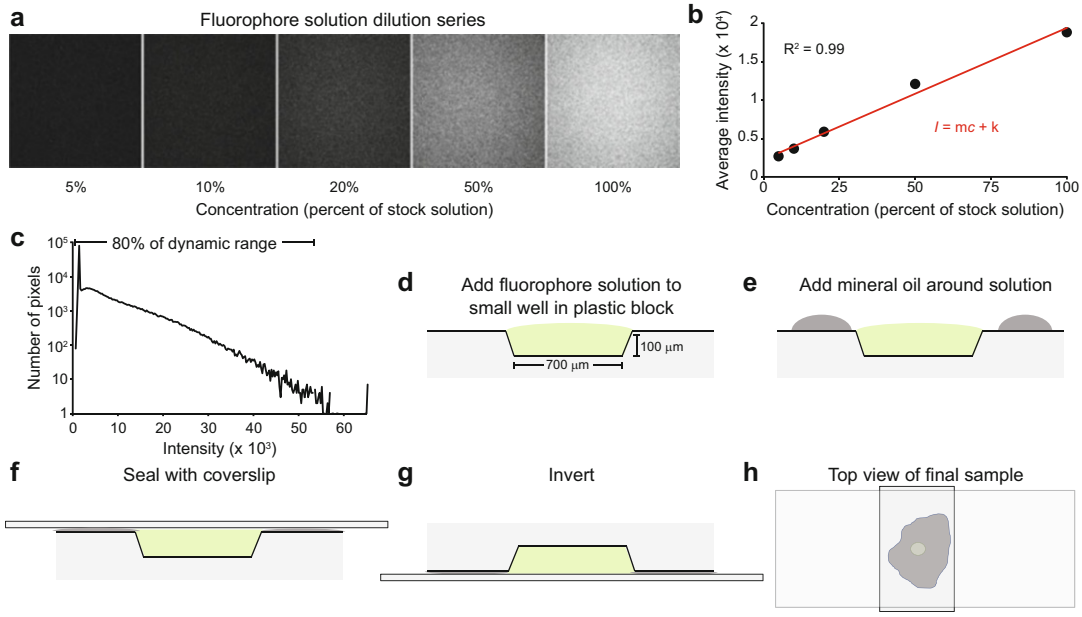

Fig. 2 FRAP control experiments. (**a**–**c**) Dilution series to determine whether the relationship between fluorescence intensity and fluorophore concentration is linear. (**a**) A dilution series (5%, 10%, 20%, 50%, 100%) is made from a fluorescent dextran solution that produces similar intensity as in vivo samples with the selected confocal microscope settings for in vivo FRAP. The images show fluorescence intensities of a 70 kDa fluorescein-labeled dextran dilution series made from a 25 µg/mL stock solution (= 100%, corresponding to a concentration of 360 nM). (**b**) The average intensities of the images are then measured (e.g., using Fiji [19]) and plotted against the fluorophore concentration. This should yield a linear fit (red) with an R^2 value of at least 0.9. (**c**) The optimal signal of the stock solution should fill about 75–80% of the 16-bit dynamic range of the confocal microscope settings with similar intensity as the in vivo sample. (**d**–**h**) In vitro FRAP experiments using molecules with previously measured diffusion coefficients. (**d**) Well geometry for in vitro experiments and FRAP sample preparation. First, the fluorophore solution is pipetted into the plastic block well. (**e**) Mineral oil is pipetted around the well, so that it completely surrounds the well. (**f**) A rectangular coverslip is then placed over the well. The fluorescent solution must remain completely surrounded by the mineral oil after the coverslip has been placed. (**g**) Invert the sample for imaging on an inverted confocal microscope. (**h**) Schematic of the final sample preparation

8. Heat block at 42 °C for molten agarose (place next to dissection stereomicroscope).
9. Inverted confocal microscope system with lasers and filters appropriate for the fluorophore to be imaged (*see* **Note 7**).

2.4 Analysis Software

1. PyFRAP [16]. Download the free Python-based software from https://mueller-lab.github.io/PyFRAP.
2. Fiji [19]. Download the commonly used free software for biological image processing from https://fiji.sc/#download.

3 Methods

All procedures are carried out at room temperature.

3.1 Control Experiments

3.1.1 Test of Confocal Microscope Settings

Before executing a FRAP experiment, it is crucial to confirm a linear relationship between the detected intensity and concentration of a fluorescent solution over a wide range of input concentrations (Fig. 2a–c). This ensures that the intensity measured by the microscope corresponds to the concentration of the fluorophore.

1. Prepare a dilution series of a fluorescent dextran with excitation-emission spectra similar to the fluorescent protein to be analyzed at concentrations of 90, 180, 360, and 720 nM.
2. Pipette 2 μL of the dextran solution onto the center of a rectangular coverslip, and then place a square coverslip over it.
3. Image the solutions with the confocal settings to be used for the in vivo FRAP experiments. Important parameters are the laser power, the detector gain, and offset. These settings will depend on the fluorescence intensity of the sample as well as the microscope (*see* **step 4** in Subheading 3.2.2).
4. Determine the concentration that yields a signal filling about 75–80% of the 16-bit dynamic range of the selected confocal microscope settings (Fig. 2c) with similar intensity as the in vivo sample (*see* Subheading 3.2).
5. Using that concentration, prepare a 2×, 5×, 10×, and 20× dilution series of the solution (Fig. 2a). For example, if the concentration determined in **steps 1–4** is 360 nM, prepare 180, 72, 36, and 18 nM dilutions.
6. Image the solutions generated in **step 5** (Fig. 2a) and measure their average fluorescence intensities. Fluorescence intensity can be measured with Fiji [19]. Open the image and go to Edit → Selection → Select All, then Analyze → Measure.
7. Plot average intensity against concentration and fit a linear trend line to the data using the equation $I = mc + k$, where I is the fluorescence intensity, m is the slope, c is the concentration, and k the background fluorescence (Fig. 2b). This can be done for example in Excel: Organize the data in columns, then select Insert → Scatter. Go to Layout → Trendline → Format trendline, and select "*Linear*" and "*Display R-squared value on chart*." Generally, an R^2 value larger than 0.9 indicates a good fit.
8. If the linear equation fits the data well (R^2 value >0.9), then the imaging settings are appropriate. If the intensity values plateau at high or low concentrations, the signal is too strong or too weak, respectively. To address this problem, adjust the microscope settings or change the amount of injected mRNA for in vivo FRAP experiments (*see* Subheading 3.2).

3.1.2 In Vitro FRAP Sample Preparation

After establishing a linear relationship between fluorophore concentration and intensity, in vitro control experiments using molecules with known diffusion coefficients (*see* **Note 1**) in a defined geometry can be used to validate the experimental setup (Fig. 2d–h). Incorrect diffusion coefficients may indicate problems with the experimental setup.

1. Prepare aqueous solutions containing fluorescent molecules with known diffusion coefficients. When using a fluorescent protein (such as 4 μM recombinant GFP, *see* Subheading 2.1), add 5% bovine serum albumin (BSA, *see* **Note 8**). The BSA blocks potential protein binding sites in the plastic well. 100–500 nM solutions of fluorescein-labeled dextrans of different sizes can also be used to carry out the positive controls (*see* **Note 1**).
2. Place the plastic block with a small well on a dissection stereomicroscope.
3. Transfer 2 μL of fluorescent solution into the small well until it slightly flows over (Fig. 2d).
4. Pipette a few microliters of mineral oil in a donut shape around the small well, such that the oil completely surrounds the fluorophore solution (Fig. 2e). Leave a small gap between the mineral oil and the well (*see* **Note 9**).
5. Place a rectangular coverslip over the solution (Fig. 2f), such that the sides of the plastic block protrude (Fig. 2h) and it can be manually transported without moving the coverslip.
6. Carefully flip the plastic block over, so that the sample can be imaged on an inverted confocal microscope (Fig. 2g). The mineral oil should cause the coverslip and the plastic block to stick together via capillary action. If they fall apart, more mineral oil is needed.
7. Place the plastic block on the confocal microscope with the coverslip facing the objective (Fig. 2h).
8. Add immersion solution onto the objective. We use an LD LCI Plan-Apochromat 25×/0.8 NA Imm Korr DIC objective (Zeiss) and immersion oil (Immersol™ W, $n = 1.334$ at 23 °C, Zeiss).
9. *See* Subheading 3.2.2 for instructions on performing the FRAP experiment.

3.2 FRAP Measurements of Secreted Molecules In Vivo

3.2.1 Zebrafish Embryo Sample Preparation

1. Inject mRNA encoding the fluorescently tagged secreted molecule directly into the cell of zebrafish embryos at the one-cell stage, or inject purified recombinant fluorescent protein into the extracellular space of zebrafish embryos around high or dome stage [6, 20, 21]. The amount to be injected has to be empirically determined, but a good starting point is 30 pg of mRNA or 500 pg of fluorescent protein.
2. Incubate the injected zebrafish embryos at 28 °C until they reach oblong stage.
3. Proteolytically dechorionate the embryos in bulk by incubation in 10 mL of 1 mg/mL pronase in a glass petri dish for 7–10 min at room temperature (*see* **Note 10**). A movie of this procedure has been published recently [20]. Embryos can also be proteolytically dechorionated immediately before or after injection. Alternatively, embryos can be dechorionated manually using fine forceps.
4. Carefully pour the embryos into a 200 mL glass beaker filled with E3 medium.
5. Wait for the embryos to settle at the bottom of the glass beaker, and decant approximately 80% of the E3 medium without pouring out the embryos.
6. Rinse the embryos by pouring E3 medium into the side of the glass beaker until the beaker is nearly filled.
7. Repeat **steps 5** and **6**, then decant 80% of the E3 medium. This will cause the chorions to fall apart and release the embryos.
8. Using a flame-polished glass pipette connected to a pipette pump, transfer the embryos into a glass petri dish or an agarose-coated 6-well plate filled with E3 medium.
9. Using a glass pipette with a flame-polished tip, transfer a single zebrafish embryo into molten 1% low melting point agarose (LMA) incubated at 42 °C in a heat block (Fig. 3a) without carrying over a large amount of E3 medium into the LMA.
10. Quickly remove excess medium from the glass pipette.
11. With the same glass pipette, carefully pick up the zebrafish embryo along with some molten LMA (Fig. 3a) and place it on a glass bottom microscopy dish (Fig. 3a′).
12. Using a dissection needle (or an eyelash glued to a glass pipette) and a dissection stereomicroscope, carefully rotate the embryo so that the animal pole is pressed onto the glass bottom (Fig. 3a″). Ensure that the embryo maintains this position until the LMA solidifies (Fig. 3a‴).
13. Once the LMA is fully solidified, pour E3 medium without methylene blue onto the glass bottom dish to keep the agarose hydrated.

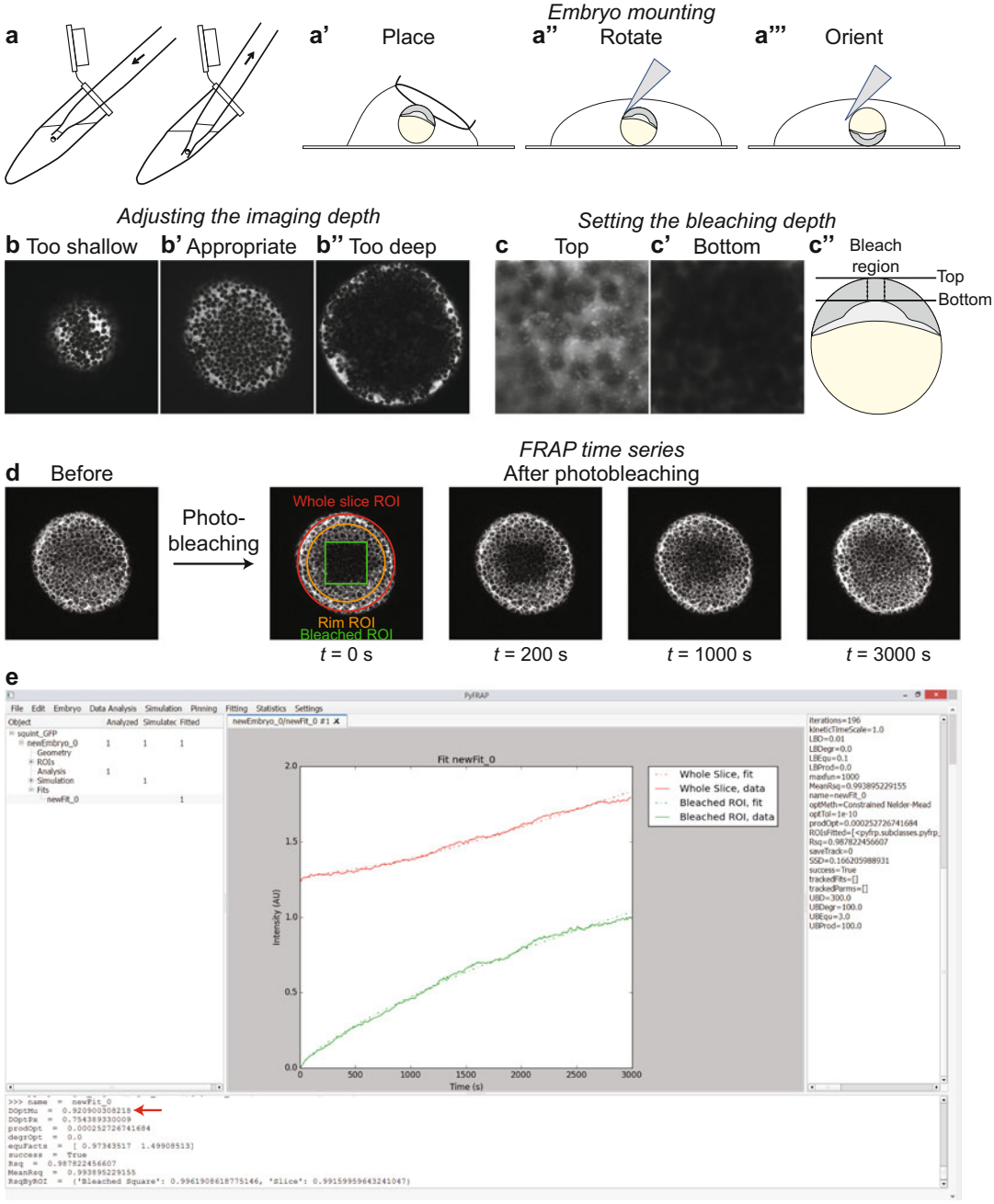

Fig. 3 FRAP experiments to measure effective extracellular diffusion in zebrafish embryos. (**a**) Mounting zebrafish embryos for FRAP experiments using an inverted confocal microscope. Use a glass pipette to submerge an embryo in molten 42 °C-warm low melting point agarose (LMA), then withdraw it along with some LMA. (**a**′) Place the embryo with molten LMA on a glass bottom microscopy dish. (**a**″) Position the embryo with a dissection needle, such that the animal pole (gray) is pressed against the glass. (**a**‴) Maintain the embryo in this position until the agarose solidifies. (**b** and **c**) Identifying optimal in vivo FRAP imaging settings. (**b**) Adjusting the imaging depth in a zebrafish embryo around dome stage expressing the fluorescently tagged signaling molecule Squint-GFP [6]. The imaging depth of the sample must not be too shallow

3.2.2 FRAP Experiment and Image Acquisition

Some microscope software has built-in FRAP settings to automatically execute the bleaching and subsequent image acquisition. For maximum flexibility independent of the microscope system, here we describe how to perform FRAP experiments without automated FRAP settings using a Zeiss LSM 780 confocal microscope.

1. Use the lowest magnification objective to find the sample and bring it into focus.
2. Switch to the objective with the desired magnification. We use a 25× objective because an entire zebrafish embryo fits in the field of view, but lower or higher magnifications can also be used depending on the size of the sample.
3. Adjust the confocal microscope settings by changing the laser power and detector gain. Start with a detector gain of 800 using the shortest pixel dwell time and laser power of 0.1%, and adjust the laser power (to a maximum of 5% to avoid photobleaching) until a clear image with minimal speckle is seen. The signal should fill about 75–80% of the 16-bit dynamic range (Fig. 2c). If a laser power of 5% is insufficient, start increasing the pixel dwell time. Note that a high pixel dwell time will increase the time needed to acquire each image, which will be problematic if fluorescence recovery is fast. If the image is still too dim, increase the amount of mRNA injected for the next round of experiments. Before the first FRAP experiment, perform the control experiments described in Subheading 3.1 to ensure that the fluorescence output with the selected imaging settings is in the middle of the linear range (Fig. 2b).
4. Determine the *z*-plane in which fluorescence recovery will be imaged. For the in vitro samples, a good position is approximately halfway down the well (~50 μm). The optimal imaging

Fig. 3 (continued) (**b**) or too deep (**b″**). An optimal compromise (**b′**) is an imaging plane in which the center remains clearly visible and the sample fills most of the field of view. (**c**–**c″**) Adjusting the bleaching conditions. When performing the bleaching z-scan, start from the top of the sample (**c**) and move the focus deep into the tissue until almost no fluorescence can be detected (**c′**). The schematic in (**c″**) indicates the top and bottom bleaching positions in a blastula stage zebrafish embryo. (**d** and **e**) Example of expected results. FRAP analysis of Squint-GFP diffusion in a zebrafish embryo around dome stage previously injected at the one-cell stage with 30 pg Squint-GFP-encoding mRNA [6]. (**d**) Raw images from a FRAP time series before and after photobleaching. The regions of interest (ROI) for selection in PyFRAP are highlighted in the first postbleach image. PyFRAP uses these ROIs to identify the entire sample ("Whole slice ROI," red) and the bleached region ("Bleached ROI, green), and to define an annulus ("Rim ROI," orange) for the estimation of fluorophore concentration outside of the field of view and in regions below the imaging plane. (**e**) PyFRAP GUI output from analysis of the FRAP experiment in (**d**). The curves describing the recovery in the bleached region (green) and the fluorescence intensity changes in the entire imaging slice (red) do not converge due to a significant immobile fraction (compare to Fig. 1a). The diffusion coefficient of Squint-GFP is displayed in the GUI console at the bottom (red arrow)

plane for zebrafish embryos must be deep enough to cover a large portion of the embryo but shallow enough to ensure homogenous illumination of the imaging plane (Fig. 3b–b″, *see* **Note 11**).

5. Set this *z*-position as the reference point. The microscope software must be able to rapidly return to this position after bleaching.
6. Determine the depth of the *z*-position relative to the surface of the sample. Record this information for subsequent data analysis (*see* Subheading 3.2.3).
7. Acquire two images to provide a record of the sample before bleaching; use the same time interval between images as in **step 13**.
8. Zoom in so that the region to be bleached completely fills the field of view (*see* **Note 12**). Assuming the sample fills the image at 1× zoom, bleach by zooming in using a factor of around 2.5×.
9. Move to the surface of the sample. Set this as the first *z*-position (Fig. 3c).
10. Move deep into the tissue, ideally the lower end of the sample. Set this as the last *z*-position (Fig. 3c′–c″). The z-stack should cover about 80–100 μm.
11. Bleach the volume by acquiring a z-stack at highest laser power from the first to the last *z*-position. A longer pixel dwell time and a larger number of scanned slices can be used to compensate for low laser power, but bleaching should not take longer than a few minutes. Ideally, the bleached area should be at least 30% dimmer after bleaching. If bleaching is insufficient, use a stronger laser (e.g., an argon laser with a total power output of 250 mW across its emission wavelengths) or a more bleachable fluorophore (e.g., fluorescein is more bleachable than Alexa 488, and Dendra2 is more bleachable than GFP).
12. Immediately after bleaching, return to the reference *z*-plane set in **step 5**, e.g., using the "*return home*" option in the Zeiss Zen software (*see* **Note 13**). Set the laser power to the percentage used for the prebleaching image and use the same imaging conditions and zoom factor as in **step 7**.
13. Acquire a time series of 300 images (see snapshots before and after bleaching in Fig. 3d). The appropriate imaging time interval depends on the mobility of the fluorescent molecule—faster molecules require shorter intervals between images—and must be determined empirically. One frame per second is generally a good timescale to try initially (*see* **Notes 14–16**).

14. Save the images. To facilitate data analysis using PyFRAP (see below), add the identifiers "*pre*," "*bleach*," and "*post*" to the prebleach, bleach, and postbleach image series, respectively.

3.2.3 FRAP Data Analysis

PyFRAP [16] is an open-source software for analyzing FRAP data sets on Windows, MacOS X, and Linux operating systems (Fig. 3e). Below, we provide basic instructions to use the software with default parameters. For a full description of PyFRAP's versatile data analysis options, please refer to the GitHub wiki (https://github.com/mueller-lab/PyFRAP/wiki).

1. Download PyFRAP from https://mueller-lab.github.io/PyFRAP.
2. Follow the instructions for installing PyFRAP from https://github.com/mueller-lab/PyFRAP/wiki/Installation#short.
3. Open the GUI by double-clicking on runPyFRAP.bat (Windows), runPyFRAP.command (MacOS X), or runPyFRAP.sh (Linux).
4. Go to → File → New Molecule and enter a name for the molecule.
5. Go to → Edit → PyFRAP Wizard. This will open a wizard, which systematically guides the user through the analysis steps.
6. Select "*Create embryo from microscope data*" if the microscope saves the data acquired in Subheading 3.2.2 in .czi or .lsm file formats.

   OPTIONAL: It is also possible to select "*Create embryo from already prepared data*" to load a TIFF stack containing the FRAP recovery series (see https://github.com/mueller-lab/PyFRAP/wiki/FirstSteps for details).
7. Select "*Change*" and go to the folders containing the prebleach and postbleach files.
8. Fill in the required parameters. Essential parameters are the resolution (μm/pixel), imaging depth (μm), and frame interval (s). Once finished, select "*Done*." When using .czi or .lsm formats, resolution and frame intervals are recognized automatically.
9. The "Select Geometry" popup will appear. Select the option that best suits the sample. PyFRAP provides several preloaded sample geometries. The zebraFishDomeStage geometry is appropriate for zebrafish embryo samples, while the cylinder or cone geometries suit the in vitro samples. Select "*Done*."
10. In the next dialog box, several parameters for the geometry will appear. Values for these parameters will be automatically populated by the software during subsequent image analysis steps (*see* below). Select "*Done*."

11. A new dialog will pop up with three different options for ROI (region of interest) creation. These ROIs will be used to identify the entire sample as well as the bleached region. Select "*Use ROI Wizard*."
12. First, create an ROI containing the entire sample ("Whole Slice ROI," Fig. 3d). Use the drop-down menu to choose the appropriate shape for the ROIs. The default is a circle (radialSlice). Select "*Create ROI*." Draw the ROI by left-clicking on the picture or adjusting the parameters in the dialog box. The ROI can be moved using the arrow keys, and the diameter of the ROI can be increased/decreased by pushing Ctrl and up/down arrow keys at the same time. Right-click on the image to cancel the selection and redraw the ROI if necessary. Select "*Done*."
13. Next, create an ROI containing the bleached area ("Bleached ROI," Fig. 3d). Use the drop-down menu to choose the appropriate shape for the ROIs. The default is a square, but it can also be changed to other polygons or a circle. Select "*Create ROI*" and draw the ROI.
14. Create an ROI for the rim of the sample ("Rim ROI," Fig. 3d). An annulus covering the rim of the sample is used to estimate the fluorophore concentration outside of the field of view and in regions below the imaging plane, and the selected rim radius should be approximately 80% of the slice ROI. Select "*Create ROI*" and draw the ROI.
15. The "Edit Geometry" popup will appear again. Select the first option "*Grab from ROI*." Select the ROI that contains the entire sample (This should be named "*Slice*."), then select "*Done*." Do the same for the second "*Grab from ROI*," click "*Slice*," then select "*Done*."
16. The "Mesh Settings" popup will appear. Change Element Size (px) to 17. Select "*Done*." This will generate a mesh with the shape of the sample to discretize the data for numerical simulation and will take several minutes to finish. Increasing the mesh element size value can drastically increase the computation time, but a finer mesh may be necessary depending on the imaging data.
17. The "Analysis Settings" popup will appear. Select "*Done*" to use the default settings (*see* **Note 17**).
18. The "Simulation Settings" popup will appear. Enter a value of 1000 for the simulation timesteps. Select "*Done*." This will start a numerical simulation of the fluorescence recovery based on the fluorescence distribution of the first time point. Depending on the settings, the simulation can take around 15–30 min to finish.

19. The "Fit Settings" popup will appear. Select "*Add*" to add the "Slice" and "Bleached Square" ROIs. If you are working with in vivo samples, tick "*Fit Production*" and "*Fit Degradation*" (*see* **Note 18**). If production and degradation parameters are known [6, 9, 20, 22], they can also be directly entered here. Select "*Done*."
20. The "Ideal Pinning" popup will appear. Select "*Done*." This will fit the simulated recovery curve to the measured recovery data.
21. Go to → Fitting → Print fit results to display the fitted curve and other results of the analysis.
22. The diffusion coefficient is given by DOptMu in $\mu m^2/s$ in the text output of the console at the bottom (Fig. 3e) and in the panel on the right of the PyFRAP GUI.

4 Notes

1. The following fluorescein-coupled dextrans from Thermo Fisher have well characterized diffusion coefficients [16]: 70 kDa ($D = 27 \pm 5\ \mu m^2/s$)—Catalog No. D1823, 40 kDa ($D = 45 \pm 11\ \mu m^2/s$)—Catalog No. D1844, 10 kDa ($D = 83 \pm 8\ \mu m^2/s$)—Catalog No. D1821, 3 kDa ($D = 170 \pm 22\ \mu m^2/s$)—Catalog No. D3305.
2. mRNA can be produced by in vitro transcription from suitable purified and linearized plasmid DNA using the mMESSAGE mMACHINE kit from Thermo Fisher.
3. We recommend using Fisherbrand Disposable Borosilicate Glass Pasteur Pipets (Catalog No. 13-678-20A) and 10 mL Bel-Art SP Scienceware Pipette Pump Pipetters (Catalog No. 13-683C) to handle zebrafish embryos. The glass pipettes can be flame-polished to prevent the tip from scratching the embryos.
4. Sometimes new dissection needles are too sharp and will puncture the embryo. They can be blunted by grinding the needle tip repeatedly on a hard stone until the tip becomes flat. Take care not to bend the tip while blunting it.
5. There are various types of microinjection setups and approaches (e.g., the micromanipulation system by Narishige, as well as micropipette holders and pressure injection regulators from World Precision Instruments). Detailed protocols for microinjection have been published previously [23, 24]. The injection volume has to be adjusted by measuring the injection drop in mineral oil on a micrometer calibration slide.

6. A plastic block such as the PLEXIGLAS XT (allround) Clear 0A000 GT with 3 mm thickness from Evonik Industries is appropriate.
7. We use a Zeiss LSM780 confocal microscope with a GaAsP array. The filter sets and lasers depend on the desired fluorophore used. A range of 494–542 nm is useful to image GFP and fluorescein. A pinhole diameter yielding a slice thickness of 5 μm works well for in vitro and in vivo FRAP experiments.
8. Aqueous solutions of fluorescent proteins such as recombinant GFP must contain 5% bovine serum albumin to prevent GFP from sticking to the plastic block walls (similar to blocking a membrane during Western blotting).
9. It is crucial that the mineral oil completely surrounds the aqueous sample when the coverslip is placed over the plastic block. If not, the very small volume of aqueous sample will quickly evaporate.
10. Dechorionated embryos are easily damaged by contact with plastic or air. Keep dechorionated embryos in glass dishes or plastic dishes coated with 2% agarose.
11. Zebrafish embryos are spherical, and signal intensity will diminish more rapidly in the center than at the sides since the tissue is thicker in the center. Therefore, image at an optimal depth where the signal intensities in the center and on the sides are similar (Fig. 3b′).
12. The size of the bleached area must not be too small or too big. If it is too small, the signal will recover too quickly to be properly measured. If it is too big, bleaching will take too long, and recovery might start before imaging. While the software PyFRAP accounts for the finite sample geometries in FRAP experiments, an overly large bleaching area will greatly affect analysis with other software packages, which assume that the fluorescent pool is infinitely large.
13. Image acquisition must start within seconds after bleaching to ensure a significant perturbation in the fluorescence profile and an extensive difference between the unbleached image and the first postbleach image.
14. Molecules with large diffusion coefficients should be imaged at a faster frame rate (e.g., GFP with a diffusion coefficient of ~100 $\mu m^2/s$ in vitro should be imaged at a rate of one frame per second for 5 min), while images of molecules with a smaller diffusion coefficient can be recorded with a slower frame rate (e.g., Squint-GFP with a diffusion coefficient of ~3 $\mu m^2/s$ in vivo can be imaged around one frame every 10 s for 50 min [6]). However, production and degradation of the fluorescent protein can significantly contribute to changes in

fluorescence intensity over longer imaging times (Fig. 1c, d) and have to be taken into account for data analysis (also *see* **Note 18**). In case of high pixel dwell times, it is important to keep in mind that the time needed to record each frame must be less than the time step between each frame to ensure that the frame rate reported by the imaging software is accurate.

15. The sample could experience inadvertent photobleaching during imaging of the recovery. PyFRAP can correct for bleaching during imaging (also *see* **Note 18**), but this should be minimized if possible. To assess potential photobleaching, image the sample for 300 frames with the shortest possible interval and compare the first and last images. If the average intensity of the last image is lower than the first, bleaching is an issue and the laser power should be reduced. Alternatively, acquire 300 images rapidly and determine whether the data series shows differences compared to an experiment with only 30 images taken over the same time period.
16. Potential artifacts in FRAP experiments might arise from inhomogeneous bleaching and overexpression. PyFRAP can correct for inhomogeneous bleaching since the software simulates fluorescence recovery using the first image of the potentially inhomogeneously bleached sample as the initial condition. In some instances, overexpression artifacts can be uncovered by repeating FRAP experiments with different amounts of injected mRNA.
17. PyFRAP offers several methods to correct imaging artifacts for FRAP data. If images are noisy, a Gaussian or median filter can be used for smoothing and denoising. For some microscope settings, the center of the sample is more strongly illuminated than the peripheral regions. This inhomogeneous illumination can be accounted for in PyFRAP using a prebleach image or a "flattening" data set [16]. A prebleach image can be used for in vitro samples and requires the input of a sample image before bleaching. A flattening data set can be used for any sample type. This is a homogenously fluorescent sample as described in Subheading 3.1.1 (**steps 1–4**), which can be used to detect and correct for inhomogeneous illumination.
18. During the recovery process, production and degradation/clearance of the fluorescent protein in living samples can additionally influence fluorescence recovery (Fig. 1c, d). This effect becomes significant when imaging over a long time (e.g., around 50 min). PyFRAP can account for these processes and output the corrected diffusion coefficient if the options "*Fit Production*" and "*Fit Degradation*" are selected. Select "*Fit Degradation*" to take bleaching into account if this is an issue during recovery and if this cannot be prevented by changing the imaging conditions.

Acknowledgments

We thank Katherine W. Rogers, Alexander Bläßle, David Mörsdorf, and Hannes Preiß for useful discussions. This work was supported by the Max Planck Society and ERC Starting Grant 637840.

References

1. Wolpert L (1969) Positional information and the spatial pattern of cellular differentiation. J Theor Biol 25(1):1–47. https://doi.org/10.1016/S0022-5193(69)80016-0
2. Müller P et al (2013) Morphogen transport. Development 140(8):1621–1638. https://doi.org/10.1242/dev.083519
3. Crick F (1970) Diffusion in embryogenesis. Nature 225(5231):420–422. https://doi.org/10.1038/225671b0
4. Rogers KW, Schier AF (2011) Morphogen gradients: from generation to interpretation. Annu Rev Cell Dev Biol 27:377–407. https://doi.org/10.1146/annurev-cellbio-092910-154148
5. Harmansa S et al (2015) Dpp spreading is required for medial but not for lateral wing disc growth. Nature 527(7578):317–322. https://doi.org/10.1038/nature15712
6. Müller P et al (2012) Differential diffusivity of Nodal and Lefty underlies a reaction-diffusion patterning system. Science 336 (6082):721–724. https://doi.org/10.1126/science.1221920
7. Rogers KW, Müller P (2018) Nodal and BMP dispersal during early zebrafish development. Developmental Biology pii:S0012-1606(17) 30925-9. http://doi.org/10.1016/j.ydbio.2018.04.002
8. Zinski J et al (2017) Systems biology derived source-sink mechanism of BMP gradient formation. eLife 6:e22199. https://doi.org/10.7554/eLife.22199
9. Pomreinke AP et al (2017) Dynamics of BMP signaling and distribution during zebrafish dorsal-ventral patterning. eLife 6:e25861. https://doi.org/10.7554/eLife.25861
10. Poo MM, Cone RA (1973) Lateral diffusion of rhodopsin in Necturus rods. Exp Eye Res 17 (6):503–510. https://doi.org/10.1016/0014-4835(73)90079-1
11. Liebman PA, Entine G (1974) Lateral diffusion of visual pigment in photoreceptor disk membranes. Science 185(4149):457–459. http://doi.org/10.1126/science.185.4149.457
12. Lorén N et al (2015) Fluorescence recovery after photobleaching in material and life sciences: putting theory into practice. Q Rev Biophys 48(3):323–387. https://doi.org/10.1017/S0033583515000013
13. Kicheva A et al (2007) Kinetics of morphogen gradient formation. Science 315 (5811):521–525. https://doi.org/10.1126/science.1135774
14. Gregor T et al (2007) Stability and nuclear dynamics of the Bicoid morphogen gradient. Cell 130(1):141–152. https://doi.org/10.1016/j.cell.2007.05.026
15. Umulis DM, Othmer HG (2012) The importance of geometry in mathematical models of developing systems. Curr Opin Genet Dev 22 (6):547–552. https://doi.org/10.1016/j.gde.2012.09.007
16. Bläßle A et al (2018) Quantitative diffusion measurements using the open-source software PyFRAP. Nature Communications 9(1):1582. http://doi.org/10.1038/s41467-018-03975-6
17. Nüsslein-Volhard C, Dahm R (2002) Zebrafish: a practical approach. The practical approach series, vol 261, 1st edn. Oxford University Press, Oxford
18. Westerfield M (2007) The zebrafish book: a guide for the laboratory use of zebrafish (*Danio rerio*). University of Oregon Press, Oregon
19. Schindelin J et al (2012) Fiji: an open-source platform for biological-image analysis. Nat Methods 9(7):676–682. https://doi.org/10.1038/nmeth.2019
20. Rogers KW et al (2015) Measuring protein stability in living zebrafish embryos using Fluorescence Decay After Photoconversion (FDAP). J Vis Exp 95:e52266. https://doi.org/10.3791/52266
21. Kimmel CB et al (1995) Stages of embryonic development of the zebrafish. Dev Dyn 203 (3):253–310. http://doi.org/10.1002/aja.1002030302
22. Bläßle A, Müller P (2015) PyFDAP: automated analysis of Fluorescence Decay After

Photoconversion (FDAP) experiments. Bioinformatics 31(6):972–974. https://doi.org/10.1093/bioinformatics/btu735

23. Xu Q (1999) Microinjection into zebrafish embryos. In: Guille M (ed) Molecular methods in developmental biology: xenopus and zebrafish. Humana Press, Totowa, NJ, pp 125–132. https://doi.org/10.1385/1-59259-678-9:125
24. Rosen JN, Sweeney MF, Mably JD (2009) Microinjection of zebrafish embryos to analyze gene function. J Vis Exp 25:e1115. https://doi.org/10.3791/1115

ARTICLES
https://doi.org/10.1038/s41556-018-0155-7
nature cell biology

Appendix 4

Scale-invariant patterning by size-dependent inhibition of Nodal signalling

María Almuedo-Castillo[1,3], Alexander Bläßle[1], David Mörsdorf[1], Luciano Marcon[1,3], Gary H. Soh[1], Katherine W. Rogers[1,2], Alexander F. Schier[2] and Patrick Müller[1*]

Individuals can vary substantially in size, but the proportions of their body plans are often maintained. We generated smaller zebrafish by removing 30% of their cells at the blastula stages and found that these embryos developed into normally patterned individuals. Strikingly, the proportions of all germ layers adjusted to the new embryo size within 2 hours after cell removal. As Nodal–Lefty signalling controls germ-layer patterning, we performed a computational screen for scale-invariant models of this activator–inhibitor system. This analysis predicted that the concentration of the highly diffusive inhibitor Lefty increases in smaller embryos, leading to a decreased Nodal activity range and contracted germ-layer dimensions. In vivo studies confirmed that Lefty concentration increased in smaller embryos, and embryos with reduced Lefty levels or with diffusion-hindered Lefty failed to scale their tissue proportions. These results reveal that size-dependent inhibition of Nodal signalling allows scale-invariant patterning.

Despite often substantial variability in size, embryos faithfully generate the correct tissue proportions[1–5]. During development, tissue patterning is achieved by gradients of signalling proteins that induce distinct differentiation programmes in discrete spatial domains[6–10]. To adjust tissue patterning and organ proportions to their body size, embryos need to appropriately scale the underlying signalling gradients[11]. Scaling mechanisms for individual tissue-specific signalling systems at different stages of development have been proposed, but how these mechanisms are integrated and coordinated during development to generate the correct proportions of all tissues is currently unclear[11–21]. Here, we analysed how signalling gradients adjust tissue proportions in differently sized zebrafish embryos and identified a size-dependent mechanism that mediates scale-invariant germ-layer patterning to provide the correct amount of progenitor cells for all future tissues.

Results

Scaling of tissue proportions in differently sized zebrafish embryos. We found that the removal of ~30% of cells by extirpation from the animal pole before gastrulation (Fig. 1a) generates zebrafish embryos that become normally patterned adults. Extirpated embryos developed into smaller individuals with the same number of proportionally thinner somites as untreated embryos (Fig. 1a). Consistently, the size of various organs, including the hatching gland (a mesodermal derivative, *hgg1* positive) and the eye (an ectodermal derivative, *vsx2* positive), was reduced in individuals developing from extirpated embryos (Fig. 1b). Strikingly, scaling of tissue proportions to embryo size already occurred during the gastrulation stages within 2 hours following extirpation. Using in situ hybridization, we quantified the extent of the presumptive ectoderm (*sox3* positive; Fig. 1c) and mesendoderm (*fascin* positive; Fig. 1d) and found that the germ-layer proportions adjusted progressively after extirpation: at 1-hour post-extirpation (1 hpe), extirpated embryos had excess mesendoderm and insufficient ectodermal progenitors as cells were removed from the animal pole containing presumptive ectoderm (Fig. 1c,d). Interestingly, 1 hour later (2 hpe), the ectoderm and mesendoderm proportions had adjusted in extirpated embryos (Fig. 1c,d). Using in toto light-sheet imaging, we confirmed that the mesendoderm scaled throughout the embryonic marginal zone (Fig. 1e–g). Even though cells were removed from the animal pole, the number of endodermal precursor cells (*sox17* and *sox32* positive) at the opposite side within the marginal zone of extirpated embryos was also proportionally reduced by the gastrulation stages (Fig. 1h).

Smaller embryos do not adjust developmental speed after extirpation. The cell density did not change (Fig. 2a) and the proliferation rates did not increase in extirpated embryos (Fig. 2b,c), indicating that neither changes in cell density nor compensatory proliferation underlie germ-layer scaling. Moreover, the spatial expression kinetics of *goosecoid*[22]—a highly sensitive indicator of developmental progression—were similar in untreated and extirpated embryos at different developmental time points (Supplementary Fig. 1). Even though smaller embryos displayed a reduced apparent epiboly due to the shortened blastoderm but unchanged yolk extent after extirpation, the spreading of the blastoderm during epiboly occurred at a similar pace (Fig. 2d–i). Thus, scaling can also not be explained by altered developmental speed in differently sized embryos.

Nodal signalling scales in smaller embryos. As the Nodal–Lefty activator–inhibitor system patterns the germ layers during early development[10,23], we hypothesized that Nodal signalling adjusts in smaller embryos to allow proportionate patterning. The activator Nodal is secreted from the marginal zone of the embryo and induces the endoderm and mesoderm, whereas the highly diffusive Nodal inhibitor Lefty[24], which is also expressed at the margin and induced by Nodal signalling, limits the mesendodermal domain[23,25–34]. To test whether Nodal signalling adjusts in smaller embryos, we measured the extent of Nodal activity by assessing the phosphorylation of the Nodal signal transducer Smad2/3 (pSmad2/3)[23,35,36] (Fig. 3a–d and

[1]Friedrich Miescher Laboratory of the Max Planck Society, Tübingen, Germany. [2]Department of Molecular and Cellular Biology, Harvard University, Cambridge, MA, USA. [3]Present address: Centro Andaluz de Biología del Desarrollo, Universidad Pablo de Olavide, Sevilla, Spain.
*e-mail: patrick.mueller@tuebingen.mpg.de

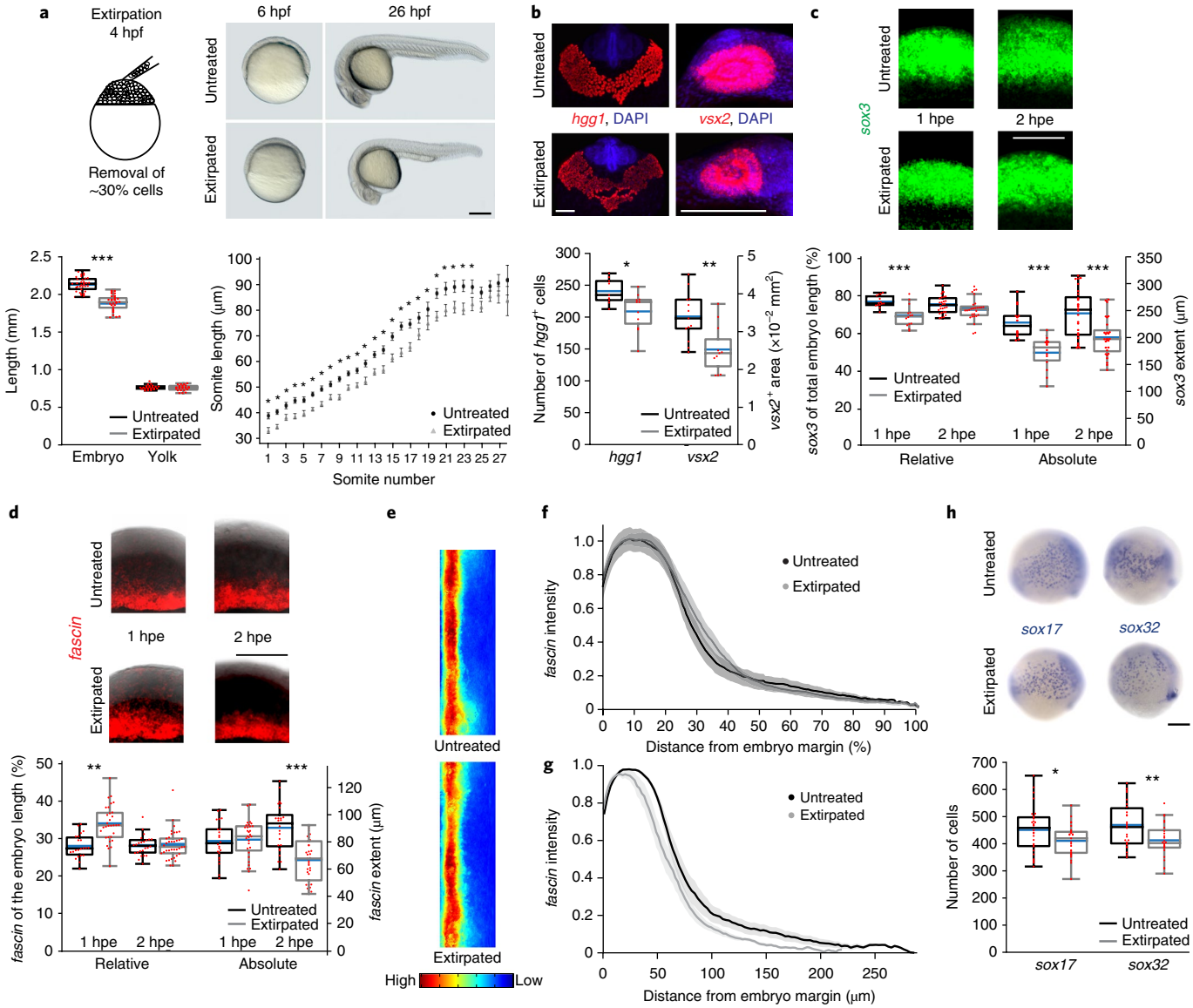

Fig. 1 | Scaling in smaller embryos after extirpation. a, Schematic of embryo extirpation (lateral views); hpf, hours post-fertilization. The total length of extirpated embryos at 1-day post-fertilization is smaller than untreated individuals (n of untreated = 40, n of extirpated = 37; ***$P < 0.00001$), whereas the yolk size remains unchanged (n of untreated = 23, n of extirpated = 24; $P > 0.05$) (bottom left). The length of the 24 posterior-most somites is proportionately smaller in extirpated embryos (bottom right, n of untreated = 15, n of extirpated = 13; *$P < 0.05$). The error bars in the 'Somite length' graph are the s.e.m. **b**, Maximum intensity projections of confocal FISH stacks (top) and the quantification of *hgg1*-positive cells (n of untreated = 9, n of extirpated = 11; *$P < 0.05$) and *vsx2*-positive cells (n of untreated = 13, n of extirpated = 11; **$P < 0.01$) (bottom). **c**,**d**, Maximum intensity projections of lateral confocal FISH stacks (top) and the quantification of the relative and absolute length of *sox3* (ectoderm; **c**) and *fascin* (mesendoderm; **d**) domains (bottom). The ectoderm proportions are smaller at 1 hpe (n of untreated = 14, n of extirpated = 14; ***$P < 0.001$) but scale by 2 hpe (n of untreated = 28, n of extirpated = 28; $P > 0.05$). Similarly, the mesendoderm proportions are too large at 1 hpe (n of untreated = 23, n of extirpated = 31; **$P < 0.01$) but scale by 2 hpe (n of untreated = 24, n of extirpated = 37; $P > 0.05$). **e**–**g**, 2D maps of 3D-reconstructed embryos imaged by light-sheet microscopy (**e**) and the quantification (**f**,**g**) of normalized *fascin* domains along the vegetal–animal axis show scaling (n of untreated = 9, n of extirpated = 9). The shaded regions in **f** and **g** are the s.e.m. **h**, Lateral views and the quantification of the number of endodermal cells positive for *sox17* (n of untreated = 30, n of extirpated = 27; *$P < 0.05$) or *sox32* (n of untreated = 26, n of extirpated = 28; **$P < 0.01$). The box plots show the median (blue line), the mean (black (untreated) and grey (extirpated) lines inside the box), the 25% and 75% quantiles (box) and all included data points (red markers). Whiskers extend to the smallest data point within the 1.5 interquartile range of the lower quartile and to the largest data point within the 1.5 interquartile range of the upper quartile. Two-sided Student's t-tests were performed ($\alpha = 0.05$). See Supplementary Table 1 for statistics source data. Scale bars, 200 μm.

Supplementary Fig. 2a,b). Similar to the mesendodermal domain (Fig. 1e,f), Nodal signalling scaled throughout the embryonic marginal zone by 2 hpe (Fig. 3b,c). Interestingly, Nodal signalling had already scaled by 1 hpe (Fig. 3a and Supplementary Fig. 2a,b), preceding the scaling of the presumptive ectoderm/mesendoderm (Fig. 1c,d) and the feedback-induced Nodals (*cyclops* and *squint*) and Leftys (*lefty1* (*lft1*) and *lefty2* (*lft2*)) (Fig. 3e–i).

A computational screen to identify scaling mechanisms. To identify the mechanism by which Nodal signalling might sense embryo size

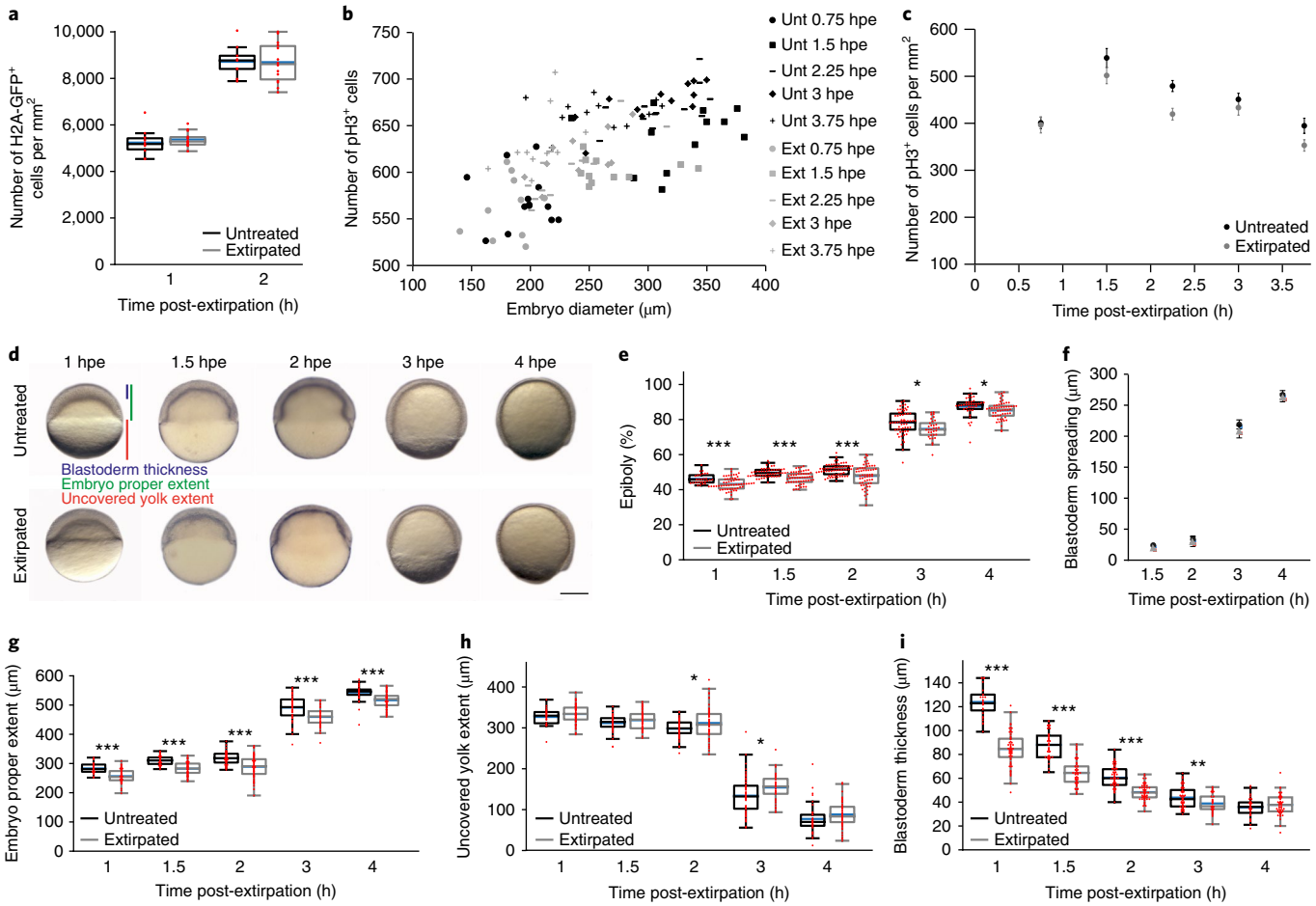

Fig. 2 | Germ-layer proportions scale in extirpated embryos without increases in cell proliferation or changes in cell density or developmental speed. a, Cell density measured in untreated and extirpated H2A-GFP embryos at different time points after extirpation. 1 hpe: *n* of untreated = 10, *n* of extirpated = 14, $P > 0.05$; 2 hpe: *n* of untreated = 9, n of extirpated = 14; $P > 0.05$. **b**,**c**, The number of proliferating cells (pH3 positive) relative to the embryo diameter (**b**) and the density of proliferating cells (**c**) in untreated (Unt) and extirpated (Ext) embryos at different time points after extirpation. 0.75 hpe: *n* of untreated = 13, *n* of extirpated = 11, $P > 0.05$; 1.5 hpe: *n* of untreated = 12, *n* of extirpated = 11, $P > 0.05$; 2.25 hpe: *n* of untreated = 12, *n* of extirpated = 12, $^{**}P < 0.01$; 3 hpe: *n* of untreated = 12, *n* of extirpated = 10, $P > 0.05$; 3.75 hpe: *n* of untreated = 12, *n* of extirpated = 11, $P > 0.05$. Individual data points are shown in **b**; the mean and s.e.m. of the same data are shown in **c**. **d**, Lateral views of untreated and extirpated embryos. The progression of gastrulation and epiboly spreading is unchanged after extirpation. Scale bar, 200 µm. **e**–**i**, Quantification of the epiboly (%) (that is, the ratio of the embryo proper extent to the total length (embryo proper + uncovered yolk) (**e**), blastoderm spreading (that is, the difference between the embryo proper extent at 1.5, 2, 3 and 4 hpe and the embryo proper extent at the first time point of analysis (1 hpe) (**f**), the extent of the embryo proper (**g**), the uncovered yolk (**h**) and the blastoderm thickness (**i**) at different time points after extirpation. 1 hpe: *n* of untreated = 28, *n* of extirpated = 59; 1.5 hpe: *n* of untreated = 51, *n* of extirpated = 55; 2 hpe: *n* of untreated = 62, *n* of extirpated = 58; 3 hpe: *n* of untreated = 59, *n* of extirpated = 33; 4 hpe: *n* of untreated = 38, *n* of extirpated = 55. $^{*}P < 0.05$; $^{**}P < 0.01$; $^{***}P < 0.001$. The mean and s.e.m. are shown in **f**. The box plots show the median (blue line), the mean (black (untreated) and grey (extirpated) lines), 25% and 75% quantiles (box) and all included data points (red markers). Whiskers extend to the smallest data point within the 1.5 interquartile range of the lower quartile and to the largest data point within the 1.5 interquartile range of the upper quartile. Two-sided Student's *t*-tests were performed ($\alpha = 0.05$). See Supplementary Table 1 for statistics source data.

and adjust tissue proportions, we performed a computational screen that included known positive and negative interactions in the Nodal–Lefty system[23,33,34] while keeping model complexity to a minimum (Fig. 4a,b and Supplementary Note 1). We constrained the screen with the measured biophysical properties, including Nodal/Lefty diffusivities and half-lives[33], and systematically varied the unknown parameters to identify systems that recapitulate the scaling observed during germ-layer patterning. To keep model complexity to a minimum, we did not account for spatial biases influencing the Nodal–Lefty system[37] and did not explicitly model receptor interactions[38].

We screened more than 400,000 parameter combinations representing the production of Lefty, the inhibition strength and the Nodal-mediated feedback on Nodal and Lefty production. By assessing the overlap between Nodal signalling in simulations of normally sized and shortened embryos, we found that systems that are capable of scaling require precise levels of highly diffusive Lefty, whose concentration increases in extirpated embryos to adjust the Nodal signalling gradient (Fig. 4c–e). In such systems, the boundary located more proximal to the marginal zone in shortened compared to normally sized embryos affects the long-range Lefty but not the short-range Nodal gradient (Fig. 4c). As we shortened embryos before the onset of Lefty protein secretion without removing *lft*-expressing cells from the marginal zone (Fig. 3e–i), the same amount of Lefty should be produced in early extirpated and untreated embryos. Thus, the concentration of Lefty should increase in smaller embryos, contracting the Nodal activity range to re-establish the correct tissue dimensions relative to the new size of the embryo.

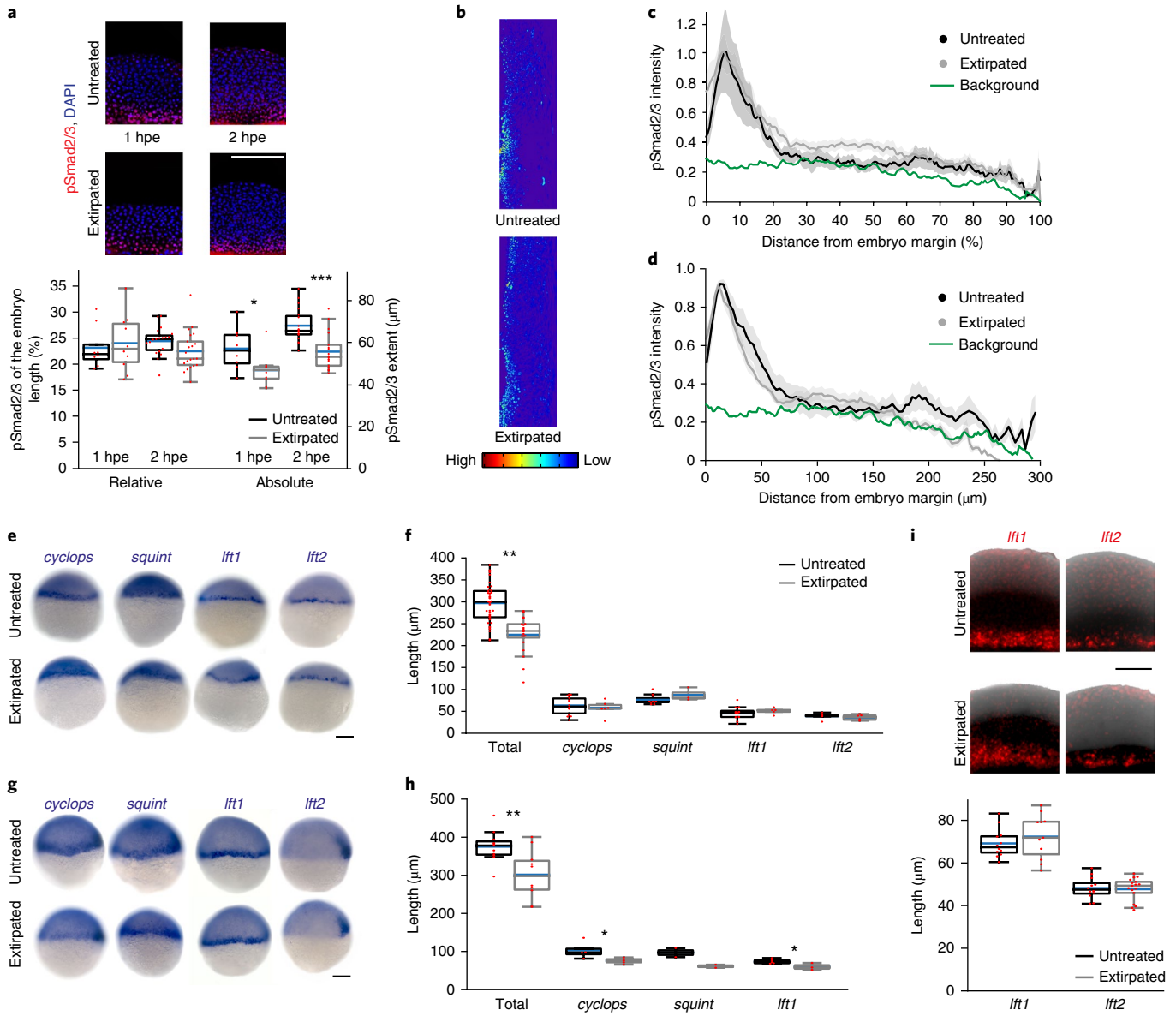

Fig. 3 | Scaling of Nodal-mediated patterning. a, Maximum intensity projections of lateral confocal pSmad2/3 immunostaining stacks (top) and the quantification of the absolute and relative length of the pSmad2/3 domain (bottom). 1 hpe: *n* of untreated = 7, *n* of extirpated = 10; 2 hpe: *n* of untreated = 19, *n* of extirpated = 21. **b**–**d**, 2D maps of 3D-reconstructed embryos imaged by light-sheet microscopy (**b**) and the quantification of normalized pSmad2/3 domains along the vegetal–animal axis show scaling (*n* of untreated = 5, *n* of extirpated = 6). Intensity as a function of embryo length (%) (**c**) and intensity as a function of the absolute distance from the margin (**d**) are shown. The shaded regions in **c** and **d** are the s.e.m. **e**–**h**, Lateral images showing the expression of *cyclops* and *squint* Nodals and *lft1* and *lft2* Leftys in untreated and extirpated embryos at 1 hpe (**e**) and 2 hpe (**g**), and the quantification of embryo length and expression domains at 1 hpe (**f**) and 2 hpe (**h**). 1 hpe: total: *n* of untreated = 42, *n* of extirpated = 20; *cyclops*: *n* of untreated = 14, *n* of extirpated = 6; *squint*: *n* of untreated = 11, *n* of extirpated = 3; *lft1*: *n* of untreated = 12, *n* of extirpated = 5; *lft2*: *n* of untreated = 5, *n* of extirpated = 6. 2 hpe: total: *n* of untreated = 11, *n* of extirpated = 10; *cyclops*: *n* of untreated = 4, *n* of extirpated = 5; *squint*: *n* of untreated = 2, *n* of extirpated = 2; *lft1*: *n* of untreated = 5, *n* of extirpated = 3. Nodal and Lefty domains are unchanged in differently sized embryos at 1 hpe but scale by 2 hpe. **i**, Maximum intensity projections of lateral confocal *lft1* and *lft2* FISH stacks in untreated and extirpated embryos at 1 hpe (top) and the quantification of expression domains (bottom). *lft1*: *n* of untreated = 12, *n* of extirpated = 11; *lft2*: *n* of untreated = 12, *n* of extirpated = 17. The box plots show the median (blue line), the mean (black (untreated) and grey (extirpated) lines), 25% and 75% quantiles (box) and all included data points (red markers). Whiskers extend to the smallest data point within the 1.5 interquartile range of the lower quartile and to the largest data point within the 1.5 interquartile range of the upper quartile. Two-sided Student's *t*-tests were performed ($\alpha = 0.05$). $^*P < 0.05$; $^{**}P < 0.01$; $^{***}P < 0.001$. See Supplementary Table 1 for statistics source data. Scale bars, 200 μm (**a**,**e**,**g**) and 100 μm (**i**).

In our simulations of the Nodal–Lefty system (Supplementary Video 1), scale-invariant germ-layer patterning only became apparent around 2 hpe, as observed experimentally (Fig. 1c,d). The simulations further closely matched the time window of germ-layer specification: Nodal signalling levels and mesendoderm specification expand as development proceeds, Nodal signalling levels peak around 2 hpe (6 hours post-fertilization (6 hpf)) and Nodal signalling rapidly decreases afterwards (Supplementary Video 1). Together, the experimental observations and computational simulations suggest that germ-layer scaling at 2 hpe results from

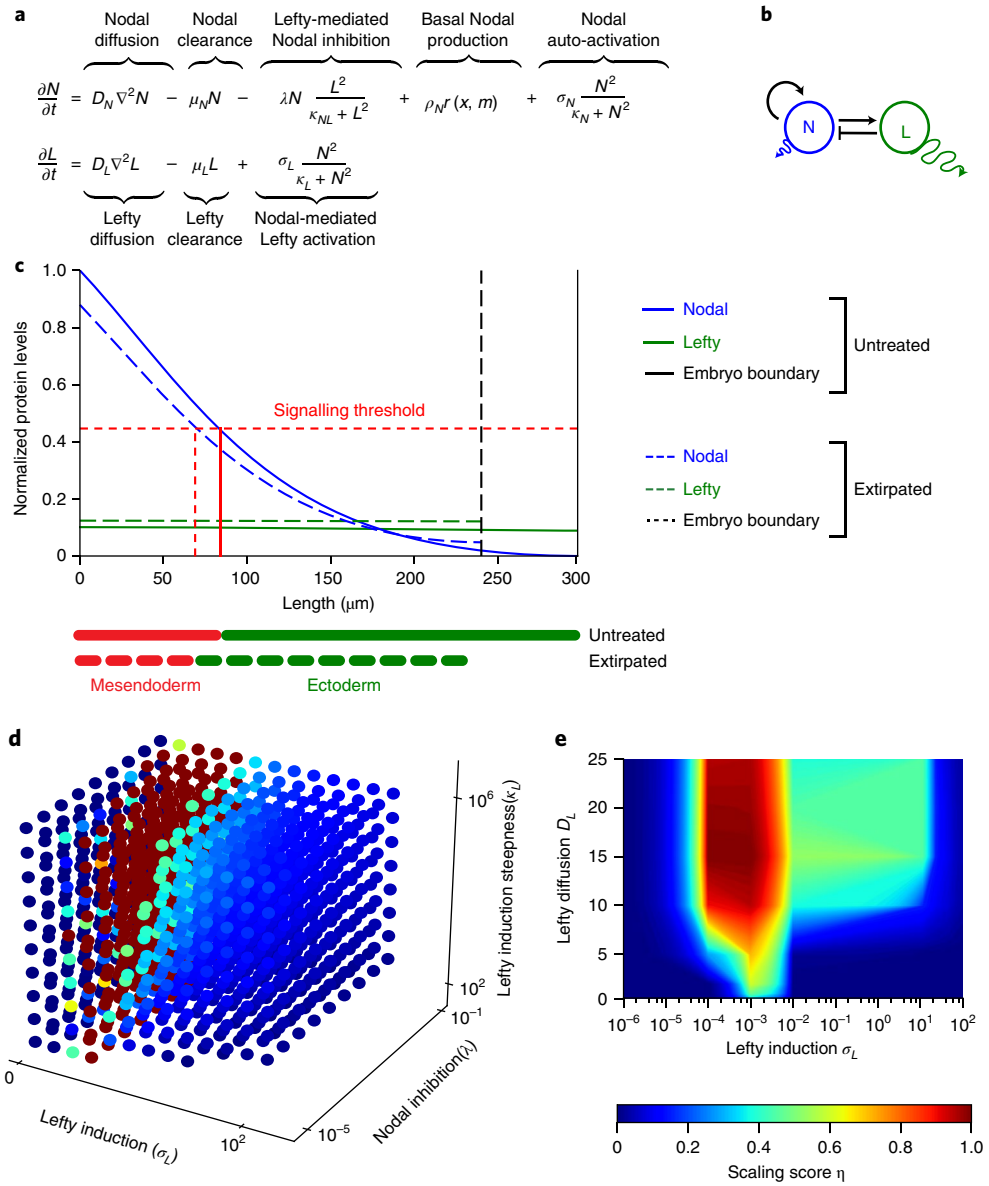

Fig. 4 | Computational screen for parameters conferring scale invariance. a,**b**, Equations (**a**) and network (**b**) describing the known interactions in the Nodal (N)–Lefty (L) activator–inhibitor system. The change in Nodal concentration over time (t) is a function of Nodal diffusion with the diffusion coefficient D_N, Nodal removal with the clearance rate constant μ_N, Lefty-mediated Nodal inhibition with the inhibition strength λ and the steepness parameter κ_{NL}, basal Nodal production described by the space (x)-dependent rectangular pulse function $r(x,m)$ representing the length m of the Nodal source, and Nodal auto-activation with the rate constant σ_N and the steepness parameter κ_N. Similarly, the change in Lefty concentration over time is a function of Lefty diffusion with the diffusion coefficient D_L, Lefty removal with the clearance rate constant μ_L, and Nodal-dependent Lefty induction with the rate constant σ_L and the steepness parameter κ_L. **c**, Example of a scale-invariant system identified by the screen, showing an increase in Lefty and dampening of Nodal signalling after extirpation. Simulations were fitted to the experimentally measured total length and mesendoderm extent (vertical red solid (untreated) and dashed (extirpated) lines). **d**, A parameter screen showing the influence of Lefty levels (σ_L), Nodal inhibition strength (λ) and Lefty induction steepness (κ_L) on scaling; the maximum projection through the six-dimensional parameter space is shown with the following discrete values: for σ_L: 0, 10^{-4}, 10^{-3}, 10^{-2}, 11.12, 22.23, 33.34, 44.45, 55.56, 66.67, 77.78, 88.89 and 10^2; for λ: 10^{-5}, 1.12×10^{-2}, 2.23×10^{-2}, 3.34×10^{-2}, 4.45×10^{-2}, 5.56×10^{-2}, 6.67×10^{-2}, 7.78×10^{-2}, 8.89×10^{-2} and 10^{-1}; for κ_L: 10^2, 1.12×10^5, 2.23×10^5, 3.34×10^5, 4.45×10^5, 5.56×10^5, 6.67×10^5, 7.78×10^5, 8.89×10^5 and 10^6. Parameter configurations that resulted in biologically unrealistic gradients were excluded. **e**, A parameter screen showing the influence of Lefty diffusivity on scaling; the maximum projection through the six-dimensional parameter space is shown. The model predicts that scaling should fail if Lefty induction (σ_L) or diffusion (D_L) is too low (that is, less than ~7 μm^2 s^{-1}).

adjustments in mesendoderm expansion dynamics over time rather than from shrinking an initially too broadly specified mesendodermal domain.

Scaling depends on Lefty levels. Our model predicted that scaling crucially depends on the levels of Lefty (Figs. 4d and 5a,b). To test this prediction, we assessed mesendoderm proportions in embryos with varying numbers of functional *lft* alleles (*lft1* and *lft2*)[36]. As expected, both untreated and extirpated double-homozygous *lft1*$^{-/-}$; *lft2*$^{-/-}$ mutants showed dramatically increased Nodal signalling and an expanded mesendoderm[36] (Fig. 5c–g and Supplementary Fig. 3a–c). By contrast, untreated and shortened double-heterozygous

lft1$^{+/-}$;*lft2*$^{+/-}$ embryos exhibited nearly normal Nodal signalling and mesendoderm and ectoderm proportions, indicating that one functional allele of each *lft* is sufficient for proper spatial Nodal signalling and scaling, possibly due to dosage adjustments that result in similar amounts of protein (Fig. 5c–h and Supplementary Fig. 3a–c). Normally sized and extirpated single-homozygous *lft2*$^{-/-}$ mutants had excess Nodal signalling and mesendoderm at the expense of the ectoderm (Fig. 5c–h and Supplementary Fig. 3a–c). By striking contrast, single-homozygous *lft1*$^{-/-}$ embryos displayed expanded Nodal signalling and mesendoderm and a reduced ectoderm only after extirpation (Fig. 5c–h and Supplementary Fig. 3a–c). Interestingly, Lefty1 is less inhibitory than its paralogue Lefty2 (Supplementary Fig. 3d,e); thus, although highly active Lefty2 is sufficient for germ-layer patterning in normally sized embryos, the correct levels of less-active Lefty1 are required for scale-invariant patterning in substantially smaller embryos. These experimental findings support the simulations of our size-dependent inhibition model (Figs. 4d and 5a,b), showing that a small reduction in Lefty production, which does not significantly affect mesendoderm formation, abrogates scaling.

Scaling depends on highly diffusive Lefty. The second prediction of our model is that scaling depends on the high diffusivity of Lefty, which must reach the end of the patterning field (Figs. 4e and 6a,b). To test this prediction, we decreased Lefty diffusivity and determined the consequences on scaling. To obtain a patterning system in which the diffusion of Lefty1 can be experimentally manipulated, we first generated embryos in which the only source of Lefty was Lefty1-GFP (green fluorescent protein). We rescued *lft1*$^{-/-}$;*lft2*$^{-/-}$ double mutants by injecting highly precise and physiologically relevant amounts (see Methods for details) of *lft1-GFP* mRNA into the yolk syncytial layer (YSL) to mimic the secretion of endogenous Lefty from the marginal zone (Fig. 6c). Consistent with the high diffusivity of Lefty[33,39], Lefty1-GFP reached the end of the patterning field within 60 minutes after YSL injection (Fig. 6d,e and Supplementary Video 2). A large proportion of *lft1*$^{-/-}$;*lft2*$^{-/-}$ mutant embryos was rescued to adulthood with this method in normally sized (~70% fully or partially rescued) and extirpated (~60% fully or partially rescued) embryos (Fig. 6f–h and Supplementary Fig. 4a–d). Thus, Lefty1-GFP provided from the marginal zone is sufficient not only to pattern germ layers but also to allow scaling. Next, to hinder Lefty1-GFP diffusion, we used a 'morphotrap'—an mCherry-labelled membrane-localized GFP-binding nanobody[40]. Co-injection of mRNA encoding the morphotrap and *lft1-GFP* mRNA into one-cell-stage embryos changed the localization of Lefty1-GFP from uniform extracellular to strongly membrane associated (Supplementary Fig. 4e). Crucially, the diffusion coefficient (D) of Lefty1-GFP in embryos expressing the morphotrap was significantly lower ($D = 7.7 \pm 3.2\,\mu m^2\,s^{-1}$ for Lefty1-GFP and $0.2 \pm 0.2\,\mu m^2\,s^{-1}$ for Lefty1-GFP + morphotrap (mean ± s.d.); Fig. 6i,j). In addition, the activity of Lefty was decreased by morphotrap binding (Supplementary Fig. 4f,g).

We then injected mRNA encoding the morphotrap into *lft1*$^{-/-}$;*lft2*$^{-/-}$ mutant embryos at the one-cell stage and generated local sources of Lefty1-GFP at the marginal zone (Fig. 6d,e). The expression of the morphotrap dramatically changed the range of Lefty1-GFP from a nearly uniform distribution to a short-range gradient that did not reach the end of the embryo (Fig. 6d,e and Supplementary Videos 2 and 3). In normally sized embryos, hindered Lefty diffusion did not significantly affect germ-layer patterning (Fig. 6f–h), possibly owing to decreased Lefty activity in the presence of morphotrap (Supplementary Fig. 4f,g). The change in Lefty distribution correlated with a steep drop in the rescue of extirpated embryos (Fig. 6f,g) and with an expanded mesendoderm (Fig. 6h and Supplementary Fig. 4c,d). Simulations of the size-dependent inhibition model with hindered Lefty diffusion recapitulated the experimentally observed change in Lefty distribution (Fig. 6a,b,d,e): the decreased Lefty range precludes scaling of Nodal signalling as Lefty cannot reach the distal end of the patterning field. Together, these observations show that hindering Lefty diffusion prevents scaling in extirpated embryos, supporting the prediction of the size-dependent inhibition model.

Lefty concentration increases in smaller embryos. The third prediction of our model is that the inhibitor concentration increases to reduce Nodal signalling in extirpated embryos (Figs. 4c and 7a), whereas the total amount of Lefty should slightly decrease over time due to feedback regulation (Fig. 7b). To test this prediction, we used quantitative immunoblotting and measured the amount of endogenous Lefty1 and histone H3 as a proxy for cellular mass. Histone H3 levels were reduced by approximately one-third after extirpation (Supplementary Fig. 5a–c). Importantly, the histone H3 signal intensity increased proportionally when 5, 10 or 15 embryos were loaded, showing that changes in total protein can be detected reliably (Supplementary Fig. 5c). The decrease in Lefty1 amounts in extirpated embryos was less pronounced than histone H3 levels, resulting in an increased Lefty1 concentration as predicted by the model (Supplementary Fig. 5b). However, Lefty1 intensities detected by the only currently available antibody against a zebrafish Lefty[35] were low (Supplementary Fig. 5a and see Supplementary Fig. 8 for unprocessed data); sufficient Lefty1 levels could only be reliably detected after 50% epiboly stages, so that earlier dynamics of potential changes in Lefty1 levels could not be analysed. To corroborate these findings and to uncouple the rise in Lefty concentration from feedback regulation, we quantified the GFP intensity after injection of physiologically relevant amounts of *lft1-GFP* mRNA in the YSL and found that extirpated embryos exhibited a higher GFP intensity than normally sized embryos (Fig. 7c).

Exogenous inhibitor can mediate scaling in lieu of Lefty. To assess whether this increase in inhibitor concentration is required for germ-layer scaling, we analysed mesendoderm patterning in untreated and extirpated *lft1*$^{-/-}$;*lft2*$^{-/-}$ mutants upon exposure to the small-molecule Nodal inhibitor SB-505124 (ref. [36]). In contrast to the YSL injection rescue approach, a reduction in embryo size should not affect the concentration of the tonic Nodal inhibitor in this experimental setup (Supplementary Fig. 6a–d). A large fraction of untreated *lft1*$^{-/-}$;*lft2*$^{-/-}$ mutants (~90%; Fig. 7d,e) was rescued by 4.8 µM of Nodal inhibitor exposure. By contrast, exposure of extirpated *lft1*$^{-/-}$;*lft2*$^{-/-}$ mutants to the same inhibitor concentration resulted in abnormal mesendoderm proportions and only ~30% displayed some phenotypic rescue (Fig. 7d,e and Supplementary Fig. 6e,f). These results show that tonic size-independent inhibition levels that are effective in normally sized embryos do not allow scaling, as the inhibitor concentration cannot increase in shortened embryos.

Our model implies that increasing tonic Nodal inhibitor levels should restore the appropriate Nodal signalling range in extirpated embryos. Consistent with this prediction, increasing the exposure of the small-molecule Nodal inhibitor from 4.8 µM to 6–7 µM significantly improved the rescue of extirpated *lft1*$^{-/-}$;*lft2*$^{-/-}$ mutants from ~26% to ~64% (Fig. 7e and Supplementary Fig. 6g), demonstrating that increased inhibitor levels are required for scaling in extirpated embryos.

Discussion

Together, four lines of evidence suggest that scale-invariant germ-layer patterning is achieved by size-dependent inhibition of Nodal signalling. First, the reduction of Lefty levels (Fig. 5) precludes scaling. Second, decreasing Lefty diffusivity interferes with scale-invariant patterning (Fig. 6). Third, the concentration of the Nodal inhibitor Lefty increases in extirpated embryos (Fig. 7c and

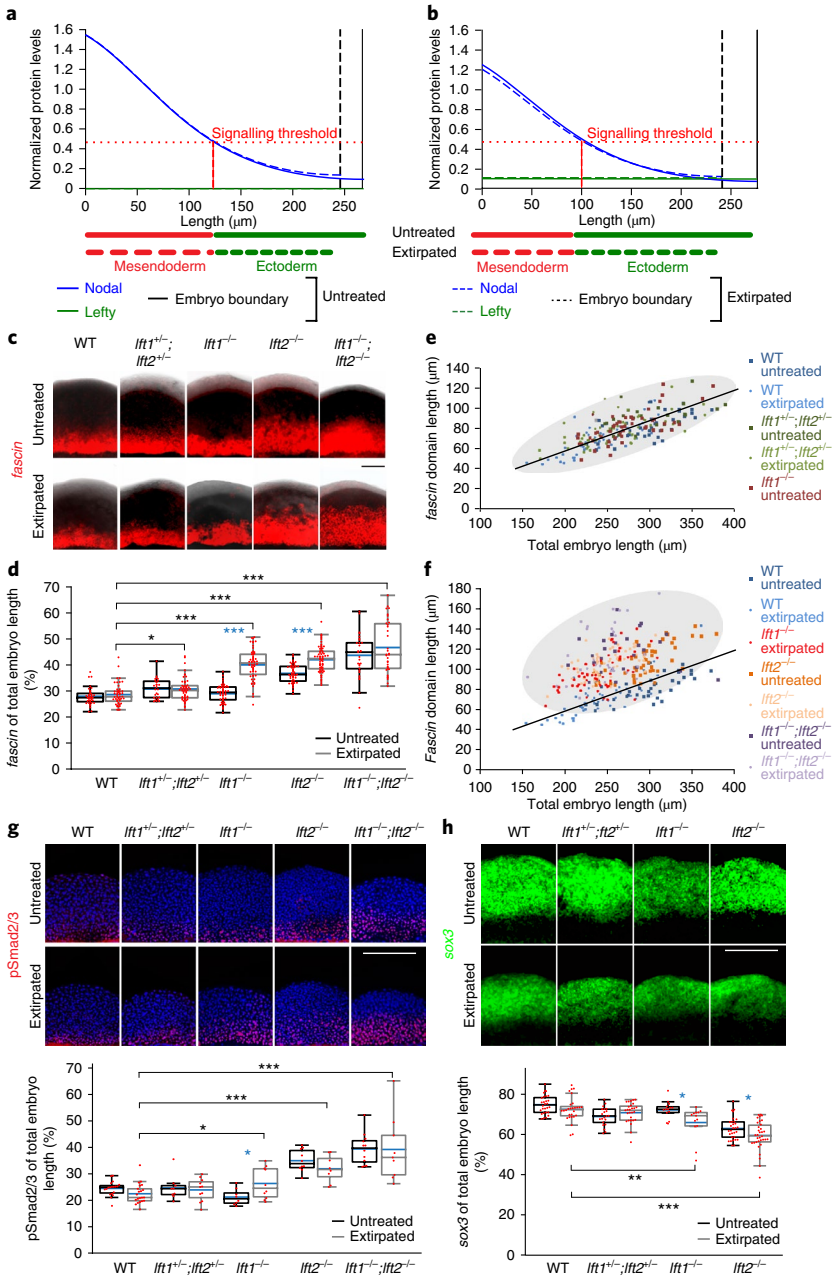

Fig. 5 | Germ-layer scaling depends on Lefty levels. a,**b**, Simulations of the size-dependent inhibition predict that, in the absence of Lefty, the mesendoderm is extended and does not scale (**a**), whereas reduced Lefty induction should prevent scaling in shortened embryos without a significant change in mesendoderm specification in normally sized individuals (**b**). **c**, Maximum intensity projections of lateral confocal stacks of *fascin* FISH in untreated and extirpated embryos with different numbers of *lft* alleles. **d**, Quantification of *fascin*-positive mesendoderm proportions. The asterisks show differences between untreated and extirpated embryos (blue asterisks) and between WT and *lft* mutant extirpated embryos (black asterisks) (*$P<0.05$, ***$P<0.001$). **e**,**f**, Quantification of *fascin* relative to embryo length. The data for WT untreated and extirpated are plotted in both **e** and **f**. For the *lft* mutants, the encircled domains cluster two groups: group 1 shows a similar mesendoderm proportion as WT individuals and a linear increase of mesendoderm with embryo size (**e**), whereas group 2 clusters in a wider domain with larger mesendodermal proportions, indicating an absence of scaling (**f**). In **c**–**f**, WT: *n* of untreated = 38, *n* of extirpated = 49; *lft1*$^{+/-}$;*lft2*$^{+/-}$: *n* of untreated = 26, *n* of extirpated = 55; *lft1*$^{-/-}$: *n* of untreated = 50, *n* of extirpated = 58; *lft2*$^{-/-}$: *n* of untreated = 50, *n* of extirpated = 63; *lft1*$^{-/-}$;*lft2*$^{-/-}$: *n* of untreated = 29, *n* of extirpated = 34. **g**,**h**, Maximum intensity projections of lateral confocal pSmad2/3 immunostaining (**g**) and *sox3* FISH stacks (**h**), and quantification in 2 hpe embryos with different numbers of *lft* alleles. For pSmad2/3: WT: *n* of untreated = 19, *n* of extirpated = 21; *lft1*$^{+/-}$;*lft2*$^{+/-}$: *n* of untreated = 10, *n* of extirpated = 11; *lft1*$^{-/-}$: *n* of untreated = 8, *n* of extirpated = 10; *lft2*$^{-/-}$: *n* of untreated = 9, *n* of extirpated = 8; *lft1*$^{-/-}$;*lft2*$^{-/-}$: *n* of untreated = 12, *n* of extirpated = 9. For *sox3*: WT: *n* of untreated = 28, *n* of extirpated = 28; *lft1*$^{+/-}$;*lft2*$^{+/-}$: *n* of untreated = 21, *n* of extirpated = 27; *lft1*$^{-/-}$: *n* of untreated = 14, *n* of extirpated = 13; *lft2*$^{-/-}$: *n* of untreated = 30, *n* of extirpated = 33. The asterisks show differences between untreated and extirpated embryos (blue asterisks) and between extirpated WT and *lft* mutant embryos (black asterisks) (*$P<0.05$; **$P<0.01$; ***$P<0.001$). The box plots show the median (blue line), the mean (black (untreated) and grey (extirpated) lines), 25% and 75% quantiles (box) and all included data points (red markers). Whiskers extend to the smallest data point within the 1.5 interquartile range of the lower quartile and to the largest data point within the 1.5 interquartile range of the upper quartile. Two-sided Student's *t*-tests were performed ($\alpha = 0.05$). See Supplementary Table 1 for statistics source data. Scale bars, 70 μm (**c**) and 200 μm (**g**,**h**).

Supplementary Fig. 5b). Fourth, the rescue of extirpated *lft1*$^{-/-}$;*lft2*$^{-/-}$ mutants requires higher amounts of a Nodal inhibitor drug than non-extirpated mutants (Fig. 7e and Supplementary Fig. 6g). In agreement with our mathematical model (Fig. 4, Supplementary Fig. 7 and Supplementary Note 1), these results support the idea that the concentration and high diffusivity of Lefty are essential to adjust germ-layer proportions.

The initial computational screen used *fascin* as a proxy for mesendoderm formation, which, in addition to Nodal, is also under the control of fibroblast growth factor (FGF) signalling[10,35]. For the simplified screening model, we subsumed the action of Nodal and FGF into one effective signalling gradient, as the induction of both *fgf* and *fascin* depends on Nodal signalling[35,41–44], Nodal and FGF signals have similar effective mobilities in zebrafish embryos[33,39], and the range of *fascin* can be changed by Lefty-dependent modulation of Nodal signalling[32,33]. Thus, our conclusions are not affected by how FGF, acting downstream of Nodal signalling, helps to regulate *fascin* expression together with Nodal. In more-refined simulations, we demonstrate the plausibility of our model for Nodal signalling based on pSmad2/3 activity (Supplementary Fig. 7m,n), a direct readout of Nodal activity. Although tissue proportions might be further refined by interactions with other signalling pathways, such as bone morphogenetic protein (BMP) and FGF[10,35,43,45] (Supplementary Fig. 7o,p and Supplementary Note 1), the scaled distribution of the Nodal signal transducer pSmad2—which is independent of BMP and FGF—and the scaled tissue proportions in *lft* mutants rescued by feedback-uncoupled Lefty—in which Lefty production is not under any transcriptional regulation—demonstrate the central role of Lefty in germ-layer scaling.

In agreement with previous findings[10,36,46,47], our results suggest that Nodal-mediated germ-layer patterning is robust to variations in signalling. Although the mesendoderm is significantly expanded in *lft1*$^{-/-}$ extirpated and *lft2*$^{-/-}$ untreated embryos (Supplementary Fig. 3c), most of them develop with normal morphology (Fig. 5 and

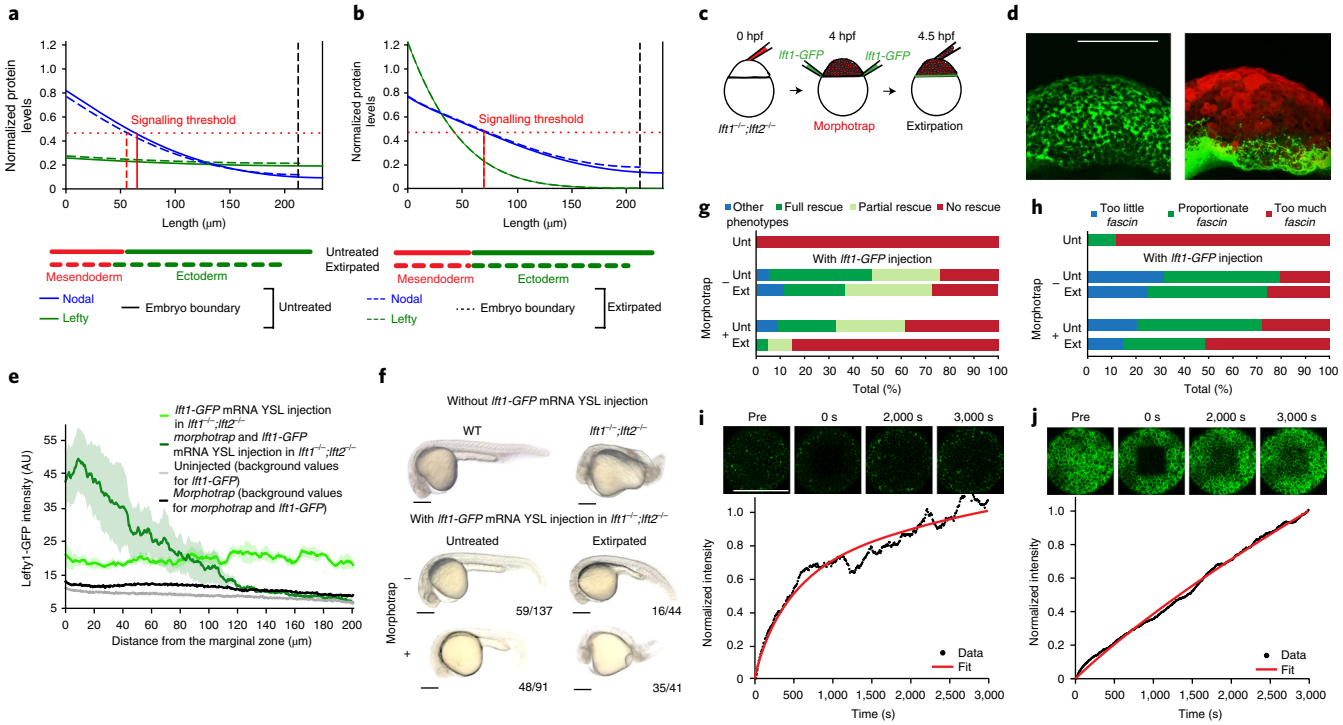

Fig. 6 | High Lefty diffusivity is required for scaling. a,**b**, Simulations of the model without feedback inhibition (*lft1-GFP* injected in the YSL; **a**) and hindered Lefty diffusion (morphotrap binds to *lft1-GFP*; **b**) predict that a reduction in Lefty diffusivity—preventing Lefty from reaching the animal pole—should preclude scaling. **c**, Schematic of morphotrap-mediated Lefty1-GFP diffusion hindrance in extirpated embryos. **d**, Maximum intensity projections of confocal stacks of *lft1*$^{-/-}$;*lft2*$^{-/-}$ embryos injected with (right panel) or without (left panel) morphotrap (injected at the one-cell stage) and *lft1-GFP* mRNA in the YSL (injected at the sphere stage). Lateral views are shown. **e**, Spatial distribution of Lefty1-GFP secreted from the YSL. The morphotrap prevents spreading of Lefty1-GFP towards the animal pole of the embryo. *n* of *lft1-GFP* mRNA injection = 6, *n* of *morphotrap* + *lft1-GFP* mRNA injection = 3, *n* of background values = 1, *n* of background values for morphotrap = 2. The experimentally determined distributions of Lefty1-GFP with morphotrap-mediated diffusion hindrance resemble the simulation of the scenario in **b**. The shaded regions are the s.e.m. **f**, Lateral views of representative 26 hpf *lft1*$^{-/-}$;*lft2*$^{-/-}$ embryos with different treatments. The numbers in the figure panel indicate the fraction of these representative embryos. **g**, Phenotype distributions in *lft1*$^{-/-}$;*lft2*$^{-/-}$ embryos after different treatments (*n* of *lft1*$^{-/-}$;*lft2*$^{-/-}$ = 39; *lft1*$^{-/-}$;*lft2*$^{-/-}$ + *lft1-GFP*: *n* of untreated (Unt) = 137, *n* of extirpated (Ext) = 44; *lft1*$^{-/-}$;*lft2*$^{-/-}$ + *morphotrap* + *lft1-GFP*: *n* of untreated = 91, *n* of extirpated = 44). Embryos with partial rescue display imperfect tails and reduced cephalic structures (that is, very mild Lefty mutant phenotypes). **h**, The fraction of treated *lft1*$^{-/-}$;*lft2*$^{-/-}$ embryos with low (<22%), normal (22–33%) and high (>34%) mesendoderm proportions (*n* of *lft1*$^{-/-}$;*lft2*$^{-/-}$ = 44; *lft1*$^{-/-}$;*lft2*$^{-/-}$ + *lft1-GFP*: *n* of untreated = 67, *n* of extirpated = 66; *lft1*$^{-/-}$;*lft2*$^{-/-}$ + *morphotrap* + *lft1-GFP*: *n* of untreated = 35, *n* of extirpated = 37). The fraction of rescued and non-rescued *lft1*$^{-/-}$;*lft2*$^{-/-}$ embryos correlates with the fraction of normal and high mesendoderm proportions in **g** and **h**. **i**,**j**, FRAP experiments demonstrate that Lefty1-GFP diffusion is hindered by the morphotrap. Representative FRAP data for Lefty1-GFP (**i**) and Lefty1-GFP with morphotrap (**j**) are shown. Microscopy images are shown before photobleaching (Pre), immediately after (0 s), as well at 2,000 s and 3,000 s after photobleaching. Diffusion coefficients and production rates were fitted to the recovery curves using previously published values for Lefty1-GFP protein stability[33]. The mean (±s.d.) diffusion coefficients were 7.7 ± 3.2 μm^2 s^{-1} for Lefty1-GFP (from *n* = 6 independent experiments) and 0.2 ± 0.2 μm^2 s^{-1} for Lefty1-GFP with morphotrap (from *n* = 4 independent experiments). See Supplementary Table 1 for statistics source data. Scale bars, 200 μm (**d**,**f**,**i**,**j**).

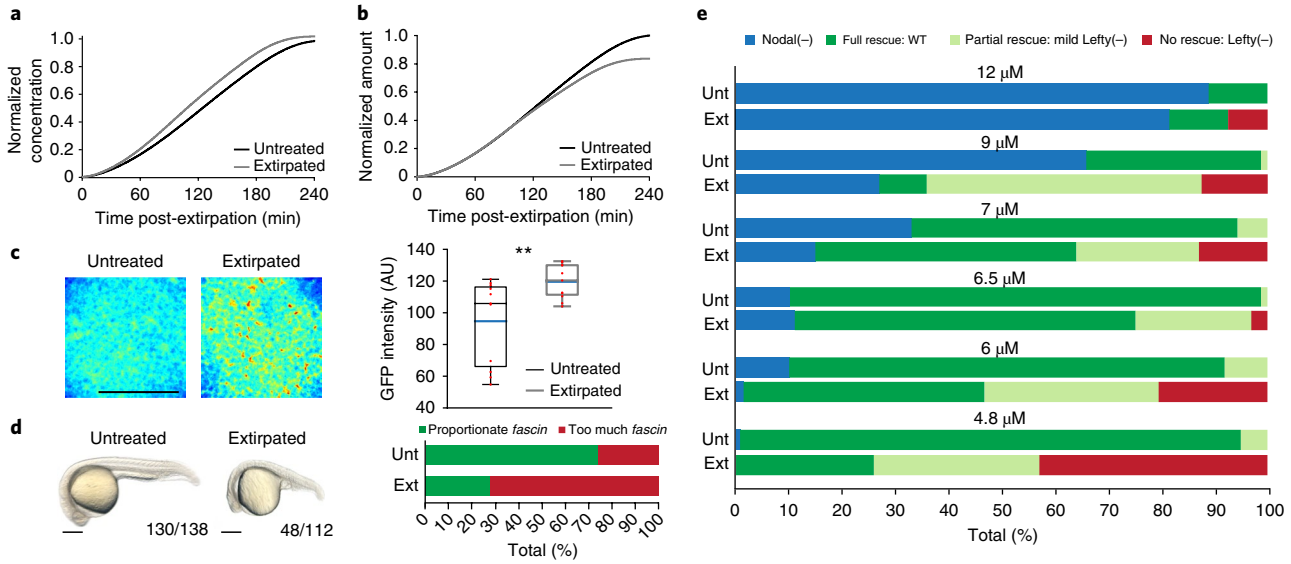

Fig. 7 | Lefty concentration increases in smaller embryos to allow scaling. a, The increase in Lefty concentration over time in smaller embryos predicted by the size-dependent inhibition model. **b**, The decrease in Lefty amount over time in smaller embryos predicted by the size-dependent inhibition model. **c**, Animal pole views of the maximum intensity confocal stack projections of WT untreated and extirpated embryos injected with *lft1-GFP* mRNA in the YSL (left) and the quantification of GFP intensity; $^{**}P < 0.01$; *n* of untreated = 11, *n* of extirpated = 11 (right). The box plot shows the median (blue line), the mean (black (untreated) and grey (extirpated) lines), 25% and 75% quantiles (box) and all included data points (red markers). Whiskers extend to the smallest data point within the 1.5 interquartile range of lower quartile and to the largest data point within the 1.5 interquartile range of the upper quartile. Two-sided Student's *t*-test were performed ($\alpha = 0.05$). **d**, Lateral views of representative 26 hpf *lft1*$^{-/-}$;*lft2*$^{-/-}$ embryos exposed to 4–4.8 µM of the Nodal inhibitor SB-505124. The numbers in the figure panel indicate the fraction of these representative embryos. Mesendoderm quantification (right panel) of *lft1*$^{-/-}$;*lft2*$^{-/-}$ embryos exposed to 4–4.8 µM of the Nodal inhibitor SB-505124 (*n* of untreated (Unt) = 27, *n* of extirpated (Ext) = 18). **e**, Phenotype quantification in *lft1*$^{-/-}$;*lft2*$^{-/-}$ embryos exposed to different concentrations of the Nodal inhibitor SB-505124. Untreated: 4.8 µM: *n* = 138, 6 µM: *n* = 160, 6.5 µM: *n* = 80, 7 µM: *n* = 106, 9 µM: *n* = 85, 12 µM: *n* = 36. Extirpated: 4.8 µM: *n* = 77, 6 µM: *n* = 146, 6.5 µM: *n* = 64, 7 µM: *n* = 108, 9 µM: *n* = 56, 12 µM: *n* = 27. Exposure to higher concentrations of the Nodal inhibitor SB-505124 increases *lft1*$^{-/-}$;*lft2*$^{-/-}$ mutant rescue after extirpation. The fraction of rescued and non-rescued *lft1*$^{-/-}$;*lft2*$^{-/-}$ embryos correlates with the fraction of normal and high mesendoderm proportions in **d**. See Supplementary Table 1 for statistics source data. Scale bars, 200 µm (**c**,**d**).

Supplementary Fig. 3b). This suggests that embryos can adapt to a certain degree of mesendoderm expansion, possibly up to ~42% (Supplementary Fig. 3a–c). However, this margin of tolerance is reduced in *lft1*$^{-/-}$;*lft2*$^{-/-}$ embryos rescued with YSL-expressed Lefty1-GFP, and an increase in the mesendoderm domain above ~35% in this context seems to invariably prevent phenotypic rescue. Thus, patterning robustness might arise from Nodal–Lefty regulatory feedback, which is absent in *lft1*$^{-/-}$;*lft2*$^{-/-}$ mutant embryos but present in embryos with at least one intact Lefty paralogue.

Previously postulated feedback-dependent scaling systems rely on modulators whose concentrations change depending on tissue size to adjust the signalling activity range by modulating the diffusion or clearance of the signal[11,14,48–56]. The Nodal–Lefty activator–inhibitor system is an excellent candidate for a modulator-based scaling mechanism: (1) Lefty (modulator) inhibits Nodal activity by binding and preventing it from activating its receptors, (2) the Nodal activity range is unaffected by the size reduction in extirpated embryos, as the Nodal distribution is restricted to the marginal zone owing to its low diffusivity[33], (3) Lefty diffuses significantly faster than Nodal and exhibits a nearly uniform distribution[33,36] (Figs. 4c and 6d,e,i and Supplementary Video 2), and (4) the production of Lefty is largely independent of the changes in size as Lefty-producing cells are located at the margin, which remains unaffected immediately following extirpation (Fig. 3e–i). An example of a modulator-based scaling mechanism is the recently proposed 'expansion–repression' model, in which scaling of signalling gradients is achieved by an expander that increases the range of the signal and that is itself repressed by the signal[51]. Superficially, our model can be interpreted as a mirror image of the 'expansion–repression' model—that is, a 'contraction–activation' system—as the 'inhibitor' (or the 'contractor') Lefty restricts the range of the signal (Nodal) and is activated by the signal. However, our theoretical model does not depend on feedback between the signal and the modulator. Because in our system the modulator inhibits the signal, it is sufficient to couple the changes in the concentration of the inhibitor to size to confer proportionate patterning. Similarly, we showed experimentally that Nodal-mediated Lefty activation is dispensable for scaling (Figs. 6 and 7 and Supplementary Figs. 4 and 6). This suggests that scale-invariant patterning is purely based on size-dependent Nodal inhibition that is mediated by Lefty, providing a foundation for the proportionate allocation of all future tissues.

The scaling mechanism that we found crucially depends on the coupling of the inhibitor concentration to embryo size, which is conferred by the high diffusivity of Lefty. Strikingly, a similar mechanism based on the coupling of cell volume to the concentration of a cell-cycle inhibitor has recently been found to control cell size in yeast[57]. Thus, it is possible that this simple mechanism might be widespread across various levels of biological organization to coordinate growth with cellular functions and patterning.

Methods

Methods, including statements of data availability and any associated accession codes and references, are available at https://doi.org/10.1038/s41556-018-0155-7.

Received: 2 August 2017; Accepted: 27 June 2018;
Published online: 30 July 2018

References

1. Morgan, T. H. Half embryos and whole embryos from one of the first two blastomeres. *Anat. Anz.* **10**, 623–685 (1895).
2. Cooke, J. Control of somite number during morphogenesis of a vertebrate, *Xenopus laevis*. *Nature* **254**, 196–199 (1975).
3. Inomata, H. Scaling of pattern formations and morphogen gradients. *Dev. Growth Differ.* **59**, 41–51 (2017).
4. Garcia, M., Nahmad, M., Reeves, G. T. & Stathopoulos, A. Size-dependent regulation of dorsal–ventral patterning in the early *Drosophila* embryo. *Dev. Biol.* **381**, 286–299 (2013).
5. Lauschke, V. M., Tsiairis, C. D., Francois, P. & Aulehla, A. Scaling of embryonic patterning based on phase-gradient encoding. *Nature* **493**, 101–105 (2013).
6. Kicheva, A. et al. Kinetics of morphogen gradient formation. *Science* **315**, 521–525 (2007).
7. Wartlick, O., Kicheva, A. & González-Gaitán, M. Morphogen gradient formation. *Cold Spring Harb. Perspect. Biol.* **1**, a001255 (2009).
8. Yu, S. R. et al. Fgf8 morphogen gradient forms by a source–sink mechanism with freely diffusing molecules. *Nature* **461**, 533–536 (2009).
9. Rogers, K. W. & Schier, A. F. Morphogen gradients: from generation to interpretation. *Annu. Rev. Cell Dev. Biol.* **27**, 377–407 (2011).
10. Rogers, K. W. & Müller, P. Nodal and BMP dispersal during early zebrafish development. *Dev. Biol.* https://doi.org/10.1016/j.ydbio.2018.04.002 (2018).
11. Umulis, D. M. & Othmer, H. G. Mechanisms of scaling in pattern formation. *Development* **140**, 4830–4843 (2013).
12. Gregor, T., Bialek, W., de Ruyter van Steveninck, R. R., Tank, D. W. & Wieschaus, E. F. Diffusion and scaling during early embryonic pattern formation. *Proc. Natl Acad. Sci. USA* **102**, 18403–18407 (2005).
13. Gregor, T., McGregor, A. P. & Wieschaus, E. F. Shape and function of the bicoid morphogen gradient in dipteran species with different sized embryos. *Dev. Biol.* **316**, 350–358 (2008).
14. Ben-Zvi, D., Shilo, B.-Z., Fainsod, A. & Barkai, N. Scaling of the BMP activation gradient in *Xenopus* embryos. *Nature* **453**, 1205–1211 (2008).
15. Ben-Zvi, D., Pyrowolakis, G., Barkai, N. & Shilo, B. Z. Expansion–repression mechanism for scaling the Dpp activation gradient in *Drosophila* wing imaginal discs. *Curr. Biol.* **21**, 1391–1396 (2011).
16. Hamaratoglu, F., de Lachapelle, A. M., Pyrowolakis, G., Bergmann, S. & Affolter, M. Dpp signaling activity requires pentagone to scale with tissue size in the growing *Drosophila* wing imaginal disc. *PLoS Biol.* **9**, e1001182 (2011).
17. Wartlick, O. et al. Dynamics of Dpp signaling and proliferation control. *Science* **331**, 1154–1159 (2011).
18. Cheung, D., Miles, C., Kreitman, M. & Ma, J. Scaling of the bicoid morphogen gradient by a volume-dependent production rate. *Development* **138**, 2741–2749 (2011).
19. Wartlick, O., Jülicher, F. & González-Gaitán, M. Growth control by a moving morphogen gradient during *Drosophila* eye development. *Development* **141**, 1884–1893 (2014).
20. Kicheva, A. et al. Coordination of progenitor specification and growth in mouse and chick spinal cord. *Science* **345**, 1254927 (2014).
21. Uygur, A. et al. Scaling pattern to variations in size during development of the vertebrate neural tube. *Dev. Cell* **37**, 127–135 (2016).
22. Schulte-Merker, S. et al. Expression of zebrafish goosecoid and no tail gene products in wild-type and mutant no tail embryos. *Development* **120**, 843–852 (1994).
23. Schier, A. F. Nodal morphogens. *Cold Spring Harb. Perspect. Biol.* **1**, a003459 (2009).
24. Chen, C. & Shen, M. M. Two modes by which Lefty proteins inhibit Nodal signaling. *Curr. Biol.* **14**, 618–624 (2004).
25. Feldman, B. et al. Zebrafish organizer development and germ-layer formation require Nodal-related signals. *Nature* **395**, 181–185 (1998).
26. Rebagliati, M. R., Toyama, R., Fricke, C., Haffter, P. & Dawid, I. B. Zebrafish Nodal-related genes are implicated in axial patterning and establishing left–right asymmetry. *Dev. Biol.* **199**, 261–272 (1998).
27. Sampath, K. et al. Induction of the zebrafish ventral brain and floorplate requires Cyclops/Nodal signalling. *Nature* **395**, 185–189 (1998).
28. Meno, C. et al. Mouse Lefty2 and zebrafish antivin are feedback inhibitors of nodal signaling during vertebrate gastrulation. *Mol. Cell* **4**, 287–298 (1999).
29. Feldman, B. et al. Lefty antagonism of Squint is essential for normal gastrulation. *Curr. Biol.* **12**, 2129–2135 (2002).
30. Chen, Y. & Schier, A. F. Lefty proteins are long-range inhibitors of Squint-mediated Nodal signaling. *Curr. Biol.* **12**, 2124–2128 (2002).
31. Cheng, S. K., Olale, F., Brivanlou, A. H. & Schier, A. F. Lefty blocks a subset of TGFβ signals by antagonizing EGF-CFC coreceptors. *PLoS Biol.* **2**, e30 (2004).
32. Choi, W. Y., Giraldez, A. J. & Schier, A. F. Target protectors reveal dampening and balancing of Nodal agonist and antagonist by miR-430. *Science* **318**, 271–274 (2007).
33. Müller, P. et al. Differential diffusivity of Nodal and Lefty underlies a reaction-diffusion patterning system. *Science* **336**, 721–724 (2012).
34. Wang, Y., Wang, X., Wohland, T. & Sampath, K. Extracellular interactions and ligand degradation shape the Nodal morphogen gradient. *eLife* **5**, e13879 (2016).
35. van Boxtel, A. L. et al. A temporal window for signal activation dictates the dimensions of a Nodal signaling domain. *Dev. Cell* **35**, 175–185 (2015).
36. Rogers, K. W. et al. Nodal patterning without Lefty inhibitory feedback is functional but fragile. *eLife* **6**, e28785 (2017).
37. Xu, C. et al. Nanog-like regulates endoderm formation through the Mxtx2–Nodal pathway. *Dev. Cell* **22**, 625–638 (2012).
38. Marcon, L., Diego, X., Sharpe, J. & Müller, P. High-throughput mathematical analysis identifies Turing networks for patterning with equally diffusing signals. *eLife* **5**, e14022 (2016).
39. Müller, P., Rogers, K. W., Yu, S. R., Brand, M. & Schier, A. F. Morphogen transport. *Development* **140**, 1621–1638 (2013).
40. Harmansa, S., Hamaratoglu, F., Affolter, M. & Caussinus, E. Dpp spreading is required for medial but not for lateral wing disc growth. *Nature* **527**, 317–322 (2015).
41. Gritsman, K. et al. The EGF-CFC protein one-eyed pinhead is essential for Nodal signaling. *Cell* **97**, 121–132 (1999).
42. Mathieu, J. et al. Nodal and Fgf pathways interact through a positive regulatory loop and synergize to maintain mesodermal cell populations. *Development* **131**, 629–641 (2004).
43. Bennett, J. T. et al. Nodal signaling activates differentiation genes during zebrafish gastrulation. *Dev. Biol.* **304**, 525–540 (2007).
44. Liu, Z. et al. Fscn1 is required for the trafficking of TGF-β family type I receptors during endoderm formation. *Nat. Commun.* **7**, 12603 (2016).
45. van Boxtel, A. L., Economou, A. D., Heliot, C. & Hill, C. S. Long-range signaling activation and local inhibition separate the mesoderm and endoderm lineages. *Dev. Cell* **44**, 179–191 (2018).
46. Dougan, S. T. The role of the zebrafish Nodal-related genes squint and cyclops in patterning of mesendoderm. *Development* **130**, 1837–1851 (2003).
47. Pei, W., Williams, P. H., Clark, M. D., Stemple, D. L. & Feldman, B. Environmental and genetic modifiers of squint penetrance during zebrafish embryogenesis. *Dev. Biol.* **308**, 368–378 (2007).
48. Gierer, A. & Meinhardt, H. A theory of biological pattern formation. *Kybernetik* **12**, 30–39 (1972).
49. Othmer, H. G. & Pate, E. Scale-invariance in reaction-diffusion models of spatial pattern formation. *Proc. Natl Acad. Sci. USA* **77**, 4180–4184 (1980).
50. Francois, P., Vonica, A., Brivanlou, A. H. & Siggia, E. D. Scaling of BMP gradients in *Xenopus* embryos. *Nature* **461**, E1 (2009).
51. Ben-Zvi, D. & Barkai, N. Scaling of morphogen gradients by an expansion–repression integral feedback control. *Proc. Natl Acad. Sci. USA* **107**, 6924–6929 (2010).
52. Umulis, D. M. Analysis of dynamic morphogen scale invariance. *J. R. Soc. Interface* **6**, 1179–1191 (2009).
53. Inomata, H., Shibata, T., Haraguchi, T. & Sasai, Y. Scaling of dorsal–ventral patterning by embryo size-dependent degradation of Spemann's organizer signals. *Cell* **153**, 1296–1311 (2013).
54. Ben-Zvi, D., Fainsod, A., Shilo, B. Z. & Barkai, N. Scaling of dorsal–ventral patterning in the *Xenopus laevis* embryo. *Bioessays* **36**, 151–156 (2014).
55. Werner, S. et al. Scaling and regeneration of self-organized patterns. *Phys. Rev. Lett.* **114**, 138101 (2015).
56. Rasolonjanahary, M. & Vasiev, B. Scaling of morphogenetic patterns in reaction-diffusion systems. *J. Theor. Biol.* **404**, 109–119 (2016).
57. Schmoller, K. M., Turner, J. J., Koivomagi, M. & Skotheim, J. M. Dilution of the cell cycle inhibitor Whi5 controls budding-yeast cell size. *Nature* **526**, 268–272 (2015).

Acknowledgements

We thank C. Hill for providing the Lefty1 antibody, M. Affolter for providing the morphotrap construct and J. Raspopovic and N. Lord for helpful comments. This work was supported by EMBO (M.A.-C., L.M. and P.M.) and HFSP (P.M.) long-term fellowships, the NSF Graduate Research Fellowship Program (K.W.R.), NIH grant GM56211 (A.F.S.), and funding from the Max Planck Society, ERC Starting Grant 637840 and HFSP Career Development Award CDA00031/2013-C (P.M.).

Author contributions

M.A.-C., A.F.S. and P.M. conceived the study. P.M. developed the extirpation assay and supervised the project. G.H.S. developed the extirpation device and the 2D map visualization workflow and optimized the pSmad2/3 immunostaining protocol. D.M. performed the experiments in Fig. 6i,j, Supplementary Figs. 4f,g, 5 and 8 and contributed to experiments in Fig. 6f,h. K.W.R. and A.F.S. contributed the data in Supplementary

Fig. 3d,e and provided the *lft* mutants before publication. M.A.-C. performed all other experiments. M.A.-C., A.B., D.M. and P.M. analysed the data. A.F.S. and P.M. conceptualized the scaling model. A.B. performed the mathematical analysis and simulations with assistance from L.M. and P.M. M.A.-C. and P.M. wrote the manuscript with input from all authors.

Competing interests

The authors declare no competing interests.

Additional information

Supplementary information is available for this paper at https://doi.org/10.1038/s41556-018-0155-7.

Correspondence and requests for materials should be addressed to P.M.

Methods

Generating smaller embryos by extirpation. All procedures involving animals were executed in accordance with the guidelines of the State of Baden-Württemberg (Germany) and approved by the Regierungspräsidium Tübingen (35/9185.46-5 and 35/9185.81-5).

Extirpation assays were performed using a glass capillary holder mounted on a Hamilton syringe and fixed in a micromanipulator (Narishige). Extirpations were performed in 4-hpf pronase-dechorionated sphere-stage embryos in Ringer's solution (116 mM NaCl, 2.8 mM KCl, 1 mM $CaCl_2$ and 5 mM HEPES). To allow wound healing after extirpation, embryos were left undisturbed for 30 min at 28 °C. The wound typically healed within 15 min after extirpation and the extirpated embryos were then transferred to normal embryo medium. To assess the survival of extirpated embryos without considering other mechanical disruptions of the extirpation assay (such as wound-healing failure or mechanical constraints due to changes in the embryo/yolk ratio), embryos that did not survive extirpation or that did not proceed to gastrulation were discarded.

For the quantification of cell numbers, extirpated cells from pools of ten embryos were transferred to individual PCR tubes containing 0.05% trypsin solution (Gibco) and incubated for 15 min at 37 °C. Dissociated cells were then quantified using a Neubauer chamber on an Olympus CKX41 microscope. Pools (10–20) of extirpated cells from 10 embryos were quantified per extirpation experiment. The average number of extirpated cells per embryo was 820 ± 130 cells, which corresponds to ~30% of the cells of an embryo at the sphere stage with ~3,000 cells.

Whole-mount in situ hybridization. *fascin*, *hgg1*, *vsx2*, *sox3*, *sox17* and *sox32* RNA probes for in situ hybridization assays were synthesized using SP6 or T7 polymerase (Roche) and digoxigenin (DIG)-modified (Roche) or dinitrophenol (DNP)-modified (Perkin Elmer) ribonucleotides. RNA probes were purified by ethanol precipitation with 7.5 M lithium chloride. For chromogenic in situ hybridizations, embryos were fixed overnight at 4 °C in 4% formaldehyde and then processed using an In situ Pro hybridization robot (Abimed/Intavis) and, as previously described[58], with the following modifications: no proteinase K treatment before the 90% epiboly stage; no pre-absorption of the anti-DIG antibody (11093274910, Roche); 5% dextran sulfate (Sigma) added to the hybridization solution[59]; riboprobes were denatured at 80 °C for 15 min and chilled on ice prior to hybridization using a final concentration of 1–2 ng µl^{-1}.

For fluorescent in situ hybridization (FISH), the following modifications were used: the blocking solution contained 2% Blocking Reagent (Roche) in 1× MABTw; incubation with anti-DIG (Roche) or anti-DNP-POD (FP1129, Perkin-Elmer) antibodies at a dilution of 1:150 in blocking solution was carried out overnight with shaking at 4 °C; after antibody incubation, embryos were washed six times for 20–30 min at room temperature with PBS containing 0.1% Tween (PBST) and the signal was developed with 100 µl TSA Cy3 or Cy5 at a dilution of 1:75 in amplification buffer (Perkin Elmer) for 1 h at room temperature without shaking.

For imaging, embryos were embedded in 1% low-melting point agarose, transferred to glass-bottom culture dishes (MatTek corporation) and oriented manually. Only embryos that were mounted with the vegetal–animal axis completely parallel to the cover glass were used for analysis. For chromogenic in situ samples, images were captured using an Axio Zoom.V16 (Zeiss). For fluorescent in situ samples, confocal laser scanning microscopy was performed using an LSM 780 NLO microscope (Zeiss). Images were processed using Fiji[60]. The number of *hgg1*-, *sox17*- and *sox32*-positive cells was quantified using the 'multi-point selection' tool[60]. *fascin* and *sox3* expression domains[44,61] in the central-most embryo regions were quantified using the 'measure' tool in Fiji. *fascin* was quantified from the margin of the embryo to the end of the domain with high expression values. *sox3* was quantified from the animal pole to the end of the domain with high expression values. The shield was excluded in the selection due to a higher expression of mesendodermal markers in this region. The size of embryos (from the margin to the animal pole) was measured similarly using bright-field images.

Immunostaining. For immunostainings, anti-phospho-histone H3 (anti-pH3; 3377S, Cell Signaling Technologies) and anti-pSmad2/3 (8828, Cell Signaling Technologies) antibodies were used.

Immunostaining for pH3 was carried out as described previously[62] with a 1:500 dilution of the primary antibody. For pSmad2/3, specimens were incubated in cold acetone at −20 °C for 20 min before blocking[35]. To ensure staining specificity, samples were exposed to low concentrations of anti-pSmad2/3 antibody (1:2,000 or 1:5,000) and samples were washed for 24 h with PBST before adding the secondary antibody. The signal was then amplified using horseradish peroxidase (HRP)-conjugated anti-rabbit antibodies (111-035-003, Jackson ImmunoResearch) and TSA Cy3 or Cy5 at a dilution of 1:75 in amplification buffer (Perkin Elmer) for 45 min at room temperature without shaking. Embryos were mounted for imaging as described above for FISH, but with the dorsal–ventral axis parallel to the cover glass in the case of pH3 staining. Confocal laser scanning microscopy was performed using an LSM 780 NLO (Zeiss) confocal microscope and images were processed using Fiji. The number of pH3-positive cells was quantified over a depth of 140 µm using the 'find maxima' plug-in in Fiji, with a fixed noise tolerance of 10,000 and manual correction. pSmad2/3 distributions were quantified from the margin of the embryo to the end of the pSmad2/3 nuclear staining using the 'measure' tool in Fiji. Non-nuclear staining was excluded. The extent of pSmad2/3 signalling was variable along the embryonic margin, and the mean of the pSmad2/3 domain at ten different points along the marginal zone is shown in all figures. The size of embryos from the margin to the animal pole was measured similarly using 4,6-diamidino-2-phenylindole (DAPI)-stained images.

Cell density quantification. Cell density measurements were performed in untreated and extirpated H2A-GFP[63] transgenic embryos. Embryos were mounted at 1 hpe and 2 hpe as described above for pH3 immunostaining. The number of cells was quantified as described above for pH3-positive cells but over a depth of 80 µm. The automatic segmentation and assignment of nuclei within the highly dense field of cells were carefully inspected visually and manually corrected.

Epiboly measurements. Untreated and extirpated embryos were imaged every 30 min after extirpation. Lateral images were taken. The extent of the embryo proper, the uncovered yolk, the blastoderm thickness and the total length (embryo proper + yolk) were measured. To calculate the percentage of epiboly, the percentage of the total length that was covered by the embryo proper was calculated. Blastoderm spreading during epiboly was calculated by subtracting the extent of the embryo proper at 1.5, 2, 3 and 4 hpe from the embryo proper extent at the first time point of analysis (1 hpe).

Light-sheet imaging for 3D reconstructions of *fascin* and pSmad2/3 domains. For 3D imaging, a Light-sheet Z.1 microscope (Zeiss) was used. Embryos were embedded in 1% low-melting point agarose and mounted in glass capillaries. For merging of the different views, far-red or green fluorescent beads (Thermo Fischer Scientific) were added to the agarose at a 1:200,000 dilution. After 3D reconstruction, 2D maps were generated as described previously[64] and rotated to the correct perspective using Hugin panorama photo stitcher software (http://hugin.sourceforge.net).

To quantify the signal distribution in the resulting 2D maps, images were opened in Fiji and rotated by 90°. The region corresponding to the whole embryo was selected, and the average intensity of *fascin* or pSmad2/3 from every point of the embryonic vegetal–animal axis was obtained using the 'plot profile' plug-in in Fiji. Distances in pixels were transformed into percentages of the total embryo length with the vegetal-most side defined as 0% and the animal-most side as 100%. Intensity was then normalized by subtracting background values (that is, the lowest intensity value closest to the animal pole of the embryo) and setting the highest intensity value to 1. For the quantification of pSmad2/3 distributions, background values were obtained by imaging *lefty* mRNA-injected embryos after pSmad2/3 immunostaining and normalized using the highest intensity value from the uninjected experimental data sets. 2D maps of DAPI were used as controls to rule out spatial inhomogeneities along the embryonic vegetal–animal axis. The graphs in Figs. 1e and 3b represent scaled average maps obtained from several embryos.

To re-dimensionalize the scaled 2D maps (Figs. 1g and 3d), distances were multiplied by the measured embryo diameter and divided by π/2. Intensities were averaged in bins of 2 µm, and the mean and standard error of different individuals were calculated piece wise.

Assessment of Lefty1 and Lefty2 activity. mRNA encoding Lefty1-GFP or Lefty2-GFP[33] was generated by plasmid linearization with NotI (NEB), purification with a Qiagen PCR clean-up kit and in vitro transcription using SP6 mMessage mMachine kits (Ambion). Pronase-dechorionated wild-type (WT; TLAB) embryos at the one-cell stage were injected with different amounts of *lft1-GFP* (22 pg, 43 pg and 86 pg) or *lft2-GFP* (5 pg, 10 pg and 20 pg) mRNA along with 100 pg of 10 kDa Alexa546-dextran (Life Technologies). At the sphere stage, three to five embryos per condition were imaged on an LSM 780 (Zeiss) confocal laser scanning microscope, and eight embryos with three replicates per condition were collected for qRT–PCR at 50% epiboly. Extracellular fluorescence intensity quantifications and qRT–PCR measurements with Promega Go-Taq qPCR Master Mix were executed as described previously[33] using the zebrafish elongation factor *ef1a* as a normalization control.

Immunoblotting. WT (TE strain) zebrafish embryos around the 50% epiboly stage were deyolked manually with tweezers and a dissection needle. 'Negative control' embryos were treated from 4-cell to 8-cell stages onward with the Nodal inhibitor SB-505124 (S4696, Sigma Aldrich) at 50 µM as described previously[35]. The efficiency of inhibitor treatment was confirmed by assessing the phenotypes of inhibitor-treated and dimethylsulfoxide-treated embryos at 24 hpf. 'Positive control' embryos were injected with 10 pg Squint-encoding mRNA[33] to induce endogenous *lft1* expression and were staged according to the development of uninjected siblings. Deyolked embryo caps were transferred to microcentrifuge tubes, excess embryo medium was removed, embryos were mixed with sample buffer (94 mM Tris pH 6.8, 3% SDS, 15% glycerol, 150 mM dithiothreitol and 0.003% bromophenol blue; 1 µl per embryo) and lysed by vortexing and incubation at 95 °C for 10 min. Before loading, the samples were vortexed again and cleared by brief centrifugation.

The Lefty1 and H3 signals originated from different SDS–polyacrylamide gels and polyvinylidene difluoride (PVDF) membranes owing to differences in the abundance and molecular weights of these proteins. For anti-Lefty1 western blots 5, 10 or 15 embryos were loaded on 10% SDS–polyacrylamide gels (5 µl, 10 µl or 15 µl, respectively). The loading of samples at the concentration used for Lefty1 blots resulted in a saturated H3 signal; thus, samples were diluted fivefold to quantify H3 levels using 12% SDS–polyacrylamide gels. To resolve Lefty1 well and separate it from unspecific bands, we let proteins with a molecular weight of less than 25 kDa run off the gels for Lefty1 immunoblots, making subsequent detection of H3 (~15 kDa) impossible.

Proteins were blotted onto PVDF membranes using the Trans-Blot Turbo Transfer System (Bio-Rad) in 'mixed molecular weight' mode. Blotted membranes were blocked in PBST containing 5% milk powder for 1 h at room temperature and incubated with the primary antibody (diluted in PBST containing 5% milk powder; 1:2,000 for the Lefty1 antibody[35] and 1:10,000 for the histone H3 antibody (ab1791, Abcam)) at 4 °C overnight. The membranes were briefly rinsed with PBST, washed twice with PBST for 5 min and washed two more times with PBST for 10 min at room temperature. Membranes were then incubated with HRP-coupled anti-rabbit antibody (111-035-003, Jackson ImmunoResearch; diluted 1:10,000 in PBST containing 5% milk powder) for 1.5 h at room temperature, followed by a brief rinse with PBST, two washes with PBST for 5 min and two washes for 10 min at room temperature. Fresh PBST was added to the membranes before application of SuperSignal West Dura Extended Duration Substrate (Thermo Fisher Scientific). Chemiluminescence was detected with a Fusion Solo imaging system (Vilber Lourmat).

TIFF images were analysed in Fiji. Regions of interest were drawn around Lefty1 or H3 bands and the mean intensity values were used for further analysis. For lanes without clear Lefty1 bands, the signal intensity was measured at the position of the expected molecular weight based on embryos overexpressing *squint*. The region of interest dimensions were constant for all lanes measured on a given membrane (Supplementary Fig. 8). We did not subtract background intensities for the quantifications in Supplementary Fig. 5, which seemed to be higher in untreated than in extirpated embryos (Supplementary Fig. 8), although single bands in the untreated or extirpated samples did not consistently follow this general trend (perhaps representing yolk proteins[65] and possibly reflecting sample-related differences in deyolking efficiency). The Lefty1 signal from samples with 10 embryos provided the most reliable signal, whereas the signal for samples with 5 embryos was not robustly detectable and the signal from samples with 15 embryos might be close to saturation (Supplementary Fig. 5c).

Injection of *lft1-GFP* mRNA into the YSL. mRNA encoding Lefty1-GFP[33] was generated by plasmid linearization with NotI-HF (NEB), purification with a Qiagen PCR clean-up kit and in vitro transcription using SP6 mMessage mMachine kits (Ambion). To mimic endogenous Lefty secretion, a physiologically relevant amount of 100 pg *lft1-GFP* mRNA was precisely injected into 4 hpf (the sphere stage) pronase-dechorionated embryos at two equidistant points (1 nl of 50 ng µl^{-1} *lft1-GFP* mRNA per point) within the embryonic YSL. To identify physiologically relevant amounts, 40, 60, 80, 100, 160 and 200 pg *lft1-GFP* mRNA were tested in a careful titration series, and 100 pg *lft1-GFP* mRNA were found to most efficiently rescue *lft1*$^{-/-}$;*lft2*$^{-/-}$ mutants.

Extirpations were performed 20–30 min after YSL injections. Embryos were divided into three groups: one group was fixed at the shield stage and processed for FISH, the second was incubated in embryo medium at 28 °C in 24-well plates covered with 2% agarose (1 embryo per well) for phenotypic analysis at 24 hpf, and the third group was processed for imaging 45–60 min after YSL injections. Mounting for imaging was done as described above for FISH samples. Movies were recorded with identical imaging conditions. Embryos were imaged for a total of approximately 100 min and Fiji was used to generate the movies. For measurements of Lefty1-GFP intensity, injections of *lft1-GFP* mRNA in the YSL and extirpations were performed as described above, but imaging was carried out 1.5–2 h after injection. Samples were captured with identical imaging conditions. Twenty confocal slices were used for *z*-projections over a depth of 53 µm, and the intensity of equivalent areas of the images was quantified using the 'measure' plug-in in Fiji.

Hindering Lefty1-GFP diffusion. The morphotrap construct[40] comprises a strong GFP binder (K_d: ~0.3 nM)[66]. The morphotrap construct was digested with *Xho*I and *Xba*I to insert the morphotrap into a pCS2$^+$ expression plasmid. mRNA was generated as described above for *lft1-GFP*. One nanolitre containing 100–150 pg mRNA encoding the morphotrap was injected into one-cell-stage embryos for experiments shown in the middle panel of Supplementary Fig. 4e. Transplantation of cells expressing the morphotrap (bottom panel of Supplementary Fig. 4e) was performed as described above for the extirpation experiments. Briefly, 50–100 cells were transplanted from a sphere-stage donor previously injected with 200 pg morphotrap-encoding mRNA into the sphere-stage host embryos previously injected with 50 pg *lft1-GFP* mRNA.

Time-lapse imaging experiments (Supplementary Videos 2 and 3) showed that Lefty1-GFP mobility from the YSL is strongly affected by the presence of the morphotrap. However, Lefty1-GFP mobility is not abolished entirely. This outcome is expected—even for a high-affinity GFP binder—if binding is reversible and the on/off kinetics are fast[39]. The strong membrane localization of Lefty1-GFP in embryos expressing the morphotrap confirmed the high affinity. The movement of the Lefty1-GFP signal appeared to follow the membranes in these embryos and is slow, consistent with a low fraction of mobile Lefty1-GFP. However, morphogenetic movements during epiboly might play an additional role in Lefty1-GFP transport, possibly facilitating Lefty spreading towards the animal pole.

Testing the effect of morphotrap binding on Lefty1-GFP activity. WT (TE) embryos were injected at the one-cell stage with 1 nl injection mix containing 5 pg or 30 pg *lft1-GFP* mRNA and 0.05% phenol red. To test the effect of the morphotrap on Lefty1-GFP activity, 150 pg *morphotrap* mRNA was included in the injection mix. Lefty overexpression phenotypes were evaluated at 24 hpf. Three groups of Nodal loss-of-function phenotypes were defined according to their strength (Supplementary Fig. 4f,g): mild (S1), intermediate (S2) and severe (S3). For imaging, embryos were mounted in 2% methylcellulose in embryo medium. Bright-field images were acquired with an Axio Zoom.V16 (Zeiss).

Lefty1-GFP gradient measurements. A physiologically relevant amount of 100 pg mRNA encoding Lefty1-GFP was injected into the YSL of *lft1*$^{-/-}$;*lft2*$^{-/-}$ embryos. One group of embryos was additionally injected with 150 pg *morphotrap* mRNA at the one-cell stage. Ninety minutes after YSL injections, embryos were mounted and imaged using an LSM 780 NLO (Zeiss) confocal laser scanning microscope. Embryos were imaged between 90 min and 140 min after YSL injections. To measure the gradients of secreted Lefty1-GFP from the YSL, maximum intensity projections were generated from 28 confocal slices over a depth of 194 µm, and the 'plot profile' plug-in in Fiji was used to obtain the intensity of Lefty1-GFP from every point of the vegetal–animal axis in a central region of the embryo. Background values were obtained by imaging *lft1*$^{-/-}$;*lft2*$^{-/-}$ uninjected embryos (for the group injected with *lft1-GFP* mRNA) or *lft1*$^{-/-}$;*lft2*$^{-/-}$ injected with morphotrap (for the group injected with *morphotrap* + *lft1-GFP* mRNA).

Fluorescence recovery after photobleaching. WT (TE) embryos were injected at the one-cell stage with 1 nl injection mix containing 50 pg *lft1-GFP* mRNA and 0.05% phenol red. In experiments in which the effect of the morphotrap on Lefty1-GFP diffusivity was measured, 200 pg mRNA encoding the morphotrap were included in the injection mix. Pronase-dechorionated embryos were selected for homogeneous expression of the morphotrap using an Axio Zoom.V16 (Zeiss). Embryos were mounted around the oblong to the sphere stage in 1% low-melting agarose using 35-mm glass-bottom microwell dishes (MatTek). Fluorescence recovery after photobleaching (FRAP) was performed and analysed as described previously[33,67,68] using an LSM 780 NLO (Zeiss) confocal microscope at an imaging depth of 30–40 µm. Diffusion coefficients and production rates were fitted to the recovery curves using previously published values for Lefty1-GFP protein stability[33]. The fit was constrained with a minimal diffusion coefficient of 0.1 µm^2 s^{-1}, which is on the order of the speed of cell movements during early zebrafish development[33].

***lft1*$^{-/-}$;*lft2*$^{-/-}$ mutant rescue with the small-molecule Nodal inhibitor SB-505124.** Rescue experiments were performed as recently described[36]. Extirpations were performed in 4 hpf pronase-dechorionated embryos at the sphere stage as described above. Thirty to forty minutes after extirpation, embryos were transferred to 24-well plates covered with 2% agarose (1 embryo per well) and treated with 4.8 µM SB-505124 in embryo medium starting 40 min after extirpation (~30% epiboly stage). Embryos were then separated into two groups: one group was fixed 2–2.5 h after extirpation (the shield stage) and processed for FISH, and the second group was further incubated with the inhibitor at 28 °C until 24 hpf (20 h after extirpation) for phenotypic analysis. For the experiments with increasing Nodal inhibitor exposure, different concentrations from 6 µM to 12 µM SB-505124 in embryo medium were tested.

Mathematical modelling. Details of the computational screen and the parameters used for modelling of the size-dependent inhibition system are described in Supplementary Note 1 and Supplementary Table 2.

Statistics and reproducibility. Two tests were performed to assess whether experimental data were normally distributed: the Kolmogorov–Smirnov ($\alpha = 0.05$) and the Shapiro–Wilk tests ($\alpha = 0.05$). To analyse whether experimental groups were significantly different, two-sided Student's t-tests ($\alpha = 0.05$) were performed.

Embryos from zebrafish crosses were randomly allocated into experimental groups for extirpation, injections and drug treatments. Most experiments were carried out at least twice, and the findings of all key experiments were reliably reproduced. All replicates and precise *P* values are documented in the 'Summary' sheet of Supplementary Table 1, which states the number of independent samples, embryos and independent experiments.

Reporting Summary. Further information on experimental design is available in the Nature Research Reporting Summary linked to this article.

Code availability. The source code for the custom scripts used for data analysis in this study is available from the corresponding author on reasonable request.

Data availability. Supplementary Table 1 contains the source data for Figs. 1a,c,d,h, 2b,c,e–i, 3a, 5c–h, 6f–j and 7e and Supplementary Figs. 2a,b, 3a–c and 4a–d. The data that support the findings of this study are available from the corresponding author on reasonable request.

References

58. Thisse, C. & Thisse, B. High-resolution in situ hybridization to whole-mount zebrafish embryos. *Nat. Protoc.* **3**, 59–69 (2008).
59. Lauter, G., Soll, I. & Hauptmann, G. Two-color fluorescent in situ hybridization in the embryonic zebrafish brain using differential detection systems. *BMC Dev. Biol.* **11**, 43 (2011).
60. Schindelin, J. et al. Fiji: an open-source platform for biological-image analysis. *Nat. Methods* **9**, 676–682 (2012).
61. Dee, C. T. et al. A change in response to BMP signalling precedes ectodermal fate choice. *Int J. Dev. Biol.* **51**, 79–84 (2007).
62. Feng, X., Adiarte, E. G. & Devoto, S. H. Hedgehog acts directly on the zebrafish dermomyotome to promote myogenic differentiation. *Dev. Biol.* **300**, 736–746 (2006).
63. Pauls, S., Geldmacher-Voss, B. & Campos-Ortega, J. A. A zebrafish histone variant H2A.F/Z and a transgenic H2A.F/Z:GFP fusion protein for in vivo studies of embryonic development. *Dev. Genes Evol.* **211**, 603–610 (2001).
64. Schmid, B. et al. High-speed panoramic light-sheet microscopy reveals global endodermal cell dynamics. *Nat. Commun.* **4**, 2207 (2013).
65. Link, V., Shevchenko, A. & Heisenberg, C. P. Proteomics of early zebrafish embryos. *BMC Dev. Biol.* **6**, 1 (2006).
66. Saerens, D. et al. Identification of a universal VHH framework to graft non-canonical antigen-binding loops of camel single-domain antibodies. *J. Mol. Biol.* **352**, 597–607 (2005).
67. Pomreinke, A. P. et al. Dynamics of BMP signaling and distribution during zebrafish dorsal–ventral patterning. *eLife* **6**, e25861 (2017).
68. Blässle, A. et al. Quantitative diffusion measurements using the open-source software PyFRAP. *Nat. Commun.* **9**, 1582 (2018).

nature cell biology

SUPPLEMENTARY INFORMATION

https://doi.org/10.1038/s41556-018-0155-7

In the format provided by the authors and unedited.

Scale-invariant patterning by size-dependent inhibition of Nodal signalling

María Almuedo-Castillo[1,3], Alexander Bläßle[1], David Mörsdorf[1], Luciano Marcon[1,3], Gary H. Soh[1], Katherine W. Rogers[1,2], Alexander F. Schier[2] and Patrick Müller[1]*

[1]Friedrich Miescher Laboratory of the Max Planck Society, Tübingen, Germany. [2]Department of Molecular and Cellular Biology, Harvard University, Cambridge, MA, USA. [3]Present address: Centro Andaluz de Biología del Desarrollo, Universidad Pablo de Olavide, Sevilla, Spain.
*e-mail: patrick.mueller@tuebingen.mpg.de

nature cell biology

SUPPLEMENTARY INFORMATION

https://doi.org/10.1038/s41556-018-0155-7

In the format provided by the authors and unedited.

Scale-invariant patterning by size-dependent inhibition of Nodal signalling

María Almuedo-Castillo[1,3], Alexander Bläßle[1], David Mörsdorf[1], Luciano Marcon[1,3], Gary H. Soh[1], Katherine W. Rogers[1,2], Alexander F. Schier[2] and Patrick Müller[1]*

[1]Friedrich Miescher Laboratory of the Max Planck Society, Tübingen, Germany. [2]Department of Molecular and Cellular Biology, Harvard University, Cambridge, MA, USA. [3]Present address: Centro Andaluz de Biología del Desarrollo, Universidad Pablo de Olavide, Sevilla, Spain.
*e-mail: patrick.mueller@tuebingen.mpg.de

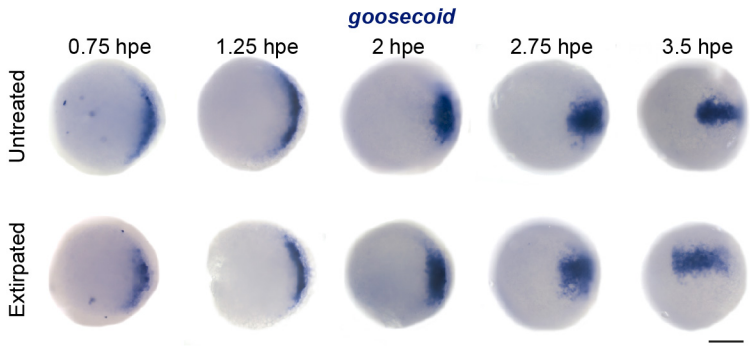

Supplementary Figure 1

Similar developmental speed in untreated and extirpated embryos.

Animal pole view images of *goosecoid* expression. Changes in the *goosecoid* expression domain during development proceed with a similar speed in untreated and extirpated embryos. Unt: Untreated; Ext: Extirpated. 0.75 hpe: n[untreated]=9, n[extirpated]=7; 1.25 hpe: n[untreated]=12, n[extirpated]=11; 2 hpe: n[untreated]=9, n[extirpated]=11; 2.75 hpe: n[untreated]=7, n[extirpated]=13; 3.5 hpe: n[untreated]=10, n[extirpated]=14. Scale bar: 200 μm.

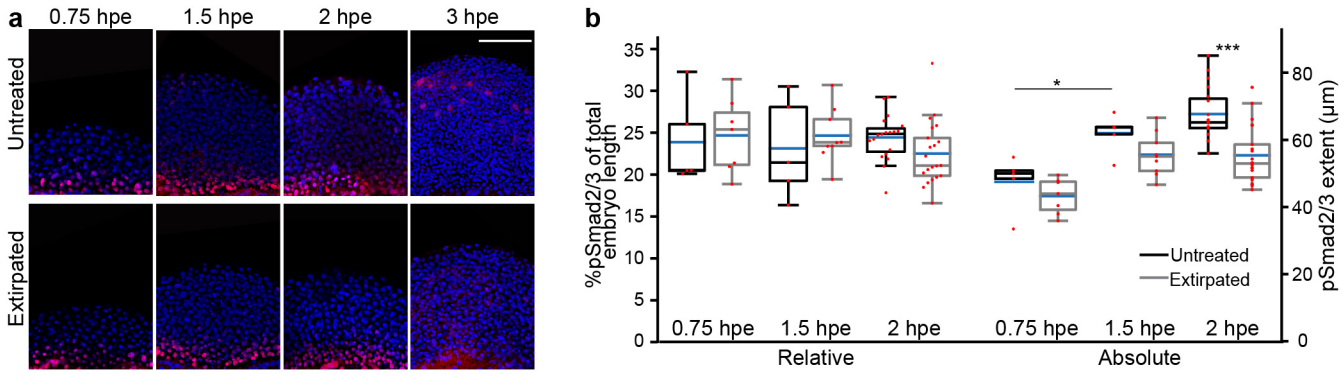

Supplementary Figure 2

Scaling of Nodal signaling after extirpation.

(a) Maximum intensity projections of lateral confocal pSmad2/3 immunostaining stacks, and **(b)** quantification of relative and absolute pSmad2/3 domains in untreated and extirpated embryos at different times after extirpation. 0.75 h post extirpation (hpe): n[untreated]=5, n[extirpated]=7; 1.5 hpe: n[untreated]=5, n[extirpated]=9; 2 hpe: n[untreated]=19, n[extirpated]=21. *p<0.05, ***p<0.001. Two-sided Student's t-tests were performed (α=0.05). See Supplementary Table 1 for statistics source data. Box plots show median (blue line), mean (untreated: black; extirpated: grey lines), 25% quantiles (box), and all included data points (red markers). Whiskers extend to the smallest data point within the 1.5 interquartile range of the lower quartile, and to the largest data point within the 1.5 interquartile range of the upper quartile. Scale bar: 200 μm.

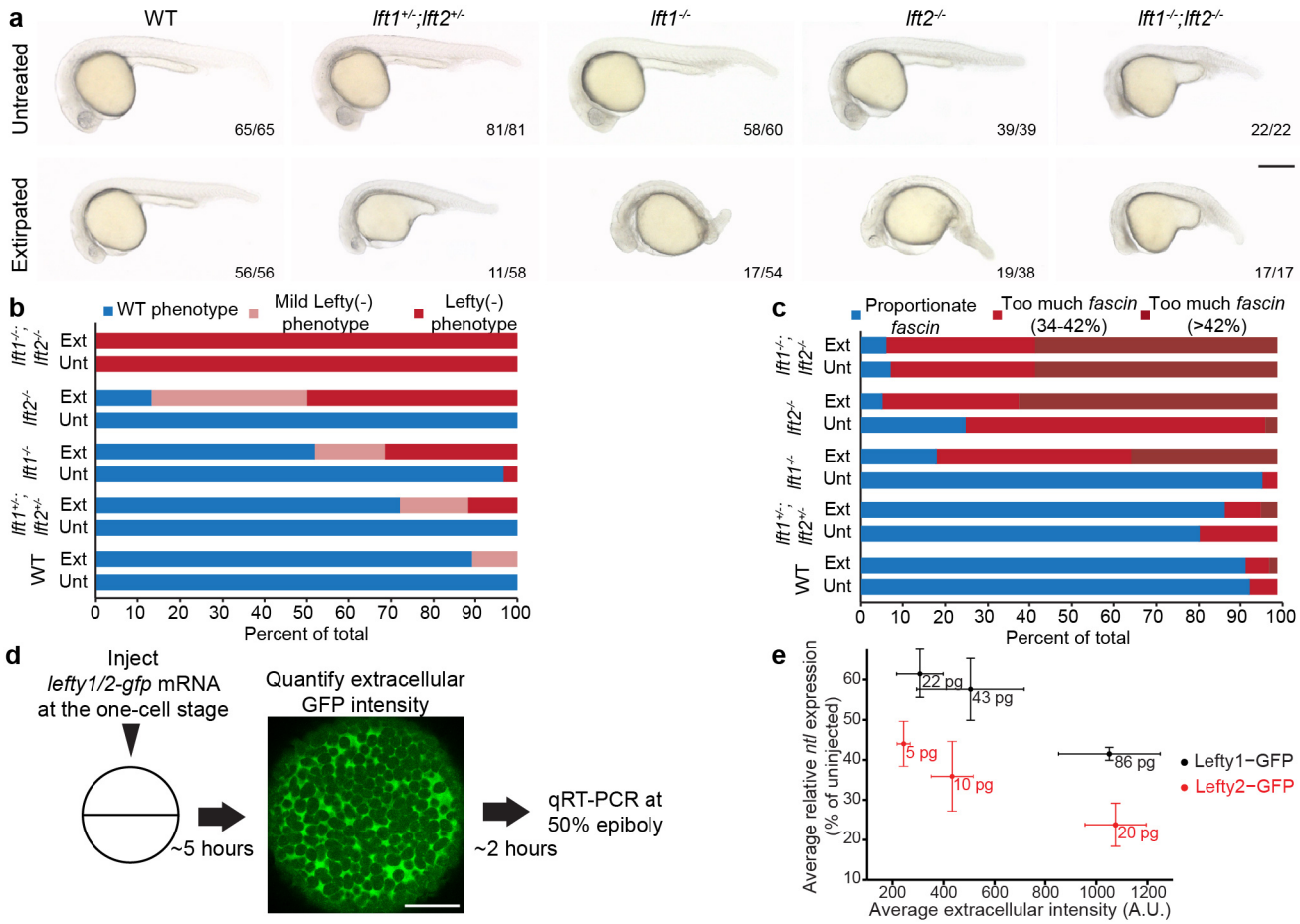

Supplementary Figure 3

Lack of Lefty1 precludes germ layer scaling.

(a) Lateral views of representative 24 hpf untreated and extirpated embryos with different numbers of functional *lefty* alleles. Numbers in the figure panel represent the fraction of these representative embryos. **(b)** Chart showing the fraction of phenotypes in different *lefty* mutants. "Mild *lft1*$^{-/-}$;*lft2*$^{-/-}$ phenotype" refers to embryos that do not exhibit the severe *lft1*$^{-/-}$;*lft2*$^{-/-}$ phenotype but show shorter or thicker tails or slightly reduced cephalic structures. **(c)** Fraction of *lefty* mutants with normal mesendoderm proportion (22-33%), high mesendoderm proportion (34-42%), and very high mesendoderm proportion (>= 42%). **(d)** Schematic of experiments to assess the activity of Lefty1 and Lefty2. Embryos were injected at the one-cell stage with different amounts of *lefty1*- or *lefty2-gfp* mRNA as indicated in figure panel (e). Some embryos were also injected with 100 pg Alexa546-dextran for subsequent generation of intracellular masks for extracellular intensity measurements. Extracellular GFP intensity was quantified at 5 hpf, and sibling embryos were collected at 50% epiboly. qRT-PCR using primers for the Nodal target gene *no tail* (*ntl*) was used to assess inhibitory activity. **(e)** Average *ntl* expression is plotted against average extracellular intensity. At similar intensities, Lefty2-GFP consistently repressed *ntl* expression more effectively than Lefty1-GFP. For fluorescence measurements: n[5 pg Lefty2-GFP]=5, n[10 pg Lefty2-GFP]=4, n[20 pg Lefty2-GFP]=3, n[22 pg Lefty1-GFP]=4, n[43 pg Lefty1-GFP]=5, n[86 pg Lefty1-GFP]=4. For qRT-PCR measurements, 3 samples with 8 embryos each were analysed per condition. Error bars: SEM. See Supplementary Table 1 for statistics source data. Scale bars: 200 μm (a) and 100 μm (d).

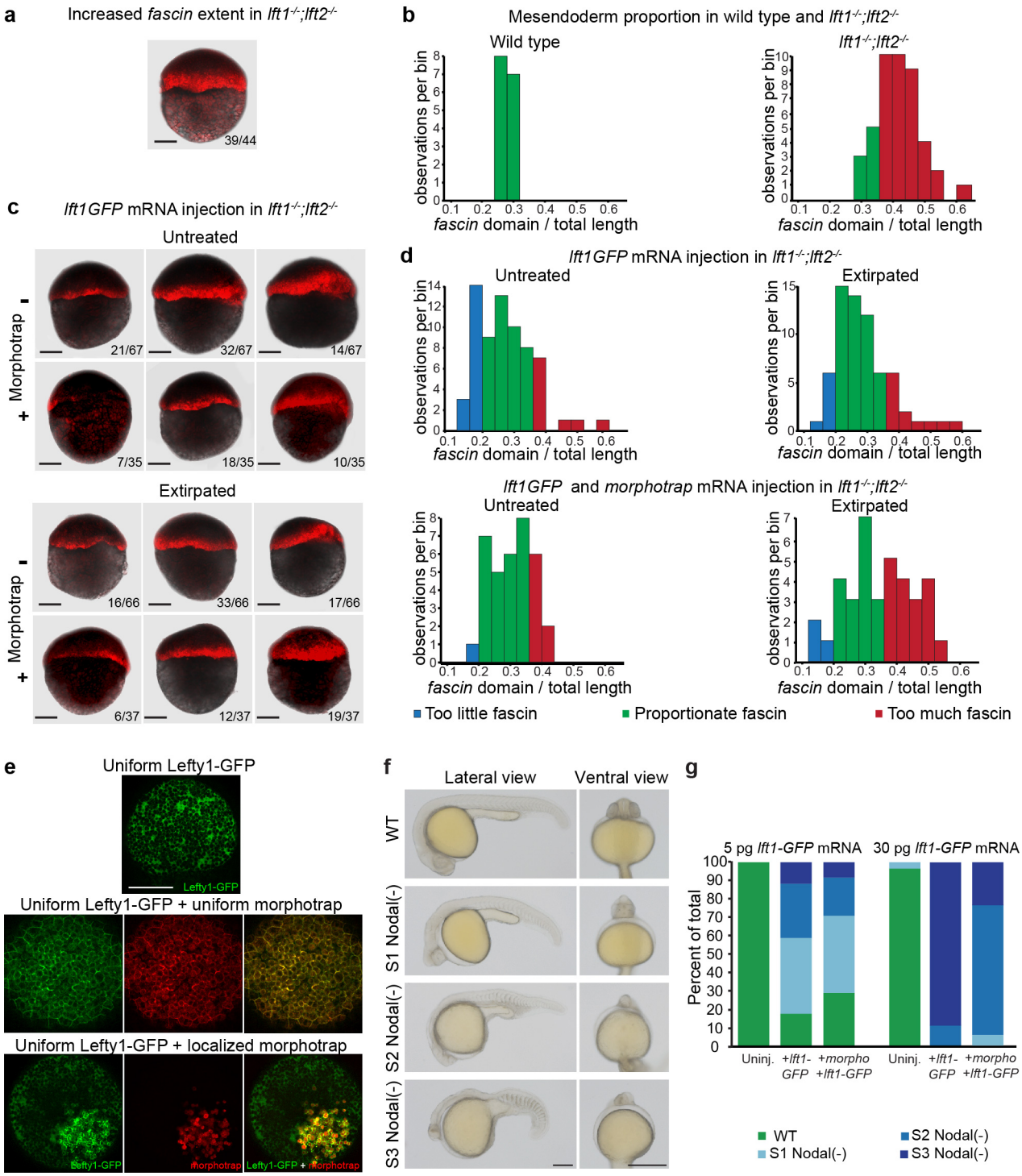

Supplementary Figure 4

Manipulation of Lefty1-GFP diffusion in zebrafish embryos.

(a,c) Maximum intensity projections of lateral confocal stacks of *fascin* expression in *lft1*$^{-/-}$;*lft2*$^{-/-}$ embryos subjected to different treatments. Representative embryos for each treatment are shown. Numbers in the figure panel represent the fraction of these representative embryos. **(b,d)** Mesendoderm proportions in differently sized embryos. Note that the fraction of embryos with normal mesendoderm extent is equivalent to the fraction of rescued *lft1*$^{-/-}$;*lft2*$^{-/-}$ embryos shown in Fig. 6. **(e)** Maximum intensity projections of

confocal stacks of 30-50% epiboly stage embryos. Animal pole views. The upper image shows an embryo injected with *lefty1-GFP* mRNA at the one-cell stage. The middle panel shows an embryo co-injected with morphotrap-encoding mRNA and *lefty1-GFP* mRNA at the one-cell stage. The lower panel shows an embryo injected with *lefty1-GFP* mRNA at the one-cell stage and transplanted with a morphotrap-expressing clone at sphere stage. The morphotrap changes the distribution of Lefty1-GFP from uniform extracellular to strongly membrane-associated. **(f,g)** Morphotrap binding affects Lefty activity. Lateral and ventral views of 24 hpf wild type embryos injected with morphotrap and different concentrations of *lefty1-GFP* mRNA. Representative embryos for each phenotypic category are shown (f). Distribution of phenotypes after different treatments (g). Three groups of Nodal loss-of-function phenotypes were defined according to their strength: mild (S1), intermediate (S2), and severe (S3). For 5 pg of *lft1-GFP* mRNA: n[uninjected]=32, n[+*lft1-GFP*]=34, n[+*morphotrap*+*lft1-GFP*]=24. For 30 pg of *lft1-GFP* mRNA: n[uninjected]=30, n[+*lft1-GFP*]=26, n[+*morphotrap*+*lft1-GFP*]=34. See Supplementary Table 1 for statistics source data. Scale bars: 200 μm.

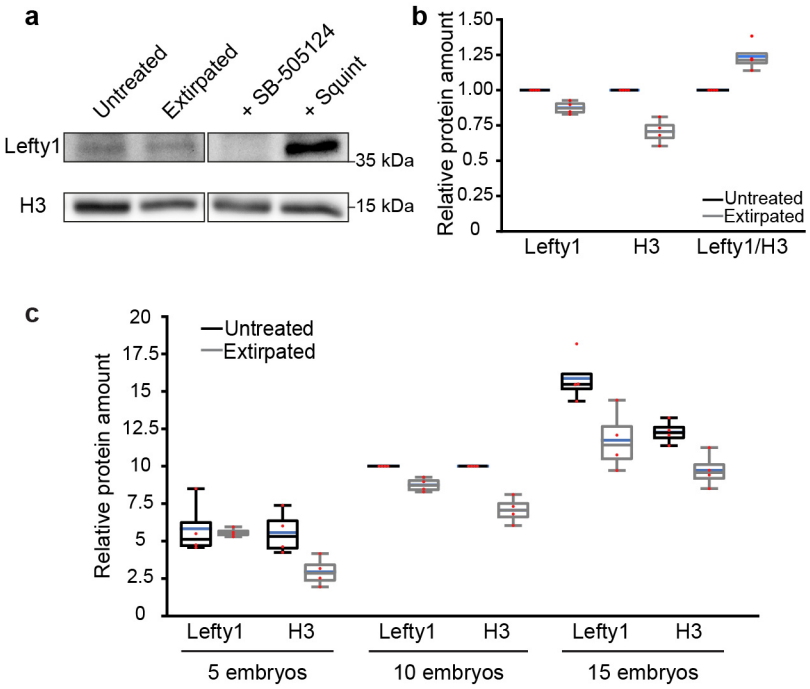

Supplementary Figure 5

Endogenous Lefty1 concentration increases in smaller embryos.

(a,b) Immunoblot analysis indicates a more pronounced decrease of the cellular marker Histone H3 compared to Lefty1, suggesting an increase in Lefty concentration in extirpated embryos (b). The samples derive from the same experiment, but for technical reasons (see Methods) Lefty1 and H3 levels were determined from independent immunoblots (see Supplementary Fig. 8 for raw data). **(c)** Quantification of Lefty1 and Histone H3 levels in the blots shown in Supplementary Fig. 8. All Lefty1 levels were normalised to the Lefty1 levels in the “10 embryos” sample, and all H3 levels were normalised to the H3 levels in the “10 embryos”. The Lefty1 and H3 levels in the “10 embryos” sample were set to 10. Note the approximately linear increase in Lefty1 and H3 levels between samples with different embryo numbers. On average, the decrease in H3 levels in extirpated compared to untreated embryos is more pronounced than the decrease in Lefty1 levels, similar to the model prediction in Fig. 7b. Box plots shows median (blue line), mean (untreated: black; extirpated: grey lines), 25% quantiles (box) and all included data points (red markers). Whiskers extend to the smallest data point within the 1.5 interquartile range of the lower quartile, and to the largest data point within the 1.5 interquartile range of the upper quartile.

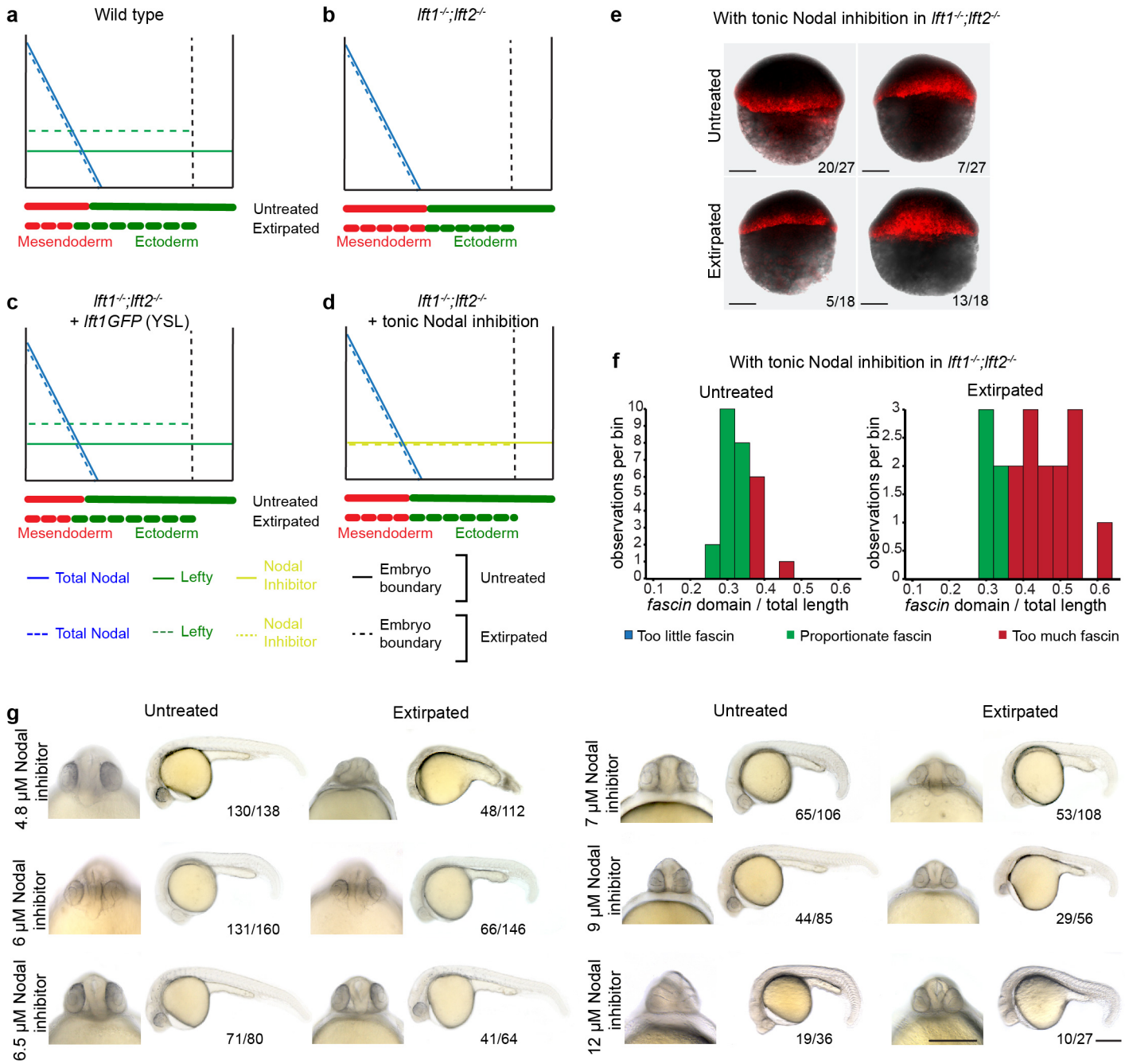

Supplementary Figure 6

An increase in Lefty concentration is required for scale-invariant patterning.

(a-d) Simplified qualitative models of Nodal (i.e. total Nodal, in contrast to the free Nodal shown in the simulations throughout the paper) and Lefty gradients in different scenarios to explain experimental observations. In contrast to our approach using ectopic Lefty gradients, most of the extirpated *lft1*$^{-/-}$;*lft2*$^{-/-}$ mutants exposed to levels of the Nodal inhibitor SB-505124 that rescue normally sized embryos are unable to restore normal mesendoderm proportions. In contrast to ectopic Lefty proteins (c), the Nodal inhibitor is provided tonically, and its concentration does not increase after a reduction in embryo size (d). **(e)** Maximum intensity projections of confocal stacks of *fascin* expression in *lft1*$^{-/-}$;*lft2*$^{-/-}$ embryos exposed to 4.8 µM of the Nodal inhibitor SB-505124. Lateral views. Representative embryos for each treatment are shown. Numbers in the figure panel represent the proportion of these representative embryos. **(f)** Mesendoderm proportions in embryos treated with 4.8 µM of the Nodal inhibitor SB-505124. **(g)** Lateral views of 26 hpf *lft1*$^{-/-}$;*lft2*$^{-/-}$ embryos exposed to different concentrations of the Nodal inhibitor SB-505124. Embryos representing the majority of phenotypes are

shown for each treatment. Numbers in the figure panel indicate the number of these representative phenotypes out of all analysed embryos. Scale bars: 200 μm.

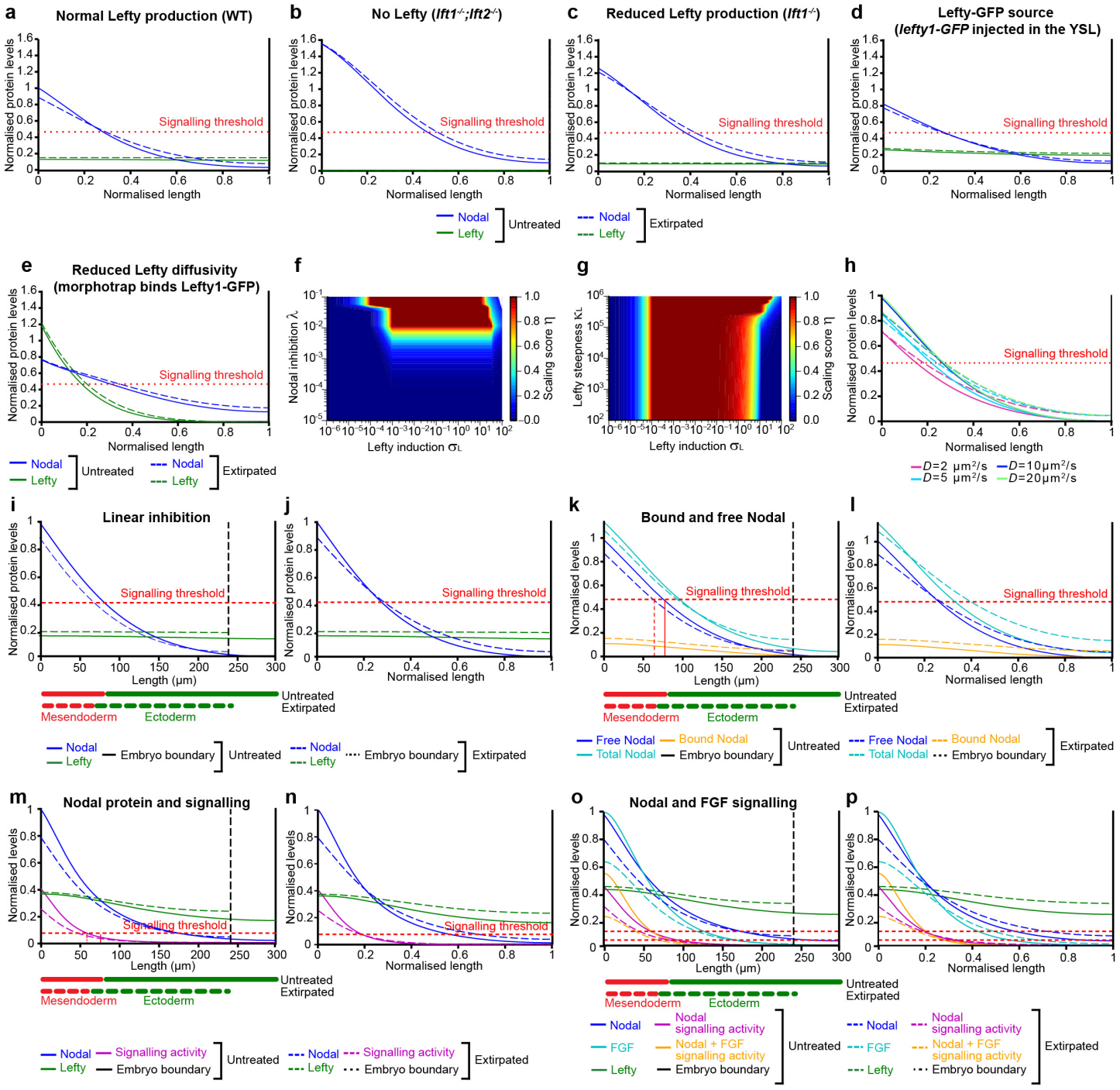

Supplementary Figure 7

Summary and extensions of the size-dependent inhibition model for scale-invariant patterning.

(a-e) Normalised Nodal and Lefty protein profiles scaled to embryo size for simulations of the size-dependent inhibition model with normal Lefty production (a), no Lefty production (b), reduced Lefty production (c), and feedback-less Lefty inhibition in the absence (d) or presence of morphotrap (e). In contrast to the graphs shown in Fig. 4, Fig. 5, and Fig. 6, these graphs show normalised length for both untreated and extirpated embryos. Here, models scale when the dashed and solid lines overlap at the intercept with the signaling threshold. In (c), Lefty induction was reduced by 30%. Normal Lefty diffusivity was set to D_L = 15 $\mu m^2/s$, and Lefty diffusivity in the presence of morphotrap (e) was set to D_L = 0.35 $\mu m^2/s$. All simulation parameter values are listed in Supplementary Table 2 [Parameter

Tables 3 and 4]. **(f,g)** Relationship between the maximum rate of Lefty induction and the strength of Lefty-mediated Nodal inhibition (f) or between the maximum rate of Lefty induction and Lefty induction steepness (g). The plots show maximum projections through the six-dimensional parameter space of the size-dependent inhibition model. **(h)** Simulation of the full model with different values for Lefty diffusivities. A minimal diffusion coefficient of approximately 7-10 $\mu m^2/s$ is required for scale-invariant patterning. **(i,j)** Implementation of the size-dependent inhibition model with linear Lefty inhibition. Scaling solutions are also found with a linear inhibition term, showing that the general mechanism of the size-dependent inhibition model is not dependent on the assumption of non-linear inhibition. (k-p) Extensions of the size-dependent inhibition model. **(k,l)** Simulations of the size-dependent inhibition system explicitly modelling total, free, and Lefty-bound (inhibited) Nodal protein, showing results for absolute (k) and normalised (l) embryo length. **(m,n)** Simulations with separate variables for signalling and protein levels showing results for absolute (m) and normalised (n) embryo length. **(o,p)** Simulations with separate variables for Nodal and FGF proteins and signalling.

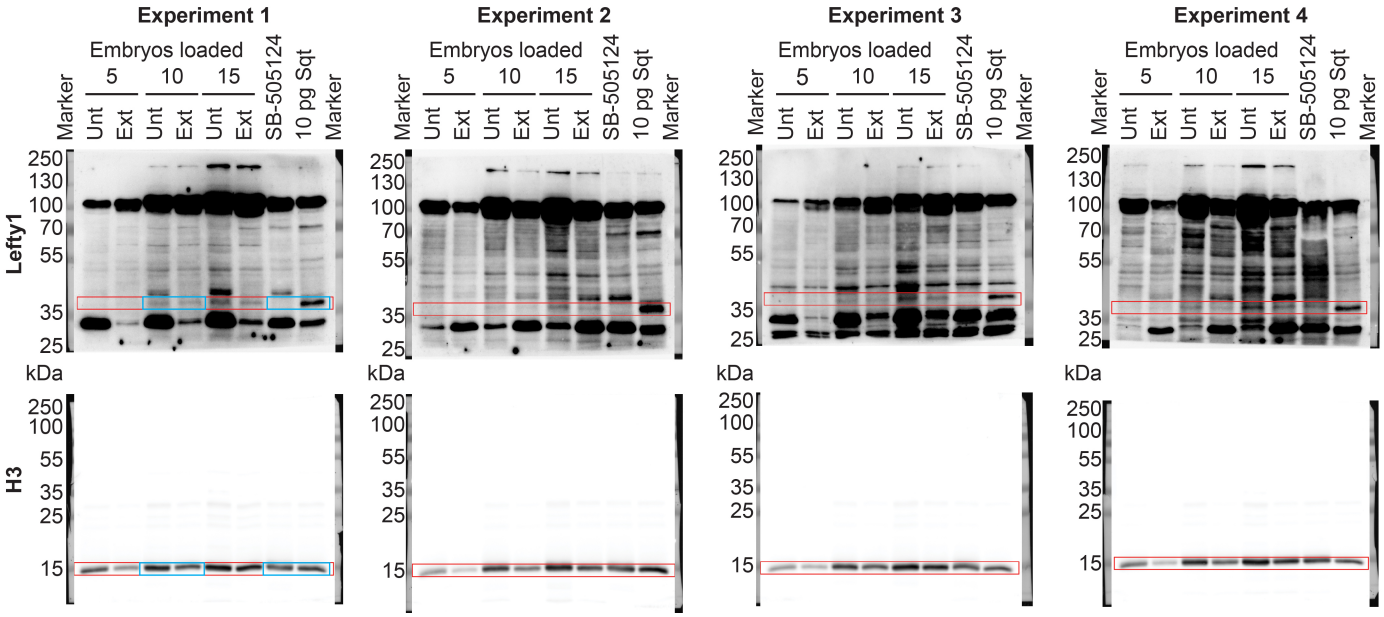

Supplementary Figure 8

Raw immunoblot data.

(a) Marker lanes are shown as overlay of the white light image at the edge of the membranes. Experiments 1, 2, and 4 are biological replicates, whereas experiment 3 is a technical replicate of experiment 1. Turquoise boxes indicate the regions shown in Supplementary Fig. 5a, and red boxes outline the regions used for quantification in Supplementary Fig. 5b,c. Unt: Untreated, Ext: Extirpated.

Supplementary Note 1
Screening for models of scale-invariant patterning. This note includes details about the mathematical modelling of Nodal/Lefty spatio-temporal dynamics, the execution of computational screens to identify the size-dependent inhibition system, and possible model extensions.

Supplementary Table 1
Statistics source data. The "Summary" sheet contains information about the number (n) of biologically independent samples / embryos / independent experiments, and precise p values from statistical tests. The other sheets contain the source data for all instances where the figures show representative experiments of multiple independent repeats, or averages of two independent experiments.

Supplementary Table 2
Simulation parameters. The file contains Parameter Tables 1-8, organized into individual sheets.

Supplementary Movie 1
Temporal dynamics of the scaling model. Nodal signalling levels (blue, solid line: normally sized embryo, dashed line: extirpated embryo) peak at the time of Nodal readout (red). Nodal signalling levels decrease rapidly afterwards, matching the time window of germ layer specification. Grey bars indicate the extent of the mesendodermal domain, and green lines show Lefty levels (solid line: normally sized embryo, dashed line: extirpated embryo).

Supplementary Movie 2
Lefty1-GFP diffusion from the marginal zone in *lefty1*$^{-/-}$;*lefty2*$^{-/-}$ embryos. Time-lapse imaging over 70 min after yolk syncytial layer (YSL) injections reveals high mobility of Lefty1-GFP emerging from the YSL. Lefty1-GFP levels increase in the YSL and over time localize to the extracellular space. Lefty1-GFP moves over a long distance to the animal pole within ≈40 min. Maximum intensity projection of a 60 μm *z*-stack. The animal pole is at the top, and Lefty1-GFP signal is shown in green. The experiment was repeated three times independently with similar results.

Supplementary Movie 3
Lefty1-GFP diffusion from the marginal zone in *lefty1*$^{-/-}$;*lefty2*$^{-/-}$ embryos expressing the GFP binding morphotrap. Time-lapse imaging over 70 min after YSL injections reveals hindered movement of Lefty1-GFP from the YSL in the presence of morphotrap. The morphotrap drastically changes the distribution of Lefty1-GFP from diffuse extracellular to membrane-bound. Maximum intensity projection of a 60 μm *z*-stack. The animal pole is at the top, and an overlay of the Lefty1-GFP signal (green) with the morphotrap signal (red) is shown. The experiment was repeated three times independently with similar results.

Supplementary Movie 4
Temporal dynamics of the extended scaling model. Nodal signalling, i.e. pSmad2/3 levels (magenta, solid line: normally sized embryo, dashed line: extirpated embryo), peaks at the time of Nodal readout (red). Dashed-dotted lines indicate the extent of the pSmad2/3 domain, blue lines show Nodal, and green lines show Lefty levels (solid line: normally sized embryo, dashed line: extirpated embryo).

Supplementary Note 1. Screening for models of scale-invariant patterning

We found that zebrafish embryos rapidly adjusted their tissue proportions after they were shortened by removal of ≈30% of their cells. This assay allowed us to generate smaller embryos at a defined developmental stage and directly analyse both short- and long-term developmental consequences. Previous studies analysed the long-term developmental consequences of size manipulations, making it difficult to directly link size-sensing mechanisms to later changes in morphology. We did not find evidence for changes in cell density nor increased proliferation rates in response to experimental shortening (Fig. 2), thus ruling out the possibility that cells change their size in smaller embryos. Instead smaller embryos must adjust the dimensions of their tissues to the smaller embryo size for proportionate patterning (Fig. 1).

Based on the analysis of early development following extirpation (Fig. 1, Supplementary Fig. 1, Supplementary Fig. 2, Fig. 3), we hypothesised that the Nodal/Lefty germ layer patterning system might sense embryo size and proportionally adjust tissue dimensions. We therefore performed a systematic computational screen and identified a scale-invariant patterning model based on size-dependent changes in the concentration of the highly diffusive long-range Nodal inhibitor Lefty. The screen comprised more than 400,000 parameter configurations constrained with all of our previous biophysical *in vivo* measurements[33] as well as the quantitative spatiotemporal aspects of germ layer patterning that we found in this study. This approach represents one of the most exhaustive multi-objective data fitting pursuits based on quantitative biological data, and yielded insights into the behaviour of the scale-invariant Nodal/Lefty patterning system over a wide range of parameter configurations (Fig. 4). Importantly, our model can directly recapitulate the kinetics of scale-invariant patterning over relevant time scales during zebrafish embryogenesis (Supplementary Movie 1), whereas efforts based on steady-state assumptions often model patterning over unrealistic time scales.

We experimentally confirmed four major predictions of this size-dependent inhibition model with direct experimental manipulations and quantification of protein levels and diffusivity. We measurably altered inhibitor concentration (Fig. 5, Supplementary Fig. 3) and diffusivity (Fig. 6, Supplementary Fig. 4), and determined that these factors are crucial for the scaling mechanism to function.

Our model explains how early signalling adjustments in response to shortening of the patterning field assure the correct proportions of all future tissues. Previously postulated scaling mechanisms rely on a tight feedback-mediated coupling between signalling molecules and modulators that change the signals diffusion or clearance to adjust patterning to tissue size. In contrast, we identified a scale-invariant patterning mechanism – size-dependent inhibition – that can act independently of a feedback-mediated coupling between the signal Nodal and its modulator Lefty. Instead, the long-range distribution of Lefty acts as a size sensor to scale the spatial extent of Nodal signalling, and it is sufficient to couple the changes in Lefty concentration to embryo size in order to confer scaling.

Modelling spatio-temporal Nodal/Lefty dynamics in wild type embryos

The minimal Nodal/Lefty system can be described by the following equations:

$$\begin{aligned} \frac{\partial N}{\partial t} &= D_N \nabla^2 N - \mu_N N - \lambda N \frac{L^2}{\kappa_{NL} + L^2} + \rho_N r(x,m) + \sigma_N \frac{N^2}{\kappa_N + N^2} \quad x \in [0,l] \\ \frac{\partial L}{\partial t} &= D_L \nabla^2 L - \mu_L L + \sigma_L \frac{N^2}{\kappa_L + N^2} \qquad\qquad\qquad\qquad\quad x \in [0,l] \end{aligned} \tag{1}$$

$N(x,t)$ and $L(x,t)$ denote Nodal and Lefty protein levels at time t and position $x \in [0,l]$ across the vegetal-animal axis. Nodal and Lefty have the diffusion coefficients D_N and D_L, and are removed with the clearance rate constants μ_N and μ_L[33].

Nodal is initially induced at the marginal zone independently of Nodal feedback[23] (Fig. 3), which was modelled with the constant Nodal production term $\rho_N r(x,m)$, where ρ_N is the production rate constant, and $r(x,m)$ is a rectangular pulse function given by

$$r(x,m) = \begin{cases} 1 & \text{if } x < m, \\ 0 & \text{else} \end{cases}$$

with m corresponding to the length of Nodal's production domain.

Moreover, Nodal feeds back on its own transcription[23] and thus undergoes auto-activation with the rate constant σ_N. Since Nodal feedback is limited by the finite amount of cellular material, we account for the saturation of Nodal auto-activation using a Hill-type function with the steepness parameter κ_N.

Nodal also induces its inhibitor Lefty. Similar to the term for Nodal auto-activation described above, Nodal-mediated Lefty induction is limited by the finite amount of cellular material, which we account for using a Hill-type function with steepness κ_L and a maximum induction rate σ_L.

Our experiments with *lefty1*$^{-/-}$ mutants indicate that Nodal inhibition might work cooperatively, and the inhibition of Nodal might be non-linear (see "Non-linear inhibition by Lefty" in the section "Extensions of the size-dependent inhibition model" below). We therefore chose a Hill-type function with steepness κ_{NL} and maximum inhibition rate λ to describe Lefty-mediated Nodal inhibition.

Since molecules cannot leave the embryo (modelled for a length of $[0, l]$) due to a tight enveloping layer, we used the following Neumann boundary conditions:

$$\left.\frac{\partial N}{\partial x}\right|_{x=0} = 0, \left.\frac{\partial L}{\partial x}\right|_{x=0} = 0, \left.\frac{\partial N}{\partial x}\right|_{x=l} = 0, \left.\frac{\partial L}{\partial x}\right|_{x=l} = 0 \tag{2}$$

In the following, we will refer to the system given by equations (1) and (2) as the *size-dependent inhibition* model.

Modelling spatio-temporal Nodal/Lefty dynamics without feedback

A subset of our perturbation experiments was conducted in double-homozygous *lefty1*$^{-/-}$;*lefty2*$^{-/-}$ mutants rescued by generation of highly precise and physiologically relevant (see Methods for details) Lefty1-GFP sources in the yolk syncytial layer (YSL). In these experiments, Lefty is no longer controlled by Nodal, but constantly produced in a similar region as Nodal specified by $r(x,m)$ with rate ρ_L, resulting in the following equations:

$$\begin{aligned} \frac{\partial N}{\partial t} &= D_N \nabla^2 N - \mu_N N - \lambda N \frac{L^2}{\kappa_{NL} + L^2} + \rho_N r(x,m) + \sigma_N \frac{N^2}{\kappa_N + N^2} && x \in [0,l] \\ \frac{\partial L}{\partial t} &= D_L \nabla^2 L - \mu_L L + \rho_L r(x,m) && x \in [0,l] \end{aligned} \tag{3}$$

This system is subject to the same boundary conditions as the size-dependent inhibition model. In the following, we will refer to the system given by equations (3) and (2) as the *size-dependent inhibition without feedback* model.

Screening for scaling solutions

We performed a computational screen to identify parameter combinations that can recapitulate the timing and spatial extent of Nodal signalling that we measured during germ layer patterning in differently sized zebrafish embryos.

A signalling threshold as a readout of Nodal signalling can be defined as

$$\tau_i := N(t, x = F_i) \tag{4}$$

where $i \in \mathrm{U}, \mathrm{E}$ represent results from experiments in untreated (U) and extirpated (E) embryos, respectively, and F_i is the extent of the mesendodermal domain determined using *fascin* FISH measurements.

To assess how well a given parameter combination scales in differently sized embryos, a "scaling score" can be defined as

$$\eta := \begin{cases} 1 & \text{if } R_\mathrm{U} \subseteq R_\mathrm{E} \vee R_\mathrm{E} \subseteq R_\mathrm{U} \\ \dfrac{|R_\mathrm{U} \cap R_\mathrm{E}|}{|R_\mathrm{U} \cup R_\mathrm{E}| - |R_\mathrm{U} \cap R_\mathrm{E}|} & \text{else} \end{cases} \tag{5}$$

Here R_i, $i \in \mathrm{U}, \mathrm{E}$ represents the interval between the threshold $\tau_{i,-}$ required to produce a Nodal signalling-dependent domain of size $F_{i,-} = \bar{F}_i - 2\sigma_i$ and the threshold that generates a Nodal readout of size $F_{i,+} = \bar{F}_i + 2\sigma_i$, where $\bar{F}_i$ is the mean size of the Nodal readout domain and σ_i the respective standard error. In other words, the scaling score η describes the overlap of the two threshold intervals produced by two times the standard error of the *fascin* domain measurements for the untreated and extirpated experiments. In the case that one interval completely overlaps with the other, η yields a score of 1. Thus, η provides a measure of scaling within the experimental measurement error.

To assess whether the model described by equations (1) and (2) can scale with a similar spatial extent as the measured *fascin* domains, we performed an extensive screen over a parameter space Θ for all unknown model parameters. The screened parameter space Θ was defined within a similar range as previously used values for inhibition strength[14, 53] and production rates[6]. We explored the space Θ of unknown parameters by varying each parameter over multiple orders of magnitude in three separate screens. Due to high computational costs, we kept either σ_L or κ_N fixed while varying all other parameters in the screens. A list of all known or fixed parameters can be found in Supplementary Table 2 [Parameter Table 1], and details about the screens are listed in Supplementary Table 2 [Parameter Table 2]. For each set of unknown parameters $\theta \in \Theta$, one simulation was run until time T, where T represents the time of Nodal signalling readout. For the size-dependent inhibition model, θ was defined as

$$\theta = \{\sigma_L, \sigma_N, \lambda, \kappa_L, \kappa_N, \kappa_{NL}\} \tag{6}$$

The scaling score η was then determined for each simulation to assess whether the tested parameter configuration leads to scaling. To provide a good degree of scaling, we required scenarios to have $\eta(\theta) \geq 0.9$, i.e. at least a 90% overlap of the untreated and extirpated measurement error. All simulations used the experimentally measured total embryo lengths l_i and mesendoderm domain sizes F_i (Supplementary Table 2 [Parameter Table 3]). Scenarios with the required degree of scaling are denoted as $\Theta_{\text{scaling}} \subset \Theta$.

Filtering of screen results

To exclude parameter configurations that produce unrealistic Nodal gradients and Lefty levels, we implemented three filters for the screening results as described in the following.

There is currently no information about endogenous Nodal or Lefty protein levels or their production rates, but we assume that the ratio between Nodal and Lefty levels does not exceed two orders of magnitude. With this filter, parameter configurations were excluded for which

$$\frac{\max(N(x,T))}{\max(L(x,T))} \notin (\frac{1}{100}, 100)$$

The second filter excluded unrealistically flat Nodal gradients. We only selected Nodal gradients that showed a substantial difference between the level at the margin $N(0,T)$ and the animal pole $N(l,T)$ by considering parameter configurations for which the Nodal gradient at readout time T decreases to 10 percent of the levels at the marginal zone, i.e.

$$\frac{N(l,T)}{N(0,T)} \leq 0.1$$

Similarly, all parameter configurations that result in signalling thresholds

$$\tau > 0.5 \max(N(x,T))$$

were excluded. With a signalling threshold below 50% of the maximum Nodal level throughout the embryo at readout time T, we only consider systems that can produce sufficiently steep gradients and signalling thresholds.

An intermediate level of Lefty-mediated Nodal inhibition is required for scaling

The central finding from our screen was that the shrunken mesendodermal domain results from an increase in Lefty concentration throughout the embryo. To show the relationship between Lefty induction and Nodal inhibition, we reduced the 6-dimensional parameter space Θ using a maximum projection of scaling scores by

$$\eta_{\max}(\theta, I) = \max_{i \notin I} H(k_i \in \theta)$$

where H are all scaling scores over the complete parameter space Θ, and $I = i_1, i_2, ...$ are the indices of the parameters of interest.

Maximum projections of scaling scores are displayed in Fig. 4d,e and in Supplementary Fig. 7f,g. From these plots it is clear that Lefty has an important role in scaling. Only large values for the maximum inhibition rate λ provide good scaling (Supplementary Fig. 7f). However, as the maximum Lefty induction rate σ_L increases, large values of λ become less favourable, indicating that the abundance of Lefty and its inhibition strength on Nodal need to be balanced (Supplementary Fig. 7f).

Similar conclusions can be drawn about the relationship between σ_L and the steepness parameter of Lefty induction κ_L. For intermediate values of σ_L, both a quick or a slow rise in Lefty levels allow scaling, whereas scaling is precluded with low values of σ_L (Supplementary Fig. 7g). However, with larger maximum Lefty induction rates σ_L, Lefty induction needs to be slowed down by higher values of the steepness parameter κ_L (Supplementary Fig. 7g), ensuring that Lefty is produced at the right rate to provide scaling at the proper time.

In double-homozygous *lefty1*$^{-/-}$;*lefty2*$^{-/-}$ mutants mesendoderm does not scale, resulting in expanded *fascin* domains of similar size in untreated ($F_U = 115$ µm) and extirpated ($F_E = 114$ µm) embryos. To test whether the size-dependent inhibition model can reproduce these experimental observations, we simulated all parameter configurations $\theta \in \Theta_{\text{scaling}}$ of the full model (equations (1) and (2)) with $\sigma_L = 0$, mimicking the absence of Lefty. If the simulations reproduced the measured *fascin* domains (Supplementary Table 2 [Parameter Table 3]) within 20 µm, we recorded the original parameter configuration θ of the full model in $\Theta_{\text{NoLft}} \subset \Theta_{\text{scaling}}$. A non-scaling Nodal profile can be seen in Supplementary Fig. 7b; since the dashed and solid lines do not overlap at the intercept with the signalling threshold, this parameter configuration does not scale.

Mesendoderm scaling fails if Lefty diffusion is reduced

We propose that Lefty senses embryo size due to its high diffusivity, allowing it to reach the animal pole within the time scale of germ layer formation. To test this hypothesis, multiple scenarios with Lefty diffusion coefficients ranging from $D_L = 0.35$ µm^2/s to $D_L = 20.0$ µm^2/s were analysed. Simulations with $D_L \geq 7$ µm^2/s showed good scaling behaviour, while lower rates of diffusion abrogated scaling (Fig. 4e, Fig. 6b, Supplementary Fig. 7h).

We further tested whether the model can reproduce the rescue experiments with Lefty1-GFP. Since these experiments were executed in *lefty1*$^{-/-}$;*lefty2*$^{-/-}$ mutants, Nodal cannot induce Lefty. In the *size-dependent inhibition without feedback* model, we therefore removed Nodal-mediated Lefty induction and simulated equations (3) and (2) with the parameter configuration

$$\tilde{\theta} = \{\rho_L, \sigma_N, \lambda, \kappa_N, \kappa_{NL}\}$$

We first tested whether the feedback-less model can reproduce the *fascin* domains in mutants rescued by exogenous *lefty1-GFP* mRNA injection. Simulations were performed using values for auto-activation σ_N and steepness parameters κ_N and κ_{NL} taken from scaling parameter configurations $\theta \in \Theta_{\text{lowP}}$ of the full model with feedback. We screened the remaining two unknown parameters ρ_L and λ, which represent exogenous production of Lefty1-GFP and its inhibition strength, respectively. The scaling configuration $\tilde{\theta}$ was selected that reproduced the measured *fascin* domains of $F_U = 68$ µm and $F_E = 60$ µm with the threshold $\tau(\theta)$ of the corresponding simulation of the full model with feedback.

We then simulated the feedback-less model for each scaling parameter configuration $\tilde{\theta}$ with the reduced Lefty1-GFP diffusion coefficients measured in the presence of the morphotrap ($D_L = 0.35$

$\mu m^2/s$). Since the morphotrap lowers Lefty activity (Supplementary Fig. 4f,g), λ was allowed to be smaller than the one in $\tilde{\theta}$. Finally, we selected parameter configurations $\tilde{\theta} \in \tilde{\Theta}_{\text{lowD}}(\theta)$ that fit the *fascin* domains measured in embryos with Lefty1-GFP + morphotrap ($F_U = 69$ µm and $F_E = 71$ µm) within a 20 µm range.

Nodal gradients for the feedback-less model with and without morphotrap are shown in Supplementary Fig. 7d,e. While the feedback-less model with normal Lefty diffusion scales, reducing Lefty diffusion to $D_L = 0.35\ \mu m^2/s$ precludes scaling.

Calculation of Lefty concentration and amount for Fig. 7a,b

The size-dependent inhibition model given by equations (1) and (2) was numerically simulated in COMSOL Multiphysics 3.5a, similar to previous studies[33, 39, 68]. Simulations were executed using the parameters in Supplementary Table 2 [Parameter Table 1] and Supplementary Table 2 [Parameter Table 4] in domains of 298 µm (untreated) and 241 µm (extirpated) with a fixed production domain ("marginal zone") of 0.298 µm for both conditions.

To calculate protein amount, Lefty levels were integrated in all domains for each time step. To calculate protein concentrations, the integrated Lefty amount per time point was divided by the size of the domains.

Extensions of the size-dependent inhibition model

To reduce model complexity for computational feasibility, we executed our screens with a minimal two-component system that describes one possible implementation of Lefty-mediated inhibition of Nodal signalling. This minimal system also included direct interactions between diffusible Nodal and Lefty, which are known to occur via intracellular signalling pathways. Furthermore, the minimal system did not explicitly take signalling crosstalk between Nodal and FGF into account, which can modulate the range of mesendodermal genes such as *fascin*[10, 35]. In the following, we analyse the influence of an alternative mode of Lefty-mediated Nodal inhibition and extend the minimal system to more realistic descriptions of developmental signalling systems.

Non-linear inhibition by Lefty

Lefty has been shown to inhibit Nodal signalling by two different mechanisms: Nodals form dimers, and Lefty can bind to Nodal ligands in the extracellular space or to Nodal receptors on cell membranes[24, 31, 34]. These observations suggest that two molecules of Lefty are required to inhibit one Nodal dimer or to bind to both the Nodal dimer and the co-receptor. To capture these modes of Lefty-mediated Nodal signalling inhibition, we used a non-linear second degree Hill-type inhibition term in equation (1).

To analyse whether scaling crucially depends on non-linear inhibition, we tested an implementation of the *size-dependent inhibition model with linear inhibition*:

$$\begin{aligned} \frac{\partial N}{\partial t} &= D_N \nabla^2 N - \mu_N N - \lambda N L + \rho_N r(x,m) + \sigma_N \frac{N^2}{\kappa_N + N^2} \quad x \in [0,l] \\ \frac{\partial L}{\partial t} &= D_L \nabla^2 L - \mu_L L + \sigma_L \frac{N^2}{\kappa_L + N^2} \qquad\qquad\qquad\quad x \in [0,l] \end{aligned} \tag{7}$$

Using this model, we found parameter configurations that produced scaling scores with $\eta = 1$ (Supplementary Table 2 [Parameter Table 5]).

The *size-dependent inhibition model with linear inhibition* showed a similar behaviour as the experimental results for untreated and extirpated wild type embryos (Supplementary Fig. 7i,j), and captured the expanded *fascin* expression domains in *lefty1*$^{-/-}$;*lefty2*$^{-/-}$ embryos. These findings demonstrate that the general mechanism behind the size-dependent inhibition model, i.e. the accumulation of the inhibitor Lefty, is not dependent on the assumption of non-linear inhibition.

However, the implementation of the *size-dependent inhibition model with linear inhibition* did not reproduce the experimental observations in untreated and extirpated *lefty1*$^{-/-}$ mutants: Reducing Lefty

production (σ_L) in the *size-dependent inhibition model with linear inhibition* (equation (7)) led to an expanded *fascin* domain in normally sized and smaller domains. These results indicate that the non-linear inhibition term used for the *size-dependent inhibition model* in equation (1) and all of its subsequent extensions more closely reflects the behaviour of Lefty-mediated Nodal signalling inhibition in zebrafish embryos.

Modelling of bound and free Nodal

The *size-dependent inhibition model* in equation (1) relies on the assumption that free, unbound Nodal protein activates signal transduction and correlates with Nodal signalling. In the following, we extend the model to also take into account inactive Nodal bound in a complex $C(x,t)$ with Lefty :

$$\begin{aligned}
\frac{\partial N}{\partial t} &= D_N\nabla^2 N - \mu_N N - \lambda N\frac{L^2}{\kappa_{NL}+L^2} + \rho_N r(x,m) + \sigma_N\frac{N^2}{\kappa_N+N^2} && x\in[0,l]\\
\frac{\partial L}{\partial t} &= D_L\nabla^2 L - \mu_L L + \sigma_L\frac{N^2}{\kappa_L+N^2} && x\in[0,l]\\
\frac{\partial C}{\partial t} &= D_C\nabla^2 C - \mu_C C + \lambda N\frac{L^2}{\kappa_{NL}+L^2} && x\in[0,l]
\end{aligned} \tag{8}$$

The total Nodal concentration can be calculated as

$$N_{\text{total}}(x,t) = N(x,t) + C(x,t) \tag{9}$$

We assume that the complex of Lefty-bound Nodal ($C(x,t)$) diffuses with a diffusion coefficient D_C and is removed with a clearance rate constant μ_C. No-flux Neumann boundary conditions for the system are given by

$$\left.\frac{\partial N}{\partial x}\right|_{x=0} = 0,\ \left.\frac{\partial L}{\partial x}\right|_{x=0} = 0,\ \left.\frac{\partial C}{\partial x}\right|_{x=0} = 0,\ \left.\frac{\partial N}{\partial x}\right|_{x=l} = 0,\ \left.\frac{\partial L}{\partial x}\right|_{x=l} = 0,\ \left.\frac{\partial C}{\partial x}\right|_{x=l} = 0 \tag{10}$$

For bound Nodal $C(x,t)$ we chose the mean of Lefty and Nodal diffusion and clearance ($D_C = 8.5$ µm^2/s and $\mu_C = 0.86\cdot 10^{-4}$/s). Simulations of the model (equations (8) and (10)) with the parameters defined for the two-component *size-dependent inhibition model* (Supplementary Table 2 [Parameter Table 4]) are shown in Supplementary Fig. 7k,l. Despite a difference in absolute values, the shape of the total Nodal profile $N_{\text{total}}(x,t)$ is similar to free Nodal $N(x,t)$.

Separate modelling of Nodal protein distributions and Nodal signalling

To keep model complexity minimal, we executed our screens with a system that describes both signalling and protein levels in the single variable N. This was based on the assumption that signal transduction acts at faster time scales than other kinetics in the model, such as protein clearance and inhibition.

In a more realistic description of the biological system, the merged $N(x,t)$ can be uncoupled into separate variables $S(x,t)$ – representing pSmad2/3 levels over space and time – and $N(x,t)$ – representing Nodal protein levels over space and time – as follows:

$$\begin{aligned}
\frac{\partial N}{\partial t} &= D_N\nabla^2 N - \mu_N N - \lambda N\frac{L^2}{\kappa_{NL}+L^2} + \rho_N r(x,m) + \sigma_N\frac{S^2}{\kappa_N+S^2} && x\in[0,l]\\
\frac{\partial L}{\partial t} &= D_L\nabla^2 L - \mu_L L + \sigma_L\frac{S^2}{\kappa_L+S^2} && x\in[0,l]\\
\frac{\partial S}{\partial t} &= \sigma_S\frac{N^2}{\kappa_S+N^2} - \mu_S S && x\in[0,l]
\end{aligned} \tag{11}$$

Here, σ_S represents the maximum rate of signal transduction that is described by a Hill-type function with steepness parameter κ_S. Moreover, Nodal signalling $S(x,t)$ decays linearly with the rate constant μ_S. Similar to our original model, we applied no-flux Neumann boundary conditions to all reactants:

$$\left.\frac{\partial N}{\partial x}\right|_{x=0} = 0,\ \left.\frac{\partial L}{\partial x}\right|_{x=0} = 0,\ \left.\frac{\partial S}{\partial x}\right|_{S=0} = 0,\ \left.\frac{\partial N}{\partial x}\right|_{x=l} = 0,\ \left.\frac{\partial L}{\partial x}\right|_{x=l} = 0,\ \left.\frac{\partial S}{\partial x}\right|_{x=l} = 0 \tag{12}$$

In contrast to the models used for the initial computational screens (equations (1) and (3)), Nodal auto-activation and Lefty induction are no longer directly dependent on the levels of $N(x,t)$, but are now under the control of $S(x,t)$.

The extended model (equations (11) and (12)) also scales. We simulated this model with similar parameters as the two-component *size-dependent inhibition model* and chose parameters for the clearance rate constant μ_S, a maximum transduction rate constant σ_S, and a steepness parameter κ_S (Supplementary Table 2 [Parameter Table 6]) that result in much faster turnover kinetics of S compared to the rest of the system.

Simulations of this extended model also yielded a flat Lefty profile (Supplementary Fig. 7m,n, Supplementary Movie 4). Nodal signalling levels read out at the threshold indicated by the dashed red line in Supplementary Fig. 7m,n result in gradients with a similar extent as the experimentally measured pSmad2/3 gradients (Fig. 3a) at roughly 23% of total embryo length around 1 hpe.

Modelling Nodal signalling and mesendoderm induction

In the *size-dependent inhibition model*, the scaling readout is the *fascin* expression domain. Since expression of the mesendodermal marker *fascin* depends on Nodal signalling[43, 44], we extended the model with separate variables for Nodal signalling-induced pSmad2/3 (P) and *fascin* (S) as follows:

$$\begin{aligned}
\frac{\partial N}{\partial t} &= D_N\nabla^2 N - \mu_N N - \lambda N\frac{L^2}{\kappa_{NL}+L^2} + \rho_N r(x,m) + \sigma_N\frac{P^2}{\kappa_N+P^2} && x\in[0,l]\\
\frac{\partial L}{\partial t} &= D_L\nabla^2 L - \mu_L L + \sigma_L\frac{P^2}{\kappa_L+P^2} && x\in[0,l]\\
\frac{\partial P}{\partial t} &= \sigma_P\frac{N^2}{\kappa_P+N^2} - \mu_P P && x\in[0,l]\\
\frac{\partial S}{\partial t} &= \sigma_S\frac{P^2}{\kappa_S+P^2} - \mu_S S && x\in[0,l]
\end{aligned} \tag{13}$$

Here, Nodal (N) activates pSmad2/3 (P) via a second-degree Hill term, while pSmad2/3 decays linearly. pSmad2/3 then activates *fascin* (S), introducing a delay between the activation of the signal transducer pSmad2/3 and the induction of *fascin*. Moreover, in contrast to the *size-dependent inhibition model*, both Nodal auto-activation and Lefty induction are mediated via pSmad2/3 activity. An example of a parameter configuration that reflects the experimental observations, i.e. scaled pSmad2/3 domains around 1.5 hpe and scaled *fascin* domains at 2 hpe, is shown in Supplementary Table 2 [Parameter Table 7].

Simplified model of Nodal- and FGF-mediated mesendoderm patterning

Proper specification of mesendoderm depends on both Nodal and FGF signalling[10, 35, 42]. In the *size-dependent inhibition model*, expression of the mesendodermal marker *fascin* is induced by N, which incorporates both Nodal and FGF signalling in a single variable. This was biologically motivated by the similar effective diffusivities of Nodal and FGF8[39], the dependence of *FGF* expression on Nodal signalling[41], and the overlapping production domains of Nodal and FGF in zebrafish embryos[43].

The *size-dependent inhibition model* can be extended to include the combined effects of FGF ($F(x,t)$)

signalling and pSmad2/3 ($P(x,t)$) on the induction of mesendoderm ($S(x,t)$) as follows:

$$\begin{aligned}
\frac{\partial N}{\partial t} &= D_N\nabla^2 N - \mu_N N - \lambda N\frac{L^2}{\kappa_{NL}+L^2} + \rho_N r(x,m) + \sigma_N\frac{P^2}{\kappa_N+P^2} && x\in[0,l]\\
\frac{\partial L}{\partial t} &= D_L\nabla^2 L - \mu_L L + \sigma_L\frac{P^2}{\kappa_L+P^2} && x\in[0,l]\\
\frac{\partial F}{\partial t} &= D_F\nabla^2 F - \mu_F F + \sigma_F\frac{P^2}{\kappa_F+P^2} && x\in[0,l]\\
\frac{\partial P}{\partial t} &= \sigma_P\frac{N^2}{\kappa_P+N^2} - \mu_P P && x\in[0,l]\\
\frac{\partial S}{\partial t} &= \sigma_{SP}\frac{P^2}{\kappa_{SP}+P^2} + \sigma_{SF}\frac{F^2}{\kappa_{SF}+F^2} - \mu_S S && x\in[0,l]
\end{aligned} \tag{14}$$

In this model, Nodal (N) activates pSmad2/3 (P). pSmad2/3 then induces Nodal, Nodal's inhibitor Lefty (L), and FGF (F). All activation/induction kinetics are represented by Hill functions with the steepness factors κ_N, κ_L, and κ_F, respectively. FGF has a similar effective diffusivity as Nodal ($D_F \approx D_N$), and a protein half-life of approximately 20 min[8] was used for the simulations. A combination of pSmad2/3 and FGF signalling then induces mesendoderm ($S(x,t)$) through two second-degree Hill-type functions. $S(x,t)$ was modelled to respond differently to FGF and pSmad2/3 since the parameters of the two inducing Hill functions (κ_{SF}, κ_{SP} ,σ_{SF}, σ_{SP}) could be different for FGF and pSmad2/3.

Using a computational screen, we identified parameter configurations that allow this model to scale for pSmad2/3 at 25% axis length and mesendodermal genes S such as *fascin* at 28% axis length (Supplementary Table 2 [Parameter Table 8], Supplementary Fig. 7o,p). While this analysis illustrates the general principle that scaling of mesendoderm is also plausible under the influence of an interaction between Nodal and a different signalling pathway, the simplified model does not take into account the full complexity of the system (e.g. scaling of pSmad2/3 and *fascin* at different times after extirpation, Lefty regulation by FGF signalling[35], and the different effects of FGF signalling on Nodal-dependent endoderm and mesoderm patterning[45]) and needs to be extended with future insights on the mechanisms by which Nodal and FGF control mesendoderm specification.

Appendix 5

Article

Cell Reports

Integration of Nodal and BMP Signaling by Mutual Signaling Effector Antagonism

Graphical Abstract

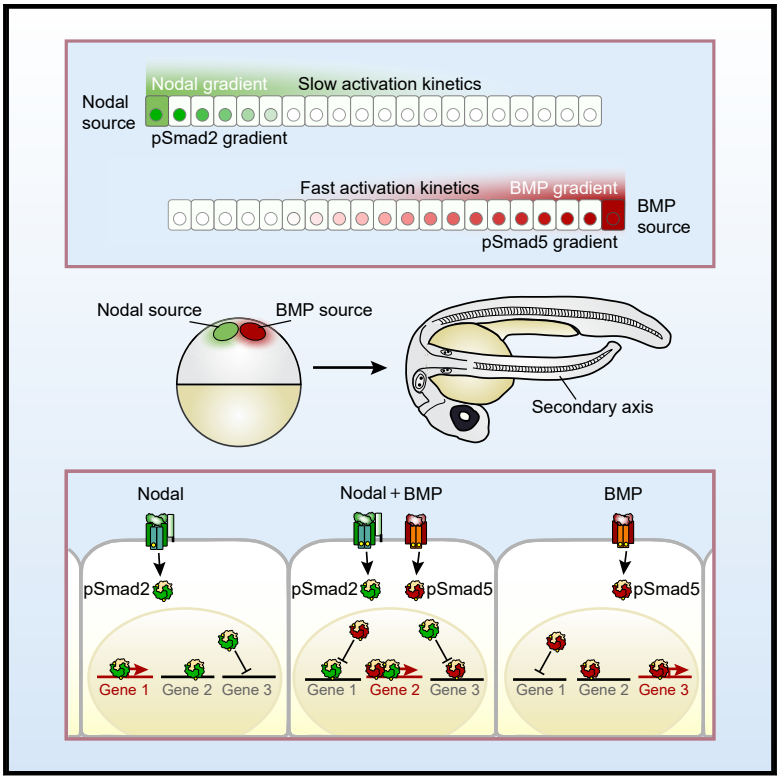

Highlights

- Nodal induces pSmad at a shorter range than BMP due to slower activation kinetics
- Different ratios of active Smad2 and Smad5 can induce different embryonic structures
- Smad2 and Smad5 inhibit each other or act synergistically to induce specific cell fates

Authors

Gary Huiming Soh,
Autumn Penecilla Pomreinke,
Patrick Müller

Correspondence

patrick.mueller@tuebingen.mpg.de

In Brief

Juxtaposed Nodal and BMP sources can induce the formation of a secondary axis in zebrafish embryos. Soh et al. analyze the input-output relationships in this patterning system and find that differential signaling kinetics lead to different activity ranges of Nodal and BMP, which are crucial for secondary axis formation.

Soh et al., 2020, Cell Reports *31*, 107487
April 7, 2020
https://doi.org/10.1016/j.celrep.2020.03.051

CellPress

Cell Reports
Article

Integration of Nodal and BMP Signaling by Mutual Signaling Effector Antagonism

Gary Huiming Soh,[1] Autumn Penecilla Pomreinke,[1] and Patrick Müller[1,2,3,*]
[1]Systems Biology of Development Group, Friedrich Miescher Laboratory of the Max Planck Society, Max-Planck-Ring 9, 72076 Tübingen, Germany
[2]Modeling Tumorigenesis Group, Translational Oncology Division, Eberhard Karls University Tübingen, Otfried-Müller-Straße 10, 72076 Tübingen, Germany
[3]Lead Contact
*Correspondence: patrick.mueller@tuebingen.mpg.de
https://doi.org/10.1016/j.celrep.2020.03.051

SUMMARY

Opposing sources of bone morphogenetic protein (BMP) and Nodal signaling molecules are sufficient to induce the formation of a full axis in zebrafish embryos. To address how these signals orchestrate patterning, we transplant sources of fluorescently tagged Nodal and BMP into zebrafish embryos, robustly inducing the formation of secondary axes. Nodal and BMP signal non-cell-autonomously and form similar protein gradients in this context, but the signaling range of Nodal (pSmad2) is shorter than the BMP range (pSmad5). This yields a localized region of pSmad2 activity around the Nodal source, overlapping with a broad domain of pSmad5 activity across the embryo. Cell fates induced in various regions stereotypically correlate with pSmad2-to-pSmad5 ratios and can even be induced BMP- and Nodal-independently with different ratios of constitutively active Smad2 and Smad5. Strikingly, we find that Smad2 and Smad5 antagonize each other for specific cell fates, providing a mechanism for how cells integrate and discriminate between overlapping signals during development.

INTRODUCTION

During development, cells need to know their location and fate in order to form an embryo. The required positional information can be conveyed by gradients of secreted signaling molecules that diffuse from a localized source to induce exposure-dependent cell responses (reviewed in Müller et al., 2013; Rogers and Schier, 2011). The earliest cell-fate decisions during vertebrate development are controlled by the signaling molecules Nodal and BMP, which form orthogonal overlapping activity gradients in zebrafish embryos (Figure 1A). Nodal induces the formation of the germ layers, which are subdivided into ventral and dorsal territories by BMP signaling (reviewed in Rogers and Müller, 2019). Nodal and BMP are secreted transforming growth factor β (TGF-β) superfamily ligands (Zhou et al., 1993; Wozney et al., 1988), which signal through a hetero-tetrameric complex composed of ligand-specific serine/threonine kinase receptors (Wrana et al., 1992) as well as co-receptors (Shen and Schier, 2000). Nodal signaling leads to the phosphorylation of the latent cytoplasmic signaling effectors Smad2/3, whereas BMP signaling causes the phosphorylation of Smad1/5/8. These pSmads then accumulate in the nucleus, where they regulate the expression of target genes (Heldin et al., 1997).

During zebrafish germ-layer patterning, the two Nodals Squint and Cyclops are produced at the embryonic margin and induce endoderm and mesoderm formation at a distance from the source (Bisgrove et al., 2017; Montague and Schier, 2017; Pelliccia et al., 2017; Chen and Schier, 2001; Feldman et al., 1998). Fgf8, a Nodal target gene, further extends the range of mesoderm (van Boxtel et al., 2018; van Boxtel et al., 2015; Mathieu et al., 2004; Rodaway et al., 1999). At the same time, the two BMPs Bmp2b and Bmp7 are produced predominantly on the ventral side to control dorsal-ventral patterning (Pomreinke et al., 2017; Zinski et al., 2017; Ramel and Hill, 2013). Bmp2b and Bmp7 form heterodimers, and homodimers of Bmp2b and Bmp7 alone do not elicit signaling (Little and Mullins, 2009). Additionally, Bmp2b is produced in the dorsal organizer to moderate the production of Chordin, a BMP inhibitory protein (Xue et al., 2014).

Strikingly, Nodal and BMP signaling together are sufficient to trigger all processes required to form an embryo. This was spectacularly demonstrated by generating ectopic juxtaposed sources of Nodal and BMP to induce a secondary embryonic axis in zebrafish (Figure 1A) (Xu et al., 2014). The ratio of Nodal to BMP signaling was suggested to be the determining factor in specifying the necessary cell fates for the embryonic axis. Nodal by itself creates axial structures, high Nodal-to-BMP ratios induce posterior head structures, low Nodal-to-BMP ratios organize the tail, and intermediate ratios generate the middle trunk (Fauny et al., 2009). However, it is unknown how Nodal and BMP gradients form, it is currently debated whether Nodal and BMP signal over long distances (Rogers and Müller, 2019; Pomreinke et al., 2017; Zinski et al., 2017; van Boxtel et al., 2015; Ramel and Hill, 2013; Müller et al., 2012; Chen and Schier, 2001), and the molecular mechanisms that allow cells to respond to different ratios of Nodal and BMP signaling are unclear.

To address these questions, we transplanted sources expressing fluorescently tagged Nodal and BMP into zebrafish embryos and generated secondary axes with high efficiency. Interestingly, Nodal and BMP formed protein gradients with similar shape and

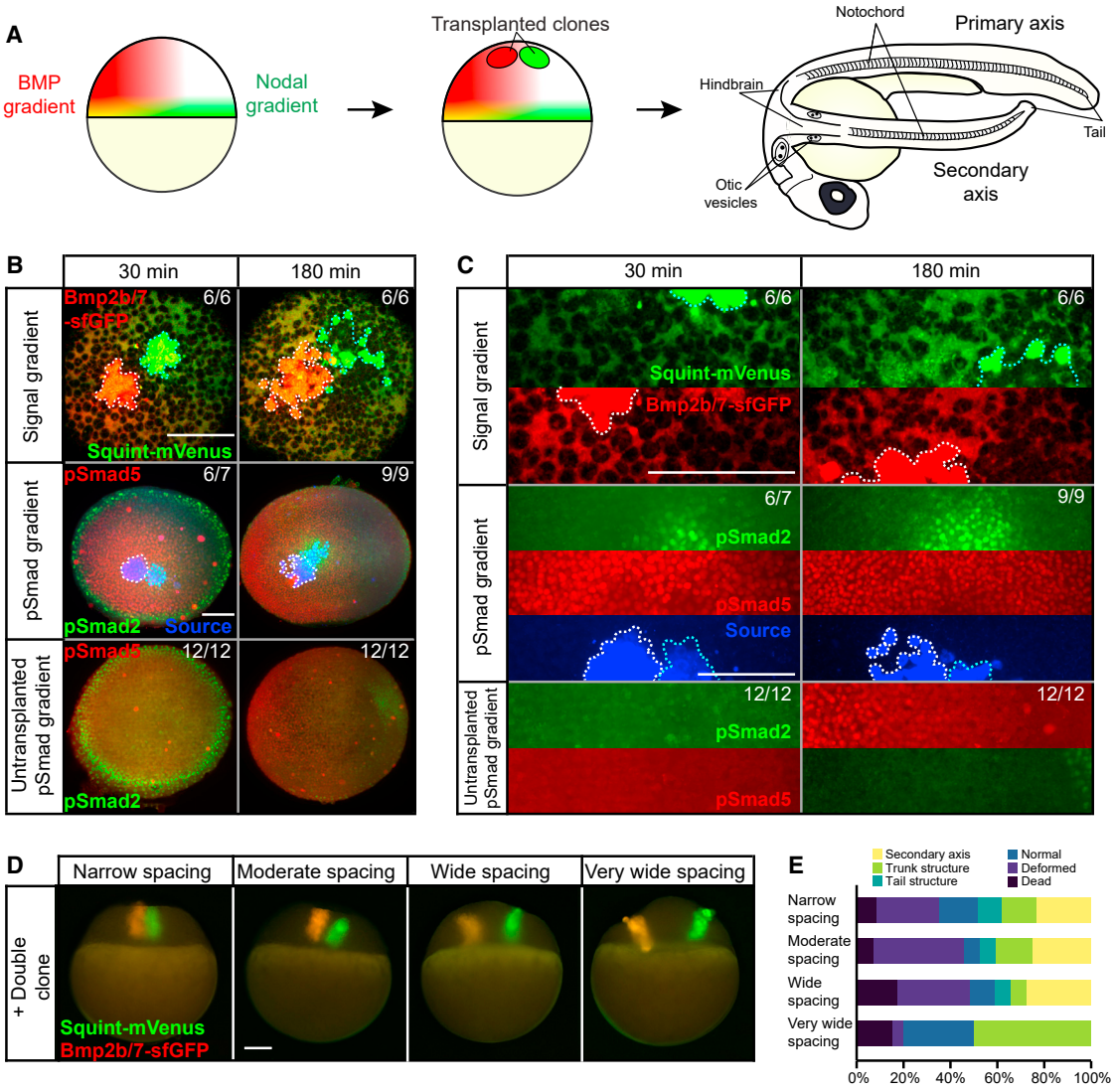

Figure 1. Secondary Axis Inducing Nodal and BMP Double Clones Produce a Localized Region of pSmad2 Activity Overlapping with a Broad Domain of pSmad5 Activity

(A) Nodal and BMP form orthogonal overlapping gradients in zebrafish embryos. Transplanting ectopic sources of Nodal and BMP induces the formation of a secondary axis, which contains both anterior and posterior structures such as the hindbrain, otic vesicles, notochord, and tail.

(B) Double clones of Bmp2b/7-sfGFP and Squint-mVenus imaged 30 min and 180 min post-transplantation. The first row depicts confocal microscopy images of Bmp2b/7-sfGFP (red) and Squint-mVenus (green). The second row shows light-sheet microscopy images of embryos immunostained with anti-pSmad2 (green) or anti-pSmad5 (red) antibodies as well as a cross-reactive anti-GFP antibody to detect Bmp2b/7-sfGFP and Squint-mVenus (blue). The third row shows comparable wild-type embryos. Nodal clones are traced in cyan and BMP clones are traced in white. Scale bar, 150 μm.

(C) Higher magnification of images shown in (B) with separate fluorescent channels. Scale bar, 150 μm.

(D) Images showing Nodal/BMP double clones with different spacings of transplanted cells taken immediately after transplantation. Scale bar, 150 μm.

(E) Nodal/BMP double clones were transplanted with different spacings into blastula-stage zebrafish embryos: narrow (~0 μm between clones, n = 60), moderate (40–50 μm between clones, n = 44), wide (120–150 μm between clones, n = 29), and very wide (>170 μm between clones, n = 20). Narrow to wide spacings support the formation of secondary axes, whereas secondary axis formation fails with extremely wide spacing between Nodal and BMP clones. Quantification was performed at 24 h post-transplantation.

amplitude in these secondary axis formation assays, but BMP had a long signaling range whereas Nodal induced pSmad signaling only locally around the transplanted clone. We found that the difference in signaling ranges can be explained by differential signaling activities of BMP and Nodal. Strikingly, specific ratios of constitutively active Smad2 and Smad5 were also able to generate a variety of embryonic structures, showing that the organizing ability of different Nodal/BMP ratios is mediated by different ratios of Smad2 and Smad5. We discovered that Smad2 and Smad5 selectively antagonize each other for certain cell fates while acting synergistically for others, which allows cells to respond differently to varying Nodal/BMP ratios. This selective

mutual antagonism might represent a general mechanism for how cells integrate and discriminate between two overlapping signals during development.

RESULTS

BMP and Nodal Induce pSmad Signaling with Different Ranges

To visualize the organizing signaling gradients during secondary axis formation, we optimized a protocol to generate secondary axes by transplanting juxtaposed sources of fluorescently tagged Nodal and BMP into zebrafish embryos (Figure 1A). In contrast to the original blastomere injection approach (Xu et al., 2014), this method allows for precise control over the timing, placement, and spacing of Nodal- and BMP-producing sources. We tagged the signaling molecules with various fluorophores and tested different ratios of the fusion proteins to assess their efficiency in generating secondary axes after transplantation. Many combinations of fluorophores showed good activity in generating secondary axes (Table S1), similar to the previously reported efficiency using untagged Nodal and BMP (Xu et al., 2014). Interestingly, both zebrafish Nodals (Squint and Cyclops) were able to generate secondary axes (only Cyclops was used in the previous work of Xu et al., 2014), albeit at different amounts of the injected mRNAs. Although mCherry-tagged versions also induced secondary axes, the required relative molar amounts differed drastically from those of the untagged versions (Table S1). In contrast, mVenus- and sfGFP-labeled Nodal and BMP had similar activity as the untagged versions (Figure S1). Furthermore, immunoblots of extracellular extracts showed that the fusion proteins were properly processed without releasing free fluorophores (Figure S1). We therefore decided to use Squint-mVenus and a 1:1 mixture of Bmp2b-sfGFP plus Bmp7-sfGFP (Bmp2b/7-sfGFP) for all subsequent axis-induction assays.

By generating localized sources of Squint-mVenus and Bmp2b/7-sfGFP, we found that these signaling molecules formed extracellular protein gradients within 30 min (Figures 1B and 1C). The gradients remained largely unchanged over the following 2 h (Figures 1B and 1C), similar to previous descriptions of Bmp2b-sfGFP and Squint-GFP gradient formation (Pomreinke et al., 2017; Müller et al., 2012). Interestingly, at 30 min post-transplantation, Nodal signaling (as assessed by pSmad2 induction; Figures 1B and 1C) was mostly limited to regions near the Nodal source, whereas BMP signaling (as assessed by pSmad5 induction; Figures 1B and 1C) had already spread extensively across the embryo. At 180 min, the pSmad2 signal was extended but still largely restricted to regions near the Nodal source, whereas pSmad5 remained more widely distributed (Figures 1B and 1C).

The wide and flat distribution of BMP signaling implied that the previously postulated close juxtaposition of opposing Nodal and BMP clones (Xu et al., 2014) might not be necessary for secondary axis induction and that localized Nodal signaling might be sufficient as long as there is some additional BMP signaling in the embryo. To test this prediction, we varied the spacing between Nodal and BMP sources and found that secondary axes could be generated for a wide range of different spacings (Figures 1D and 1E). The formation of secondary axes only failed when we placed the Nodal source much farther away from the BMP source than the range spanned by the pSmad5 gradient (~220 μm; Figure 1E). These results suggest that the BMP source generates a much more extensive signaling gradient than the Nodal source, even though the extracellular distributions of Nodal and BMP appear to be similar.

Secondary Axis Formation Does Not Depend on Relay Signaling

It had previously been suggested that secondary axis formation requires relay signaling through endogenous TGF-β superfamily ligands (de Olivera-Melo et al., 2018; Xu et al., 2014). To test this idea and measure signaling kinetics in the absence of endogenous signals, we transplanted clones secreting BMP and Nodal into wild-type and mutant zebrafish embryos that lack the endogenous signaling molecules. We first transplanted clones secreting zebrafish BMP into wild-type embryos and compared the induction kinetics of pSmad5 to *MZswr* (maternal-zygotic *swirl*$^{-/-}$ mutant) embryos that had received *MZswr* clones ectopically producing BMP. *MZswr* embryos lack functional Bmp2b (Schmid et al., 2000; Kishimoto et al., 1997) and are ideally suited to analyze the kinetics of pSmad5 induction in the absence of endogenous BMP signaling during embryonic development. Local BMP sources in wild-type embryos caused ventralization (Figure 2A, middle left), indicative of increased BMP activity in the entire embryo. The ubiquitous induction of BMP signaling was corroborated by the effects of small BMP clones in *MZswr* embryos (Figure 2A, middle right) that were well rescued except for tail defects, indicating that the BMP clone indeed induced long-range signaling. Consistent with these phenotypes, BMP clones induced signaling rapidly, and pSmad5 signal filled up the entire field in both wild-type and *MZswr* embryos (Figures 2B, 2C, S2, and S3A). The ability of the BMP source to induce pSmad5 signaling in *MZswr* embryos demonstrates that a relay through the induction of endogenous *bmp2b* is not required. Strikingly, local BMP juxtaposed to Nodal clones even induced secondary axes in *MZswr* embryos (Figure 2A, bottom right), indicating that BMP can work non-cell-autonomously and without relay signaling in this context.

To test the role of potential relays and quantify the dynamics of Nodal signaling, we transplanted cells producing Squint-mVenus into wild-type or *MZsqt;cyc* mutant host embryos (clones transplanted into *MZsqt;cyc* host embryos were *MZsqt;cyc* mutant as well). *MZsqt;cyc* mutants lack all maternal and zygotic Nodal ligands (Feldman et al., 1998) and serve as a background to analyze Nodal signaling in the absence of endogenous Nodal signals. Squint-mVenus clones in wild-type and *MZsqt;cyc* embryos generated ectopic axial trunk structures (Figure 2D, middle). Strikingly, Nodal and BMP double clones were able to generate a secondary axis with anterior mesodermal structures such as anterior somites (Figure 2D, bottom right, blue arrowhead), which are normally absent in Nodal-deficient *MZsqt;cyc* embryos (Figure 2D, top right, cyan arrowhead). The primary axis in these embryos lacked anterior mesodermal structures (Figure 2D, bottom right), as is expected for *MZsqt;cyc* embryos (Feldman et al., 1998).

In agreement with the restricted effect of anterior mesoderm rescue, pSmad2 staining was found locally around the Nodal

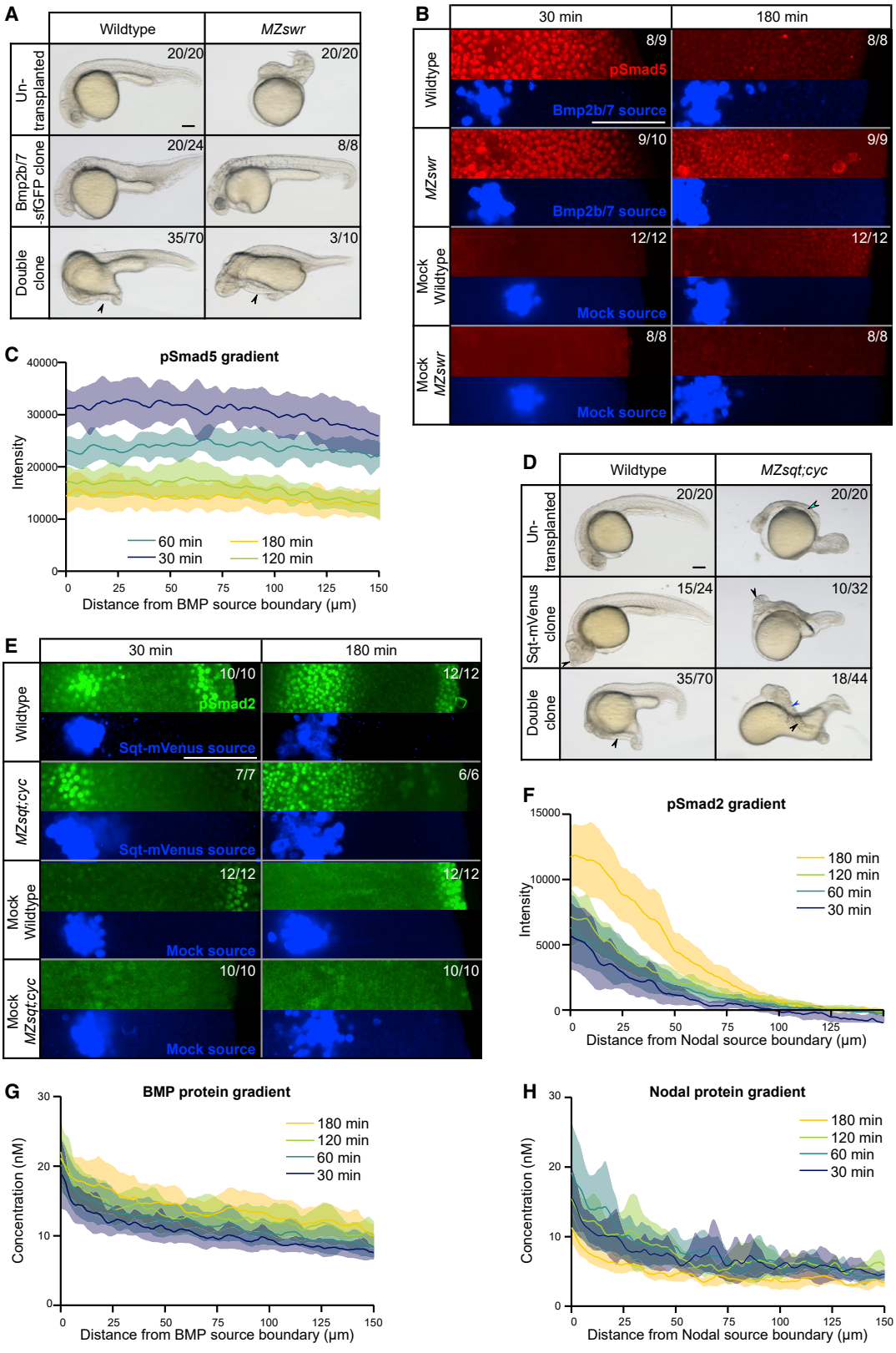

(legend on next page)

clones (Figure 2E). pSmad2 signal in *MZsqt;cyc* embryos extended up to several cell diameters away from the clone (Figures 2E and S3B), demonstrating that Nodal acts non-cell autonomously and without the need for a relay-based mechanism in this context as well. However, the range of Nodal-induced pSmad2 was significantly shorter than the range of BMP-induced pSmad5 (Figures 2C, 2F, and S3B). Importantly, untagged Squint and Bmp2b/7 generated a similarly large difference in the spatial ranges of Nodal and BMP signaling (Figures S2A and S2B), ruling out the possibility that the fluorescent tags are causal for the range differences.

Nodal and BMP Have Different Signaling Ranges despite Similar Ligand Distributions

Our finding that secondary axis formation is independent of relay signaling and purely relies on exogenously supplied signals provides an ideal system to test whether differences in signal gradient formation kinetics can explain the different signaling activity ranges. To relate the signal gradients to the signaling ranges, we developed a method to quantify the absolute concentrations of labeled Nodal and BMP in living zebrafish embryos based on their fluorescence intensities. We first purified recombinant sfGFP and mVenus proteins and established calibration curves relating the molar concentrations to their fluorescence intensities (Figure S4). We then used these calibration curves to determine the concentrations of fluorescently tagged Nodal and BMP expressed from local sources in zebrafish embryos. We found that the BMP gradient spanned a concentration range from 20 nM to 7 nM over 150 μm at 30 min post-transplantation (Figure 2G). At this time point, the pSmad5 gradient was similarly broad (Figure 2C), even when 5-fold less *bmp2b/7-sfGFP* mRNA was used (Figure S2C). Interestingly, although the concentration of BMP slightly increased over time (Figure 2G), most likely due to a larger effect of BMP production compared to its degradation, pSmad5 intensity concomitantly decreased (Figures 2C, S2A, and S2C). The decrease in pSmad5 intensity was also observed in *chordin* morphants (Figure S2D), arguing against the possibility of BMP signaling dampening by this major BMP antagonist (Fisher and Halpern, 1999; Blader et al., 1997; Schulte-Merker et al., 1997) in this context. In contrast, other Chordin-independent BMP-feedback inhibitors such as Bambia and Smad7 might be responsible for the down-regulation of BMP signaling over time (Pogoda and Meyer, 2002; Tsang et al., 2000).

The Squint-mVenus gradient produced from a localized clone formed with similar concentration distributions and dynamics as the BMP protein gradient at early time points but sharply dropped by 180 min post-transplantation (Figure 2H), possibly due to unstable mRNA, decreased translation, reduced secretion, or rapid internalization. In contrast to the drop in the Nodal gradient amplitude (Figure 2H), the levels of pSmad2 increased over time (Figure 2F).

Together, these results show that although Nodal and BMP form similar proteins distributions, their respective pSmad gradients are radically different, similar to the distinct distributions of pSmads induced by endogenous signaling molecules (Figure S2E). Therefore, the drastic differences in the pSmad gradients cannot be explained by the small differences in the amount of secreted Nodal and BMP proteins or by their similar effective diffusion coefficients (~3 $\mu m^2/s$) (Bläßle et al., 2018; Pomreinke et al., 2017; Zinski et al., 2017; Müller et al., 2012).

Different Signaling Ranges Arise from Differences in Signaling Activity

Nodal signaling is antagonized by the feedback-induced Nodal inhibitors Lefty1 and Lefty2 during early zebrafish development (Rogers and Müller, 2019; Rogers et al., 2017; Agathon et al., 2001; Meno et al., 1999; Thisse and Thisse, 1999). To test whether the shorter signaling range of Nodal compared to BMP is due to inhibition by Lefty1 or Lefty2, we assessed signaling in Squint-mVenus clone experiments in which both the donor and the recipient embryo were *MZlefty1;lefty2* double mutants lacking all maternal and zygotic Lefty activity (Rogers et al., 2017). Interestingly, in the absence of Lefty antagonism, the pSmad2 signal was extended (Figures S2F and S3C) but still much shorter than the range of pSmad5 induced by BMP clones

Figure 2. Nodal and BMP Form Similar Protein Gradients but Have Different Signaling Ranges during Secondary Axis Formation

(A) Bmp2b/7-sfGFP as well as Squint-mVenus and Bmp2b/7-sfGFP double clones in wild-type or maternal-zygotic *swirl* mutant (*MZswr*) embryos at 1 day post-transplantation, with untransplanted embryos for comparison. The arrowheads point to ectopic secondary axes. Scale bar, 150 μm.

(B) Bmp2b/7-sfGFP clones compared to uninjected mock clones 30 min and 180 min post-transplantation in wild-type or *MZswr* embryos. Embryos were immunostained with anti-pSmad5 (red) and anti-GFP (blue) antibodies. Mock sources were labeled with cascade blue-dextran (blue). Scale bar, 150 μm.

(C) pSmad5 distributions in embryos with single Bmp2b/7-sfGFP clones in *MZswr* embryos at 30 min (n = 9), 60 min (n = 8), 120 min (n = 10), and 180 min (n = 9) post-transplantation. Shaded regions indicate 95% confidence intervals around the mean (lines). Scale bar, 150 μm.

(D) Squint-mVenus as well as Squint-mVenus and Bmp2b/7-sfGFP double clones in wild-type or maternal-zygotic *squint* and *cyclops* double mutant (*MZsqt;cyc*) embryos 1 day post-transplantation, with untransplanted embryos for comparison. The arrowheads point to ectopic structures or secondary axes. Scale bar, 150 μm.

(E) Squint-mVenus clones compared to uninjected mock clones 30 min and 180 min post-transplantation in wild-type or *MZsqt;cyc* embryos. Embryos were immunostained with anti-pSmad2 (green) and anti-GFP (blue) antibodies. Mock sources were labeled with cascade blue-dextran (blue). Scale bar, 150 μm.

(F) pSmad2 distributions in embryos with single Squint-mVenus clones in wild-type embryos at 30, 60, 120, and 180 min post-transplantation (n = 11 each). Shaded regions indicate 95% confidence intervals around the mean (lines).

(G) BMP protein gradients in wild-type embryos with single Bmp2b/7-sfGFP clones at 30, 60, 120, and 180 min post-transplantation. The same embryos were imaged throughout the time course (n = 14). Fluorescence intensity was converted to concentration based on a calibration curve using recombinant sfGFP imaged with the same microscope settings. Shaded regions indicate 95% confidence intervals around the mean (lines).

(H) Nodal protein gradients in wild-type embryos with single Squint-mVenus clones at 30, 60, 120, and 180 min post-transplantation. The same embryos were imaged throughout the time course (n = 12). Fluorescence intensity was converted to concentration based on a calibration curve using recombinant mVenus imaged with the same microscope settings. Shaded regions indicate 95% confidence intervals around the mean (lines).

See also Figures S2–S4.

(compare to Figure 2C). These results show that signaling range modulation by Lefty cannot explain the drastic difference between Nodal distribution and signaling in this context.

We therefore hypothesized that the different signaling ranges (pSmad5 and pSmad2) from similar input gradients (BMP and Nodal) might result from different signaling activation kinetics. According to the law of mass action and Hill kinetics, signals with higher sensitivity can induce activation faster, leading to a longer signaling range, whereas signals with low sensitivity might require extended exposure until activation is induced in a threshold-type manner, leading to a shorter signaling range (Michaelis et al., 2011). To test this idea, we took advantage of the recent discovery that a single source of mouse BMP4 can generate a secondary zebrafish axis (de Olivera-Melo et al., 2018), which suggested the possibility that mouse BMP4 might carry both BMP and Nodal signal activities with different ranges. Previous experiments were carried out with commercial preparations of recombinant mouse BMP4 (de Olivera-Melo et al., 2018), but we found that a single source of mRNA encoding mouse BMP4 can also induce secondary axes in zebrafish embryos (Figure 3A), ruling out the possibility that potential contaminations of commercial mouse BMP4 with other TGF-β superfamily ligands are responsible for secondary axis formation.

To assess the plausibility that a single source of mouse BMP4 might generate different pSmad distributions, we developed a mathematical model based on Hill kinetics that we parameterized with the diffusion coefficient and protein half-life previously measured for zebrafish BMP (Pomreinke et al., 2017; Zinski et al., 2017) (Figure 3B). In this model, the differential readout of the mouse BMP4 gradient by pSmad5 and pSmad2 is dependent on a single parameter, i.e., the steepness of the pSmad activation term (k_d for pSmad5, k_e for pSmad2) that convolves the affinity of the BMP4 ligand for the BMP and Nodal receptors as well as the pSmad activation kinetics (Figure 3B). Simulations with smaller k_d compared to k_e values predicted that pSmad2 should be activated close to the mouse BMP4 source, whereas pSmad5 should have a wider range (Figure 3B).

In agreement with this model prediction, we found that pSmad2 and pSmad5 were indeed activated at different ranges by mouse BMP4. Local sources of mouse BMP4 in zebrafish embryos induced locally restricted pSmad2 but widespread pSmad5 (Figures 3C and 3D), providing further support that opposing sources of Nodal and BMP are not strictly needed for secondary axis formation. To rule out the possibility that pSmad2 activation is due to indirect induction of endogenous Nodal signals (de Olivera-Melo et al., 2018), we generated clones expressing mouse *bmp4* in Nodal-deficient *MZsqt;cyc* mutant zebrafish embryos. We found that mouse BMP4 can indeed directly induce both pSmad2 and pSmad5 non-cell-autonomously (Figures 3E and 3F). Together, these results support our model that the exact same signal gradient can induce signaling effector activation at different ranges solely due to differences in signaling activity.

Our model implies that the action range of a signaling molecule with high signaling activity should be limited by its diffusion coefficient, whereas the action range of a signaling molecule with low signaling activity should be limited by its signaling activity rather than its diffusivity. To test this prediction, we sought to artificially reduce the diffusion coefficients of Nodal and BMP and measure how this affects their signaling ranges. We perturbed the protein distributions of Nodal and BMP using morphotraps, transmembrane proteins with extracellularly facing anti-GFP nanobodies that can drastically reduce the diffusivity of extracellular proteins tagged with GFP derivatives (Mörsdorf and Müller, 2019; Almuedo-Castillo et al., 2018; Harmansa et al., 2017). The protein distributions of Bmp2b/7-sfGFP and Squint-mVenus expressed from localized sources were strongly restricted in the presence of the morphotrap (Figure 3G). The sharp Bmp2b/7-sfGFP distribution led to a strongly restricted pSmad5 signal around the clone, whereas the already narrow range of pSmad2 was only marginally affected when the Squint-mVenus distribution was perturbed (Figures 3G and S2G). These findings provide additional support for our model that BMP has a longer signaling range than Nodal due to its higher signaling activity.

Strikingly, morphotrap-mediated range-restricted Nodal and BMP still supported the formation of secondary axes when the clones were closely juxtaposed (~0 μm between clones), whereas secondary axes could no longer be induced when the clones were far apart (>120–150 μm) from each other (Figure 3H, top). To test whether the long-range activity of Nodal or BMP is required in this context, we next perturbed the ranges of Nodal or BMP individually. Interestingly, morphotrap-mediated range restriction of Nodal was without consequence for narrowly or widely spaced clones (Figure 3H, middle), whereas secondary axis formation was abrogated when range-restricted BMP clones were placed far away from normal Nodal clones (Figure 3H, bottom). These results show that differences in the Nodal and BMP signaling ranges are functionally relevant for the formation of secondary axes. We note, however, that in normal embryos BMPs do not form a discrete source but are expressed in a broad domain, which gives rise to a broad signaling domain of pSmad5. Nodal by contrast is localized to the margin in a much more restricted domain, and pSmad2 is likewise activated in a much more restricted domain (reviewed in Rogers and Müller, 2019).

In conclusion, we showed that Nodal and BMP can induce signaling with different ranges, differential signaling activity can explain the differences in signaling ranges, and differential signaling ranges are relevant for secondary axis formation.

Different Structures Can Be Induced by Specific Amounts of Active Smad2 and Smad5

Our results suggest that the formation of a secondary axis requires a broad distribution of BMP and highly localized Nodal signaling. However, in addition to the spatial distributions, the relative signaling levels may also important for secondary axis formation (Fauny et al., 2009). By varying the relative levels of BMP and Nodal, we found that it is the ratio of Nodal to BMP rather than the absolute signaling level that determines whether a secondary axis can form. Lowering Nodal levels with respect to BMP levels precluded secondary axis induction (Figure S5A), whereas a commensurate reduction in both Nodal and BMP levels restored secondary axis formation (Figure S5A), correlating with a specific distribution of pSmad2 to pSmad5 ratios (Figures S5B and S5C).

To test whether the observed pSmad2-to-pSmad5 signaling effector ratio is causal for secondary axis induction, we

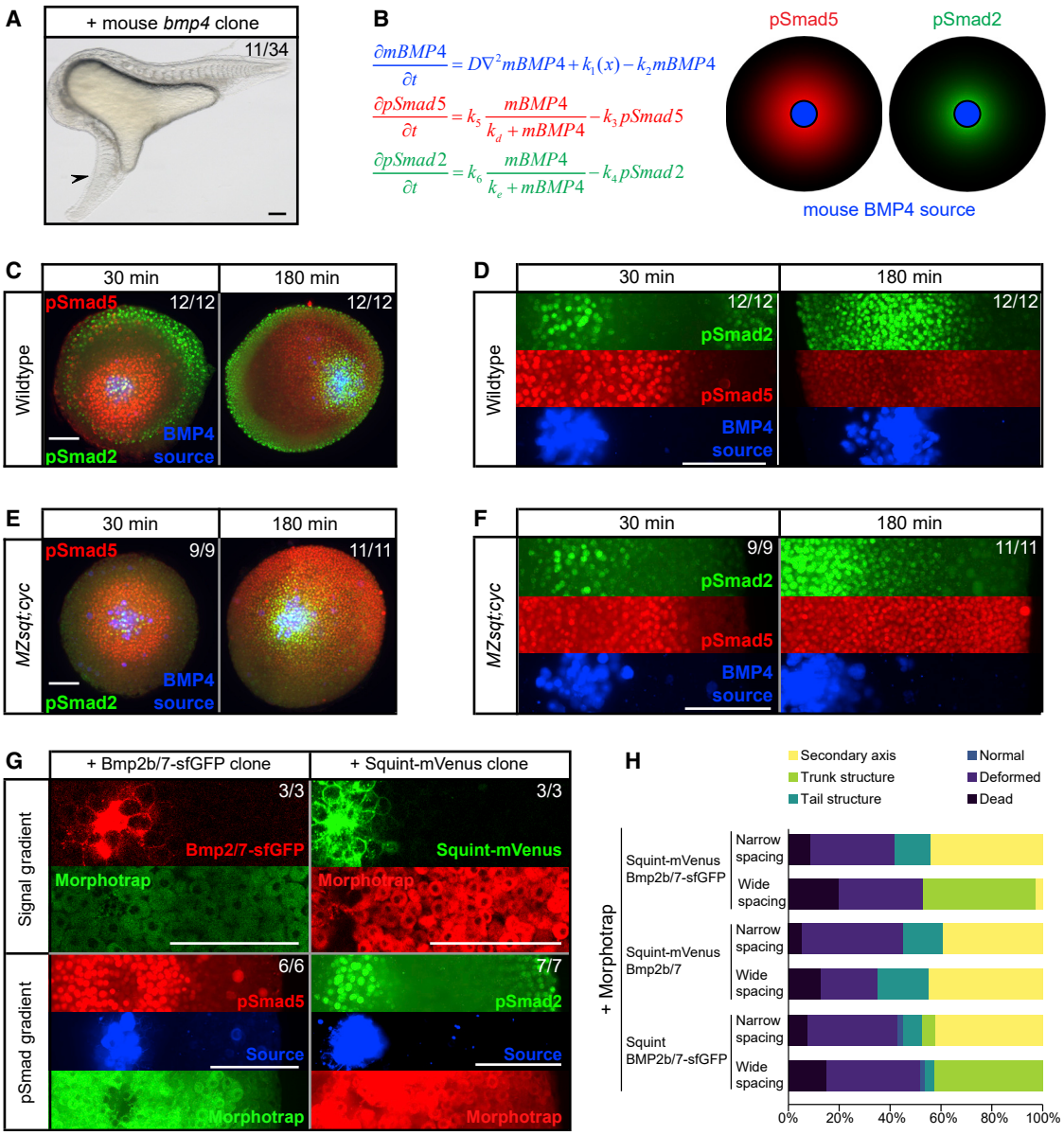

Figure 3. Different BMP and Nodal Signaling Ranges Arise from Differential Signaling Activation Kinetics

(A) Single clones expressing mouse *BMP4* (mBMP4) induce the formation of a secondary axis in zebrafish embryos (arrowhead). Scale bar, 150 μm.

(B) Mathematical modeling shows that a difference in signaling activation kinetics could explain how a single gradient of mBMP4 induces pSmad5 and pSmad2 at different ranges.

(C) Wild-type zebrafish embryos with clones expressing *mBMP4* 30 min and 180 min post-transplantation immunostained with anti-pSmad5 (red) and anti-pSmad2 (green) antibodies. The clones were labeled with cascade blue-dextran (blue). Scale bars, 150 μm.

(D) Higher magnification of images shown in (C) with separated fluorescent channels. Scale bar, 150 μm.

(E) *MZsqt;cyc* embryos with clones expressing *mBMP4* 30 min and 180 min post-transplantation immunostained with anti-pSmad5 (red) and anti-pSmad2 (green) antibodies. The clones were labeled with cascade blue-dextran (blue). Scale bars, 150 μm.

(F) Higher magnification of images shown in (E) with separated fluorescent channels. Scale bar, 150 μm.

(G) Zebrafish Bmp2b/7-sfGFP and Squint-mVenus clones in morphotrap-expressing wild-type embryos 30 min post-transplantation. Scale bar, 150 μm.

(H) Double clones with fluorescently tagged or untagged zebrafish Nodal and BMP and with narrow or wide spacing were generated in morphotrap-expressing embryos. The frequency of the different structures induced by the clones was assessed 24 h post-transplantation.

generated embryos in which we activated specific ratios of Smads in a localized region independently of the extracellular signaling molecules. By exchanging the three C-terminal serines with aspartates, we generated constitutively active Smad2 (Smad2-CA) and Smad5 (Smad5-CA) signaling effectors, which can activate the transcription of their respective target genes

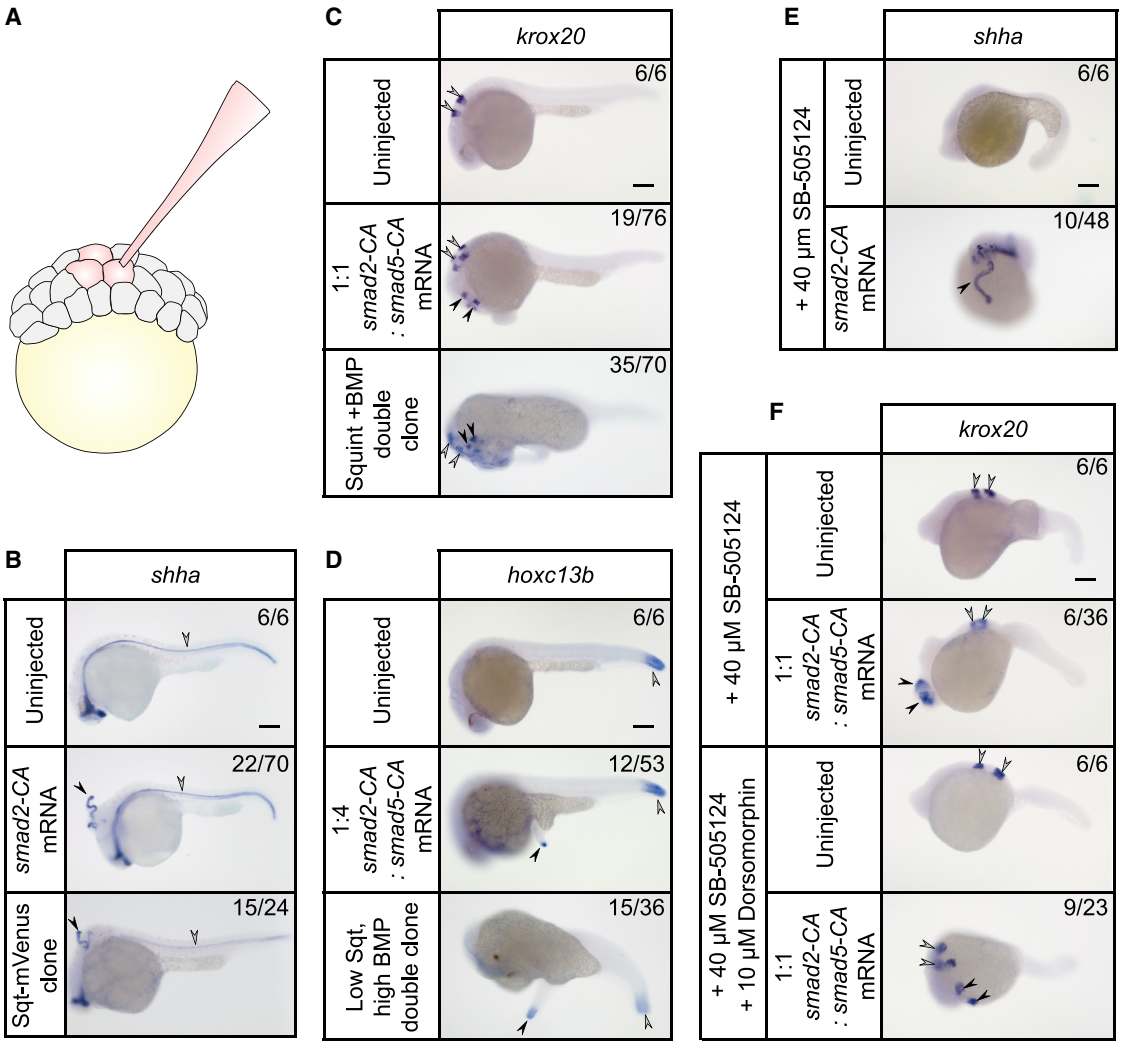

Figure 4. Ectopic Expression of Different Amounts of *smad2-CA* and *smad5-CA* mRNA Generates Distinct Embryonic Structures

(A) Ectopic structures were generated by injecting three adjacent blastomeres in 64- to 128-cell-stage embryos.

(B) The floorplate marker *shha* is expressed throughout the axis (gray arrowhead) of wild-type embryos 24 h post-fertilization (hpf). Injection of *smad2-CA* mRNA into animal pole blastomeres results in the formation of an ectopic axial structure (black arrowhead) that expresses *shha*, similar to the results with a *squint-mVenus*-expressing clone.

(C) *krox20* is expressed as a pair in rhombomeres 3 and 5 in the hindbrain (gray arrowhead) of wild-type embryos at 24 hpf. Injection of *smad2-CA* and *smad5-CA* mRNA in animal pole blastomeres results in the formation of anterior trunk structures with paired *krox20* expression (black arrowhead), similar to the outcome with a *squint-mVenus* and *bmp2b/7-sfGFP*-expressing double clone.

(D) *hoxc13b* is expressed in the tail tip (gray arrowhead) in wild-type embryos at 24 hpf. Injection of *smad2-CA* and four times more *smad5-CA* mRNA into animal pole blastomeres results in the formation of a tail structure expressing *hoxc13b* (black arrowhead), similar to the outcome with a double clone expressing low *squint-mVenus* and high *bmp2b/7-sfGFP* (Figure S5).

(E) *shha* is not expressed in embryos exposed to the Nodal receptor inhibitor SB-505124. Injection of *smad2-CA* mRNA into animal pole blastomeres results in ectopic *shha*-positive axial structures despite Nodal receptor inhibition.

(F) *krox20* remains expressed (gray arrowheads) in embryos exposed to SB-505124. Injection of *smad2-CA* and *smad5-CA* mRNA into animal pole blastomeres stage results in the formation of anterior trunk structures with paired *krox20* expression (black arrowheads). Nodal and BMP receptor inhibition by combined exposure to SB-505124 and Dorsomorphin generates embryos with reduced tails compared to the treatment with SB-505124 alone, but *krox20* expression persists (gray arrowhead). Injection of *smad2-CA* and *smad5-CA* mRNA into animal pole blastomeres results in the formation of anterior trunk structures with paired *krox20* expression (black arrowhead) despite Nodal and BMP receptor inhibition. Scale bar in all images, 150 µm.

(Figure S6). We found that expression of *smad2-CA* and *smad5-CA* in a localized region (Figure 4A) can generate various ectopic embryonic structures. Injecting *smad2-CA* alone generated an ectopic trunk structure containing axial tissues expressing the floorplate marker *shha* (Krauss et al., 1993) (Figure 4B, black arrowhead), just like in the case of an ectopic source of Nodal (Figure 4B) (Fauny et al., 2009). When we injected *smad2-CA* mixed with increasing amounts of *smad5-CA* mRNA (Figures

4C and 4D), structures expressing more ventral genes were induced, similar to previous findings in which the extracellular signaling molecules Nodal and BMP instead of the active signaling effectors were used (Fauny et al., 2009). Using Smad2-CA and Smad5-CA in a 1:1 ratio led to the induction of an ectopic structure with paired *krox20* expression, similar to the secondary axis generated by Nodal and BMP double clones (Figure 4C). *krox20* is expressed in rhombomeres 3 and 5 of the hindbrain (Ghosh et al., 2018), indicating that the ectopic structure represents an anterior trunk (Figure 4C). 4-fold more Smad5-CA over Smad2-CA can generate ectopic tail structures (Figure 4D) expressing the tail tip marker *hoxc13b* (Fauny et al., 2009). The induction of these structures was robust to the absence of endogenous Nodal and BMP signaling. Embryos expressing *smad2-CA* that were exposed to 40 μM of SB-505124, which fully inhibits signaling from the upstream Nodal receptor (Almuedo-Castillo et al., 2018; Rogers et al., 2017; Hagos and Dougan, 2007), were still able to generate ectopic trunk structures expressing *shha* (Figure 4E). Furthermore, embryos expressing *smad2-CA* and *smad5-CA* that were exposed to 40 μM of SB-505124 and 10 μM of the BMP receptor inhibitor Dorsomorphin were also able to generate anterior trunk structures expressing *krox20* (Figure 4F).

Since the inductive capabilities of constitutively active Smad2 and Smad5 are similar to those of the upstream signaling molecules Nodal and BMP, we conclude that the organizing activities of Nodal and BMP are mediated by specific amounts and ratios of active Smad2 and Smad5.

Selective Mutual Antagonism of Active Smad2 and Smad5 Yields Specific Responses to Different Signaling Ratios

We found that different ectopic structures can be induced by specific ratios of Smad2 and Smad5. To determine how the induction of these structures is related to the activation of target genes, we injected embryos with different ratios of Smad2-CA and Smad5-CA and assessed the expression of Nodal and BMP target genes with representative endogenous expression domains (Figure 5A). *gsc* is induced by Nodal signaling and a marker of axial mesoderm (Bennett et al., 2007; Gritsman et al., 1999) but only expressed at the dorsal margin (despite pSmad2 activity throughout the margin), suggesting that it is induced by high pSmad2 and low pSmad5 levels; *foxi1* is a BMP target gene and an epidermal marker that is expressed on the ventral side but appears to be excluded from the ventral margin at shield stage (Hans et al., 2007) (although pSmad5 signaling is also present at the ventral margin), suggesting that is induced by high pSmad5 and low pSmad2 levels; and *eve1* is expressed in the ventral margin (where both pSmad2 and pSmad5 are active) and a marker for ventral mesoderm, suggesting that it is induced by high pSmad2 and high pSmad5 levels. Interestingly, we found that Smad2-CA and Smad5-CA antagonized each other for the induction of *gsc* and *foxi1*, whereas *eve1* showed a biphasic sensitivity to these signaling effectors. Smad2-dependent *gsc* expression was suppressed by high levels of Smad5-CA compared to Smad2-CA (Figure 5B), whereas Smad5-dependent *foxi1* expression was inhibited by high Smad2-CA levels (Figure 5C). Strikingly, *eve1* was induced synergistically by both Smad2-CA and Smad5-CA at a moderate amount of Smad2-CA (Figure 5D). In contrast, high amounts of Smad2-CA led to reduced *eve1* expression (Figure 5D), consistent with the absence of dorsal *eve1* expression (Joly et al., 1993) where Nodal signaling is active over a long period of time (van Boxtel et al., 2018; Dubrulle et al., 2015). These results suggest that the selective mutual antagonism of Smad2 and Smad5 allows cells to respond specifically to different ratios of Smad2 and Smad5.

Our selective mutual antagonism mechanism predicted specific expression patterns of *gsc*, *foxi1*, and *eve1* in the Nodal/BMP double clone secondary axis formation assay. *gsc* is induced by high Smad2 activity and suppressed by Smad5 activity (Figure 5B) and should therefore be expressed near the Nodal source opposite to the BMP clone, *foxi1* is induced by high Smad5 activity and suppressed by Smad2 activity (Figure 5C) and should therefore be expressed near the BMP source opposite to the Nodal clone, and *eve1* has a biphasic activation profile (Figure 5D) and should therefore be expressed in a complex pattern. To test these predictions, we subjected embryos carrying Nodal/BMP double clones to *in situ* hybridization with various probes followed by pSmad2 and pSmad5 immunostaining (Figure 5E). In agreement with the predictions of our selective mutual antagonism model, we found that *gsc* was expressed in the presence of pSmad2, but not when pSmad2 overlapped with pSmad5 (Figure 5E). In contrast, *foxi1* was expressed in regions of pSmad5 activity, but expression was reduced when pSmad5 overlapped with pSmad2 (Figure 5E). Strikingly, *eve1* was expressed in the predicted complex domain; *eve1* was induced where pSmad2 overlapped with pSmad5, but it was not detected at the highest pSmad2 activity in the overlapping region (Figure 5E).

In conclusion, we found that the organizing activities of Nodal and BMP are mediated by specific amounts of active Smad2 and Smad5, whose selective mutual antagonism allows cells to respond specifically to different Nodal/BMP input ratios.

DISCUSSION

Understanding the dynamics of axis formation during early vertebrate development has largely been hampered by the lack of tools to relate the input from signaling gradients to the patterning output in terms of signaling effector activation and target gene expression. Transgenic animals expressing fluorescent fusions of the relevant signaling molecules under the control of endogenous regulatory elements are currently not available, and the timing and amplitudes of signaling gradients cannot be easily manipulated with good spatiotemporal control. Here, we used our optimized secondary zebrafish axis induction assay as an experimentally tractable model system to understand signaling input-output relationships and to decipher how Nodal and BMP signaling are integrated to form a secondary embryo.

Using active fluorescent fusions of Nodal and BMP expressed from clonal sources, we found that the signaling molecules form similar protein gradients of comparable shape and amplitude in zebrafish embryos. The similar protein gradients are in stark contrast to the differential distributions of the signaling effectors. The Nodal source generates a localized pSmad2 gradient that is overlaid by a broader pSmad5

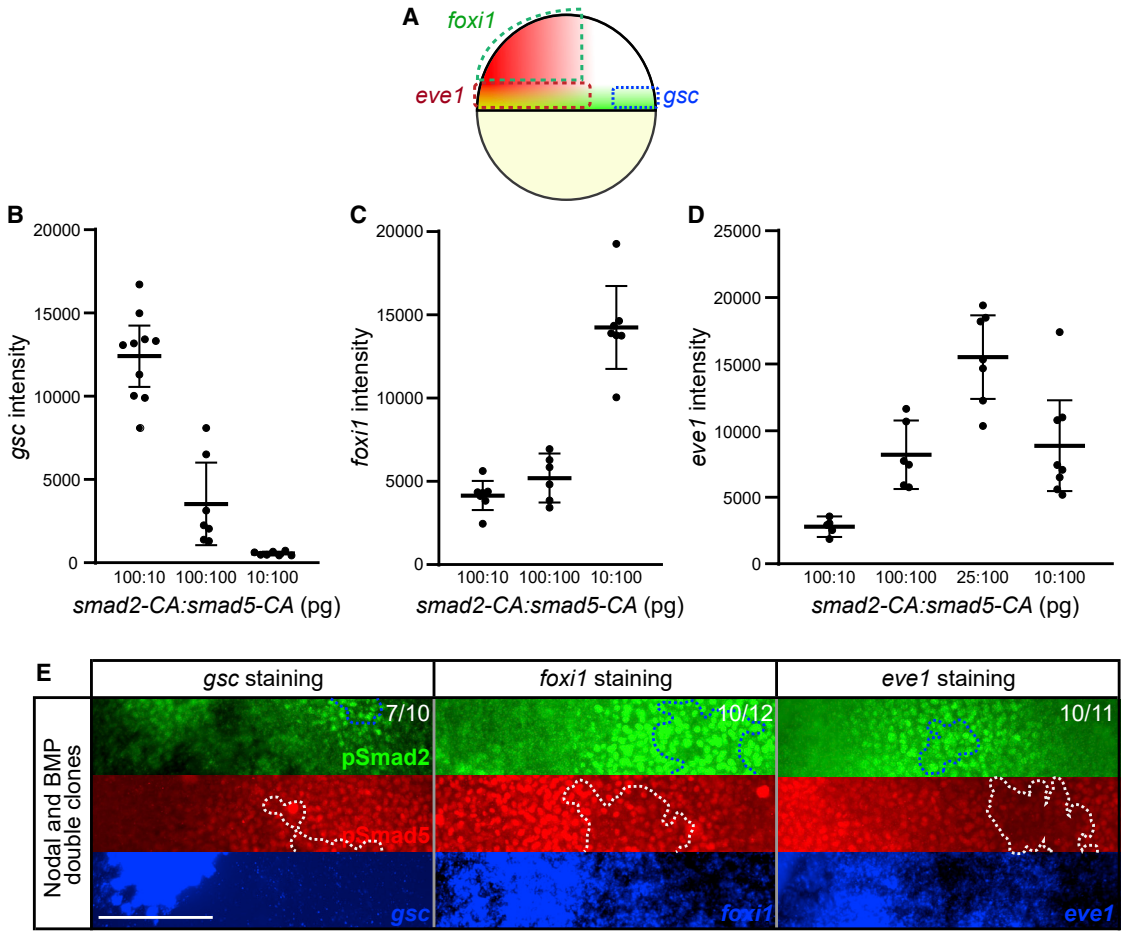

Figure 5. Mutual Antagonism of Smad2 and Smad5 for Specific Cell Fates

(A) *gsc* is expressed at the dorsal margin (Stachel et al., 1993), while *foxi1* is expressed on the ventral side but excluded from the margin (Dal-Pra et al., 2006), and *eve1* is expressed at the ventral margin (Joly et al., 1993) where Nodal and BMP signaling overlap (Figure 1A).

(B) Average *gsc* fluorescence *in situ* hybridization (FISH) intensity in 6-hpf embryos that were injected with the indicated *smad2-CA* and *smad5-CA* mRNA amounts at the one-cell stage (n = 10, 7, and 7).

(C) Average *foxi1* FISH intensity in 6-hpf embryos that were injected with the indicated *smad2-CA* and *smad5-CA* mRNA amounts at the one-cell stage (n = 7, 6, and 7).

(D) Average *eve1* FISH intensity of 6-hpf embryos that were injected with the indicated *smad2-CA* and *smad5-CA* mRNA amounts at the one-cell stage (n = 5, 6, 7, and 8).

(E) Embryos with Nodal and BMP double clones subjected to FISH with *gsc* (left, blue), *foxi1* (middle, blue), or *eve1* (right, blue) probes followed by pSmad2 (green) and pSmad5 (red) immunostaining. Blue dotted lines trace Nodal clones, and white dotted lines trace BMP clones. Scale bar, 150 μm. Error bars indicate 95% confidence intervals around the mean (horizontal lines) in (B)–(D).

gradient induced by the BMP source. Taking advantage of the dual BMP/Nodal activity of mouse BMP4, we experimentally confirmed the prediction of our model that different signaling ranges of a single protein gradient can be explained by differences in signaling activity. In addition to differences in diffusion/clearance-based signal dispersal (Rogers and Müller, 2019), differences in signaling activity might therefore represent an additional knob to tune the ranges of signaling molecules and may play a role in restricting Nodal signaling to the margin. Consistent with this hypothesis, similar differences in TGF-β superfamily signaling dynamics were recently identified in cultured cells (Miller et al., 2019; Yoney et al., 2018). For example, Activin exogenously added to mouse embryonic stem cells was found to activate Smad2 rapidly and had a long signaling range, whereas BMP4 activated Smad1 more slowly and had a shorter signaling range (Yoney et al., 2018). In agreement with law of mass action considerations (Michaelis et al., 2011), it may thus be a general feature of developmental signaling systems that ligands that rapidly activate their effectors have a longer range, whereas ligands that slowly activate their effectors have a shorter range.

The difference in Nodal and BMP signaling ranges arises due to differences in signaling activation kinetics and yields a field of various positional information values in terms of pSmad2-to-pSmad5 ratios. Previous work has shown that ectopic expression of different amounts of Nodal and BMP induces the

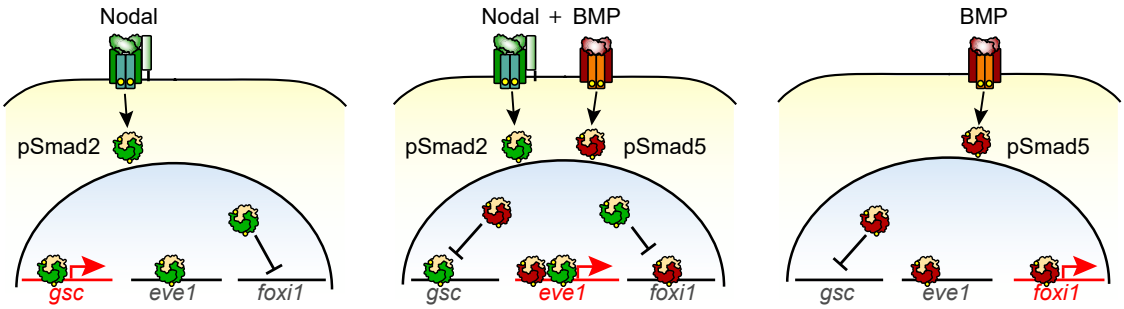

Figure 6. Selective Mutual Antagonism of pSmad2 and pSmad5 Allows Cells to Respond to Different Ratios of Nodal and BMP Signaling
Schematic of a parsimonious model explaining the present findings. The antagonism of pSmad2 and pSmad5 to *foxi1* and *gsc* induction, respectively, allows cells with both high pSmad2 and pSmad5 to express *eve1* without expressing *foxi1* or *gsc*. The activation and inhibition arrows are an abstraction, and the underlying mechanisms may be direct or indirect.

formation of specific embryonic structures (Fauny et al., 2009). Here, we found that ectopic expression of different amounts of constitutively active Smads is sufficient to generate these structures, indicating that varying ratios of Smads are the major factors that confer the inductive capabilities of Nodal and BMP. Mutual antagonism as well as limited synergism between activated Smad2 and Smad5 can lead to distinct combinations of target gene expression sets that correlate with their spatial expression domains (Figures 5 and 6), and an important future goal will be to decipher the molecular mechanism by which pSmad ratios are integrated at the level of signaling or at target gene promotors (Figure 6).

Similar cases of mutual antagonism also exist for other signaling pairs, such as Bicoid and Caudal (reviewed in Briscoe and Small, 2015). However, since Bicoid represses Caudal translation via direct binding to *caudal* mRNA (Niessing et al., 2002), their mutual antagonism is not selective. The selective antagonism mechanism might be needed for Nodal and BMP because they form overlapping orthogonal gradients (reviewed in Rogers and Müller, 2019) instead of anti-parallel gradients. The overlapping nature of the Nodal and BMP gradients leads to an area with both high pSmad2 and pSmad5 activity, areas with either high pSmad2 or high pSmad5 alone, as well as areas without pSmad2 or pSmad5. However, cell fates in areas with high pSmad2 alone or high pSmad5 alone are different from those in areas with both high pSmad2 and high pSmad5. Therefore, the selective antagonism mechanism not only allows cells to sense the ratio of Nodal and BMP but also can work when these gradients extensively overlap at the ventral margin. It is possible that similarly easily implemented mechanisms might generally be involved in the interpretation of other overlapping gradients.

In summary, we used the Nodal/BMP-mediated secondary axis formation assay as a model system to understand how the integration of signaling gradients leads to the activation of signaling effectors and subsequent patterning. In this context, we found that Nodal and BMP activate effector Smads non-cell autonomously and induce signaling at different spatial ranges due to differences in their signaling activities. This yields a field of positional information values in terms of differential signaling effector ratios. Varying ratios of constitutively active Smads can induce different embryonic structures, and selective mutual antagonism of activated Smad2 and Smad5 allows cells to respond to different ratios of Nodal and BMP signaling. It is tempting to speculate that, similar to the Yamanaka factors that can convert differentiated cells into pluripotent cells (Takahashi and Yamanaka, 2006), it might be possible in the future to use the inductive properties of different ratios of constitutively active Smads to induce the formation of desired embryonic structures from pluripotent stem cells for regenerative medicine.

STAR★METHODS

Detailed methods are provided in the online version of this paper and include the following:

- KEY RESOURCES TABLE
- LEAD CONTACT AND MATERIALS AVAILABILITY
- EXPERIMENTAL MODEL AND SUBJECT DETAILS
  - Zebrafish lines
- METHOD DETAILS
  - Plasmids and *in vitro* synthesis of RNA
  - Recombinant proteins
  - Immunoblotting
  - Injections and transplantations
  - Combined whole-mount immunofluorescence and *in situ* hybridization
  - Light-sheet microscopy
  - Confocal microscopy
- QUANTIFICATION AND STATISTICAL ANALYSIS
  - Image analysis
  - Mathematical modeling
- DATA AND CODE AVAILABILITY

SUPPLEMENTAL INFORMATION

Supplemental Information can be found online at https://doi.org/10.1016/j.celrep.2020.03.051.

ACKNOWLEDGMENTS

We thank Katherine Rogers and Daniel Čapek for helpful discussions and Jelena Raspopovic for providing the pCS2-mBMP4 plasmid. This work was

supported by the Max Planck Society and the ERC Starting Grant *QUANTPATTERN* (Grant Agreement No. 637840).

AUTHOR CONTRIBUTIONS

Conceptualization, G.H.S. and P.M.; Methodology, G.H.S. and P.M.; Investigation, G.H.S. and A.P.P.; Writing – Original Draft, G.H.S. and P.M.; Writing – Review & Editing, G.H.S., A.P.P., and P.M.; Funding Acquisition, P.M.; Resources, P.M.; Supervision, P.M.

DECLARATION OF INTERESTS

The authors declare no competing interests.

Received: September 5, 2019
Revised: November 26, 2019
Accepted: March 16, 2020
Published: April 7, 2020

REFERENCES

Agathon, A., Thisse, B., and Thisse, C. (2001). Morpholino knock-down of antivin1 and antivin2 upregulates nodal signaling. Genesis *30*, 178–182.

Almuedo-Castillo, M., Bläßle, A., Mörsdorf, D., Marcon, L., Soh, G.H., Rogers, K.W., Schier, A.F., and Müller, P. (2018). Scale-invariant patterning by size-dependent inhibition of Nodal signalling. Nat. Cell Biol. *20*, 1032–1042.

Bennett, J.T., Joubin, K., Cheng, S., Aanstad, P., Herwig, R., Clark, M., Lehrach, H., and Schier, A.F. (2007). Nodal signaling activates differentiation genes during zebrafish gastrulation. Dev. Biol. *304*, 525–540.

Bisgrove, B.W., Su, Y.C., and Yost, H.J. (2017). Maternal Gdf3 is an obligatory cofactor in Nodal signaling for embryonic axis formation in zebrafish. eLife *6*, e28534.

Blader, P., Rastegar, S., Fischer, N., and Strähle, U. (1997). Cleavage of the BMP-4 antagonist chordin by zebrafish tolloid. Science *278*, 1937–1940.

Bläßle, A., Soh, G., Braun, T., Mörsdorf, D., Preiß, H., Jordan, B.M., and Müller, P. (2018). Quantitative diffusion measurements using the open-source software PyFRAP. Nat. Commun. *9*, 1582.

Briscoe, J., and Small, S. (2015). Morphogen rules: design principles of gradient-mediated embryo patterning. Development *142*, 3996–4009.

Chen, Y., and Schier, A.F. (2001). The zebrafish Nodal signal Squint functions as a morphogen. Nature *411*, 607–610.

Ciruna, B., Weidinger, G., Knaut, H., Thisse, B., Thisse, C., Raz, E., and Schier, A.F. (2002). Production of maternal-zygotic mutant zebrafish by germ-line replacement. Proc. Natl. Acad. Sci. USA *99*, 14919–14924.

Dal-Pra, S., Fürthauer, M., Van-Celst, J., Thisse, B., and Thisse, C. (2006). Noggin1 and Follistatin-like2 function redundantly to Chordin to antagonize BMP activity. Dev. Biol. *298*, 514–526.

de Olivera-Melo, M., Xu, P.F., Houssin, N., Thisse, B., and Thisse, C. (2018). Generation of ectopic morphogen gradients in the zebrafish blastula. Methods Mol. Biol. *1863*, 125–141.

Dubrulle, J., Jordan, B.M., Akhmetova, L., Farrell, J.A., Kim, S.H., Solnica-Krezel, L., and Schier, A.F. (2015). Response to Nodal morphogen gradient is determined by the kinetics of target gene induction. eLife *4*, e05042.

Fauny, J.D., Thisse, B., and Thisse, C. (2009). The entire zebrafish blastula-gastrula margin acts as an organizer dependent on the ratio of Nodal to BMP activity. Development *136*, 3811–3819.

Feldman, B., Gates, M.A., Egan, E.S., Dougan, S.T., Rennebeck, G., Sirotkin, H.I., Schier, A.F., and Talbot, W.S. (1998). Zebrafish organizer development and germ-layer formation require nodal-related signals. Nature *395*, 181–185.

Fisher, S., and Halpern, M.E. (1999). Patterning the zebrafish axial skeleton requires early chordin function. Nat. Genet. *23*, 442–446.

Ghosh, P., Maurer, J.M., and Sagerström, C.G. (2018). Analysis of novel caudal hindbrain genes reveals different regulatory logic for gene expression in rhombomere 4 versus 5/6 in embryonic zebrafish. Neural Dev. *13*, 13.

Gritsman, K., Zhang, J., Cheng, S., Heckscher, E., Talbot, W.S., and Schier, A.F. (1999). The EGF-CFC protein one-eyed pinhead is essential for nodal signaling. Cell *97*, 121–132.

Hagos, E.G., and Dougan, S.T. (2007). Time-dependent patterning of the mesoderm and endoderm by Nodal signals in zebrafish. BMC Dev. Biol. *7*, 22.

Hans, S., Christison, J., Liu, D., and Westerfield, M. (2007). Fgf-dependent otic induction requires competence provided by Foxi1 and Dlx3b. BMC Dev. Biol. *7*, 5.

Harmansa, S., Alborelli, I., Bieli, D., Caussinus, E., and Affolter, M. (2017). A nanobody-based toolset to investigate the role of protein localization and dispersal in Drosophila. eLife *6*, e22549.

Hawley, S.H., Wünnenberg-Stapleton, K., Hashimoto, C., Laurent, M.N., Watabe, T., Blumberg, B.W., and Cho, K.W. (1995). Disruption of BMP signals in embryonic Xenopus ectoderm leads to direct neural induction. Genes Dev. *9*, 2923–2935.

Heldin, C.H., Miyazono, K., and ten Dijke, P. (1997). TGF-β signalling from cell membrane to nucleus through SMAD proteins. Nature *390*, 465–471.

Joly, J.S., Joly, C., Schulte-Merker, S., Boulekbache, H., and Condamine, H. (1993). The ventral and posterior expression of the zebrafish homeobox gene eve1 is perturbed in dorsalized and mutant embryos. Development *119*, 1261–1275.

Kishimoto, Y., Lee, K.H., Zon, L., Hammerschmidt, M., and Schulte-Merker, S. (1997). The molecular nature of zebrafish swirl: BMP2 function is essential during early dorsoventral patterning. Development *124*, 4457–4466.

Krauss, S., Concordet, J.P., and Ingham, P.W. (1993). A functionally conserved homolog of the Drosophila segment polarity gene hh is expressed in tissues with polarizing activity in zebrafish embryos. Cell *75*, 1431–1444.

Lambert, T.J. (2019). FPbase: a community-editable fluorescent protein database. Nat. Methods *16*, 277–278.

Little, S.C., and Mullins, M.C. (2009). Bone morphogenetic protein heterodimers assemble heteromeric type I receptor complexes to pattern the dorsoventral axis. Nat. Cell Biol. *11*, 637–643.

Liu, G., Amin, S., Okuhama, N.N., Liao, G., and Mingle, L.A. (2006). A quantitative evaluation of peroxidase inhibitors for tyramide signal amplification mediated cytochemistry and histochemistry. Histochem. Cell Biol. *126*, 283–291.

Mathieu, J., Griffin, K., Herbomel, P., Dickmeis, T., Strähle, U., Kimelman, D., Rosa, F.M., and Peyriéras, N. (2004). Nodal and Fgf pathways interact through a positive regulatory loop and synergize to maintain mesodermal cell populations. Development *131*, 629–641.

Meno, C., Gritsman, K., Ohishi, S., Ohfuji, Y., Heckscher, E., Mochida, K., Shimono, A., Kondoh, H., Talbot, W.S., Robertson, E.J., et al. (1999). Mouse Lefty2 and zebrafish antivin are feedback inhibitors of nodal signaling during vertebrate gastrulation. Mol. Cell *4*, 287–298.

Michaelis, L., Menten, M.L., Johnson, K.A., and Goody, R.S. (2011). The original Michaelis constant: translation of the 1913 Michaelis-Menten paper. Biochemistry *50*, 8264–8269.

Miller, D.S.J., Schmierer, B., and Hill, C.S. (2019). TGF-β family ligands exhibit distinct signalling dynamics that are driven by receptor localisation. J. Cell Sci. *132*, jcs234039.

Montague, T.G., and Schier, A.F. (2017). Vg1-Nodal heterodimers are the endogenous inducers of mesendoderm. eLife *6*, e28183.

Mörsdorf, D., and Müller, P. (2019). Tuning protein diffusivity with membrane tethers. Biochemistry *58*, 177–181.

Müller, P., Rogers, K.W., Jordan, B.M., Lee, J.S., Robson, D., Ramanathan, S., and Schier, A.F. (2012). Differential diffusivity of Nodal and Lefty underlies a reaction-diffusion patterning system. Science *336*, 721–724.

Müller, P., Rogers, K.W., Yu, S.R., Brand, M., and Schier, A.F. (2013). Morphogen transport. Development *140*, 1621–1638.

Mullins, M.C., Hammerschmidt, M., Kane, D.A., Odenthal, J., Brand, M., van Eeden, F.J., Furutani-Seiki, M., Granato, M., Haffter, P., Heisenberg, C.P.,

et al. (1996). Genes establishing dorsoventral pattern formation in the zebrafish embryo: the ventral specifying genes. Development *123*, 81–93.

Nagai, T., Ibata, K., Park, E.S., Kubota, M., Mikoshiba, K., and Miyawaki, A. (2002). A variant of yellow fluorescent protein with fast and efficient maturation for cell-biological applications. Nat. Biotechnol. *20*, 87–90.

Niessing, D., Blanke, S., and Jäckle, H. (2002). Bicoid associates with the 5′-cap-bound complex of caudal mRNA and represses translation. Genes Dev. *16*, 2576–2582.

Pédelacq, J.D., Cabantous, S., Tran, T., Terwilliger, T.C., and Waldo, G.S. (2006). Engineering and characterization of a superfolder green fluorescent protein. Nat. Biotechnol. *24*, 79–88.

Pelliccia, J.L., Jindal, G.A., and Burdine, R.D. (2017). Gdf3 is required for robust Nodal signaling during germ layer formation and left-right patterning. eLife *6*, e28635.

Pogoda, H.M., and Meyer, D. (2002). Zebrafish Smad7 is regulated by Smad3 and BMP signals. Dev. Dyn. *224*, 334–349.

Pomreinke, A.P., Soh, G.H., Rogers, K.W., Bergmann, J.K., Bläßle, A.J., and Müller, P. (2017). Dynamics of BMP signaling and distribution during zebrafish dorsal-ventral patterning. eLife *6*, 25861.

Ramel, M.C., and Hill, C.S. (2013). The ventral to dorsal BMP activity gradient in the early zebrafish embryo is determined by graded expression of BMP ligands. Dev. Biol. *378*, 170–182.

Rodaway, A., Takeda, H., Koshida, S., Broadbent, J., Price, B., Smith, J.C., Patient, R., and Holder, N. (1999). Induction of the mesendoderm in the zebrafish germ ring by yolk cell-derived TGF-β family signals and discrimination of mesoderm and endoderm by FGF. Development *126*, 3067–3078.

Rogers, K.W., and Müller, P. (2019). Nodal and BMP dispersal during early zebrafish development. Dev. Biol. *447*, 14–23.

Rogers, K.W., and Schier, A.F. (2011). Morphogen gradients: from generation to interpretation. Annu. Rev. Cell Dev. Biol. *27*, 377–407.

Rogers, K.W., Blässle, A., Schier, A.F., and Müller, P. (2015). Measuring protein stability in living zebrafish embryos using fluorescence decay after photoconversion (FDAP). J. Vis. Exp. *95*, 52266.

Rogers, K.W., Lord, N.D., Gagnon, J.A., Pauli, A., Zimmerman, S., Aksel, D.C., Reyon, D., Tsai, S.Q., Joung, J.K., and Schier, A.F. (2017). Nodal patterning without Lefty inhibitory feedback is functional but fragile. eLife *6*, 28785.

Samarkina, O.N., Popova, A.G., Gvozdik, E.Y., Chkalina, A.V., Zvyagin, I.V., Rylova, Y.V., Rudenko, N.V., Lusta, K.A., Kelmanson, I.V., Gorokhovatsky, A.Y., and Vinokurov, L.M. (2009). Universal and rapid method for purification of GFP-like proteins by the ethanol extraction. Protein Expr. Purif. *65*, 108–113.

Sampath, K., Rubinstein, A.L., Cheng, A.M., Liang, J.O., Fekany, K., Solnica-Krezel, L., Korzh, V., Halpern, M.E., and Wright, C.V. (1998). Induction of the zebrafish ventral brain and floorplate requires cyclops/nodal signalling. Nature *395*, 185–189.

Schindelin, J., Arganda-Carreras, I., Frise, E., Kaynig, V., Longair, M., Pietzsch, T., Preibisch, S., Rueden, C., Saalfeld, S., Schmid, B., et al. (2012). Fiji: an open-source platform for biological-image analysis. Nat. Methods *9*, 676–682.

Schmid, B., Fürthauer, M., Connors, S.A., Trout, J., Thisse, B., Thisse, C., and Mullins, M.C. (2000). Equivalent genetic roles for bmp7/snailhouse and bmp2b/swirl in dorsoventral pattern formation. Development *127*, 957–967.

Schulte-Merker, S., Lee, K.J., McMahon, A.P., and Hammerschmidt, M. (1997). The zebrafish organizer requires chordino. Nature *387*, 862–863.

Shen, M.M., and Schier, A.F. (2000). The EGF-CFC gene family in vertebrate development. Trends Genet. *16*, 303–309.

Stachel, S.E., Grunwald, D.J., and Myers, P.Z. (1993). Lithium perturbation and goosecoid expression identify a dorsal specification pathway in the pregastrula zebrafish. Development *117*, 1261–1274.

Takahashi, K., and Yamanaka, S. (2006). Induction of pluripotent stem cells from mouse embryonic and adult fibroblast cultures by defined factors. Cell *126*, 663–676.

Thisse, C., and Thisse, B. (1999). Antivin, a novel and divergent member of the TGFbeta superfamily, negatively regulates mesoderm induction. Development *126*, 229–240.

Thisse, C., and Thisse, B. (2008). High-resolution in situ hybridization to whole-mount zebrafish embryos. Nat. Protoc. *3*, 59–69.

Tsang, M., Kim, R., de Caestecker, M.P., Kudoh, T., Roberts, A.B., and Dawid, I.B. (2000). Zebrafish nma is involved in TGFbeta family signaling. Genesis *28*, 47–57.

van Boxtel, A.L., Chesebro, J.E., Heliot, C., Ramel, M.C., Stone, R.K., and Hill, C.S. (2015). A temporal window for signal activation dictates the dimensions of a Nodal signaling domain. Dev. Cell *35*, 175–185.

van Boxtel, A.L., Economou, A.D., Heliot, C., and Hill, C.S. (2018). Long-range signaling activation and local inhibition separate the mesoderm and endoderm lineages. Dev. Cell *44*, 179–191.e5.

Wozney, J.M., Rosen, V., Celeste, A.J., Mitsock, L.M., Whitters, M.J., Kriz, R.W., Hewick, R.M., and Wang, E.A. (1988). Novel regulators of bone formation: molecular clones and activities. Science *242*, 1528–1534.

Wrana, J.L., Attisano, L., Cárcamo, J., Zentella, A., Doody, J., Laiho, M., Wang, X.F., and Massagué, J. (1992). TGF β signals through a heteromeric protein kinase receptor complex. Cell *71*, 1003–1014.

Xu, P.F., Houssin, N., Ferri-Lagneau, K.F., Thisse, B., and Thisse, C. (2014). Construction of a vertebrate embryo from two opposing morphogen gradients. Science *344*, 87–89.

Xue, Y., Zheng, X., Huang, L., Xu, P., Ma, Y., Min, Z., Tao, Q., Tao, Y., and Meng, A. (2014). Organizer-derived Bmp2 is required for the formation of a correct Bmp activity gradient during embryonic development. Nat. Commun. *5*, 3766.

Yoney, A., Etoc, F., Ruzo, A., Carroll, T., Metzger, J.J., Martyn, I., Li, S., Kirst, C., Siggia, E.D., and Brivanlou, A.H. (2018). WNT signaling memory is required for ACTIVIN to function as a morphogen in human gastruloids. eLife *7*, e38279.

Zhou, X., Sasaki, H., Lowe, L., Hogan, B.L., and Kuehn, M.R. (1993). Nodal is a novel TGF-β-like gene expressed in the mouse node during gastrulation. Nature *361*, 543–547.

Zinski, J., Bu, Y., Wang, X., Dou, W., Umulis, D., and Mullins, M.C. (2017). Systems biology derived source-sink mechanism of BMP gradient formation. eLife *6*, e22199.

STAR★METHODS

KEY RESOURCES TABLE

REAGENT or RESOURCE	SOURCE	IDENTIFIER
Antibodies		
Rabbit monoclonal anti-phospho-Smad2/Smad3	Cell Signaling Technology	Cat#8828; RRID:AB_2631089
Rabbit monoclonal anti-phospho-Smad1/Smad5/Smad9	Cell Signaling Technology	Cat#13820S; RRID:AB_2493181
Goat anti-rabbit horseradish peroxidase	Jackson ImmunoResearch	Cat#111-035-003; RRID:AB_2313567
Anti-digoxigenin alkaline phosphatase Fab fragments	Roche Diagnostics	Cat#32871920
Anti-digoxigenin horseradish peroxidase Fab fragments	Sigma-Aldrich	Cat#11207733910
Chicken polyclonal anti-GFP	Aves Labs	Cat#GFP-1020; RRID:AB_10000240
Goat anti-rabbit Alexa647	Invitrogen	Cat#A21245; RRID:AB_141775
Goat anti-chicken Alexa568	Abcam	Cat#ab175477
Goat anti-chicken DyLight405	Agrisera	Cat#AS16 3624
Rabbit anti-GFP	Life Technologies	Cat#A11122; RRID:AB_221569
Bacterial Strains		
One Shot TOP10 chemically competent *E. coli*	Life Technologies	Cat#C4040
Chemicals and Recombinant Proteins		
Dorsomorphin	Abcam	Cat#ab120843
SB-505124	Sigma-Aldrich	Cat#S4696-5MG
Cascade Blue dextran, 10 kDa, anionic, lysine fixable	Thermo Fisher Scientific	Cat#D1976
Pronase	Roche	Cat#11459643001
Critical Commercial Assays		
TSA plus fluorescein system	Perkin Elmer	Cat#NEL741001KT
RNeasy kit	QIAGEN	Cat#74104
Pierce protein concentrator PES, 10K MWCO, 5-20 ml	Thermo Fisher Scientific	Cat#88528
SuperSignal West Dura extended duration substrate	Thermo Fisher Scientific	Cat#34075
Q5® site-directed mutagenesis kit	New England Biolabs	Cat#E0554S
Zero Blunt TOPO PCR cloning kit	Thermo Fisher Scientific	Cat#K2800J10
SP6 mMessage mMachine transcription kit	Thermo Fisher Scientific	Cat#AM1340
DIG RNA labeling mix	Sigma-Aldrich	Cat#11277073910
Experimental Models: Organisms/Strains		
Zebrafish: *sqt*^{cz35}	Feldman et al., 1998	N/A
Zebrafish: *cyc*^{m294}	Sampath et al., 1998	N/A
Zebrafish: *swr*^{tc300a}	Mullins et al., 1996	N/A
Zebrafish: *lefty1*^{a145}	Rogers et al., 2017	N/A
Zebrafish: *lefty2*^{a146}	Rogers et al., 2017	N/A
Oligonucleotides		
eve1_For: CTGGTTCCAGAACCGGAGA	This paper	N/A
eve1_Rev: GGAAAGCATATGTACATGGGTTTGTAT	This paper	N/A
foxi1_For: GTCGAGCCAGCAGACCAG	This paper	N/A
foxi1_Rev: CTGTTGTTGTGCGATGCTG	This paper	N/A
shha_For: ATACTGGCGTCCTGTTACGC	This paper	N/A
shha_Rev: ACATTTCCTGACACCTTGCCT	This paper	N/A
krox20_For: CAAACCCTTCCAGTGTCGGA	This paper	N/A
krox20_Rev: GACCCGCGTTAGTCACTTCA	This paper	N/A
hoxc13b_For: AAGCCGAGATGAACGGCTAC	This paper	N/A
hoxc13b_Rev:ACACAAACAGTTTAATATTGGGGGA	This paper	N/A
smad2-CA_For: TCGATTCGAATTCGCCACCATGTCCTCCATCTTGCCTTTCAC	This paper	N/A

(*Continued on next page*)

Continued

REAGENT or RESOURCE	SOURCE	IDENTIFIER
smad2-CA_Rev: ACTATAGTTCTAGATTAGTCCATGTCATCGCAGCGTACGGAGGG	This paper	N/A
smad5_For: GCGCGAATTCGCCACCATGACCTCCATGTCTAGTCTG	This paper	N/A
smad5_Rev: GCGCTCTAGATTACGAGACAGAAGAGATGGG	This paper	N/A
smad5-CA_For: GACGTCGACTAATCTAGAACTATAGTG	This paper	N/A
smad5-CA_Rev: ATCGATGGGGTTCAGAGG	This paper	N/A
Recombinant DNA		
pCS2-Bmp2b-sfGFP	Pomreinke et al., 2017	N/A
pCS2-Bmp7-sfGFP	This paper	N/A
pCS2-Bmp2b-mCherry	This paper	N/A
pCS2-Squint-mVenus	This paper	N/A
pCS2-Squint-mCherry	This paper	N/A
pCS2-Cyclops-mVenus	This paper	N/A
pCS2-Cyclops-mCherry	This paper	N/A
pCS2-Smad2-CA	This paper	N/A
pCS2-Smad5-CA	This paper	N/A
pCS2-mouseBMP4	This paper	N/A
pCRII-eve1	This paper	N/A
pCRII-foxi1	This paper	N/A
pCRII-shha	This paper	N/A
pCRII-hoxc13b	This paper	N/A
pCRII-krox20	This paper	N/A
pCS2-gsc	Müller et al., 2012	N/A
pCS2-sox32	Müller et al., 2012	N/A
pBAD-sfGFP	Pédelacq et al., 2006	Addgene Plasmid #54519; RRID:Addgene_54519
pBAD-mVenus	Nagai et al., 2002	Addgene Plasmid #54845; RRID:Addgene_54845
Software and Algorithms		
Fiji	Schindelin et al., 2012	https://fiji.sc/
Prism	GraphPad Software	https://www.graphpad.com/scientific-software/prism/
COMSOL Multiphysics 3.5a	COMSOL, Inc.	https://www.comsol.com/

LEAD CONTACT AND MATERIALS AVAILABILITY

All reagents generated in this study are available without restriction from the Lead Contact, Patrick Müller (patrick.mueller@tuebingen.mpg.de).

EXPERIMENTAL MODEL AND SUBJECT DETAILS

Zebrafish lines

Zebrafish husbandry was executed in accordance with the guidelines of the State of Baden-Württemberg (Germany) and approved by the Regierungspräsidium Tübingen (35/9185.46-5, 35/9185.81-5). The TE strain was used for experiments with wild-type zebrafish embryos. Maternal-zygotic double-homozygous *sqt*^{cz35} (Feldman et al., 1998) and *cyc*^{m294} (Sampath et al., 1998) mutants (*MZsqt;cyc*) as well as maternal-zygotic *swr*^{tc300a} (Mullins et al., 1996) (*MZswr*) mutants were generated by germline replacement (Ciruna et al., 2002). Maternal-zygotic double-homozygous *lefty1*^{a145};*lefty2*^{a146} mutants (*MZlefty1;lefty2*) were generated using a rescue approach with 4.8 μM of the Nodal inhibitor SB-505124 (Rogers et al., 2017).

METHOD DETAILS

Plasmids and *in vitro* synthesis of RNA

All plasmids for *in vitro* synthesis of mRNA were generated by inserting the sequence of interest into the EcoRI and XhoI sites of the *pCS2(+)* vector, containing the consensus Kozak sequence GCCACC directly in front of the start codon (Müller et al., 2012).

To generate pCS2-Bmp7-sfGFP, sequences encoding sfGFP flanked by LGDPPVAT linkers were inserted two amino acids downstream of the RSVR Furin cleavage site (Hawley et al., 1995). pCS2-Bmp2b-sfGFP was described previously (Pomreinke et al., 2017). pCS2-Bmp2b-mCherry was derived from pCS2-Bmp2b-sfGFP by exchanging the sfGFP-coding sequence with mCherry-encoding sequences. pCS2-Squint-mVenus and pCS2-Squint-mCherry were derived from pCS2-Squint-GFP (Müller et al., 2012) by exchanging the GFP-coding sequence with mVenus- and mCherry-encoding sequences, respectively. pCS2-Cyclops-mVenus and pCS2-Cyclops-mCherry were derived from pCS2-Cyclops-GFP (Müller et al., 2012) by exchanging the GFP-coding sequence with mVenus- and mCherry-encoding sequences, respectively.

Constitutively active Smads were generated by replacing the three C-terminal serine codons with aspartate codons. Smad5 was cloned from zebrafish shield-stage cDNA into the *pCS2(+)* vector with the primers GCGCGAATTCGCCACCATGACCTCCATGTC TAGTCTG and GCGCTCTAGATTACGAGACAGAAGAGATGGG. The Q5 site-directed mutagenesis kit (New-England Biolabs) was then used to replace the C-terminal serine codons with the primers GACGTCGACTAATCTAGAACTATAGTG and ATCGATGGGGTT CAGAGG. Smad2-CA was directly amplified and modified from zebrafish shield-stage cDNA with the primers TCGATTC GAATTCGCCACCATGTCCTCCATCTTGCCTTTCAC and ACTATAGTTCTAGATTAGTCCATGTCATCGCAGCGTACGGAGGG. The amplicon was cloned into the *pCS2(+)* vector.

mRNA for microinjection was generated using the SP6 mMessage mMachine kit (Thermo Fisher Scientific) according to the manufacturer's instructions after plasmid linearization with NotI-HF (New England Biolabs, Cat#R3189).

Plasmids containing sequence fragments of *eve1*, *foxi1*, *shha*, *krox20* and *hoxc13b* were generated using Zero Blunt TOPO PCR Cloning (Invitrogen, Thermo Fisher Scientific) and the following primers: CTGGTTCCAGAACCGGAGA and GGAAAGCATATGTA CATGGGTTTGTAT for *eve1*, GTCGAGCCAGCAGACCAG and CTGTTGTTGTGCGATGCTG for *foxi1*, ATACTGGCGTCCTGTTACGC and ACATTTCCTGACACCTTGCCT for *shha*, CAAACCCTTCCAGTGTCGGA and GACCCGCGTTAGTCACTTCA for *krox20*, AAGCCGAGATGAACGGCTAC and ACACAAACAGTTTAATATTGGGGGA for *hoxc13b*. For *foxi1,* shield-stage cDNA was used as a template, whereas genomic DNA was used as a template for *eve1*, *shha*, *krox20* and *hoxc13b*. Linear fragments for *eve1*, *foxi1*, *shha*, *krox20* and *hoxc13b* were produced by PCR with M13 forward and M13 reverse primers. To generate templates for *gsc* and *sox32* probes, plasmids were linearized with EcoRI and NotI (New England Biolabs) respectively (Müller et al., 2012). RNA probes for *in situ* hybridization were synthesized from these linearized plasmids using SP6 or T7 polymerase and DIG-modified ribonucleotides (Roche). RNA probes were purified using RNeasy kits (QIAGEN).

Recombinant proteins

sfGFP and mVenus were expressed in One Shot TOP10 *E. coli* using the plasmids pBAD-sfGFP (Addgene plasmid #54519 (Pédelacq et al., 2006)) and pBAD-mVenus (Addgene plasmid #54845 (Nagai et al., 2002)) after overnight induction with 10 mg/ml arabinose at 16°C. The fluorescent proteins were then purified by ethanol extraction as previously described (Samarkina et al., 2009). Briefly, *E. coli* cells were lysed by sonication in 20 mM Tris–HCl, 150 mM NaCl, 5 mM EDTA, pH 7.8, and sodium chloride and ammonium sulfate were added to the lysate to a final concentration of 0.41 M and 2.63 M, respectively. 1.2 volumes of 96% ethanol were then added to the lysate, and the mixture was vigorously shaken. After centrifugation, the fluorescent proteins became partitioned into the upper organic phase. The upper phase was recovered, and 0.25 volumes of n-Butanol were added. The mixture was then centrifuged, causing the fluorescent proteins to be partitioned into the lower aqueous phase from which they were recovered. The purified fluorescent proteins were then concentrated and buffer-exchanged into phosphate buffered saline (PBS) via ultrafiltration with Pierce protein concentrators (10K MWCO, Thermo Fisher Scientific). Fluorescent proteins were quantified using a Nanodrop 1000 (Thermo Fisher Scientific) by measuring their absorption spectra. The concentration was calculated according to the Beer–Lambert law using the measured peak absorption and the molar extinction coefficients taken from FPbase (Lambert, 2019).

Immunoblotting

Extra- and intracellularly enriched embryo extracts were prepared as described previously (Pomreinke et al., 2017; Müller et al., 2012). Protein samples were resolved on 12% polyacrylamide gels and transferred to polyvinylidene fluoride membranes using a semi-dry blotting system (Bio-Rad). The blots were blocked in 5% low fat milk in PBS containing 0.1% Tween 20 (PBST) for 1 hour, before being incubated overnight at 4°C with a dilution of 1:5000 rabbit anti-GFP antibody (Life Technologies) in 1% low fat milk in PBST. The blots were washed 3 times for 10 min each with PBST and then incubated for 1 h at room temperature with a dilution of 1:5000 goat anti-rabbit horseradish peroxidase (Jackson ImmunoResearch) in 1% low fat milk in PBST. Finally, the blots were washed 3 times for 10 min each with PBST, and the signal was developed with SuperSignal West Dura extended duration substrate (Thermo Fisher Scientific) for imaging with a chemiluminescence imaging system (Fusion 483 Solo, Vilber Lourmat).

Injections and transplantations

For transplantation experiments, embryos were dechorionated using 0.1 mg/ml Pronase (Roche) in 5 mL embryo medium and rinsed in embryo medium to remove the Pronase (Rogers et al., 2015). Embryos were then injected with 2 nL of injection mix at the 1- or 2-cell stage and incubated at 28°C until transplantation. Unfertilized or injured embryos were discarded. Transplantation was done when the embryos reached sphere stage. A cylinder of cells, approximately 80 μm in diameter and 100 μm in length, was transplanted from sphere-stage donor embryos expressing *squint-mVenus* or *bmp2b-sfGFP* + *bmp7-sfGFP* (termed *bmp2b/7-sfGFP* in the following) into uninjected sphere-stage sibling hosts. Combinations of 100 pg *squint-mVenus* mRNA or 100 pg + 100 pg *bmp2b/7-sfGFP* mRNA were used for most experiments, except for Figure S5, where 20 pg *squint-mVenus* mRNA along with 20 pg + 20 pg *bmp2b/7-sfGFP* mRNA and 20 pg *squint-mVenus* mRNA along with 100 pg + 100 pg *bmp2b/7-sfGFP* mRNA were additionally used. For transplantations with mouse BMP4, 40 pg of *mouse bmp4* mRNA was used. Cells for mock transplantations and those with mouse BMP4 were additionally labeled by injecting 100 pg of 10 kDa cascade blue-dextran (Thermo Fisher Scientific) at the one-cell stage. Following transplantation, the embryos were placed in Ringer's solution (116 mM NaCl, 2.8 mM KCl, 1 mM $CaCl_2$, 5 mM HEPES) for 15 min to recover and then incubated at 28°C until further processing.

To test the activity of constitutively active Smads, different amounts of *smad2-CA* or *smad5-CA* mRNA as detailed in the figures were injected into one-cell stage embryos, which were dechorionated at shield stage before fixation.

For the generation of ectopic structures with constitutively active Smads, embryos were dechorionated. Three adjacent blastomeres in embryos at the 64-cell stage were then injected with 20 pg *smad2-CA*, 20 pg *smad2-CA* + 20 pg *smad5-CA*, or 20 pg *smad2-CA* + 80 pg *smad5-CA* mRNA per blastomere. For Nodal and BMP receptor inhibition, 40 μM of SB-505124 (Sigma-Aldrich) and 10 μM of Dorsomorphin (Abcam) were used, respectively.

Combined whole-mount immunofluorescence and *in situ* hybridization

Embryos were fixed in 4% formaldehyde in PBS overnight at 4°C, dehydrated in 100% methanol and stored at −20°C until further processing. Chromogenic *in situ* hybridization was carried out as described before (Thisse and Thisse, 2008). Fluorescent *in situ* hybridization (FISH) was executed as described before (Almuedo-Castillo et al., 2018). If immunostainings were subsequently done, embryos were also incubated with 20 mM HCl for 25 min to inactivate the horse radish peroxidase (Liu et al., 2006).

For whole-mount immunostainings, embryos were washed three times with PBST and then permeabilized with cold acetone at −20°C for 20 min. Blocking and antibody incubations were performed in 10% FBS in PBST, and all washes were done with PBST. To carry out the dual pSmad2 and pSmad5 stainings, embryos were first blocked and then incubated with a 1:5000 dilution of a rabbit anti-pSmad2 antibody (Cell Signaling Technology) at 4°C overnight followed by 8 washes for 15 min each. The samples were then blocked and incubated with 1:500 goat anti-rabbit horseradish peroxidase (Jackson ImmunoResearch) at 4°C overnight followed by 8 washes for 15 min each. The signal was detected with TSA fluorescein at a dilution of 1:75 in amplification buffer (Perkin Elmer) for 45 min at room temperature followed by three washes for 5 min each. The embryos were then incubated with methanol for 3 h, washed three times for 10 min, blocked and incubated with a 1:100 dilution of a rabbit anti-pSmad5 antibody (Cell Signaling Technology) and a 1:200 dilution of chicken anti-GFP antibody (Aves Labs) at 4°C overnight. The samples were washed 8 times for 15 min each, blocked and incubated with 1:100 anti-rabbit Alexa647 IgG and 1:200 anti-chicken Alexa 568 IgG (in cases where no *in situ* hybridization was carried out) or anti-chicken DyLight 405 IgG (for combined *in situ* hybridization) at 4°C overnight. The embryos were finally washed 8 times for 15 min each and imaged immediately afterward using a light-sheet microscope.

Light-sheet microscopy

Fluorescence images of fixed samples were obtained using a Lightsheet Z.1 microscope (ZEISS). Samples were mounted in 1% low-melting agarose (Lonza, Cat#50080) in embryo medium using a size 3 glass capillary sample holder (ZEISS) and a needle to orient the embryos. The samples were imaged as a series of z stacks with the following objectives and imaging conditions: W Plan-Apochromat 20 × objective, 0.5 × zoom, separate exposure, 80 ms exposure time, 6.4 μm average light-sheet thickness, 10 μm intervals between z-slices. For samples stained by *in situ* hybridization alone, a 488 nm laser (100 mW) was used at 6% power for *foxi1*, 1% power for *gsc*, 8% power for *eve1*. For samples with double pSmad staining, a 488 nm laser (100 mW) was used at 1% power, a 561 nm laser (20 mW) at 5% power, and a 638 nm laser (75 mW) at 8% power. For samples with *in situ* hybridization signals and double pSmad staining, a 561 nm laser (20 mW) was used at 5% power, and a 405 nm laser (20 mW) was used at 10% power in addition to the other three lasers. Images were acquired with 1920 pixels × 1920 pixels (877.13 μm × 811.13 μm) dimensions.

Confocal microscopy

Live imaging of embryos was executed on an LSM 780 NLO confocal microscope (ZEISS) using an LD C-Apochromat 40 × / 1.1 NA water immersion objective. Embryos were mounted in 1% low-melting point agarose in glass bottom Petri dishes (MatTek Corporation) and covered with embryo medium. Embryos were maintained at 28°C during the experiments using a heated chamber and imaged 30, 60, 120 and 180 min post-transplantation. The fluorophores were excited with a 50 mW argon laser. sfGFP was excited at 488 nm with 16% laser power, and mVenus was excited at 514 nm with 35% power. The emission was collected as a multispectral image using a 32-channel GaAsP QUASAR array. Images were acquired with 512 × 512 pixels (425.10 × 425.10 μm) dimensions. The multispectral image was then converted into a single channel image by linear unmixing using ZEN Black (ZEISS) (Figure S2H).

QUANTIFICATION AND STATISTICAL ANALYSIS

Image analysis

Fiji was used for all image analyses (Schindelin et al., 2012). Nodal and BMP gradients were quantified similar to previous approaches (Pomreinke et al., 2017; Müller et al., 2012). A median filter of 1 pixel radius was applied to the images for denoising. This was followed by a maximum intensity projection of 14 z-slices.

Nodal, BMP, pSmad2 and pSmad5 gradients were quantified in a rectangular 66 μm wide and 150 μm long region. The "*plot profile*" function in Fiji was used, which averages the data along the width. Background levels were determined by measuring the average intensity from untransplanted embryos, and the background was subtracted from the gradient profiles. Prism (GraphPad Software) was used for data plotting. All error bars indicate 95% confidence intervals.

The pSmad ratio images were generated by first subtracting background intensities from each channel separately followed by a Gaussian blur with a sigma of 10. The Gaussian blur was performed to visualize an area of pSmad2 or pSmad5 activity instead of specific nuclei and to minimize aberrantly high ratios resulting from division by very low pSmad5 intensities. After Gaussian blurring, the pSmad2 channel was divided by the pSmad5 channel to generate the final image.

To determine the target gene response with varying amounts of Smad2-CA + Smad5-CA, the average intensity in a central circular region with half of the embryo radius was measured.

Mathematical modeling

The finite element method was used for two-dimensional numerical simulations of differential signaling activation kinetics from a single input gradient. The zebrafish animal pole was modeled as a circle with a radius of 300 μm, and the mouse *BMP4* (mBMP4) expressing clone was placed concentrically into the embryo disc with a radius of 10 μm. mBMP4 gradient formation was simulated using the following partial differentiation equation:

$$\frac{\partial mBMP4}{\partial t} = D\nabla^2 mBMP4 + k_1(x) - k_2 mBMP4$$

where $D = 3\ \mu m^2/s$ represents the diffusion coefficient of mBMP4 (based on measurements of zebrafish Bmp2b (Pomreinke et al., 2017; Zinski et al., 2017)), $k_1 = 1/s$ represents the spatially restricted production rate constant of mBMP4 exclusively within the clone, and $k_2 = 10^{-4}/s$ (based on measurements of zebrafish Bmp2b (Pomreinke et al., 2017)) represents the spatially uniform clearance rate constant.

The readout of the resulting mBMP4 gradient by pSmad5 and pSmad2 was modeled as

$$\frac{\partial pSmad5}{\partial t} = k_5 \frac{mBMP4}{k_d + mBMP4} - k_3 pSmad5$$

$$\frac{\partial pSmad2}{\partial t} = k_6 \frac{mBMP4}{k_e + mBMP4} - k_4 pSmad2$$

where $k_3 = k_4 = 10^{-4}/s$ represent the degradation rate constants of the pSmads and $k_5 = k_6 = 1/s$ represent their production rate constants. $k_d = 100$ and $k_e = 10^6$ represent the different signaling thresholds that activate pSmad5 and pSmad2, respectively.

The solution at each time step in the discretized geometry was determined using a sparse LU factorization algorithm (UMFPACK), and the time stepping was computed using a backward Euler step method (COMSOL Multiphysics 3.5a). Simulations were executed for a total of 7200 s.

While D and k_2 are based on directly measured quantities, the values for k_1, k_3, k_4, k_5, k_6, k_d and k_e have not been experimentally determined. k_1, k_5 and k_6 control the amplitude of the gradients – but not their shape – and were therefore set to an arbitrary value of 1/s. Equal values of k_3 and k_4 were chosen to reflect the timescale of gradient formation. A large difference between k_d and k_e values was chosen to illustrate that a single signaling molecule gradient can generate vastly different activity gradients based on differential signaling kinetics.

DATA AND CODE AVAILABILITY

The raw images and data used in this work are available from the Lead Contact upon request.

Cell Reports, Volume *31*

Supplemental Information

Integration of Nodal and BMP Signaling by Mutual Signaling Effector Antagonism

Gary Huiming Soh, Autumn Penecilla Pomreinke, and Patrick Müller

Table S1, Related to Figure 1.

Nodal		BMP		Ratio of Nodal to BMP mRNA	Secondary axis formation rate (%)	n
Amount (pg)	Construct	Amount (pg)	Construct			
66	Squint	132	Bmp2b/7	0.50	40	45
100	Squint-mVenus	200	Bmp2b/7-sfGFP	0.50	50	70
400	Cyclops-mVenus	40	Bmp2b/7-sfGFP	10.00	20	69
200	Squint-mCherry	2200	Bmp2b/7-sfGFP	0.09	26	66
1200	Squint-GFP	250	Bmp2b-mCherry	4.80	24	72
100	Cyclops-mCherry	800	Bmp2b-sfGFP	0.13	14	50

Secondary axis formation efficiency of different fluorescently tagged Nodal and BMP fusions. Embryos received donor cells injected with various amounts of fluorescently tagged Nodal- and BMP-encoding mRNA. The percentage of embryos with secondary axes was assessed at 24 h post-transplantation.

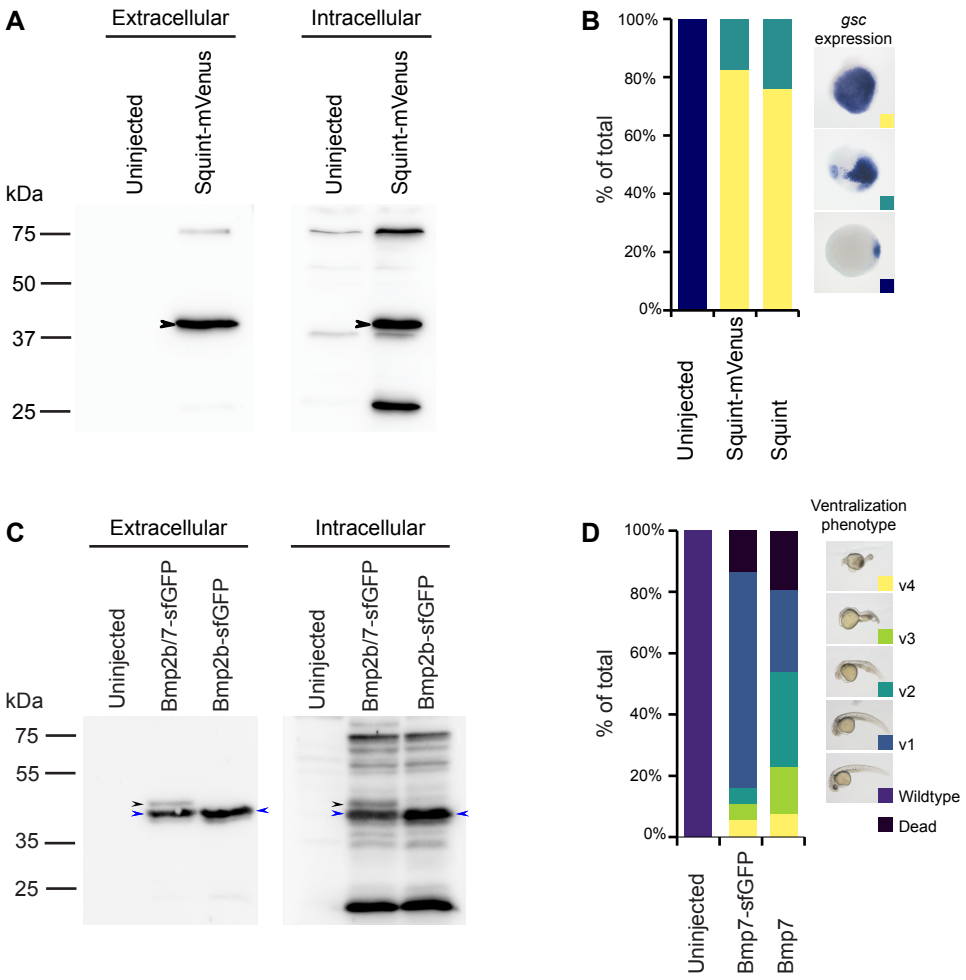

Figure S1. Characterization of Squint-mVenus and Bmp7-sfGFP, Related to Figure 1. (A) Extra- and intracellularly enriched extracts were obtained from uninjected zebrafish embryos or embryos injected with 200 pg *squint-mVenus* mRNA. The extracts were subjected to immunoblotting with anti-GFP antibodies (Müller et al., 2012). The arrowheads point to the band representing processed mature Squint-mVenus. Note that no free mVenus protein (size ≈25 kDa) was detected in the extracellularly enriched extracts. **(B)** Zebrafish embryos were injected with equimolar amounts of mRNA encoding Squint (1 pg, n=23) and Squint-mVenus (1.48 pg, n=25) at the one-cell stage. Embryos were then fixed, stained for the expression of the Nodal target gene *gsc* by whole-mount *in situ* hybridization and classified based on the staining extent. Squint and Squint-mVenus have a similar specific activity to induce *gsc* expression. **(C)** Extra- and intracellularly enriched extracts were obtained from uninjected zebrafish embryos and embryos injected with 150 pg *bmp7-sfGFP* + *bmp2b-sfGFP* or 200 pg *bmp2b-sfGFP* mRNA. The extracts were subjected to immunoblotting with anti-GFP antibodies. *bmp2b-sfGFP* mRNA was used as a control that had previously been shown to be properly processed (Pomreinke et al., 2017). The arrowheads point to the bands representing processed mature Bmp2b-sfGFP (blue arrow) and Bmp7-sfGFP (black arrow). Note that no free sfGFP protein (size ≈25 kDa) was detected in the extracellularly enriched extracts. **(D)** Zebrafish embryos were injected with equimolar amounts of mRNA encoding Bmp7 (9 pg, n=102) and Bmp7-sfGFP (11 pg, n=107) at the one-cell stage. Ventralization phenotypes at 24 h post-fertilization were categorized using established classification schemes (Pomreinke et al., 2017; Mullins et al., 1996).

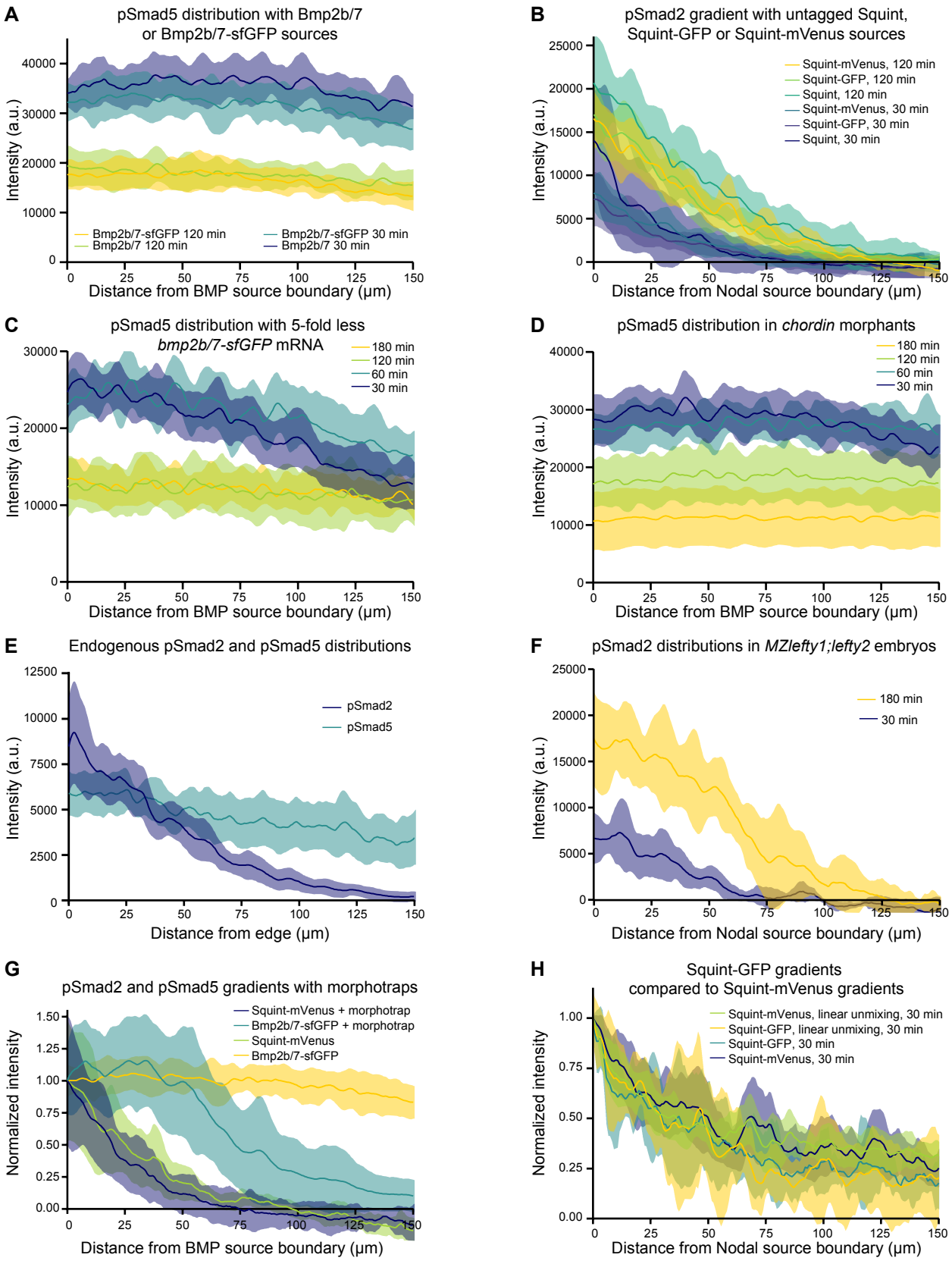

Figure S2. Quantification of endogenous and ectopic signaling distributions, Related to Figure 2. (A) Spatiotemporal pSmad5 distributions for single clones of untagged Bmp2b/7 and Bmp2b/7-sfGFP at 30 min (n[Bmp2b/7]=9, n[Bmp2b/7-sfGFP]=9) and 120 min (n[Bmp2b/7]=11, n[Bmp2b/7-sfGFP]=10) post-transplantation. **(B)** Spatiotemporal pSmad2 distributions for single clones of untagged Squint, Squint-GFP or Squint-mVenus at 30 min (n[Squint]=6, n[Squint-GFP]=8, n[Squint-mVenus]=9) and 120 min (n[Squint]=8, n[Squint-GFP]=10, n[Squint-mVenus]=9) post-transplantation. **(C)** Spatiotemporal pSmad5 distributions at 30 (n=12), 60 (n=9), 120 (n=8) and 180 (n=12) min post-transplantation in embryos with single Bmp2b/7-sfGFP clones that carried five times less *bmp2b/7-sfGFP* mRNA than the clones shown in Figure 2C. **(D)** Spatiotemporal pSmad5 distributions in embryos with single Bmp2b/7-sfGFP clones in *chordin* morphants at 30 (n=9), 60 (n=8), 120 (n=9) and 180 (n=10) min post-transplantation. **(E)** Distribution of endogenous pSmad5 along the ventral-dorsal axis (n=10), and endogenous pSmad2 signal along the vegetal-animal axis (n=12) in wildtype embryos at 50% epiboly. **(F)** pSmad2 distributions in *MZlefty1;lefty2* embryos with single Squint-mVenus clones at 30 and 180 min post-transplantation (n=6 each). **(G)** Normalized pSmad2 and pSmad5 gradients induced by Squint-mVenus and Bmp2b/7-sfGFP clones with or without morphotraps expressed in the host embryo (n[Squint-mVenus+morphotrap]=7, n[Bmp2b/7-sfGFP+morphotrap]=6, n[Squint-mVenus]=11, n[Bmp2b/7-sfGFP]=9). **(H)** Nodal protein gradients in embryos with single Squint-GFP (n=4) or Squint-mVenus (n=12) clones at 30 min post-transplantation, with or without linear unmixing. In all panels, the shaded regions represent 95% confidence intervals around the mean (lines).

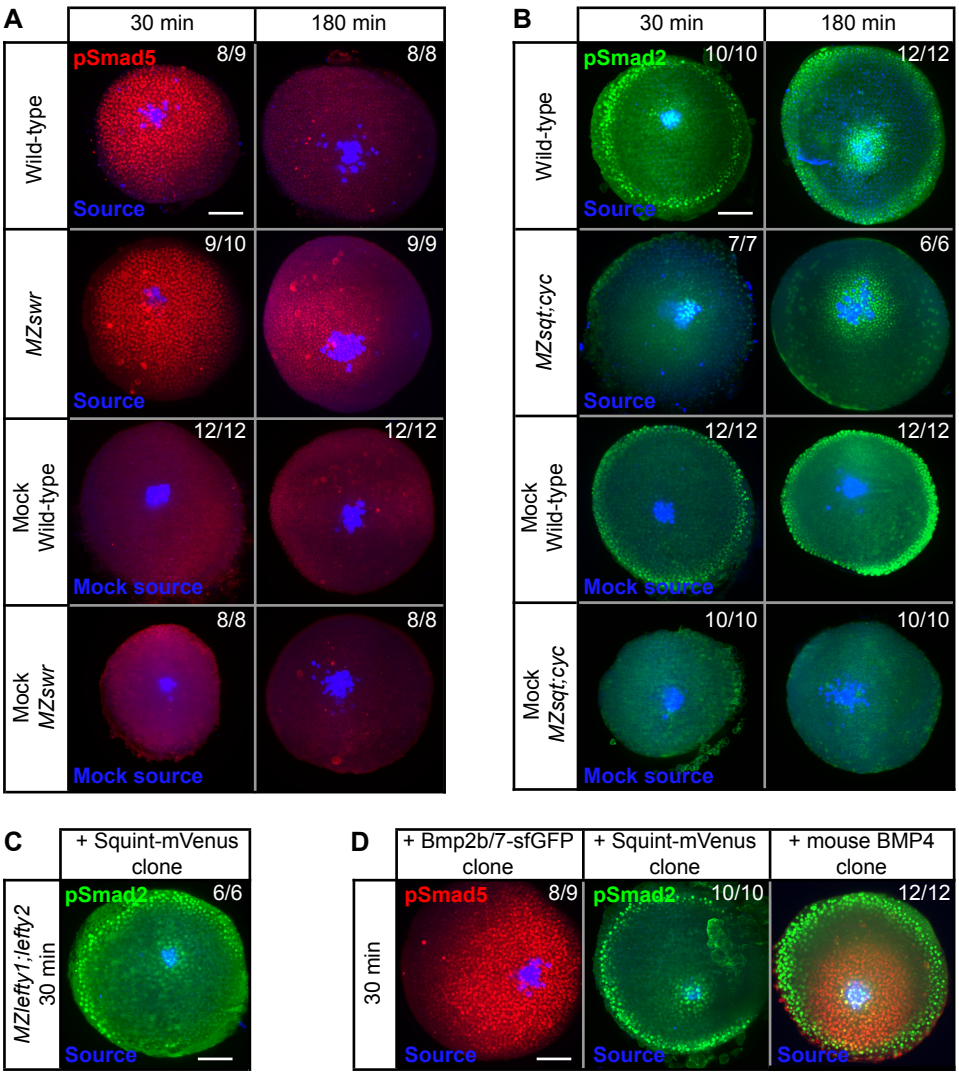

Figure S3. Comparison of pSmad5 and pSmad2 ranges in whole-embryo views, Related to Figure 2. (A) Whole-embryo views of Bmp2b/7-sfGFP clones 30 min and 180 min post-transplantation in wild-type or *MZswr* embryos compared to uninjected mock sources transplanted into wild-type or *MZswr* embryos. Embryos were immunostained with anti-pSmad5 (red) and anti-GFP (blue) antibodies. Mock sources were labeled with cascade blue-dextran (blue). Scale bar: 150 µm. **(B)** Whole-embryo views of Squint-mVenus clones 30 min and 180 min post-transplantation in wild-type or *MZsqt;cyc* embryos compared to uninjected mock sources transplanted into wild-type or *MZsqt;cyc* embryos. Embryos were immunostained with anti-pSmad2 (green) and anti-GFP (blue) antibodies. Mock sources were labeled with cascade blue-dextran (blue). Scale bar: 150 µm. **(C)** Whole-embryo views of Squint-mVenus clones derived from *MZlefty1;lefty2* donor embryos in *MZlefty1;lefty2* host embryos 30 min after transplantation. Embryos were immunostained with anti-pSmad2 (green) and anti-GFP (blue) antibodies. Scale bar: 150 µm. **(D)** Whole-embryo views of wildtype embryos with clones expressing *bmp2b/7-sfGFP*, *squint-mVenus* or mouse *bmp4*. Embryos were fixed 30 min post-transplantation and immunostained with anti-pSmad2 (green) or anti-pSmad5 (red) antibodies. Bmp2b/7-sfGFP and Squint-mVenus were stained with anti-GFP (blue) antibodies, and transplanted mouse *bmp4*-expressing cells were pre-labeled with cascade blue-dextran (blue). Scale bar: 150 µm.

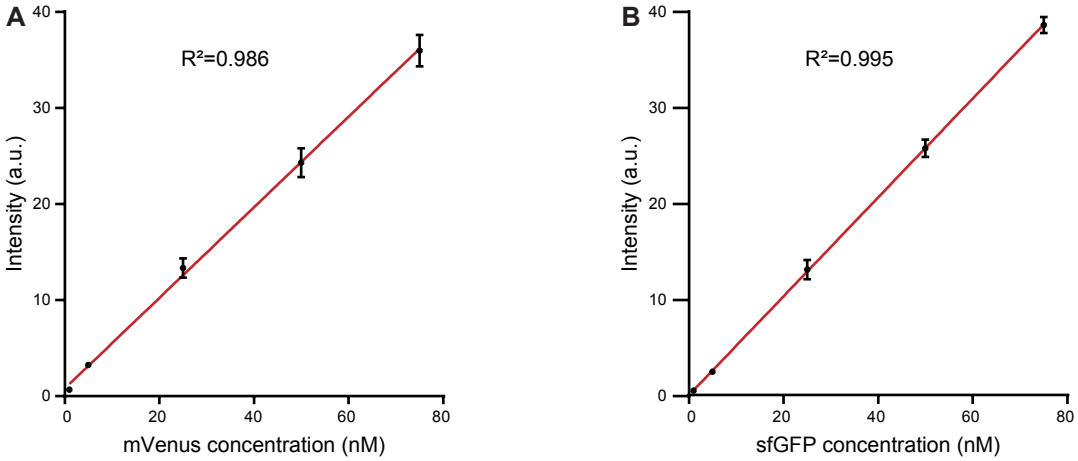

Figure S4. Calibration curves for recombinant mVenus and sfGFP to relate fluorescence intensities to concentrations, Related to Figure 2. (A,B) Calibration curves were generated for (A) recombinant mVenus (n[1 nM]=11, n[5 nM]=11, n[25 nM]=11, n[50 nM]=10, n[75 nM]=11) and (B) recombinant sfGFP (n[1 nM]=11, n[5 nM]=11, n[25 nM]=11, n[50 nM]=10, n[75 nM]=10) by applying increasing concentrations of the proteins onto a coverslip, mounting the sample on a confocal microscope, and imaging with the same settings as those that were used to image zebrafish embryos. The error bars in both graphs represent 95% confidence intervals around the mean (black dots). The red lines are linear fits that match the data with the indicated R^2 values.

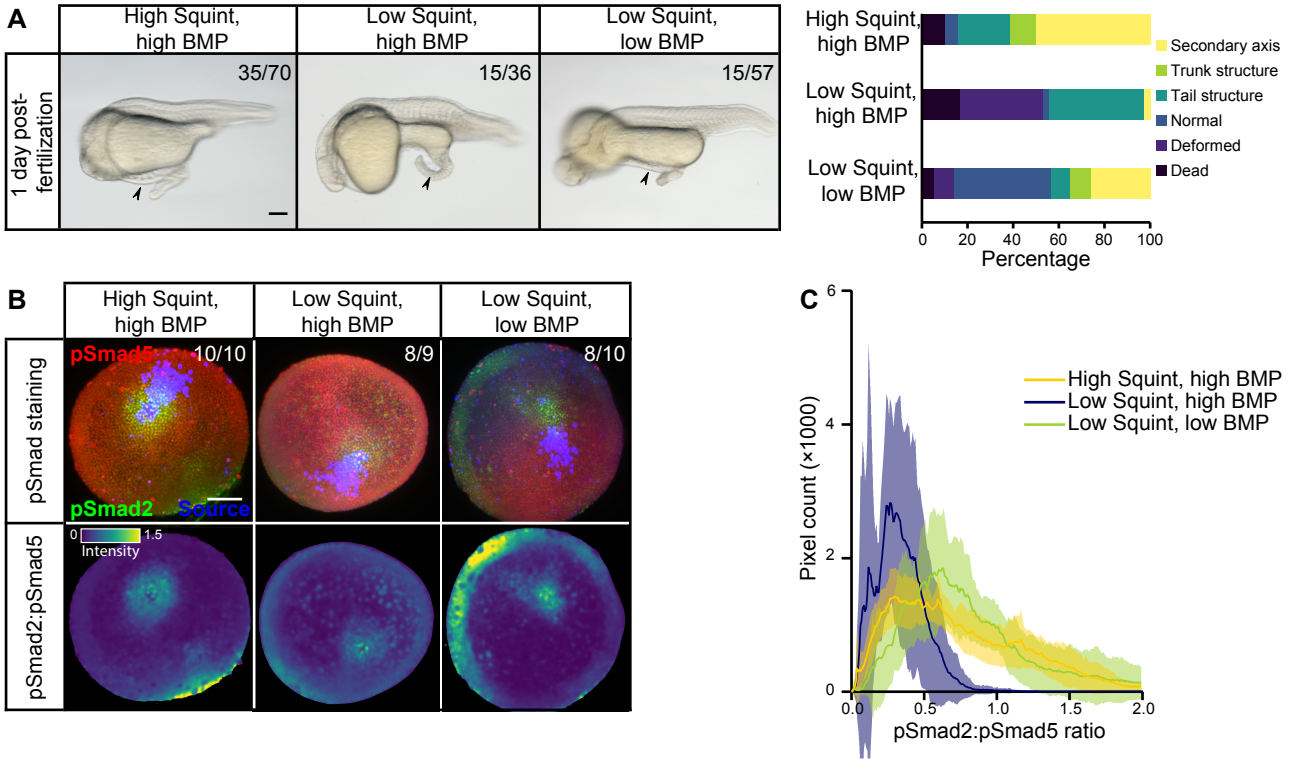

Figure S5. Nodal:BMP signaling ratios, rather than absolute signaling levels, underlie secondary axis formation, Related to Figure 4. (A) Embryonic phenotypes at 24 h post-transplantation and frequency of different structures induced by clones expressing various amounts of Bmp2b/7-sfGFP and Squint-mVenus. High Squint, high BMP: 100 pg *squint-mVenus* mRNA and 100 pg + 100 pg *bmp2b/7-sfGFP* mRNA (n=70); Low Squint, high BMP: 20 pg *squint-mVenus* mRNA and 100 pg + 100 pg *bmp2b/7-sfGFP* mRNA (n=36); Low Squint, low BMP: 20 pg *squint-mVenus* mRNA and 20 pg + 20 pg *bmp2b/7-sfGFP* mRNA (n=5). The arrowheads point to secondary axes or ectopic structures. Scale bar: 150 µm. **(B)** Double clones with various amounts of Bmp2b/7-sfGFP and Squint-mVenus generated as in (A), but immunostained for pSmad2 and pSmad5 at early gastrula stages. The lower panel shows the pSmad2:pSmad5 ratios. Scale bar: 150 µm. **(C)** Histogram of pSmad2:pSmad5 ratios from the pSmad2-positive region induced by Nodal clones in embryos generated as in (B). High Squint, high BMP: n=10; Low Squint, high BMP: n=6; Low Squint, low BMP: n=6. The shaded regions indicate 95% confidence intervals around the mean (lines).

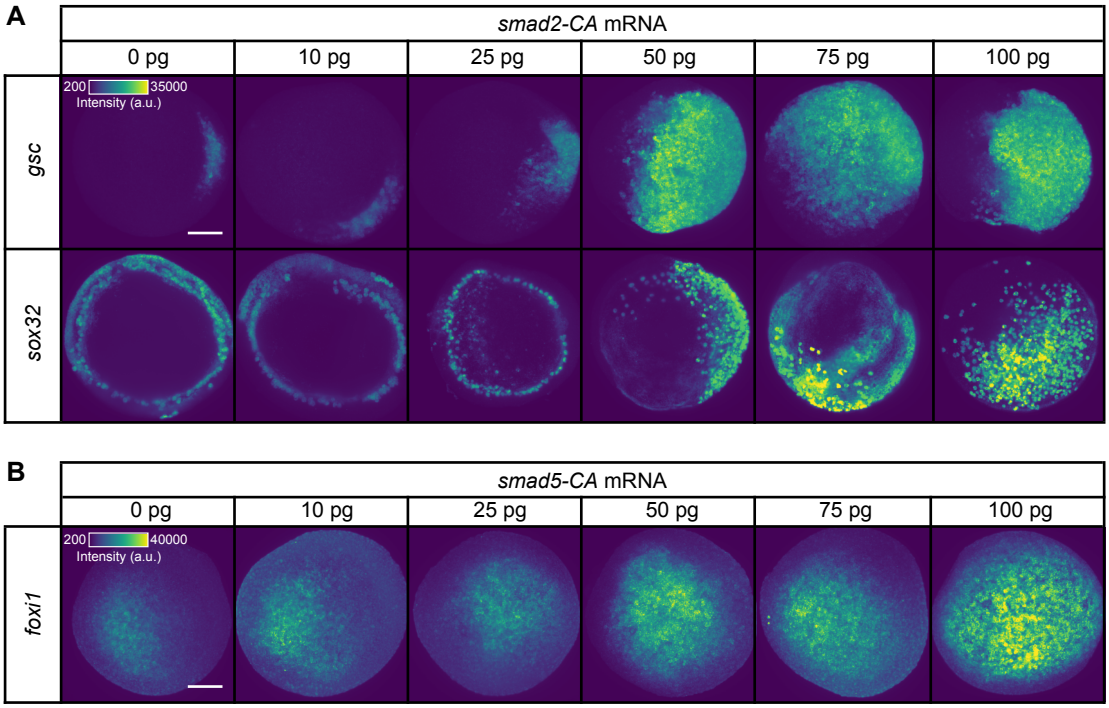

Figure S6. Constitutively active Smad2-CA and Smad5-CA activate Nodal and BMP target genes in a dose-dependent manner, Related to Figure 5. (A) Embryos were injected with increasing amounts of *smad2-CA* mRNA, and the expression of the Nodal target genes *gsc* (n[0 pg]=7, n[10 pg]=7, n[25 pg]=10, n[50 pg]=3, n[75 pg]=10, n[100 pg]=6) and *sox32* (n[0 pg]=7, n[10 pg]=7, n[25 pg]=9, n[50 pg]=5, n[75 pg]=10, n[100 pg]=7) was assessed by fluorescence *in situ* hybridization (FISH). Each experimental group gave rise to similar expression patterns. Scale bar: 150 µm. (B) Embryos were injected with increasing amounts of *smad5-CA* mRNA, and the expression of the BMP target gene *foxi1* (n[0 pg]=7, n[10 pg]=8, n[25 pg]=9, n[50 pg]=6, n[75 pg]=9, n[100 pg]=7) was assessed by FISH. Each experimental group gave rise to similar expression patterns. Scale bar: 150 µm.